

Photocatalytically Active Aerogels – Development and Characterization of (Semi-)Crystalline Titania

Inaugural-Dissertation
zur Erlangung des Doktorgrades
der Mathematisch-Naturwissenschaftlichen Fakultät
der Universität zu Köln



vorgelegt von
M.Sc. Alexandra Stefanie Rose
aus Herrenberg

Köln, 2023

Die vorliegende Arbeit wurde von der Mathematisch-Naturwissenschaftlichen
Fakultät der Universität zu Köln als Dissertation angenommen.

Gutachter:	Prof. Dr. Barbara Milow Prof. Dr. Mathias Wickleder
Vorsitzender Beisitzer:	Prof. Dr. Elmar Behrmann Dr. Pascal Vöpel
Tag der mündlichen Prüfung:	12. Dezember 2023

“To infinity and beyond!”
Buzz Lightyear, Toy Story

Acknowledgement

An dieser Stelle möchte ich mich bei Prof. Barbara Milow bedanken, die mir die Durchführung dieser Arbeit ermöglicht hat.

Prof. Mathias Wickleder danke ich herzlich für die Übernahme des Zweitgutachtens.

Ein besonderer Dank gilt Dr. Pascal Vöpel für die fachliche Betreuung meiner Doktorarbeit, sowie für die stets hilfreichen fachlichen Diskussionen und Ideen, was im Wesentlichen zum Gelingen meiner Arbeit beigetragen hat.

Insbesondere bedanke ich mich bei meiner Mentorin Prof. Marion Bartsch, die mir in jeder Phase der Promotion für fachliche Diskussion, oder mit Hilfestellungen und Rat zur Seite stand.

Dr. Klemens Kelm danke ich für die Unterstützung meiner XRD und TEM-Analysen und den wertvollen fachlichen Austausch.

Dr. Joachim Gussone und Prof. Guillermo Requena danke ich für die Unterstützung bei der Beantragung der Synchrotron-Messzeit und meiner WAXS/SAXS-Versuche. In diesem Zusammenhang möchte ich bei Benjamin Ignatzi, Hemangi Patel und Prakul Pandit bedanken, für die Unterstützung bei der Durchführung der Synchrotron-Messungen in Hamburg. Ebenfalls möchte ich den Wissenschaftlern am DESY in Hamburg für die Begleitung der Versuche und Unterstützung bei der Auswertung danken, besonders Dr. Peter Staron und Dr. Emad Maawad.

Dr. Peter Mechnich und Alexander Francke danke ich für die Unterstützung bei den Rietveld Messungen und Auswertung am XRD. Frederic Kreps danke ich für die Unterstützung am TEM.

Allen Kollegen der Abteilung Aerogele, besonders Thomas Anklam, Philipp Niemeyer und Dr. Danny Bialuschewski möchte ich für die angenehme Zusammenarbeit und die vielfachen Hilfestellungen und Unterstützung danken.

Meinen damaligen Studenten Sebastian Schumacher und Paul Kuschmitz möchte ich für ihren Beitrag zu dieser Arbeit danken.

Besonders danken möchte ich meinen Kollegen Dr. Adam Dzierbinski, Janine Wischek und Rebekka Probst, die mir jederzeit mit Rat und Tat zur Seite standen.

Dr. Anja Hofmann der Universität Bayreuth danke ich für die UV-Vis- und photokatalytischen Messungen sowie die tolle Zusammenarbeit.

Der größte Dank geht an meinen Ehemann Daniel, meinen Sohn Yoshua, meinen Vater sowie an meine beste Freundin Julia, die mir über die Dauer meiner Promotion den Rücken freigehalten, mich ermutigt, und mich vom Arbeitsalltag abgelenkt haben.

Abstract

Novel sol-gel based synthesis routes for (semi-)crystalline titania (TiO_2) aerogels were developed to achieve materials for photocatalytic applications. The influence of different synthesis parameters, *e.g.* amount of acid, type and amount of solvent, and the amount of water, was investigated with regard to adjust the crystallinity and maximize the surface area. TiO_2 aerogels are mainly amorphous and are commonly calcinated to obtain crystalline phases which are requirements for an efficient photocatalyst. This thesis provides an alternative strategy to synthesize (semi-)crystalline TiO_2 aerogels without calcination and thus to maintain the porous 3D structure. The synthesized aerogels were characterized regarding the crystallinity, phase composition, pore characteristics, and electronic properties to evaluate the impact of the synthesis parameters. Besides the structural properties, the crystallization process and formation of different phases were investigated.

It was found that the aerogel properties can be selectively controlled and adjusted by the chosen synthesis parameters. The crystallinity increases with the amount of acid used during the synthesis, while the surface area decreases; however, in much less extent compared to calcination in air or vacuum. The use of concentrated hydrochloric acid (conc. HCl) leads to macropores and broadens the pore size distribution compared to the narrow pore size distribution achieved in mesoporous calcined aerogels. Supported by scattering experiments, the increasing HCl content leads to changes in the hydrolysis and condensation reaction kinetics, by protons and chloride ions which alter the three-dimensional (3D) gel network. It is assumed that chloride ions from the HCl coordinate differently to the used titantetraisoopropoxide (TTIP) precursor dependent on the steric hindrance of the alkoxy ligands. The usage of different solvents led to a ligand exchange of the titanium-based precursor. This was assumed to lead to different intermediate complexes with coordinated chloride ions which act as template for the formation of either nanocrystalline anatase or mixtures of anatase-brookite. Dependent on the used solvent, semi- or completely crystalline aerogels could be achieved. High water:precursor ratios were observed to influence the formed phases. Analyses performed using X-ray photoelectron spectroscopy (XPS) and X-ray diffraction (XRD) experiments indicate the presence of defects and Ti^{3+} in the aerogel and support the assumption that chloride ions coordinate to the titanium-based precursor but were also incorporated into the TiO_2 crystal lattice leading to differently favored phases.

In-situ analysis methods revealed that both the anatase and brookite nanocrystals grow during aging of the wet gels within a time of three to seven days. The ratio of amorphous to crystalline

content of the wet gels can be controlled by varying the amount of acid and the aging time to achieve precisely a crystallinity from completely amorphous to completely crystalline.

A defined pore size distribution with pore diameters between 10 and 50 nm can be achieved by usage of pure solvents or ethanol-isopropanol (EtOH-*i*PrOH) solvent mixtures, based on the ligand exchange at the titanium-based precursor and presumably on changes in precursor cluster size. The coordination of both isopropoxy (OiPr) and ethoxy (OEt) groups to the titanium precursor are assumed to stabilize also the structural integrity of the obtained aerogel.

TiO₂ aerogels processed with a calcination step and the newly developed synthesis route, respectively, were successfully applied, in cooperation with the University of Bayreuth, for photocatalytic hydrogen generation and for the nitrogen reduction reaction to ammonia. The calcined aerogels, which were completely crystalline, were able to produce more hydrogen compared to the non-calcined semi-crystalline aerogel, that can be assigned to the higher charge carrier mobility and the narrower band gap of crystalline aerogels and consequently improved generation of electron-hole pairs. On the other hand, the non-calcined semi-crystalline TiO₂ aerogel exhibited superior storage properties of photogenerated electrons after irradiation with ultraviolet (UV) light because of the improved charge carrier separation based on structural properties of the aerogel. Based on the developed TiO₂ aerogel synthesis, mixed metal oxide-based and doped aerogels were successfully synthesized with a very homogeneous elemental distribution, confirmed by transmission electron microscopy (TEM). The measured positions and estimated width of the band gaps of the synthesized mixed metal oxide-based and doped aerogels fit to the reduction potential of hydrogen, so that they are theoretically as well able to photocatalytically generate hydrogen.

Zusammenfassung

Neuartige Sol-Gel-basierte Synthesewege wurden zur Herstellung von (teil-)kristallinen Titandioxid-Aerogelen für photokatalytische Anwendungen entwickelt. Für einen effizienten Photokatalysator ist eine hohe Kristallinität bei gleichzeitig hoher spezifischer Oberfläche gefordert. Eine hohe Kristallinität wird üblicherweise durch Kalzinieren erzielt, wobei jedoch die spezifische Oberfläche stark abnimmt. In dieser Arbeit wird eine zur Kalzinierung alternative Strategie zur Synthese von (teil-)kristallinen Titandioxid-Aerogelen vorgestellt, bei der die poröse 3D-Struktur der Aerogele erhalten bleibt. Systematisch untersucht wurde der Einfluss verschiedener Syntheseparameter, wie die Säure- und Wassermenge sowie Art und Menge des Lösungsmittels, auf die Kristallinität, die Zusammensetzung der entstandenen Phasen, die spezifische Oberfläche, die Poreneigenschaften und die elektronischen Eigenschaften, die alle für die photokatalytischen Eigenschaften von Bedeutung sind. Neben den strukturellen Eigenschaften der hergestellten Aerogele wurden die Kristallisation und die Bildung verschiedener Phasen während der Synthese durch *in-situ* Experimente untersucht.

Die Eigenschaften der Aerogele konnten durch die Auswahl der Syntheseparameter selektiv gesteuert werden. So steigt mit der Menge der eingesetzten Salzsäure die Kristallinität der Aerogele, jedoch nimmt die spezifische Oberfläche ab, allerdings in weitaus geringerem Maße als durch Kalzinierung an Luft oder im Vakuum. Die Verwendung von Salzsäure führt zu Makroporen und zu einer breiten Porengrößenverteilung. Im Vergleich dazu führt eine Kalzinierung von Aerogelen zu Mesoporen und einer schmaleren Porengrößenverteilung. Streuexperimente zeigten, dass der steigende Säuregehalt, und somit die steigende Konzentration an Protonen und Chloridionen, zu Veränderungen in der Gelationskinetik (Hydrolyse- und Kondensationsreaktionen) führt, wodurch der Vernetzungsgrad und die Flexibilität des 3D-Gelnetzwerks beeinflusst werden. Röntgenografische Untersuchungen deuten darauf hin, dass Chloridionen aus der Salzsäure in Abhängigkeit von der sterischen Hinderung der Alkoxy-Liganden unterschiedlich an den eingesetzten Titan-basierten Precursor koordinieren, wobei die Verwendung verschiedener Lösungsmittel einen Austausch der Alkoxy-Liganden des Precursors zur Folge hat. Als Resultat können unterschiedliche Zwischenkomplexe mit koordinierten Chloridionen gebildet werden, die als Template für die Bildung einer nanokristallinen Anatas-Phase oder eines Anatas-Brookit Phasengemisches dienen. Diese Chloridionen können auch in das TiO₂-Kristallgitter eingebaut sein, worauf röntgenspektroskopische Untersuchungen und Absorptionsmessungen hindeuten. Die Ergebnisse zeigen ebenso das Vorhandensein von Defekten und Ti³⁺ im Aerogel.

In Abhängigkeit des gewählten Lösungsmittels und der eingesetzten Säuremenge werden teil- oder vollständig kristalline Aerogele synthetisiert. Weiterhin wirkt sich bei hohen Verhältnissen von Wasser zu Precursor die Menge des für die Hydrolyse eingesetzten Wassers auf die Phasenbildung und die Porenverteilung aus. *In-situ* Analysemethoden zeigten, dass sich sowohl Anatas- als auch Brookit-Nanokristalle in den nassen Gelen bei deren Alterung in einem Zeitraum von zwei bis sieben Tagen bilden und wachsen. Das Verhältnis zwischen amorphem und kristallinem Anteil kann durch die Säuremenge und durch Variation der Alterungszeit gesteuert werden, um eine selektive und präzise Kristallinität der Gele von vollständig amorph bis vollständig kristallin zu erreichen.

Unter Verwendung von reinen Lösungsmitteln (Ethanol oder Isopropanol) oder Lösungsmittelmischungen kann in Abhängigkeit des Ligandenaustauschs der Alkoxygruppen am Titan-basierten Precursor eine definierte Porengrößenverteilung mit Porendurchmessern zwischen 10 und 50 nm erreicht werden. Durch die Wahl des Lösungsmittels werden aufgrund der unterschiedlichen sterischen Hinderung der Liganden bei der Synthese vermutlich unterschiedliche Clustergrößen erreicht, was sich auf die Porenstruktur auswirkt. Die Koordination von Alkoxy-Gruppen an den Titan-basierten Precursor dürfte auch Einfluss auf die Stabilität des überkritisch getrockneten Aerogels haben.

Die TiO₂-Aerogele wurden in Kooperation mit der Universität Bayreuth erfolgreich für die photokatalytische Wasserstofferzeugung und für die Stickstoffreduktionsreaktion zu Ammoniak eingesetzt. Mit den kalzinierten, vollständig kristallinen Aerogelen konnte im Vergleich zu den nicht wärmebehandelten teilkristallinen Aerogelen mehr Wasserstoff erzeugt werden, was auf die höhere Ladungsträgerbeweglichkeit und die schmalere Bandlücke in kristallinen Aerogelen und die dadurch verbesserte Erzeugung von Elektron-Loch-Paaren zurückzuführen ist. Insbesondere das nicht wärmebehandelte teilkristalline TiO₂-Aerogel zeigte nach Bestrahlung mit UV-Licht eine besondere Speicherkapazität für photogenerierte Elektronen, was auf die verbesserte Ladungstrennung durch die strukturellen Eigenschaften des Aerogels zurückzuführen ist. Auf der Grundlage der entwickelten TiO₂-Aerogel-Syntheseroute wurden erfolgreich Mischoxide und dotierte Aerogele synthetisiert, welche eine homogene Verteilung des zusätzlichen Metalloxides oder der entsprechenden Dotierungselemente im Titanoxid-Aerogel aufweisen. Die experimentell bestimmte Lage und Breite der Bandlücken der hergestellten Mischoxide und dotierten Aerogele erfüllen die Anforderungen an das Reduktionspotential von Wasserstoff, so dass sie theoretisch ebenfalls in der Lage sind, auf photokatalytischem Weg Wasserstoff zu erzeugen.

Contents

Abstract.....	IX
Abbreviations.....	XVII
1 Introduction	1
2 State of the Art.....	5
2.1 Titanium Oxide	5
2.1.1 General, Applications and Synthesis	5
2.1.2 Crystal Structures, Properties and Phase Transitions of TiO ₂	5
2.1.3 Crystallization Mechanism of TiO ₂ Nanoparticles in Sol-Gel Processes.....	6
2.2 Aerogels.....	9
2.3 Titanium Oxide Aerogels	11
2.3.1 General Synthesis of TiO ₂ Aerogels.....	11
2.3.2 Synthesis of Doped Aerogels and Mixed Metal Oxide Aerogels.....	13
2.3.3 Alkoxide-Based Sol-Gel Process.....	13
2.3.4 Influence of Different Synthesis Parameters on Final Aerogel Structure.....	18
2.4 Aerogels as Photocatalysts: Requirements and Material Development Approaches ..	22
2.4.1 Photocatalysis	22
2.4.2 Requirements and Strategies for Metal Oxide-Based Photocatalyst	24
2.4.3 Photocatalytic Active Materials for Hydrogen Generation	31
2.4.4 Advantages and Disadvantages of Aerogels as Photocatalysts	34
3 Synthesis of TiO₂ Aerogels.....	35
3.1 Preparation of Aerogels.....	35
3.1.1 General Synthesis Route and Parameter Variation.....	35
3.1.2 Calcination of Selected EtOH Solvent-Based Aerogels	36
3.2 Synthesis of Mixed Metal Oxide Aerogels	36
3.2.1 SnO ₂ -TiO ₂ and V ₂ O ₅ -TiO ₂ Aerogels	36
3.2.2 MoS ₂ -TiO ₂ and GO-TiO ₂ Aerogels	37
4 Characterization Methods	39
4.1 Structural Properties	39
4.1.1 Gelation and Shrinkage Behavior	39
4.1.2 Optical Microscopy	39
4.1.3 Physisorption Measurements.....	39
4.1.4 Pycnometry and Porosity Determination.....	40
4.1.5 Scanning Electron Microscopy (SEM) and Transmission Electron Microscopy (TEM) ..	40
4.1.6 X-ray Diffraction and Scattering	41
4.1.7 Raman Spectroscopy	43
4.1.8 Nuclear Magnetic Resonance Spectroscopy (NMR)	44
4.2 Electronic Properties	44
4.2.1 X-ray Photoelectron Spectroscopy (XPS)	44
4.2.2 Ultraviolet Photoelectron Spectroscopy (UPS)	44
4.2.3 Ultraviolet-Visible Diffuse Reflectance Spectroscopy (UV-Vis DRS)	44
4.3 Photocatalytic Activity.....	45
4.3.1 Photocatalytic Hydrogen Evolution.....	45

4.3.2	Photocatalytic Nitrogen Reduction.....	46
5	Results.....	47
5.1	Synthesis Procedure and Gelation Behavior of TiO₂ Wet Gels.....	47
5.1.1	Gelation and Shrinkage Behavior.....	47
5.2	Structural Properties of TiO₂ Aerogel.....	51
5.2.1	Appearance of TiO ₂ Aerogels.....	51
5.2.2	Surface and Pore Characteristics.....	57
5.2.3	Density and Porosity.....	67
5.2.4	Morphology.....	70
5.2.5	Crystallinity and Phase Formation of Aerogels.....	79
5.2.6	Verification and Formation of Crystalline Phases.....	87
5.2.7	Crystallinity and Phase Formation of Wet Gels.....	92
5.2.8	Analysis of the Nanostructure of Wet Gels.....	98
5.3	Chemical Composition.....	107
5.3.1	EtOH and <i>i</i> PrOH Solvent-Based Aerogels.....	107
5.3.2	Calcined Aerogels.....	110
5.4	Electronic Properties.....	112
5.4.1	Band gap and Position of Valence Band.....	112
5.5	Photocatalytic Activity.....	113
5.5.1	Photocatalytic Hydrogen Generation.....	113
5.5.2	Electron Storage Capability.....	114
5.5.3	Photocatalytic Reduction of Nitrogen to Ammonia.....	116
5.6	Mixed Metal Oxide and Doped Aerogels.....	117
6	Discussion.....	121
6.1	Impact of Synthesis Parameters on Gelation Kinetics and Shrinkage.....	121
6.1.1	Gelation Kinetics.....	121
6.1.2	Shrinkage.....	128
6.1.3	Separation of Hydrolysis and Condensation Reaction.....	130
6.2	Impact of Synthesis Parameters on Structural Properties.....	131
6.2.1	Appearance of Wet Gels and Aerogels.....	131
6.2.2	Surface and Pore Characteristics.....	133
6.2.3	Morphology and Particles Size.....	138
6.3	Impact of Synthesis Parameters on Crystallinity and Phase Content.....	145
6.3.1	Crystallinity.....	145
6.3.2	Crystallite Size and Crystal Growth.....	148
6.3.3	Crystallization Process and Phase Content.....	149
6.4	Chemical and Electronic Properties and Structural Defects.....	159
6.4.1	Chemical Composition.....	159
6.4.2	Electronic Properties.....	161
6.4.3	Structural Defects and Ti ³⁺ Defect Analysis.....	162
6.5	Evaluation of TiO₂ Aerogel as Catalyst for Photocatalytic Applications.....	165
6.6	Towards Mixed Metal Oxide and Doped TiO₂ Aerogels.....	168
7	Summary and Outlook.....	171
8	References.....	176

9	Appendix.....	XVIII
9.1	Chemicals.....	XVIII
9.2	Synthesis Parameters.....	XVIII
9.2.1	EtOH Solvent-Based Aerogels.....	XVIII
9.2.2	<i>i</i> PrOH Solvent-Based Aerogels.....	XIX
9.2.3	Mixed Solvent-Based Aerogels.....	XX
9.2.4	Calcined Aerogels.....	XX
9.3	Preliminary Experiments of <i>i</i>PrOH Solvent-Based Aerogels.....	XXI
9.3.1	Gelation and Shrinkage Behavior.....	XXI
9.3.2	Density and Porosity.....	XXII
9.3.3	Surface and Pore Characteristics.....	XXIII
9.3.4	Crystallinity and Phases.....	XXIV
9.4	XRD Reference Reflection Positions.....	XXV
9.5	Ethanol Solvent-Based Aerogels Using Different Solvent Purities.....	XXVIII
9.6	SAXS Curve Fits.....	XXIX
9.6.1	Wet Gel E2.....	XXIX
9.6.2	Wet Gel E5.....	XXX
9.7	XPS.....	XXXI
9.7.1	Aerogel Sample E5.....	XXXI
9.7.2	Aerogel Sample <i>i</i> P2.....	XXXII
9.7.3	Aerogel Sample <i>i</i> P5.....	XXXIII
9.7.4	Calcined Aerogel Sample E2-A-300.....	XXXIV
9.7.5	Calcined Aerogel Sample E2-V-300.....	XXXV
9.8	UV-Vis/DRS – Tauc Plots and Kubelka-Munk Plots.....	XXXVI
9.9	¹H-NMR.....	XXXVII
9.10	Mixed Metal Oxides.....	XXXIX
9.10.1	Appearance.....	XXXIX
9.10.2	SEM images.....	XL
9.10.3	TEM images.....	XL
9.10.4	Physisorption results.....	XLIII
9.10.5	Crystallinity.....	XLIV
9.10.6	Chemical Composition.....	XLIV
9.10.7	Band Gap and VB Edge.....	XLIX
9.11	Eidesstattliche Erklärung.....	LI
9.12	Publications and Conferences.....	LII
9.13	Zugänglichkeit von Daten und Materialien.....	LIII
9.14	Lebenslauf.....	LIV

Abbreviations

a	slope
Absol.	Absolute
aq.	aqueous
at.%	Atom percent
a.u.	Arbitrary unit
BET	Brunauer-Emmett-Teller method
BF	Bright field
BJH	Barett-Joyner-Halenda method
CB	conduction band
COD	Crystallography Open Database
Conc. HCl	Concentrated hydrochloric acid
CTAB	cetyltrimethylammonium bromide
CuK α	Copper K α ; type of radiation used for X-Ray diffraction
CoK α	Cobalt K α ; type of radiation used for X-Ray diffraction
d	days
DF	Dark field
DRS	diffuse reflectance spectroscopy
E ⁰	Electrode potential
E _F	Fermi level
E _g	Band gap energy
EtOH	ethanol
eV	electron volt
<i>i</i> PrOH	isopropanol
g	gaseous
GO	graphene oxide
h	hours
<i>h</i> · <i>v</i>	Radiation energy (Planck constant·wave number)
HPLC grade	High performance liquid chromatography grade
IUPAC	International Union of Pure And applied Chemistry
l	liquid
MEK	methylethylketone
min	minutes
MoIP	Molybdenum isopropoxide
NHE	Normal hydrogen electrode
NMR	Nuclear magnetic resonance
OBu	butanolate/butoxide
OEt	ethanolate/ethoxide
O <i>i</i> Pr	<i>iso</i> -propanolat/isopropoxide
p/p ⁰	Partial pressure
PDF	Powder diffraction file
PEM	proton-exchange membrane

r	radius
RF	Resorcinol-formaldehyde
R _G	Radius of gyration
s	seconds
SAXS	Small angle X-ray scattering
S _{BET}	Specific surface area
sc	Supercritical
SEM	Scanning electron microscopy
SHE	Standard hydrogen electrode
SnTIP	Tin tetraisopropoxide
STEM	Scanning transmission electron microscopy
T	Temperature
TTBT	Titanetrautoxide
TEM	transmission electron microscopy
TTE	Titanetraethoxide
TTIP	Titanetraisopropoxide
UPS	Ultra violet photoelectron spectroscopy
UV light	Ultraviolet light
VB	valence band
vis light	Visible light
VOIP	Vanadium oxytriisopropoxide
V _p	Pore volume
WAXS	Wide angle X-ray scattering
wt. %	weight percentage
XPS	X-Ray photoelectron spectroscopy
XRD	X-Ray diffraction
0D	Zero-dimensional
1D	One-dimensional
2D	Two-dimensional
3D	Three-dimensional

1 Introduction

Many states are striving for climate neutrality before 2050. Since aviation is contributing about 3 % of the worldwide CO₂ emission, zero-emission energy carrier are very important and envisaged by aircraft manufacturers. ^[1, 2] The Airbus ZEROe concepts comprise hybrid-hydrogen aircrafts with a liquid hydrogen tank for combustion in gas turbine engines and complementary hydrogen fuel cells for electrical power generation. ^[1] However, less than 1 % of the hydrogen is to date produced in a climate neutral way. ^[3, 4] One main challenge is to tackle the high demand of green hydrogen for fueling future aircrafts. Therefore, clean technologies are required to efficiently generate hydrogen. Green hydrogen can be produced by different processing routes. One way is the proton-exchange membrane (PEM) fuel cell electrolysis of water, which has an efficiency of approx. 65 %. ^[5] However, expensive catalysts, such as iridium catalysts, are required. ^[6] Also, developing such catalysts is difficult, as suitable materials have often short lifetimes due to the corrosive environment in the PEM fuel cells. ^[6] Another possibility is to use solar light to photocatalytically split water into hydrogen and oxygen. This requires a catalyst with suitable electronic properties and microstructure. Extensive research has been done to develop and design suitable nanostructured photocatalyst materials, but the achieved efficiency for hydrogen generation is still low. ^[7] But what defines a good and efficient catalyst? Highly efficient photocatalytic materials depend on many different factors which contribute to the final efficiency of the materials. The crystallinity and crystal structures are crucial for high photocatalytic activity. The crystal structure is closely linked with the band gap, which is specific for each material and determines how much light can be utilized for photocatalytic reactions. This requires band gap engineering of the material. The band gap of a semiconductor describes the electronic structure, how electron-hole pairs can be generated by irradiation with photons. These electron-hole pairs can be further used for hydrogen production. Besides, the microstructure of a material plays also an important role in developing an efficient photocatalyst and in reducing the recombination of photogenerated charge carriers. ^[7] The particle size, specific surface area, and the porosity, which are very special in aerogels, bring many important aspects along for development of new photocatalysts.

Many photocatalytic active materials, such as titanium dioxide (TiO₂) with a band gap of 3.2 eV, can only absorb light in the ultraviolet (UV) range, below 390 nm. However, this is only 2 % of the solar light. Theoretically, wavelengths below 1000 nm could be used, which

would require materials (*e.g.* inorganic materials or hybrids) with a corresponding band gap of 1.2 eV. Even wavelengths below 600 nm could enhance the efficiency to exploit solar light up to 16 %.^[8] For comparison, the efficiency of photovoltaics is about 17 %. With subsequent electrolysis of water to form green hydrogen, the efficiency of the process is reduced to 10 %.^[9] Therefore, there is a huge need of innovation to develop new photocatalysts on the basis of inorganic systems or hybrids, to increase the amounts of generated hydrogen with an efficient light absorption above 10 % but also to improve the stability of catalytic materials for technical usage.

Nanostructured materials *e.g.* nanoparticles are favored for photocatalytic reactions, since the small particles have very large surface areas, which facilitate the transfer of photogenerated electron-hole pairs to the surface of the particles and enhance the surface reactions with adsorbates. However, nanoparticles tend to agglomerate, so that only the outer surface of the particles can be penetrated by UV-light. The aggregation of nanoparticles and limitation of existing photocatalyst to exploit efficiently UV-light can be addressed by using three-dimensional (3D) nanostructured and porous aerogels as catalysts which allow sufficient light transmission through the material. Aerogels exhibit high surface areas and an open porosity. The sol-gel process is a prominent technique to synthesize such aerogels by first forming a gel from precursors and then obtaining by supercritical drying an aerogel with nanoporous structures within a network of interconnected mesopores.^[10] In this work, aerogels are synthesized with regard to improve the photocatalytic activity on the basis of TiO₂. The focus of this work is on the development of new adjustable sol-gel synthesis routes for photocatalytically active amorphous and (semi-)crystalline TiO₂ aerogels, which are doped and functionalized in a second step with other elements (*e.g.* SnO₂, MoS₂, V₂O₅) for tuning electronic, physical, and chemical properties. Aerogels are mainly amorphous, but photocatalysis requires crystalline materials. By controlling the sol-gel process for synthesizing aerogels, different materials can be designed having suitable specific surface area, pore volume, electronic structures, morphology and crystallinity. The synthesis parameters to control the aerogel properties were mainly studied for sol-gel based nanoparticles, which are treated differently during synthesis and drying. Crystalline aerogels without calcination and phases besides anatase have been rarely reported. The degree of crystallinity and the crystal phase are important for photocatalysis, especially for the generation of electron-hole pairs, while the surface area of a material or particle plays an important role for the catalytic reactions on the surface. Both parameters are therefore crucial for photocatalytic applications.^[11-13] A challenge

is to achieve crystallinity in simple synthesis routes without a calcination step, to avoid substantial reduction of the surface area. This work aims at the following main objectives:

- Development of a simple and low-cost synthesis route based on the sol-gel process to synthesize highly porous, amorphous to crystalline TiO₂ aerogels without calcination as basic material for photocatalytic applications.
- Optimizing of synthesis parameters (water (H₂O), hydrochloric acid (HCl), solvent) and characterization of the resulting gels and aerogels with respect to the surface and pore characteristics and crystallinity.
- Evaluation of strategies other than calcination to increase the crystallinity without reducing the surface area of TiO₂ aerogels, and elucidating the gelation kinetics by means of small angle X-ray scattering (SAXS).
- Investigation of crystallization processes during synthesis in the wet gel and its mechanisms with *in-situ* wide-angle X-ray scattering (WAXS) and Raman measurements.
- Determination of electronic properties and investigation of photocatalytical suitability of exemplary aerogel samples for hydrogen generation.
- Development of new sol-gel routes for mixed metal oxide or doped metal oxide aerogels on the basis of the synthesis route developed for TiO₂ aerogels but with improved interconnection of the particles by forming heterojunctions or by introducing new energy levels in the TiO₂ aerogels band gap, *e.g.* SnO₂-TiO₂, MoS₂-TiO₂, V₂O₅-TiO₂, Graphene oxide (GO)-TiO₂.

The new metal oxide-based aerogels are investigated for generating solar green hydrogen with the aim to refueling previously mentioned aircrafts. Since, the aerogels are extremely light weight materials with high porosity and high electron mobility, they can also serve as catalyst support in combination with *e.g.* iridium catalysts, improving the performance of fuel cells on board of the hybrid-hydrogen aircrafts. However, the latter aspect will not be addressed in this dissertation.

2 State of the Art

2.1 Titanium Oxide

2.1.1 General, Applications and Synthesis

Titanium oxide with the chemical formula TiO_2 is a transition metal oxide, occurring naturally as a white inorganic compound which is used as nanomaterial or pigment in different applications. As white pigment TiO_2 has been used in paints, printing inks, plastics, ceramics, paper, but also in drugs or cosmetics. ^[14, 15] TiO_2 is non-toxic, odorless, tasteless and due to its natural occurrence attractive for the mentioned applications. In Europe more than one million tons of TiO_2 are produced. ^[15] Since August 2022, TiO_2 is forbidden as food additive in Europe due to concerns about possible genotoxicity of TiO_2 . However, scientific evidence is missing. ^[15-17] In 2024, the European Medicines Agency will decide about TiO_2 as additive in drugs. Extensive research has been carried out for TiO_2 in many other applications, *e.g.* sensors, photovoltaics, and photocatalysis. ^[14] Especially, TiO_2 nanoparticles are due to their morphological and electronic properties promising for many photocatalytic applications, such as water purification, degradation of organic compounds, decarbonization, antibacterial agents, and environmental-friendly production of hydrogen or ammonia. ^[14]

Different TiO_2 nanostructures, *e.g.* TiO_2 nanoparticles ^[18], nanofibers ^[19], nanorods ^[20], thin coatings ^[21, 22], and aerogels ^[23-25], can be synthesized using various methods. Commonly used methods are the sol-gel process ^[26], hydrothermal ^[27] or solvothermal methods ^[28], physical ^[29] or chemical vapor deposition ^[20], spin/dip coating, ^[21, 22] and electro spinning. ^[19] Some procedures include already elevated temperatures to achieve crystalline TiO_2 phases. Other methods are realized at low temperatures, which result in amorphous TiO_2 structures and require calcination at higher temperatures to achieve crystalline phases. The crystallinity is crucial for photocatalysis in generating electron-hole pairs. ^[12, 13]

2.1.2 Crystal Structures, Properties and Phase Transitions of TiO_2

TiO_2 appears in different polymorphs in nature. The most common polymorphs are anatase, rutile, and brookite. They all consist of the same TiO_6^{2-} octahedral building blocks, which are connected differently leading to different arrangements of these octahedra. The crystal structures of the polymorphs are presented in Figure 2.1-1.

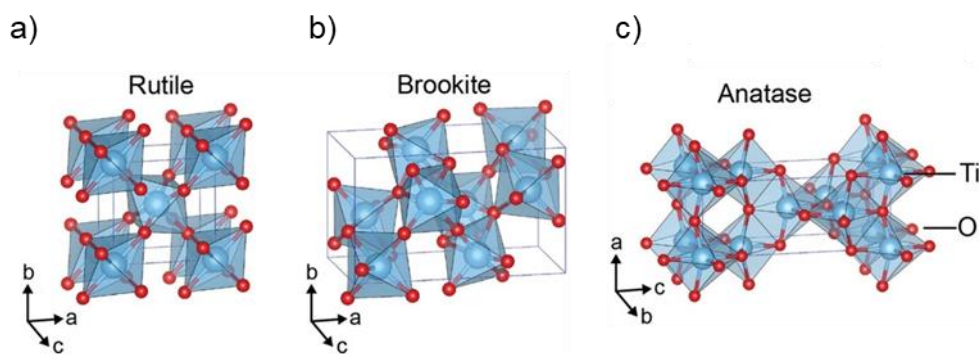


Figure 2.1-1: Unit cells of a) rutile TiO_2 , b) brookite TiO_2 and c) anatase TiO_2 . Large blue and small red spheres are Ti^{4+} and O^{2-} ions, respectively. ^[30]

The crystal structures show 6-fold coordinated titanium with surrounding oxygen atoms. The octahedra are sharing edges or corners depending on the crystal structure. Anatase and rutile exhibit a tetragonal whereas brookite exhibits an orthorhombic crystal structure. Rutile forms linear chains of octahedra by corner sharing. In anatase crystal structure the octahedra are edge-shared. ^[31, 32] Brookite consists of octahedra which share both edges and corners. ^[33]

Anatase and brookite are metastable and transform to rutile at elevated temperatures (600 to 800 °C). Rutile is thermodynamically the most stable polymorph, however, anatase is more stable at room temperature under atmospheric conditions. ^[30, 31, 34] Anatase can transform to brookite or rutile dependent on the initial particle size, which determines the thermodynamic phase stability for nanocrystalline systems. ^[35] The phase stability correlates therefore to the particle surface area and surface energy, respectively, since the surface area is dependent on the particle size. Anatase is found to be stable for small particles in the nanoscale below 11 nm, brookite between 11 and 35 nm, whereas for large particles above 35 nm rutile formation is favored. ^[36] Similar data of the particle size dependent phase formation was reported elsewhere. ^[30] Generally, anatase and rutile are used for the in chapter 2.1.1 mentioned applications, especially in photocatalysis.

2.1.3 Crystallization Mechanism of TiO_2 Nanoparticles in Sol-Gel Processes

Many researchers have studied the sol-gel synthesis with numerous different synthesis approaches to produce TiO_2 nanoparticles. Different parameters of the sol-gel synthesis which affect the structural properties and crystallinity of the nanoparticles are reported in literature. ^[37-43] These parameters include pH value of water-based synthesis, type of solvent in solvent-based synthesis, temperature, precursor concentration, type and concentration of catalyst and drying approach. Crystallization is described to occur mostly during the drying process and not

during the synthesis. High temperature calcination treatments or even drying at ambient conditions leads due to grain coarsening to a trade-off between sample crystallinity and surface area. Especially, the solvent-removal process for sol-gel prepared nanomaterials plays a major role for crystallization, leading to overestimation of the crystallinity of as-prepared (non-dried) samples.^[37] There are some reports about aqueous sol-gel processes for TiO₂ synthesis to obtain nanoparticles with crystallinities up to 85-90 % at low temperature (<100 °C) by usage of the peptization method.^[38] Peptization is defined as the “acid treatment used to transform the macroscopic oxide precipitates into colloidal particles via hydrolysis and condensation reactions”.^[44] This procedure is common for synthesizing TiO₂ nanoparticles and is applied in order to prevent agglomeration. This needs to be clearly distinguished from TiO₂ aerogels, where an interconnected highly porous gel is formed, but. agglomeration is prevented in the aerogel synthesis by a different strategy. Further, the fast precipitation step of large particles is missing for synthesizing TiO₂ aerogels.

Generally, anatase and mixed phase TiO₂ nanoparticles can be synthesized in sol-gel process by precipitation of an alkoxide or chloride precursor with excess of water. Brookite is difficult to synthesize, since it is a metastable phase. Most efficient methods to synthesize brookite nanoparticles are the sol-gel process or hydrothermal procedures supported by the usage of helper ions such as chloride ions^[40], NaOH^[39], other alkali ions^[41], or adjusting the pH value during hydrothermal processes^[42]. It was reported that by using TiCl₄ in water-based synthesis a complex of [Ti(OH)₂(Cl)₂(OH₂)₂]⁰ could be an intermediate precursor for brookite.^[40] However, the reported processes and mechanisms to grow crystalline TiO₂ nanoparticles do not lead to consistent results.

To obtain crystalline TiO₂ nanoparticles, the precipitated amorphous TiO₂ particles are slowly dissolved in the peptization agent (*e.g.* acid) and further nucleation and growth of crystalline TiO₂ occurs, *e.g.* by heating up to 95 °C. High concentration of TiO₂ precipitates results in high nucleation rate to form crystallites.^[45] This favors the formation of anatase and brookite instead of rutile, which forms during slow crystallization.^[45] However, in a different study rutile formed at high precursor concentrations and at 40 °C after short reaction times, whereas anatase and brookite formed at the same temperature and low precursor concentrations in long synthesis times.^[46]

This shows that different crystalline phases can be obtained for TiO₂ nanoparticles by precipitation, peptization of the particles with subsequent drying and calcination leading to *e.g.* anatase or brookite formation. Crystallization of amorphous TiO₂ occurs by nucleation and

crystal growth. This can be achieved by usage of a peptization agent or at elevated temperatures in a precipitation-dissolution process, calcination in a gaseous atmosphere, Teflon-lined autoclavation at high temperatures (*e.g.* 220 °C), and the high pressures occurring in hydrothermal processes.^[47] The crystallization conditions have an impact on the crystallization mechanism and the resulting crystal structure.^[48]

In comparison to the synthesis of TiO₂ nanoparticles, Moussaoui *et al.* synthesized nanocrystalline TiO₂ xerogels and aerogels powders using the sol-gel approach. The aerogel was supercritically dried in solvent at 300 °C and 100 bar and appeared to be crystalline.^[49] Supercritical drying at low temperature in CO₂ ($T_{\text{critical}} = 31$ °C, $P_{\text{critical}} = 73.8$ bar) leads to amorphous aerogels, whereas high pressures (> 100 bar) and temperatures (> 265 °C) during hot supercritical drying or temperatures above 80 °C at ambient pressure may induce crystallization. The high pressure can influence the crosslinked network, whereas at temperatures of 300 °C typical anatase phase formation was reported also elsewhere.^[49, 50] Hot supercritical drying also leads to the decomposition of residual carbon or organic groups which remain in the gel after synthesis.^[50] In literature, it was reported that a conventionally dried (200 °C, ambient pressure) xerogel exhibited crystalline structures, showing anatase and brookite. They have used HNO₃ during synthesis. The acid was reported to electrostatically charge the hydroxylated titanium agglomerates formed by van der Waals forces. These agglomerated can be broken into smaller particles by peptization. Further, stirring or reflux at *e.g.* 100 °C can be performed to increase the number of collisions between particles and consequently the probability of the crystallization processes. This favors the formation of metastable phases such as anatase or brookite. Without acid the fast growth of the agglomerates leads to amorphous particles.^[49] The type of catalyst has an influence on the type of formed phases and their crystallinity. This was also reported by Moussaoui *et al.* They observed a slower crystallization process to anatase when using NH₄OH instead of HNO₃. No brookite is observed when using NH₄OH. Typical weight fractions of anatase and brookite when using HNO₃ were found to be 65.2 % and 34.8 % respectively.^[49] It was also reported that HNO₃ favors pure anatase phase whereas HCl favors a mix of anatase and brookite.^[51] HCl is less used due to observations that it favors the rutile phase.^[52]

The pH value was reported to influence the crystallinity of TiO₂ nanoparticles as well as the achieved phases, when using TiCl₄ as precursor. The brookite content was reported to increase with decreasing pH value.^[53] Li *et al.* prepared mixed phase TiO₂ nanocomposites using a solvothermal method varying the HCl:Ti ratio and found different mixed phase compositions

dependent on the HCl:Ti ratio. ^[28] In the case of alkoxide precursors, the crystallinity and formed phases are dependent on the amount and type (acid-or base type) of the peptizing agent. ^[38] Anatase-brookite mixtures (brookite content of 46 to 65 %) were reported to be synthesized using Ti(IV)-n-propoxide and lactic acid at 80 to 100 °C. With varying acid-precursor ratios different heterophases were achieved. ^[54] Anatase-brookite nanoparticles were reported elsewhere. ^[55]

Song *et al.* investigated the acid- or base-catalyzed synthesis of TiO₂ powder at different pH values for the sol-gel reaction of titanium alkoxide when dried at 150 °C for 24 hours. They found that phase transitions from amorphous to anatase and anatase to rutile highly depend on the type of catalyst. ^[56] To obtain a high anatase fraction HNO₃ is used. HCl was reported to favor rutile formation, which is less photocatalytically active. ^[57]

This shows that there are sometimes contradictory results due to the large variety to change the reaction parameters and involved chemicals.

In water-based synthesis routes, the crystallization and phase formation are catalyzed by water. Water can adsorb on the surface of TiO₂ leading to many octahedra with hydroxyl (OH) groups. These in turn form bridges leading to rearrangement of amorphous TiO₂ to crystalline phases. ^[58] In solvent-based synthesis routes the solvent plays an important role, as it affects the crystalline phase and microstructure, as well as the appearance of the gels. Dependent on the chain length, the polarity, and the steric hindrance of the used solvent different leading to different crosslinking paths, which might influence the possible formation of complexes with titanium-based precursors. Further, the gel time and transparency are affected by the solvent properties. ^[21]

2.2 Aerogels

Aerogels are 3D, open-porous, nanomaterials which exhibit several outstanding properties, such as very large surface areas, very low densities and high porosities. Kistler invented the first (silica) aerogel 1931 by removing the liquid of the gel without or little shrinkage of the gel, which mostly occurs in the case of drying under ambient conditions. ^[59] He used a closed autoclave for the drying process in which the pressure and the temperature is raised above the critical conditions. The supercritical liquid turns during subsequent pressure reduction into a gas which can be further removed from the aerogel without damaging the microstructure of the material. Damages to the microstructure are generally caused by capillary forces which act at the surface of the pores or pore walls of the materials and lead to collapse of the porous network

and thus shrinkage. Kistler defined aerogels as “gels in which the liquid was replaced with a gas, without collapsing the gel solid network”.^[59] In contrast, Nicola Hüsing used in 1998 a longer definition for aerogels. She first stated that “all materials prepared from wet gels by a special drying process, the supercritical drying technique, were called aerogels irrespective of their structural properties.” However, as new drying methods are further developed to prevent shrinkage of the porous structure, this definition might be no longer valid. Her second statement was “materials in which the typical structure of the pores and the network is largely maintained (which is not always the case for supercritical drying) while the pore liquid of a gel is replaced by air are called aerogels”.^[10] According to the International Union of Pure and Applied Chemistry (IUPAC) (2007) the definition of an aerogel is a “gel comprised of a microporous solid in which the dispersed phase is a gas”.^[60] The original aerogel definition by Kistler was taken over by A.C. Pierre in the *Aerogel Handbook* from 2011.^[61] This demonstrates that there is no uniform definition of aerogels. Recently, Smirnova and Gurikov defined an aerogel as an “open colloidal or polymeric network consisting of loosely packed, bonded particles or fibers that is expanded throughout its volume by a gas and therefore exhibits very low density and high specific surface area”.^[62] This definition does not include the synthesis and drying method but focus on the properties which define an aerogel.

The specific properties of aerogels stem from the microstructure of the solid network. Typical properties of aerogels are a high porosity (80 to 99.8 %), a very low bulk density (0.004 to 0.5 g·cm⁻³), a low thermal conductivity (0.017 to 0.021 Wm⁻¹·K⁻¹), a high surface area (100 to 1600 m²·g⁻¹), high pore volumes and defined pore size distribution.^[10]

Aerogels can be synthesized using the sol-gel process. However, there are also other aerogel preparation methods to achieve similar physico-chemical properties. The focus will be on the sol-gel method, as it is used in this work. A gel can be formed by hydrolysis and condensation of sol colloidal particles, *e.g.* alkoxide precursors, which are dispersed in a liquid. The sol-gel synthesis can be water-based or alcohol-based. The resulting gel is then called hydrogel or alcogel, respectively. The reactions and mechanism of gelation are described in section 2.3.3. After gelation, the gels are aged to strengthen the structure before they are finally dried. Besides supercritical drying, other drying techniques can be applied, *e.g.* freeze-drying which leads to so-called cryogels and ambient drying to achieve xerogels.^[10] Aerogels may be synthesized as monolithic body or may disintegrate into fragments, as well be processed as coatings or as powder. Their appearance ranges from translucent to opaque.^[23, 63, 64]

Aerogels can be made from many kinds of chemical systems or different materials which form a gel. *E.g.*, many achievements were made on the preparation of resorcinol-formaldehyde (RF) and carbon aerogels, ^[65] biopolymeric aerogels, ^[66] and inorganic metal oxide aerogels such as, silica (SiO₂) ^[67] or TiO₂ ^[25]. Further, aerogel composites are realized for combining different physico-chemical properties. The research aims at the development of aerogels, *e.g.* as light-weight materials with thermal insulating and acoustic damping properties for buildings or aircrafts, ^[68-71] wound dressing aerogels ^[72], biodegradable aerogels for medical usage ^[73], for energy-related applications such as batteries, ^[74] supercapacitors, ^[75] or as materials for (photo)catalytic processes ^[76].

In photocatalytic applications, *e.g.* for photocatalytic hydrogen production, TiO₂ aerogels can be used. This was shown by Fujishime and Honda in 1972, who used TiO₂ electrodes for photocatalytic water splitting. ^[77] TiO₂ aerogels were first mentioned by Teichner *et al.* in 1976. ^[78] They are synthesized using alkoxide precursors, similar to silica aerogels. This is further explained in detail in chapter 2.3.3. TiO₂ aerogels are suitable for photocatalytic processes but are typically amorphous after drying under supercritical conditions in CO₂, which means that crystalline phases have to be obtained by subsequent heat-treatment. ^[76, 79]

2.3 Titanium Oxide Aerogels

2.3.1 General Synthesis of TiO₂ Aerogels

The sol-gel process is a prominent technique to synthesize 3D materials such as aerogels, which provide several advantages compared to the other mentioned methods. ^[25] The sol-gel process is a simple method and requires no complex setup, as the synthesis can be carried out at ambient pressures and temperatures. ^[10] Also, several synthesis parameters can be varied to control the nanoscale structure and physicochemical properties. ^[25, 56] Generally, a titanium precursor is mixed with solvent, acid and water to form a wet gel. This wet gel exists of a 3D network which is further build up during the aging processes. After aging the pore liquid is replaced by air *e.g.* by freeze drying, vacuum drying or supercritical drying in CO₂, ethanol (EtOH) or isopropanol (*i*PrOH). This is required for receiving mesoporous structures, exhibiting pore sizes of 15 to 50 nm and should prevent these pores to collapse. ^[10] There are several synthesis strategies to achieve TiO₂ aerogels. They differ in the titanium-based precursor and gelation mechanism that can be used, the solvent, assisted methods and different drying methods.

As titanium (Ti) precursor metal alkoxides (M-OR; M=metal, O=oxygen, R= organic residue) or metal chlorides are commonly used for sol-gel reactions. For example, Schäfer *et al.* investigated the synthesis of TiO₂ aerogels using a titanium chloride precursor and received amorphous aerogels with specific surface areas ranging from 466 to 733 m²·g⁻¹ dependent on reaction mixtures.^[80] As metal chlorides TiCl₄ or TiCl₃ can be used. They are typically used in a water-based synthesis but also solvent-based synthesis procedures *e.g.* in EtOH are reported in literature.^[24, 80, 81] Titanium chlorides are cheaper compared to titanium alkoxides, due the availability. Bernardes *et al.* investigated a water-based synthesis using TiCl₃ in a one-step synthesis. They achieved similar specific surface areas up to 735 m²·g⁻¹.^[81] However, often propylene oxide as gelation accelerator is used, which is toxic and cancerous and thus not favorable for upscaling and industrial usage.^[24, 80-82]

Metal alkoxides, *e.g.* titantetraisopropoxide (TTIP, Ti(OC₃H₇)₄) or titantetraethoxide (TTE, Ti(OC₂H₅)₄) are less toxic and do not require other dangerous chemicals apart from simple acidic catalysts and solvents, *e.g.* HNO₃ and EtOH. Sadriyeh *et al.* investigated the synthesis of TiO₂ aerogels using a titanium alkoxide precursor and received amorphous mesoporous aerogels with specific surface areas ranging from 436 to 655 m²·g⁻¹ dependent on reaction mixtures.^[79] Alkoxides are used in an alcohol-based synthesis routes to produce aerogels. They can also be used to synthesize TiO₂ nanoparticles, based on precipitation, which is water-based. Different solvents and catalysts can be used, which have an impact on the structure of the final aerogel, besides other reaction conditions. Typically, HNO₃ is used as catalyst for the hydrolysis reaction. For TiO₂ nanoparticle synthesis HCl is reported in literature to favor the rutile phase instead of anatase during calcination.^[51, 52] In this work alkoxide precursors were used, which will be explained in more detail in the following chapter.

Aerogels can also be prepared by pre-formed TiO₂ nanoparticles in an assembly method. Luna *et al.* and Kwon *et al.* prepared TiO₂ nanoparticle-based aerogels for photocatalytic hydrogen generation. The advantage of this method is that a higher crystallinity of the aerogels can be achieved by preparing already crystalline TiO₂ nanoparticles. The gelation was induced via irradiation with UV-light.^[64, 83] However, a second complex process is required to synthesize the TiO₂ nanoparticles beforehand, and is a very extensive procedure compared to classical sol-gel methods using alkoxides.^[64, 83] Titania aerogels can also be synthesized using TiOSO₄ in similar synthesis procedures to achieve high surface areas up to 1085 m²·g⁻¹.^[84] Other synthesized aerogels exhibited high surface areas but amorphous structures, which require post heat-treatment for a higher crystallinity.^[25, 31, 41, 79, 84, 85] . Specific surface areas up

to $450 \text{ m}^2 \cdot \text{g}^{-1}$ and high pore volumes up to $4.4 \text{ cm}^3 \text{ g}^{-1}$ could be achieved. [64, 83] The gelation rates can also be increased by usage of ultrasonic-assisted sol-gel method. [86] Different drying methods were reported to achieve aerogels, which include supercritical drying in supercritical CO_2 , [79] supercritical EtOH or *i*PrOH, [49, 50, 87] subcritical drying [88] or vacuum drying [86].

2.3.2 Synthesis of Doped Aerogels and Mixed Metal Oxide Aerogels

The sol-gel process can be used to introduce dopants into the aerogels or to synthesize mixed metal oxide aerogels. For doping, precursors such as copper nitrate ($\text{Cu}(\text{NO}_3)_2 \cdot 3\text{H}_2\text{O}$), cobalt nitrate ($\text{Co}(\text{NO}_3)_2 \cdot 3\text{H}_2\text{O}$) or iron nitrate ($\text{Fe}(\text{NO}_3)_3 \cdot 9\text{H}_2\text{O}$) are used, which require thermal treatment after the synthesis. [22, 89, 90] Other metal salts *e.g.* SnCl_4 or alkoxide precursors such as tin isopropoxide (SnTIP), molybdenum isopropoxide (MoIP) or vanadium oxytriisopropoxide (VOIP) can be used to synthesize mixed metal alkoxides. [90-94] However, many alkoxide precursors are solid and very sensitive to water, so special solvents or weak/diluted solution are required and they need to be handled with care under protective atmosphere to prevent premature hydrolysis. [95] For some alkoxides it is also difficult to obtain high purity and is therefore dissolved in suitable solvents, that consequently changes the reaction kinetics. Also, a titanium alkoxide precursor can be used in combination with inorganic salts or nanoparticles using the precipitation and impregnation method to synthesize such mixed metal nanoparticles. [89, 96, 97] Some alkoxide precursors *e.g.* MoIP form final =O groups in typical solvents *e.g.* EtOH or *i*PrOH which hinder the condensation reaction. Special solvents *e.g.* acetonitrile are therefore required, which make it difficult for comparison and combination with other alkoxide precursors, such as TTIP. [98] It is also important to consider that interparticle connection is key factor of highly active photocatalysts. Therefore the synthesis procedure needs to be reconsidered in the case that solid precursors or additives are used, because it might be more difficult to achieve a homogeneous distribution, whereas liquid precursors could lead to integrated structures. [28]

2.3.3 Alkoxide-Based Sol-Gel Process

To synthesize materials such as TiO_2 , alkoxide precursor can be chosen. Precursors are available having different alkoxy ligands, such as TTIP or TTE. The alkyl ligand has an impact on the reactivity of the hydrolysis reaction. The TTE precursor is more reactive compared to the TTIP precursor and is due to the inductive effect of the alkyl group on the Ti atom. This

effect is increasing for longer alkyl groups, as the electrophilic character or positive partial charge of the metal atom decreases. ^[43] Also the steric hindrance is increasing for longer alkyl groups that reduces the sensitivity to water. ^[21] The reactivity of the precursors increases as follows $\text{Ti}(\text{O}i\text{Pr})_4 < \text{Ti}(\text{O}i\text{Pr})_4 < \text{Ti}(\text{OEt})_4$. ^[21, 43] It was also described in literature, that alkyl ligands can be exchanged by excess of a different solvent, *e.g.* TTIP dissolved in EtOH leads to a ligand exchange of the *OiPr* with OEt groups. ^[99]

In comparison to silica precursors, titanium alkoxide precursors are not present as monomers. The Ti atom in precursors such as $\text{Ti}(\text{OR})_4$ are Lewis acids and the alkyl ligands are Lewis bases. This leads to aggregation of precursor molecules forming oxo-bridges or complexes. ^[41, 99] The degree of aggregation affects the reactivity of the precursor. Clusters were formed dependent on the size of the alkyl group, *e.g.* TTE in EtOH was described in literature forming clusters consisting of five to nine Ti atoms, whereas TTIP in solution forms clusters with 11 to 12 Ti atoms. ^[43] The cluster formation is shown as an example in Figure 2.3-1a. The cluster size depends also on the used solvent, as the solvent molecules can also coordinate to the Ti atom. The interaction of solvent molecules, which are Lewis bases, with the Ti atom reduces the tendency to aggregation by forming oxo-bridges. The coordinated alcohol molecules are stabilized by hydrogen bonding to surrounding alkyl ligands at the Ti atom. ^[99] This is shown as an example in Figure 2.3-1b. Silicon (Si) alkoxides are independent from the added solvent during the synthesis, and exist as monomeric molecules. This is due to the fact, that Si has a smaller covalence radius of 117 pm compared to Ti 132 pm and higher electronegativity of 1.90

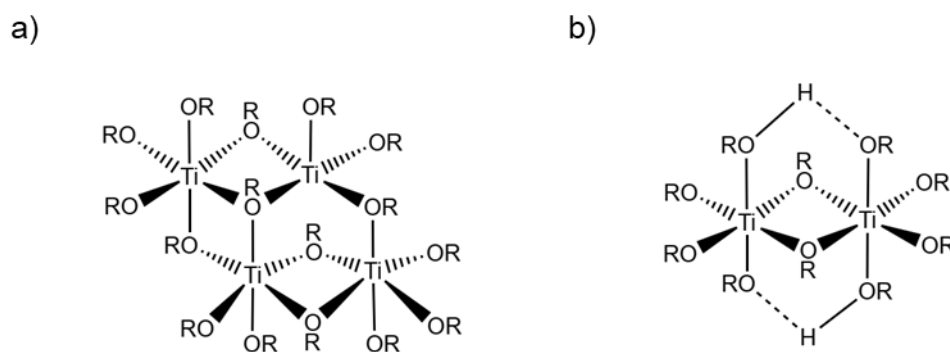


Figure 2.3-1: a) Chemical structure of $\text{Ti}_4(\text{OR})_{16}$ ($\text{R}=\text{Me},\text{Et}$) and b) alcohol adduct $\text{Ti}_2(\text{OR})_8(\text{ROH})_2$ with hydrogen bonds between coordinated alcohol molecule and neighboring OR substituent. ^[99]. Used with permission of Royal Society of Chemistry, from Chemical modification of titanium alkoxides for sol-gel processing, Ulrich Schubert, *J. Mater. Chem.*, 2005, 15, 3701-3715; permission conveyed through Copyright Clearance Center, Inc.

(Ti 1.54). This difference lead silicone to be tetrahedrally coordinated exhibiting four covalent bonds. Ti is mostly octahedrally coordinated, forming stable chemical compounds with higher and variable coordination numbers, like 5- or 6-fold coordination. This occurs by coordination of compounds having a non-binding electron pair (here referred to as lone pair), *e.g.* anions or chelating complexes, Lewis bases or bridging groups between Ti atoms. ^[99, 100]

The tendency to form the previously mentioned adducts increases with increasing Lewis acidity of the Ti center. This in turn can be achieved by increasing the electronegativity of the ligands. Chloride ions, for example, possess a lone pair and can act as Lewis base. Chloride ions additionally coordinated to the Ti atom or replacing an alkyl ligand leads to an increase of the Lewis acidity of the Ti atom. ^[99]

The reactivity of the alkoxide is therefore dependent on the first mentioned properties, *e.g.* electronegativity of the central metal atom. The electronegativity of the central metal atom decreases for isopropoxides as follows: ^[10, 101]



With decreasing electronegativity of the metal atom, the difference to the electronegative oxygen gets larger, leading to more polar and therefore more reactive species. This makes Zr(OiPr)_4 more sensitive for nucleophilic attack during the hydrolysis reaction. ^[101] It is therefore required to introduce catalysts for some alkoxy precursors to increase the reactivity, whereas other alkoxy precursors are combined with larger complexing agents or other synthesis parameters to reduce the reactivity, *e.g.* diols, β -diketonates, carboxylic acids, amines, or other organic groups. Complexing agents can also influence to condensation reaction and crosslinking reactions, due to the size and conformation of the complexing ligands. ^[41]

The sol-gel reaction is a two-step process in which a sol is prepared by molecular precursors. For the synthesis *e.g.* metal alkoxides are added into a solvent-catalyst-water mixture, which react in a hydrolysis and condensation reaction forming a wet gel. ^[43] Alkoxides are very sensitive to humidity and can hydrolyze partially in air. ^[41]

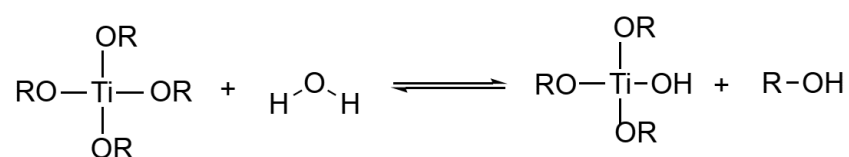


Figure 2.3-2: Hydrolysis of Ti(OR)_4 with water and formation of Ti-OH bonds.

In a first step (Figure 2.3-2) the alkoxide $M(OR)_z$ (M =metal oxide, O =oxygen, R =alkyl group, z =valency of metal) reacts with water forming $Ti-OH$ bonds. This occurs by a nucleophilic attack of water to the Ti atom, shown in the reaction mechanism (1) in Figure 2.3-3. This is due to the Lewis acidity of Ti . In step (2) of the reaction mechanism an unstable intermediate is formed by an intramolecular proton transfer from water to the alkyl ligand. The protonated alkyl ligand is eliminated as an alcohol (3). Dependent on the amount of water, this reaction happens partially or to all alkyl ligands leading to fully hydrolyzed products of $Ti(OR)_{4-x}(OH)_x$ and $Ti(OH)_4$.^[102]

However, condensation reaction occurs simultaneously to the hydrolysis reaction without catalyst. Therefore, the rate of hydrolysis can be modified by adding catalysts or complexing agents. The hydrolysis and condensation reaction rate are dependent on the synthesis temperature, type of alkoxide and concentration, used solvent, amount of water and amount and type of catalyst *e.g.* an acid. These synthesis parameters influence the final gel structure and is later discussed in chapter 2.3.4.

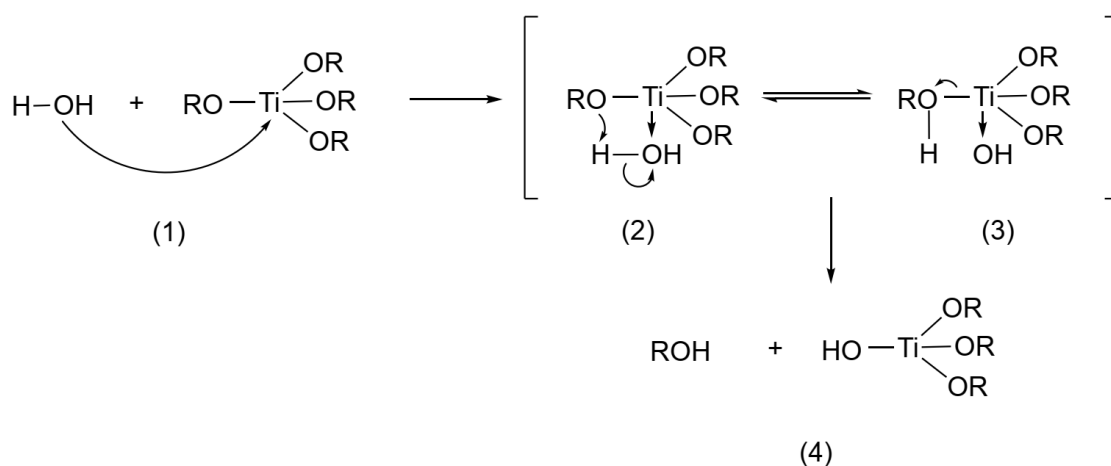


Figure 2.3-3: (1) Nucleophilic attack of water to $Ti(OR)_4$ and substitution reaction. (2) Intermediate is formed by an intramolecular proton transfer from water to the alkyl ligand. (3) The protonated alkyl ligand is eliminated as an alcohol. (4) Partially or fully hydrolyzed products of $Ti(OR)_{4-x}(OH)_x$ and $Ti(OH)_4$.^[37] Reproduced with permission from Springer Nature.

The reaction can be acid- or base catalyzed, varying the pH value, which has an impact on the hydrolysis and condensation reaction rate. The hydrolysis reaction can be catalyzed using inorganic acids (*e.g.* HNO₃, HCl), organic acids (*e.g.* acetic acid) or bases. Using bases, the hydrolysis and condensation reaction occurs simultaneously. This is due to the reduced acidic character of the Ti atom during the nucleophilic addition which includes the first step of the condensation reaction. When using inorganic acids, only the hydrolysis reaction rate is increased independently from the condensation reaction, whereas organic acids reduce the hydrolysis and condensation reaction due to the formation of chelating complexes.^[102, 103] At low pH value the hydrolysis reaction is catalyzed by the acidic conditions, leading to an increase of the partial positive charge of the OR group attached to the Ti atom, as it is protonated. The OR group is released while the OH group attaches to the metal ion, due to repulsive forces between the positively charged titanium metal ion. Acid also decreases the condensation reaction rate, due to decreased interactions of protonated species.^[31]

After hydrolysis the OH groups condense forming linked Ti-O-Ti by oxolation (Figure 2.3-4) and alcoxolation (Figure 2.3-5) reactions. Water and alcohol are released during the reaction, respectively.^[37]

Dependent on the reaction conditions mentioned above, different material structures can be obtained, so that the sol-gel process can be used to synthesize nanoparticles by precipitation, colloidal particles and gels.^[104] The pH value has been reported in literature to influence the structure. This is due to the increased or decreased rates of the hydrolysis and condensation reactions leading to different rate of particle growth. This effect was reported independent of the type of alkoxide precursor.^[43]

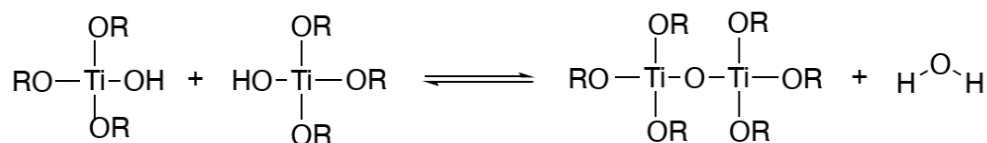


Figure 2.3-4: Formation of Ti-O-Ti bonds by oxolation with release of water.

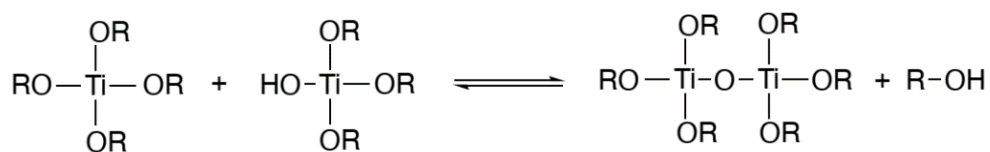


Figure 2.3-5: Formation of Ti-O-Ti bonds by alcoxolation with release of an alcohol.

At pH value of 7 or without addition of acid or base during the reaction, $\text{Ti}(\text{OR})_4$ reacts strongly with water producing titania hydroxides and hydrous oxide precipitates. [99]

Also, at basic conditions the condensation reaction is increased leading to precipitation of TiO_2 nanoparticles. At low pH value the particle formation was reported to be very slow. The hydrolysis reaction is catalyzed under acidic conditions and the condensation reaction slowed down due to protonation of OH groups of Ti atom. Transparent gels can be formed under acidic conditions. Also, protonated clusters with positive surface charges prevents aggregation because of repulsion forces. At very low pH values it was reported that only sols can be formed, due to very slow condensation reaction, so that clusters cannot condense together. [43] It has been reported that the type of titanium precursor also has an impact on the formed structure during synthesis. This can be traced back to the previously formed clusters which serve as building blocks for structures. As described before, these clusters can have different sizes, steric hindrance and reactivity dependent on the alkyl groups at the Ti atom.

Also, in the case of complexing ligands, the number of OR groups is crucial for crosslinking and forming a gel. With fewer OR groups, there are less sites for the hydrolysis reaction and further condensation reaction forming a gel. Also, a minimum quantity of water (three H_2O per TTIP molecule) or hydrolysis level is required to form an interconnected network. [99, 105] However, complexing ligands can influence the condensation path, that can be advantageous, and might support the formation of different crystalline phases and control the arrangement of TiO_6 octahedra. [41] However, aerogels are mainly amorphous or show very few crystals, as they are synthesized using the sol-gel process at low temperature. [31, 41, 79, 85] The typical high solvent content used in the sol-gel synthesis to produce aerogels, prevents aggregation of small particles. Steric and electrostatic interactions also separate these particles. The solvent can be considered as isolating organic layer on the metal surface. [106-108]

2.3.4 Influence of Different Synthesis Parameters on Final Aerogel Structure

There are several parameters and sol-gel synthesis steps, which influence the properties of the final aerogel. These steps include: synthesis/forming the wet gel; aging process; drying process; and post-treatments. Parameters during synthesis, *e.g.* amount of water, type and amount of solvent, pH value, as well as post-synthesis parameters, *e.g.* calcination temperature and duration, have been studied previously, which are described in this chapter. These parameters have an impact on physical properties, *e.g.* the specific surface area, crystallinity, particle sizes and the photocatalytic activity highly depends on the physical properties.

Regarding the first step of the sol-gel synthesis procedure, the gel formation, the water content, solvent, acid and precursor concentration play a major role. The water content can be equated with the hydrolysis level. A high hydrolysis level is required for further condensation to form a 3D network. Higher amounts of water to the reaction mixture lead to stable gels (TTIP:H₂O 1:7.35), whereas low precursor-water ratios lead to unstable gels (TTIP:H₂O 1:3.75), which dissolve. Sadriyeh *et al.* investigated the precursor-water ratio for the acid-catalyzed synthesis of TiO₂ aerogel based on TTIP precursor, using HNO₃ and EtOH (TTIP:EtOH:HNO₃:H₂O 1:21:0.08:3.75-9). They showed that the specific surface area increases proportional with the amount of water. Surface areas of 436 to 655 m²·g⁻¹ of the TiO₂ aerogels could be achieved. The pore volume (0.52 to 2.25 cm³·g⁻¹) and pore size distribution (4.8 to 14.1 nm) were found to be independent from the water amount. Also the gelation time was affected by the water content, which was faster with higher water amount.^[79] This can be explained by coordination of water to the precursor, due to excessive water at some points, leading to an increased reactivity.^[109] Higher surface areas with higher water and solvent amount were also found by Baia *et al.*^[23] Similar values for the surface area were found elsewhere.^[25, 86]

The type of solvent and acidic catalyst used in the synthesis play also an important role for the final aerogel structure. Boujday *et al.* investigated the effect of typically used acids, HNO₃ and HCl, on the physico-chemical properties of TiO₂ aerogels, as well as the impact of different solvents (precursor:solvent:HNO₃:H₂O 1:11(EtOH)/18(*i*PrOH):0.08:2-3). They found that the aerogels synthesized with hydrochloric acid and *i*PrOH showed higher specific surface areas and pore volumes compared to the aerogels synthesized with HNO₃ and EtOH.^[110]

The type of solvent and additional surfactants might play a role to achieve crystalline aerogels. Most TiO₂ aerogel are synthesized using EtOH or *i*PrOH, that lead to amorphous aerogels.^[23, 79, 110] Niu *et al.* synthesized crystalline TiO₂ aerogels using cetyltrimethylammoniumbromid (CTAB) and acetonitrile as solvent. The crystallinity was probably improved by usage of acetonitrile and the CTAB surfactant, which has also an impact on the pore size.^[111] It was reported elsewhere, that different solvents might influence the crystallinity of sol-gel synthesized TiO₂ nanoparticles.^[112] However, the degree of crystallinity of these aerogels is rarely determined. Surface areas up to 250.2 m²·g⁻¹ were found.^[111] The usage of surfactants such as CTAB can help to increase the surface area.^[113, 114] Other synthesis parameter such as ultra-sonic assistance or stirring speed might also have an impact on the reaction rates and therefore influences the aerogel structure.^[86, 109]

The type and amount of precursor influences the pore diameter and surface area. De Sario *et al.* found that the specific surface area (9 to 19 %) and pore volume (10 to 20 %) decreases significantly with increasing precursor concentration. The precursor had only small impact on the size of the mesopores, which slightly decrease with increasing precursor concentration. [115] However, the type of precursor showed to have an impact on the pore size. Doneliene *et al.* synthesized the TiO₂ aerogels using different types of Ti alkoxide precursors (precursor: EtOH:HNO₃:H₂O 1:21:0.08:7.35). They found micro- and mesoporous amorphous structures with pore sizes between 0.5 and 17 nm, with larger pore diameters for TTIP compared to TTBT (titanetetrabutoxide), indicating the impact of nature of alkoxy groups at the precursor on the kinetics of hydrolysis and condensation reaction. [88]

Besides the direct synthesis parameter, the gel structure can be influenced by the second synthesis step, the aging of the gel. The aging step is important to strengthen the gel structure. Different aging times from several hours to more than 40 days were reported. [23, 79, 88] Doneliene *et al.* synthesized the impact of aging on TiO₂ aerogels and reported that aging for three days at 40 °C of the aerogels led to an increase of pore diameter. [88] Choi *et al.* also reported that the pore size and pore volume depends on the aging time. [25] However, the choice of solvent during aging has also an impact on the stability of the gels. Gels which were aged in EtOH were found to redissolve due to syneresis effect and Ostwald ripening during aging. [79] Also shrinkage of the gels was reported during aging. [111]

After aging, the gels are dried in a specific way. There are different drying methods. Typically aerogels are supercritically dried in CO₂ to achieve high surface areas and retain the porous structure. [79] This is required for receiving mesoporous structures, exhibiting pore sizes of 15 to 50 nm and to prevent these pores to collapse. [10] This leads to a 3D nanostructure which is generally amorphous, that is disadvantageous for photocatalytic activity, [116] but exhibits very high surface areas, compared to one-dimensional (1D) or two-dimensional (2D) materials. [25] Supercritical drying can also be performed in supercritical (sc) solvent, *e.g.* EtOH or *i*PrOH, at high temperatures and pressures (scEtOH 265 °C, 60 to 110 bar; sciPrOH 300 °C, 100 bar). This leads to higher crystallinity but also to collapse of the aerogel structure, due to the high temperature. [49, 50, 87, 117]. This in turn leads to a drastic decrease of the specific surface area. [49] Boujday *et al.* compared supercritically dried (in CO₂) aerogels with xerogels which were dried at ambient conditions and found that the specific surface area was much higher for the aerogel

and showed a densely packed microstructure for the xerogel. ^[110] Moussaoui *et al.* also compared supercritically dried (in *i*PrOH) aerogels with xerogels, which were oven-dried at 200 °C. They found anatase and brookite in the oven-dried sample, whereas in other supercritical drying techniques only anatase was found. The specific surface area was found to be higher for the xerogel compared to the aerogel, which was supercritically dried at high temperature. ^[49] Qingge *et al.* used vacuum drying at 60 °C for 24 hours to receive aerogels with surface areas up to 563.6 m²·g⁻¹ but very low pore volumes of 0.42 cm³·g⁻¹. ^[86]

Generally, aerogels are amorphous after supercritical drying and require a post heat-treatment to achieve crystalline phases. ^[23, 79, 110] A post heat-treatment applied to the aerogels leads to sintering and a decrease in surface area. Typically, aerogels are calcined between 300 and 600 °C for several hours. Only anatase is observed in that temperature range. ^[23, 79, 86] However, the specific surface area of the as-prepared aerogel decreases drastically, *e.g.* from 655 m²·g⁻¹ to 132 m²·g⁻¹ while the average pore diameter increases, *e.g.* from 9.1 nm to 14.9 nm. ^[79] Boujday *et al.* compared the TiO₂ aerogel crystallinity and crystal structure before and after calcination at 450 to 550 °C. They found that all samples exhibit the anatase crystal structure after calcination but the specific surface area decreased while the crystallite size increased. ^[110] The aerogels can have different appearance after synthesis and drying. Bernardes *et al.* reported that an increased hydrolysis and condensation reaction rate can be achieved by increasing polarity and dielectric constant of the solvent. This in turn prevents particle growth resulting in high specific surface areas and high transparency of the aerogel. They reported that the usage of water as solvent leads to more transparent aerogels compared to EtOH. ^[24, 81] Also the bulk density and particle size are crucial to achieve transparent aerogels. The usage of 2-methoxyethanol and 2-ethoxyethanol showed higher transparent aerogel samples compared to *i*PrOH, due to less agglomeration. ^[85]

2.4 Aerogels as Photocatalysts: Requirements and Material Development Approaches

2.4.1 Photocatalysis

Photocatalytic processes can be described by the irradiation of different materials *e.g.* semiconductors by UV or visible (vis) light, generating electrons and holes that can be further used for different processes. ^[7, 118] These include for example, pollutant degradation from gas or liquid phase, ^[26, 119, 120] conversion of solar energy into chemical reactions or transformations such as H₂ generation. ^[89, 121, 122] Generally, semiconductors are used as photocatalysts, due to their electronic structure. Metal oxides such as TiO₂,^[24] ZnO,^[123] Fe₂O₃ ^[124] or WO₃ ^[121] are typical candidates as photocatalysts, which can be further doped with different elements to alter the electronic structure.

Semiconductors have an empty region, called band gap, between the filled valence band (VB) and the vacant conduction band (CB). In this region are no accessible energy levels. However, the charge carriers can overcome this band gap by energy absorption by *e.g.* light or elevated temperatures. Also, the position and width of band gap is characteristic for a semiconductor, that will be explained in chapter 2.4.2. When a semiconductor is irradiated by a photon of energy $h \cdot \nu$ that equals or surpasses the band gap energy (E_g) an excited electron (e^-/\ominus) moves from the VB to the CB, leaving a hole (h^+/\oplus) behind (1). These electron-hole pairs can react with electron donors or acceptors on the surface of the semiconductor (2), recombine (3) or be trapped in the surface states of the material (4). ^[7, 118] These four different steps are shown in Figure 2.4-1.

The photocatalytic hydrogen evolution reaction is one of the typical applications of metal oxide catalysts. The reaction requires a CB which is more negative than the reduction potential for hydrogen production H⁺/H₂ of 0 V. Then photogenerated electrons can react forming hydrogen. For the oxygen half reaction, the VB must be more positive than the oxidation potential O₂/H₂O of 1.23 V. ^[125] The two half reactions are as follows:



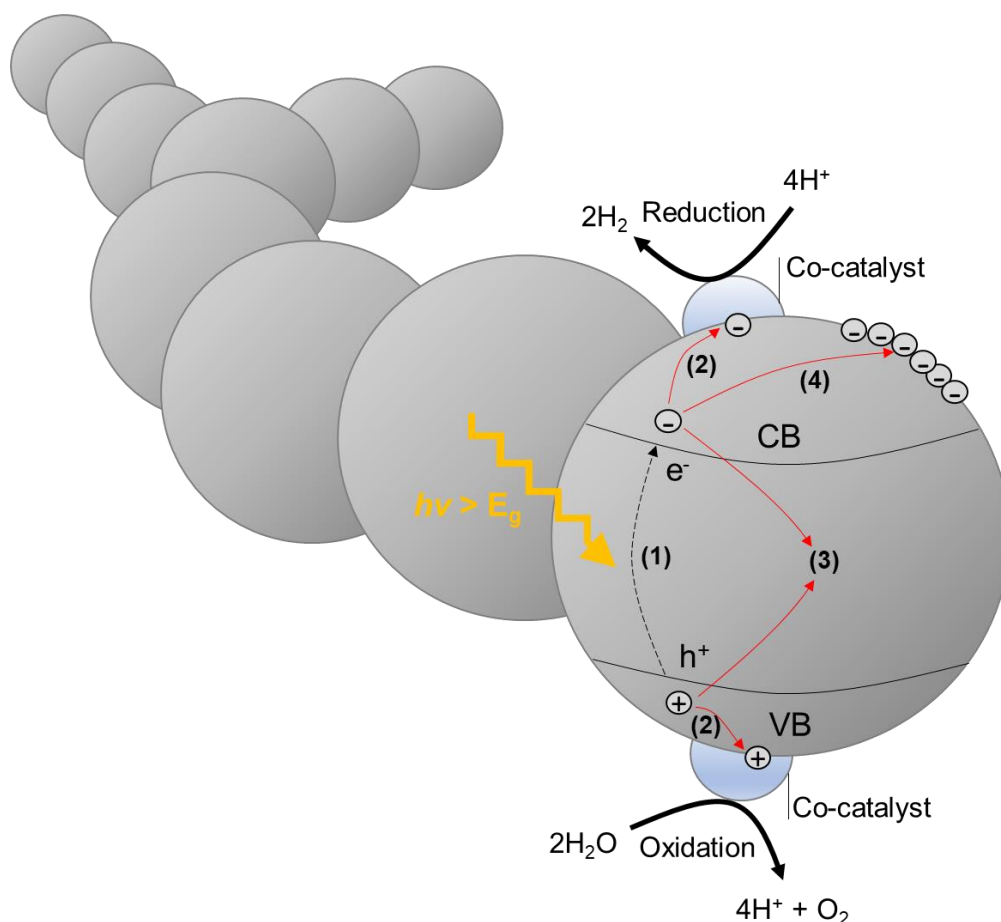


Figure 2.4-1: 3D aerogel structure with scheme of photocatalytic processes including electron-hole pair generation (1), migration of charge carriers to the surface for further reactions (2), recombination of charge carriers (3) or trapping of charge carriers in the surface states of the material (4).

For comparison, another photocatalytic reaction is the photocatalytic N_2 reduction to ammonia. This reaction can also be divided in two half reactions requiring certain positions of the VB and CB. [125]



The band gap of TiO_2 is generally suitable for photocatalytic hydrogen generation, as shown in Figure 2.4-2. However, TiO_2 possesses a large overpotential on the surface for hydrogen evolution, why TiO_2 needs to be modified *e.g.* by metal nanoparticles to get an active photocatalyst. [126]

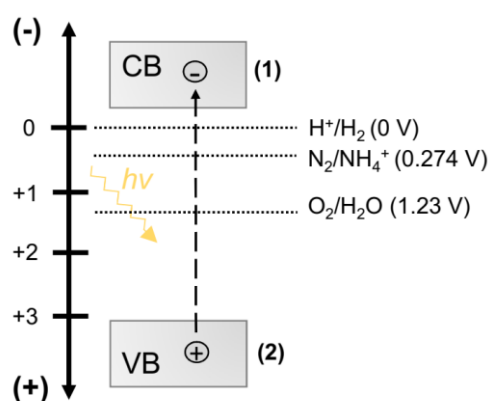


Figure 2.4-2: CB (1) and VB (2) of TiO_2 and oxidation/reduction potential for H_2 and NH_3 generation. Standard electrode potentials at pH value of 0. ^[125]

The problem of photogenerated electron and holes is the short life time. Photogenerated electron-hole pairs recombine before they can migrate and react at reactive sites on the surface. So, the aim is to increase the charge separation and inhibit the recombination of charge carriers. This can be achieved by *e.g.* surface defect states or band gap states where the electrons or holes are trapped. Also, different material combinations can improve the charge separation. ^[7, 118, 127, 128] This will be further discussed in chapter 2.4.2.

2.4.2 Requirements and Strategies for Metal Oxide-Based Photocatalyst

There are several requirements and properties of metal oxide-based photocatalytic materials. Generally, as described in chapter 2.4.1 the electronic structure of the material is very important and crucial for *e.g.* hydrogen evolution. The electronic structure including the position and width of band gap is characteristic for a semiconductor. This depends on the crystal structure, particle size and microstructure of a material. ^[7, 126] In Figure 2.4-3 the band gaps of different materials are shown.

The position of the CB is important for the ability to generate hydrogen. Also, the width of the band gap is important, how much energy is required to generate electron hole pairs. A material with a narrow band gap can absorb longwave light, which is in the vis range. Materials with large band gaps can only absorb in the UV range.

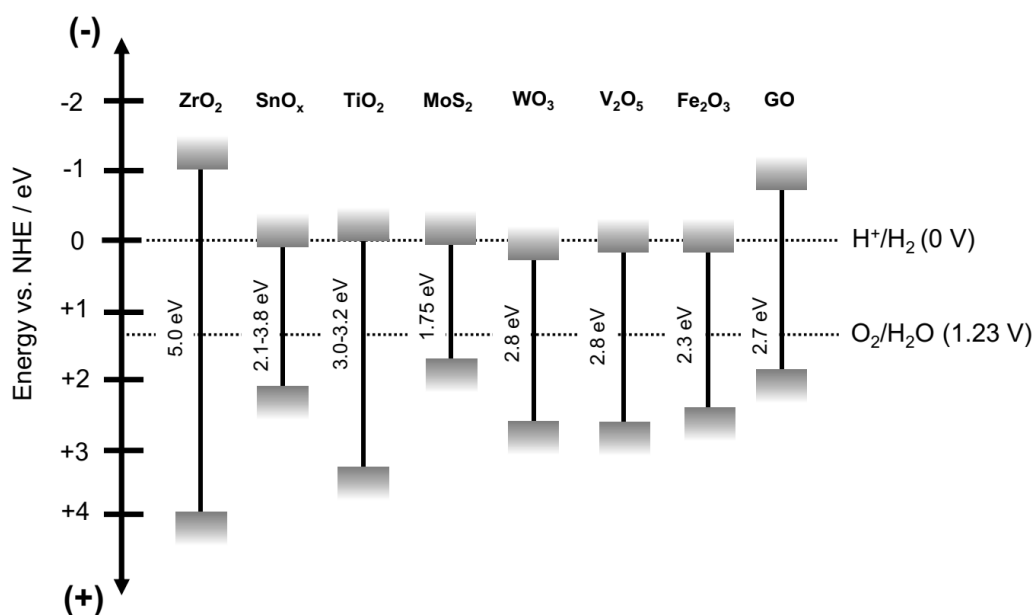


Figure 2.4-3: Band gaps and positions of VB and CB of different materials (GO^[129] SnO₂^[130] V₂O₅^[120] TiO₂^[118] ZrO₂^[131] MoS₂^[132] WO₃^[118, 133]).

For example, TiO₂ anatase with a band gap of 3.2 eV can absorb light of 390 nm, whereas WO₃ and Fe₂O₃ with a band gap of 2.6 eV and 2.1 eV, can absorb light in the wavelengths of 480 nm and 590 nm respectively. That means that anatase for example can only absorb approx. 3 to 4 % of the solar light.^[134] Different TiO₂ polymorphs exhibit different band gaps. TiO₂ anatase showed higher photocatalytic activity compared to rutile, although, rutile exhibits a narrower band gap of 3.0 eV compared to anatase of 3.2 eV. A narrower band gap increases the absorption ability of light; however, the specific surface area and surface adsorption capacity is lower due to larger grain sizes in rutile compared to anatase. Also, the high photocatalytic activity of anatase can be explained by the band gap structure which is directly associated with the crystal structure. Anatase has an indirect band gap in contrast to rutile and brookite, which have a direct band gap. This leads to longer lifetimes of photoexcited charge carriers in anatase. Also, the migration rates of photogenerated charge carriers to the surface are increased.^[135] TiO₂ with high mass fraction of brookite has been reported to be very difficult to synthesize but became more attractive in the last years, due to its photocatalytic performance. In sol-gel synthesis brookite sometimes appears as by-product. The band gap of brookite ranges from 3.1 to 3.4 eV.^[34] Also, the band gap width depends on the size of the material particles. The band gap decreases with decreasing nanoparticle size.^[136] Materials with different oxidation states of the metal ion and defect-rich structures can also alter the band gap.^[130] The polymorphs also

differ in their ability to trap electrons and holes in defect sites and influence the recombination rate. This trapping in defect sites is related to mid-gap states, which differ for each phase.^[128] The mid-gap states are located below the CB and have the effect to increase the lifetime of electron-hole pairs, however they can also reduce the reactivity of the charge carriers, dependent on the depth of the mid-gap states. In brookite the position and depth of the mid-gap states are advantageous to trap electrons and increase the lifetime of holes compared to anatase or rutile.^[128]

Defect states in TiO₂ can be achieved by calcination in reducing atmosphere *e.g.* H₂ or inert gas atmosphere Ar, N₂ or vacuum. This leads to black TiO₂. The black color is related to the formation of defective TiO_{2-x}, by Ti³⁺/oxygen vacancies and disorder in the crystal structure, which is favorable for photocatalysis.^[137] Ti³⁺ is generally not present in white TiO₂.^[138] A narrower band gap was reported for black TiO₂.^[137] Also, crystalline/amorphous core-shell structures were observed for black TiO₂. The black color was therefore related to the amorphous outer disordered layer on the surface.^[127, 138] The band gap varies also for different morphologies. For MoS₂ bulk material the band gap is 1.2 eV, whereas for MoS₂ single layer it is 1.8 eV.^[132] With material combinations *e.g.* TiO₂ or SnO₂ with MoS₂ a smaller band gap can be achieved.^[139]

There are several strategies to develop metal oxide-based materials for photocatalysis. The main goal is to improve the charge separation and migration of the charge carriers to the reactive sites at the surface without recombination. So, the lifetime of the charge carriers should be increased, but at the same time charge carrier mobility is required, so that generated charge carriers can migrate to reactive sites.^[7, 140]

One approach is to improve the charge separation by creating heterojunctions. The principle is shown in Figure 2.4-4 for a type II, p-n heterojunction. The electron separation process is caused by electron transfer from the CB of semiconductor 1 to the CB of semiconductor 2. The photogenerated holes are transferred from VB of semiconductor 2 to VB of semiconductor 1. The electrons are accumulated in semiconductor 2 whereas the holes are accumulated in semiconductor 1, that makes it impossible for these charge carriers to recombine. This requires differences in the width of the band gap, as well as in the position of the CB and VB. If the CB of semiconductor 2 is lower compared to semiconductor 1, no electrons can be transferred, as more energy would be required. Also, if the CB of semiconductor 2 is higher, allowing the electrons transfer, the VB of semiconductor 2 must not be lower, otherwise recombination can occur.

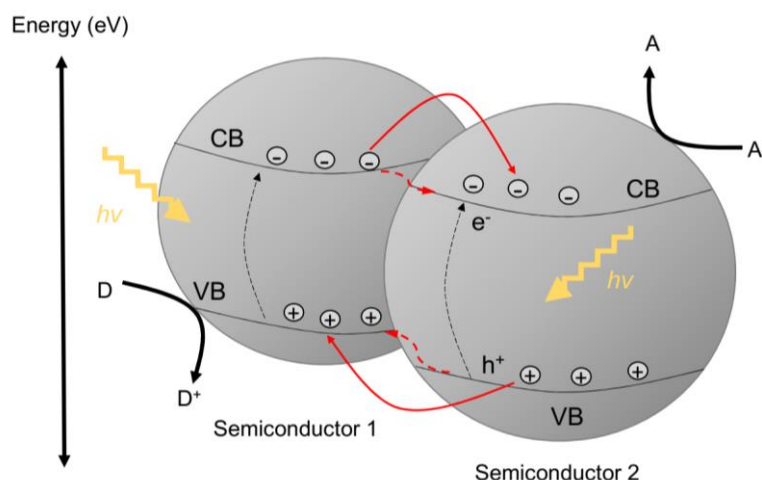


Figure 2.4-4: Two particles of 3D aerogel structure with the scheme of separation of photogenerated charge carriers in p-n heterojunction. A=Acceptor, D=Donator.

The interface of semiconductor particles 1 and 2 must be assured, so that electrons and holes can be transferred by diffusion. ^[7] This improves the overall photocatalytic efficiency due to the facilitated charge separation. Examples are TiO₂-SnO₂ heterojunctions or TiO₂ – anatase-rutile heterojunctions. ^[89, 141, 142]

Another approach is to improve the photoabsorption. As explained earlier, the position and width of the band gap determines how much energy is required to generate electron-hole pairs. Also, a suitable position of the CB is required for hydrogen generation. The electronic structure can therefore be altered by introducing a new energy level produced in the band gap of semiconductor by dispersion of dopant atoms (cation Ti⁴⁺ position or anion O²⁻ position) in the crystal structure. For example, transition metals (*e.g.* Mo, V) can be used, which narrow the band gap. This shifts the absorbed wavelengths from the UV to the vis range due to the reduced value of band gap, as shown in Figure 2.4-6. ^[7, 94, 139] There occurs a charge transfer between the d electron of the 3d-2p groups by the new created electron state. This enhances the electron trapping and charge carrier separation capability and inhibits the recombination of charge carriers. ^[7] Other examples are N, C or S anionic doping at the O²⁻ position. ^[143, 144] Scan also be used for cationic doping at the Ti⁴⁺ position. This leads to an impurity state near the VB edge. Also, doping with non-metal materials, such as C, B, I, F and P, introduces structural defects, which alter the metal oxide band gap, resulting in high visible light absorption. ^[143, 144]

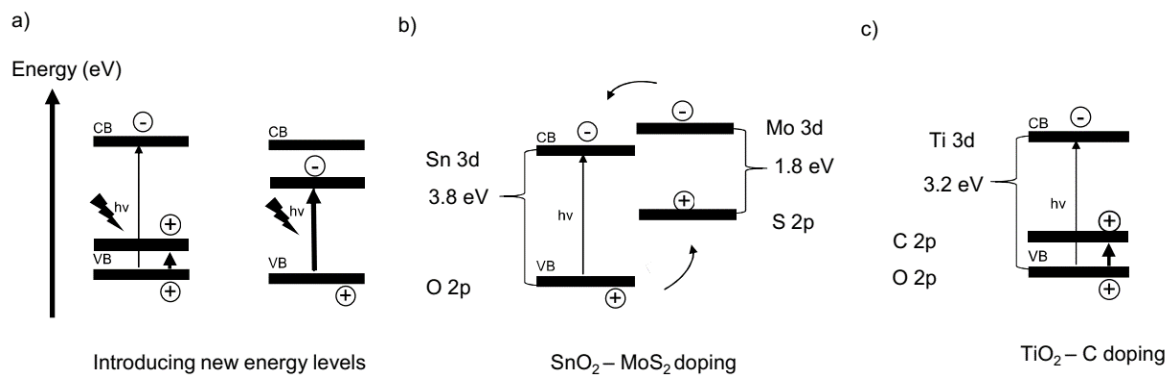


Figure 2.4-6: a) General modification of band structure by introducing new energy levels, for the examples of b) SnO_2 - MoS_2 doping and c) TiO_2 -carbon doping.

Another approach is to construct reactive sites at the surface by addition of co-catalyst such as noble metal nanoparticles. This can retard the recombination of charge carriers and enhance surface reaction rates by forming a Schottky junction. A Schottky junction can be explained by a potential energy barrier for electrons, which is formed at a metal-semiconductor junction. Electrons are transferred to the metal from the semiconductor. This continues until the fermi levels (E_F) are aligned, leading to deformation of the band structure. The electrons accumulate on the metal surface and are not able to migrate back to the semiconductor. This is demonstrated in Figure 2.4-5. Also, noble metal nanoparticles enable light absorption in the UV-vis range by localized surface plasmon resonance (LSPR). This approach is not further described, as it is not

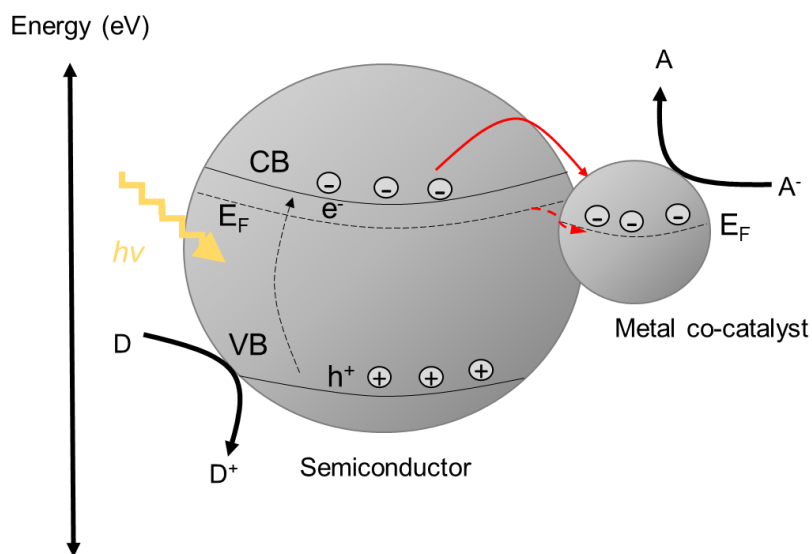


Figure 2.4-5: Formation of Schottky junction between metal nanoparticle and semiconductor. A=Acceptor, D=Donator.

topic of the dissertation and results. Examples of noble metal nanoparticles which have been used as co-catalysts are Ag, Au, Pt, Rh, Pd. [64, 145-147]

Besides the electronic structure of the materials the physical properties are very important. The morphology of particles or interconnected architectures influence several properties such as the specific surface area, porosity and surface chemistry. [148]

There are different kind of morphologies, *e.g.* spheres or nanoparticles which are described as zero-dimensional (0D) materials, which exhibit high surface areas. Nanowires, rods or fibers, such as carbon nanotubes are described as 1D nanomaterials, which exhibit high light scatterings properties. [148, 149] GO sheets are described as 2D nanomaterials which exhibit high adhesion properties. [150] Aerogels exhibit an interconnected architecture and are described as 3D materials. [148, 151, 152] They exhibit high charge carrier mobility and high surface area. A high specific surface area of the catalytic active material is important for the efficient adsorption of reactants. The specific surface area is directly associated with the particle size. [152] A smaller particle size is favored due to the higher specific surface area. Also, UV light has a penetration depth of approx. 160 nm, thus the particles size should be below this value. [7, 153]

Regarding the surface chemistry of the nanostructures, the number and kind of surface defects is crucial and determines the chemical reactivity and thus the photocatalytic potential. Defects in photocatalytic materials influence the electronic structure and charge carrier migration and consequently the photocatalytic activity. Defects can be classified according to their location in the material, if they appear in the bulk (bulk defects) or on the surface (surface defects). Defects can act as recombination centers and decrease the photocatalytic activity, but also trap charge carriers for improved electron-hole separation. [154, 155] These most found defects in TiO₂ are *e.g.* oxygen vacancies and thus unpaired electrons in Ti³⁺ which introduce new discrete energy levels below the CB, the so-called mid-gap states, [122, 145, 156] which shift the range of wavelengths of which light is absorbed. This leads to a shift of the light absorption. Calcination of the materials at elevated temperatures and different atmospheres can lead to an increased number of bulk or surface defects. [154, 155] Highly defective black TiO₂ was reported in literature. The high number of defects were produced by calcination at different oxygen-free atmospheres, [127, 137] resulting in a more narrow band gap. [127] It was also reported that photoexcited charge carriers can be trapped and stored at the surface of the materials with the formation of Ti³⁺ states. These charge carriers can be in turn used for further reactions. [157, 158] Also, a porous structure of the material can improve the charge carrier separation by decreasing

the migration distance of photogenerated charge carriers and increase the catalytic reactivity due to highly reactive environment of *e.g.* especially active crystal facets. ^[121]

For interconnected architectures such as aerogels, the porosity is also an important factor. The higher the porosity of the material, the more reactive sites are accessible at the surface which increase the photocatalytic activity. Also, the reflection of light is increased and therefore the quantum yield can be increased due to selective absorption of the light. ^[152, 159, 160] A higher efficiency for the separation of photogenerated electron-hole pairs was reported due to a higher excited-state density in the aerogel. ^[146]

Finally, the crystallinity and the crystal structure play an important role for photocatalysis. In comparison to amorphous structures, crystal phases have different electronic structures (band gaps) dependent on the exposed crystal facets which lead to different photocatalytic activities. ^[161, 162] Amorphous materials exhibit a wide band gap, large disorder and defects, originating from impurities, which cause unwanted electronic states. The so-called tail states located at the VB and CB edge are present in amorphous materials compared to crystalline materials. This is caused by disorder, *e.g.* different bond angles or a discrepant number of coordination of Ti and O atoms. ^[163, 164] This leads to a decreased ability of charge carriers to migrate to the surface and thus promote the recombination of charge carriers. The photocatalytic activity was reported in literature to increase with decreasing amorphous content. This can be explained by less charge carrier mobility in amorphous parts of the material and thus insulating parts, which favor the recombination of photogenerated holes and electrons. ^[116] Small nanocrystals of the rutile phase showed similar photocatalytic activity compared to similar sized anatase nanocrystals. ^[116] The crystalline phase promotes photocatalysis while the specific surface area is responsible for the catalysis part on the surface of the materials. ^[11-13] Both parameters are crucial for photocatalysis, but crystallinity seems to be more important for efficient electron-hole pair generation. ^[12, 13] The crystallinity of *e.g.* TiO₂ increases with calcination at temperatures above 300 °C, so that the amorphous content can be reduced. A higher crystallinity increases the mobility of charge carriers as mentioned above, but increases also the probability of the recombination of charge carriers, if they are not efficiently separated. However, the specific surface area decreases due to sintering and crystallization with calcination of the material. This leads to smaller adsorption area for the reactants in photocatalytic reactions. ^[133]

2.4.3 Photocatalytic Active Materials for Hydrogen Generation

Many materials, metal oxides and composites have been tested for hydrogen evolution and photocatalytic processes. The examples shown in this chapter are not limited on aerogels due to the loose definition of aerogels. Basically, most promising nanomaterials based on TiO₂ are described. TiO₂, as the most prominent photocatalyst, exhibits a high photostability and is chemically inert. It is a commonly used semiconductor in heterogeneous photocatalysis but exhibits a wide band gap.^[7] TiO₂ anatase has been reported to be more photocatalytically active compared to rutile. However, rutile exhibits a narrower band gap compared to anatase.^[135] Brookite became more attractive over the last years due to its interesting and special electronic properties.^[34, 165] Titania nanostructures and aerogels have been tested for photocatalytic hydrogen evolution and showed higher hydrogen evolution rates compared to nanocrystals prepared by hydrothermal method or P25 TiO₂ nanoparticles (Degussa). Also, the addition of co-catalysts such as Pt/TiO₂ aerogel had been investigated, which increased again the hydrogen evolution compared to pure aerogel.^[76] Other materials based on titania have been tested for photocatalytic performance, *e.g.* material composites with carbon *e.g.* TiO₂-on-C₃N₄^[149], TiO₂/GO^[166] or TiO₂/carbon spherogels^[167]. Mixed titanium oxides TiO₂/Ti₂O₃^[168] and TiO₂ in combination with other metal oxides *e.g.* SnO₂-TiO₂ can increase the photocatalytic catalytic activity.^[89] Additionally co-catalysts *e.g.* CuO/Cu₂O and CoO^[169-171] or Rh-loaded TiO₂^[145] were used in the literature for photocatalysts. CeO₂, V₂O₅/VO₂ and MoS₂ are also common oxides to boost the photocatalytic efficiency.^[26, 172-174]

SnO₂ is besides TiO₂ a high potential material for photocatalysis. It has been extensively studied and offers many advantages such as chemical stability, non-toxic properties, as well as good physical and chemical properties, similar to TiO₂. However, SnO₂ exhibit also a wide band gap and can therefore only absorb UV light (5 % of solar light).^[175] Despite the large band gap, SnO₂ can form heterojunctions with TiO₂ and thus improve the separation of charge carriers for enhanced charge carrier lifetime and photocatalytic activity.^[89, 97] Also, TiO₂ exhibits a very low electrical conductivity. In combination with SnO₂ the electrical conductivity could be increased to improve the charge carrier mobility.^[176] Sasikala *et al.* investigated SnO₂ on TiO₂ nanoparticles for photocatalytic hydrogen evolution. They observed that the mixed oxides absorb visible light which is due to defects, such as oxygen vacancies in the band gap of TiO₂. They suggested the mechanism, that the photoexcited electrons of TiO₂ migrate to the CB of SnO₂ (0 eV), as it is more positive compared to TiO₂ (-0.5 eV), even though the band gap is broader compared to TiO₂. This leads to a better charge separation and lower recombination

rate. However, the photocatalytic hydrogen evolution of mixed SnO₂-TiO₂ decreased with increasing SnO₂ content. This was explained by Sasikala *et al.* because of SnO₂ nanoparticle aggregation instead of a fine dispersion of SnO₂ particles on TiO₂. The synthesized nanoparticles exhibited surface areas of approx. 100 m²·g⁻¹ and pore volume approx. 0.5 cm³·g⁻¹.^[96] Guerrero-Araque *et al.* investigated SnO₂-TiO₂ nanostructures based on the hydrolysis of TTIP and SnO₂ nanoparticles (SnO₂:TiO₂ molar ratios (01:99, 03:97, 06:94, 12:88 and 20:80)). The nanostructures were synthesized by adding 6 mol% of previously synthesized SnO₂ nanoparticles to a solution of TTIP diluted with *i*PrOH in a 1:4 molar ratio under vigorous stirring, then calcined at 450 °C for three hours in air. They reported an improved photocatalytic activity and hydrogen evolution due to the direct contact of the both oxides leading to a better charge separation due to energetic states at the SnO₂-TiO₂ interface. This was explained by the tetragonal crystal structure of SnO₂ and TiO₂ which offers great compatibility. Also the band gap positions fit well for improved charge separation.^[89] High photocatalytic or photoelectrocatalytic activity of TiO₂-SnO₂ nanostructures have been reported elsewhere.^[97, 141, 177-180]

Metal sulfides *e.g.* MoS₂ exhibits advantageous properties such as a narrow band gap and high electrical conductivity. Due to its layered structure it offers high surface areas and was reported to absorb visible light for photocatalytic hydrogen production.^[181, 182] Similar effects has been reported for SnS₂.^[183] A high photocatalytic activity was reported for MoS₂ decorated TiO₂ materials or SnO₂. Liu *et al.* investigated single or few-layer MoS₂ nanosheets rooting into TiO₂. They found that the edges of MoS₂ nanosheets are highly active for hydrogen evolution and need to be exposed for high efficiency. They also stated that highly porous materials such as nanofibers are advantageous due to the large contact and consequently better charge transfer as well as better exposition of MoS₂ edge sites. The MoS₂-TiO₂ showed an increased structural stability and durability.^[184] Zhang *et al.* investigated multi-layered MoS₂ on Ti foil. They found that MoS₂ exhibits a high hydrogen evolution rate when irradiated under vis light. They also stated that the used 3D mesh-like MoS₂ nanostructures are beneficial for high photocatalytic activity.^[185] Chang *et al.* investigated MoS₂-on-SnO₂ core-shell sub-microspheres in a two-step hydrothermal process using tin(IV) chloride as precursor. They assumed the improved photocatalytic activity in the vis range due to the better surface to volume ratio of the MoS₂-SnO₂ microspheres and the better charge separation.^[186] Similar results were reported by Singh *et al.*^[187] Similar photocatalytic or photoelectrocatalytic activity of TiO₂/MoS₂ nanostructures have been reported elsewhere.^[188, 189]

TiO₂-carbon material composites are favorable for photocatalysis, due to the increased electrical conductivity, similarly to MoS₂. This improves the ability of charge carriers to migrate to the surface area to react with adsorbents. Also, carbon can replace oxygen in the crystal structure of TiO₂ and thus introduce a new energy level above the VB in the band structure. This helps to absorb more light in the vis range. [7, 190] Wang *et al.* investigated TiO₂/Graphene aerogels and reported a modified band gap, dependent on the nanostructures and the interfacial region between these nanostructures. [166] Torres-Rodriguez *et al.* combined the synthesis of RF with water-soluble titania synthesis based on titanium(IV) bis-ammonium lactate. After carbonization, the obtained aerogel was microporous with encapsulated titania, which showed improved photocatalytic activity, due to the carbon-shell structure. [167] Mallikarjuna *et al.* synthesized carbon-doped SnO₂ nanostructures based on tin chloride and urea, which absorb light in the vis range. The presence of carbon in the crystal structure of SnO₂ leads to new energy levels above the VB of SnO₂. The band gap is narrower and is therefore able to absorb more vis light, due to the C-Sn bonds. Also, the charge separation is supported by the additional energy levels, capturing the holes from the SnO₂ VB. This enhances the photocatalytic activity. [191]

Vanadium oxide (V₂O₅) belongs to the promising materials to improve the photocatalytic activity. V⁵⁺ (ionic radius 0.063 nm) can be introduced to TiO₂ (Ti⁴⁺ ionic radius 0.68 nm) due to the similar ionic radius. This makes it possible to shift the absorption from UV to vis light. [124, 192] Also an increased electrical conductivity was reported for V-doped TiO₂. [94] Mkhaldid *et al.* investigated 3 % V₂O₅-TiO₂ nanocomposite which showed an increased photocatalytic activity compared to P25 TiO₂. This was related to the formation of heterojunctions between V₂O₅ and TiO₂. [174] Sasidharan *et al.* developed V₂O₅-TiO₂ nanoparticles on GO with lower electron-hole pair recombination probability which increased the migration rates of charge carriers. Agglomeration was identified as problem of nanoparticles, so that active sites are inaccessible. GO was therefore applied to prevent agglomeration. [124] Aerogels could solve this problem, due to the high porosity. Beauger *et al.* reported that the usage of vanadium as dopant could effectively stabilize the anatase crystals and prevented the crystal growth which occurs typically during sintering and calcination. Vanadium showed to increase the specific surface area of TiO₂ aerogels after calcination in reducing atmosphere. [94]

2.4.4 Advantages and Disadvantages of Aerogels as Photocatalysts

Aerogels exhibit several advantages for photocatalytic processes. The mesoporous structure of the aerogels offers a coherent network, which is advantageous in photocatalytic applications, due to the efficient absorption of light. Aerogels exhibit very good light scattering properties due to internal multiple reflections. This means that the incident light is reflected internally achieving a high exploitation of the light, as the transmission of UV light is only approx. 160 nm, so that inner particles of agglomerated bulk material cannot be reached. [7, 148, 151-153]

Main advantage of TiO₂ aerogels in photocatalytic applications is that aerogels do not agglomerate, compared to TiO₂ nanoparticles, so reactive sites are better accessible. The catalytic active sites are therefore retained in the 3D nanostructure. [64, 152]

However, aerogels are typically amorphous after drying with scCO₂, that means that crystalline phases have to be obtained by subsequent heat-treatment at temperatures above 300 °C or even high temperature supercritical drying [49], accompanied by a strong decrease of porosity and surface area. A high specific surface area and open porosity of TiO₂ aerogels favor the adsorption and diffusion of reactants, therefore offers many active sites and their accessibility for photocatalytic reactions. [11-13, 193]

3 Synthesis of TiO₂ Aerogels

3.1 Preparation of Aerogels

3.1.1 General Synthesis Route and Parameter Variation

Three types of TiO₂ aerogels were prepared with an acid catalyzed sol-gel method using TTIP as precursor based on either EtOH (samples labelled as “E”), *i*PrOH (samples labelled as “*i*P”), or mixed solvent (samples labelled as “E-*i*P”). The general synthesis procedure is schematically shown in Figure 3.1-1. The synthesis was modified regarding the equivalents of TTIP:solvent:acid:water and in the case of mixed solvents, the molar ratio of EtOH and *i*PrOH was additionally varied. The amount of acid was increased from 0.05 to 0.33 HCl:TTIP molar ratio for the aerogel samples with increasing numbering (e.g. samples labelled as “E1” to “E6”). Additional samples were synthesized with an increased amount of acid compared to E1 and *i*P1 and increased amount of water compared to the respective samples E4, E5, and E6 or *i*P4, *i*P5 and *i*P6 (samples labelled as “EX.1” or “*i*PX.1”). A solution containing TTIP in EtOH was prepared under magnetic stirring at 0 °C. Concentrated hydrochloric acid (conc. HCl) was added after five minutes. Deionized water was added dropwise to the solution after 20 minutes. In the case of *i*PrOH as solvent a solution containing TTIP in the half amount of total *i*PrOH was prepared. After acid addition, the deionized water was diluted in the other half of total *i*PrOH and added to the solution after 20 minutes. A gel formed after few minutes. Gels were aged for seven days at 50 °C and then washed in *i*PrOH four times. The samples were stored in the lab for several days or weeks before drying all the samples with CO₂ at supercritical conditions (60 °C, 115 bar, flow rate 15 to 20 kg·h⁻¹). All chemicals used for aerogel synthesis are listed in the appendix in chapter 9.1. The detailed synthesis parameters for the three types of TiO₂ aerogels are listed in the appendix in chapter 9.2.

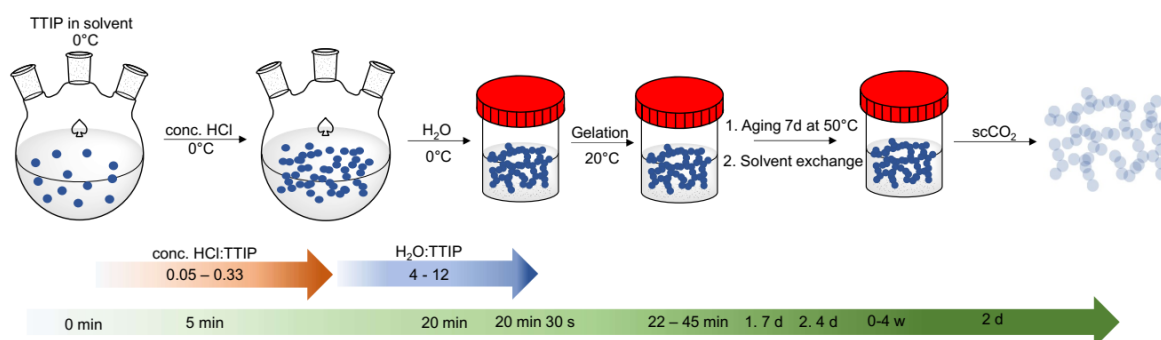


Figure 3.1-1: Scheme of the general synthesis procedure for TiO₂ aerogels.

3.1.2 Calcination of Selected EtOH Solvent-Based Aerogels

The TiO₂ aerogel E2 with the largest surface area was calcined in various conditions (atmosphere, temperature, holding time), as indicated in Table 9.2-5. The calcination in air was performed in a Nabertherm P330 furnace with a heating rate of 10 °C·min⁻¹. The aerogels were calcined at 300 °C, 400 °C and 500 °C respectively. The holding time was two hours, four hours and ten hours. The calcination in vacuum was performed in a Gero Carbolite GmbH Tubular Pyrolysis Furnace. Vacuum conditions were achieved by lowering the pressure to 50 mbar and flooding the tubular furnace with argon. The evacuation and flushing process was repeated for a total of three times. The pressure was kept constant at 50 mbar for the calcination. The heating rate was set to 10 °C·min⁻¹. The aerogels were calcined at 300 °C. The holding time was two hours and four hours, respectively. The calcination parameters are listed in the appendix in chapter 9.2. The samples were labelled as follows: “E2-atmosphere-temperature-duration”.

3.2 Synthesis of Mixed Metal Oxide Aerogels

3.2.1 SnO₂-TiO₂ and V₂O₅-TiO₂ Aerogels

For SnO₂-TiO₂ gels, TTIP and SnTIP were used as precursors. For V₂O₅-TiO₂ gels, TTIP and VOIP were used as precursors. The gels were prepared via the previously described acid catalyzed sol-gel method. The synthesis was performed under nitrogen atmosphere in a round-bottom flask with septum. The following equivalents of SnTIP/TTIP/*i*PrOH/acid/water were used: 0.05:1:35:0.11:4.2. Since the SnTIP was already dissolved in *i*PrOH, the amount of additional *i*PrOH in the synthesis was adapted to keep the total amount of solvent constant. A solution containing TTIP in *i*PrOH was prepared under magnetic stirring at 0 °C. Then, the SnTIP was added using a syringe (Figure 3.2-1).

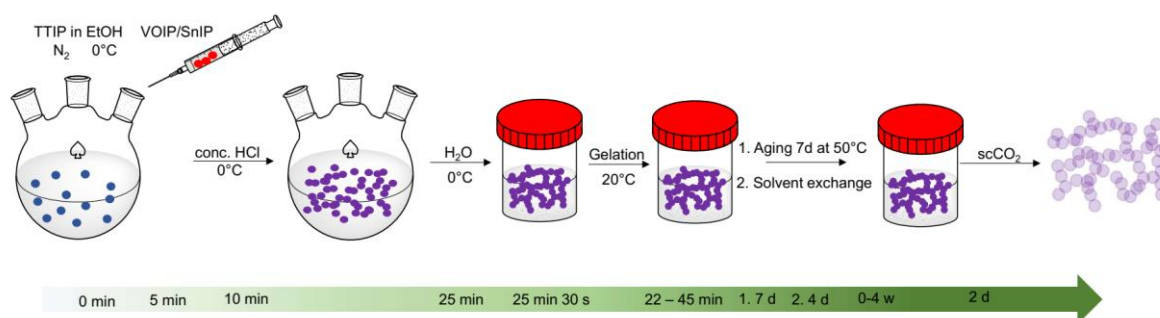


Figure 3.2-1: Scheme of the general synthesis procedure SnO₂/V₂O₅-TiO₂ aerogels.

For V₂O₅-TiO₂ gels the following equivalents of VOIP/TTIP/*i*PrOH/acid/water were used: 0.05:1:26:0.11:4.2. The liquid VOIP precursor was added with a syringe to the reaction mixture under stirring. No adjustments regarding the solvent were required, since the precursor was not pre-diluted and ready to use as liquid. The further procedure (addition of HCl/water) was performed similarly as the general TiO₂ aerogel synthesis in chapter 3.1.1 Also the aging process, solvent exchange and drying procedure was performed according to the general aerogel synthesis of this work.

3.2.2 MoS₂-TiO₂ and GO-TiO₂ Aerogels

Doped TiO₂ aerogels were also prepared with MoS₂ and GO (Figure 3.2-2). The following equivalents of TTIP/EtOH/acid/water were used: 1:26:0.11:4. The used amounts of MoS₂ or GO were 1 at.% and 5 at.% with regard to TTIP. The solid MoS₂ or GO was dispersed in the EtOH for 30 minutes in an ultrasonic bath. The TTIP was added to the MoS₂/EtOH or GO/EtOH dispersion. The further procedure was also performed similarly compared to the general TiO₂ aerogel synthesis in chapter 3.1.1

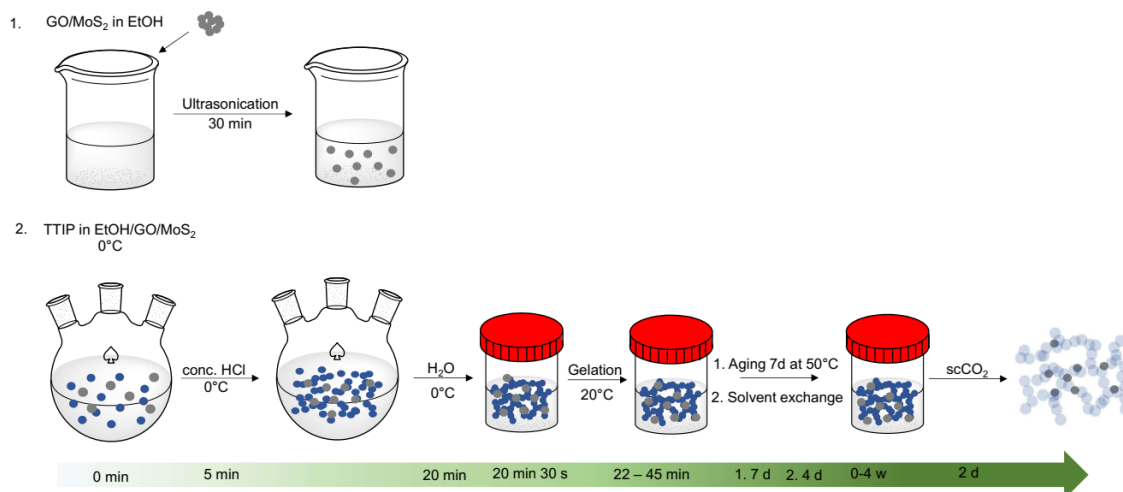


Figure 3.2-2: Scheme of the general synthesis procedure GO/MoS₂-TiO₂ aerogels.

4 Characterization Methods

4.1 Structural Properties

4.1.1 Gelation and Shrinkage Behavior

The gelation time is defined as the time from the beginning of the condensation reaction, measured (± 30 s) from the addition of water to the liquid sol until a solid gel is obtained. The sol is poured into a cylindrical plastic container prior to gelation. The diameter of the formed gel directly after gelation was measured optically with a ruler (± 0.5 cm) without removing the sample from the plastic container. The diameter of the gel was measured again after ageing. From the difference of these values, the percentage of shrinkage was calculated with an error of 5 %.

4.1.2 Optical Microscopy

Macro images of wet gels were taken by a Nikon camera D3300. The appearance of the dried and wet gel gives first indication on the pore structure and strength of the aerogels. Images of small aerogel pieces in the millimeter range, originated from fractured dried aerogels were taken by means of a digital microscope, VH-Z20R, Keyence GmbH. Dark field (DF) and bright field (BF) images were taken dependent on the color of the aerogel and the occurring light reflection.

4.1.3 Physisorption Measurements

The specific surface area was determined *via* N₂ physisorption measurements at 77 K with a Micromeritics 3Flex and Tristar instrument in a partial pressure range of $0.05 < p/p^0 < 0.3$ using the Brunauer-Emmett-Teller (BET) method. The total pore volume of the samples was obtained from the N₂ adsorption isotherms at a partial pressure of 0.98, and the pore size distribution was obtained using the Barrett-Joyner-Halenda (BJH) model. The software MicroActive (Micromeritics, Version 5.02) was used for data analysis. Prior to physisorption analysis, the samples were outgassed at 60 °C for 12 hours with a Micromeritics Smart VacPrep Gas Adsorption Sample Preparation Device. The standard deviation of the surface area, pore volume and BJH maximum was determined from ten aerogel samples (E2) from different batches prepared *via* the identical synthesis procedure (Table 4.1-1). However, the error of the

Table 4.1-1: Relative and absolute error of physisorption measurements for sample E2.

	Absolute error	Relative error
Surface area	$\pm 31 \text{ m}^2 \cdot \text{g}^{-1}$	5 %
Pore volume	$\pm 0.2 \text{ cm}^3 \cdot \text{g}^{-1}$	9 %
BJH maximum	$\pm 1.5 \text{ nm}$	9 %

measurements could not be determined for all samples. All other results are based on single measurements, due to the availability of the instrument. The calculated error of sample E2 was approximately applied to the other samples. Aerogel samples with different pore size distributions compared to E2 might behave differently in N_2 adsorption and could lead to a different error.

4.1.4 Pycnometry and Porosity Determination

The skeletal density of the aerogels was determined using a helium pycnometer AccuPyc II from Micromeritics. The measurements are based on the gas displacement method with an instrument compartment of the known volume of $V=1.3273 \text{ cm}^3$, where the sample is placed. The solid sample displaces the gas, of which the volume is used in combination with the sample mass to calculate the skeletal density of the sample. Ten measurements were performed for each sample and the values averaged. The porosity (p) of the samples was calculated by using the previously measured skeletal density (ρ_s) and total pore volume (V_P) determined in physisorption measurements, as indicated in Eq. 3^[194]:

$$p = \frac{V_P}{\frac{1}{\rho_s} + V_P} \quad \text{Eq. 5}$$

The error was calculated by the equation:

$$\Delta p = \left(\frac{V_P}{(1 + \rho_s \cdot V_P)^2} \cdot \Delta \rho_s + \frac{V_P}{(1 + \rho_s \cdot V_P)^2} \cdot \Delta V_P \right) \cdot 100 \quad \text{Eq. 6}$$

4.1.5 Scanning Electron Microscopy (SEM) and Transmission Electron Microscopy (TEM)

For microstructural analysis a scanning electron microscope Zeiss Ultra 55 was used. Small pieces of the aerogels with the dimensions in the micrometer range were deposited on a carbon pad, which was stuck onto the sample holder. The samples were coated with platinum using a Baltec SCD 500 sputter coater prior to SEM investigation in order to avoid massive charging of the sample surface. Sputtering for 90 s with 21 mA from the top and 60 s from the side was

used to achieve a homogeneous platinum layer on the porous aerogel. Secondary electron images were taken using an acceleration voltage of 3 kV and working distance of approx. 7 mm. An aperture diameter of 20 or 30 μm and the high current modus were used.

A transmission electron microscope Tecnai F30 (Philips, The Netherlands) equipped with a CCD camera (Gatan MSC 794, Gatan, USA) and a combined BF/DF scanning transmission electron microscopy (STEM) detector (Philips, The Netherlands) and a high-angle annular dark-field (HAADF) detector (Fischione, USA) was used to achieve images of aerogel particles and structure at higher resolution. D-spacing (± 0.005 nm) of the crystalline phases was determined from TEM images using ImageJ (Wayne Rasband, National Institutes of Health, USA, Version 1.52d). The transmission electron microscope was operated at an acceleration voltage of 300 kV. STEM and a detector for energy-dispersive spectroscopy (windowless Apollo EDS detector, EDAX, USA) was used to perform elemental mappings of the mixed-oxide and doped aerogel samples.

4.1.6 X-ray Diffraction and Scattering

4.1.6.1 Laboratory Powder X-ray Diffraction (XRD) Equipment

XRD measurements were performed for phase analysis on Bruker D8 ADVANCE X-ray diffractometers (in Bragg Brentano geometry) using Cu $K\alpha$ ($\lambda = 1.5406$ Å) or Co $K\alpha$ ($\lambda = 1.7889$ Å) radiation sources and LYNXEYE XE-T 1D-detectors. The diffraction data were collected in the range of $15\text{-}90^\circ$ 2θ (Cu $K\alpha$) or $20\text{-}100^\circ$ 2θ (Co $K\alpha$) with a step size of 0.01° . Phase analysis was performed using the international center for diffraction database (ICDD-PDF-2) and respective powder diffraction files (PDF) and DIFFRAC.EVA software (Bruker, Version 5.2). Phase mass fraction quantification, the crystallite size and determination of the amorphous and crystalline phase content was performed by the Rietveld method implemented in the DIFFRAC.TOPAS software (Bruker, Version 5) using high-crystalline CeO_2 (10 wt.%) as internal standard.

4.1.6.2 Synchrotron Radiation Source

WAXS and SAXS experiments were conducted at the P07 high-energy materials science beamline operated by the Helmholtz-Zentrum Geesthacht at PETRA III at the Deutsches Elektronen-Synchrotron (DESY), Germany. X-ray scattering depends on the electron density in the sample, generating contrast at nanometer length scales (SAXS) and atomic scale (WAXS). WAXS experiments were performed for phase analysis in the wet gels and to

determine the degree of crystallinity in the gels. Complementary, SAXS measurements were performed to achieve information about the gel network, the primary and secondary particle size of the wet gels and the particle shape. *In-situ* and *ex-situ* measurements were performed. For the incident X-ray beam, a mean photon energy of 75 keV ($\lambda=0.16790$ Å) was selected. A Perkin Elmer XRD 1621 flat panel detector with a pixel matrix of 2048 x 2048 and a pixel size of 200 μm x 200 μm was used for WAXS experiments. The WAXS detector was placed approx. 4 m behind the sample. A Varex XRD4343CT detector with a pixel matrix of 2880 x 2880 and a pixel size of 150 μm x 150 μm was used for SAXS experiments. A 1 mm beam stop was used that enabled the measurement of particle sizes up to 40 to 50 nm. The SAXS detector was set approx. 11 m behind the sample. The SAXS/WAXS setup is shown in Figure 4.1-1b. For calibration, LaB₆ was used for WAXS and glassy carbon, and silver behenate (AgC₂₂H₄₃O₂) was used for SAXS (detector distance and absolute intensity). The specimens were prepared in glass test tubes or quartz cuvettes and probed in transmission. The gel samples were measured with SAXS and WAXS with a beam size of 0.14 mm x 0.14 mm. For SAXS, a single measurement time of 0.1 s and accumulation of 500 images was set to avoid detector overflow. For WAXS, a single measurement time of 1 s and accumulation of 100 images was set. The obtained 2D diffraction images were integrated using the software Fit2D (Andy Hammersley, European Synchrotron Radiation Facility, Version 12.077) to receive the respective scattering curves.

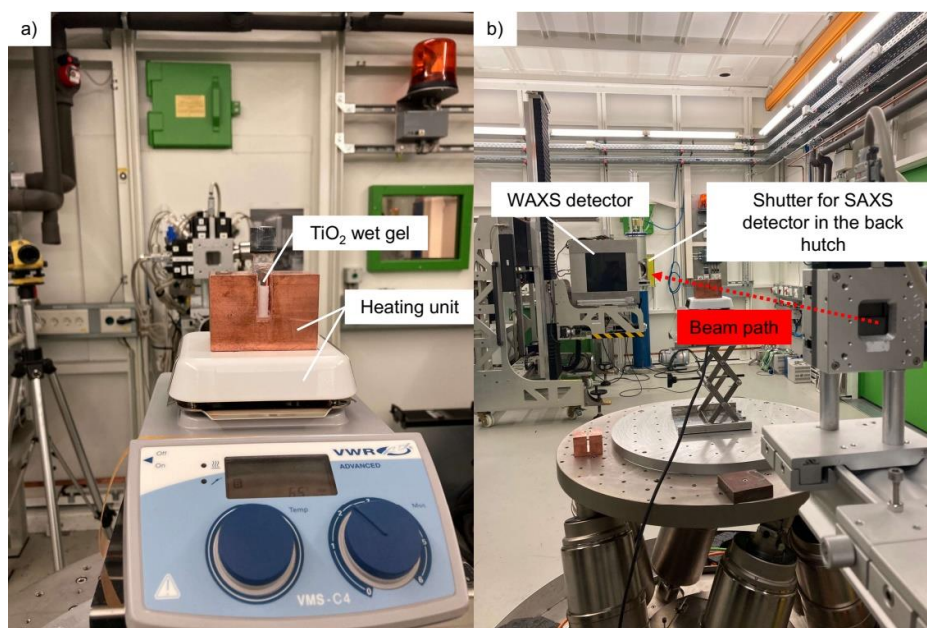


Figure 4.1-1: Experimental setup for *in-situ* and *ex-situ* SAXS/WAXS measurements of wet gels using synchrotron radiation.

Different EtOH and *i*PrOH solvent-based TiO₂ gels were synthesized in the lab and poured in glass test tubes or quartz cuvettes. The gels were pre-aged for different days at 50 °C prior to the measurements (samples labelled as “E5 X d” or “*i*P5 X d” with X= 1-7 d (days)). Some samples (*i*P1 to *i*P6) were measured only in WAXS experiments with addition of an internal standard in the wet gel (CeO₂). A beam size of 0.9 mm x 0.9 mm was used to increase the number of crystallites in the measured sample volume and therefore to increase the measured intensity. Besides the *ex-situ* experiments, the *in-situ* WAXS was performed for sample *i*P5. The sample was pre-aged for three days and measured each ten minutes during heating at 50 °C for 48 hours to observe phase transitions. The heating of the sample was achieved by a heating plate and copper block with a small opening for the sample and the beam path. This is shown in Figure 4.1-1a.

4.1.7 Raman Spectroscopy

Raman spectra of the aerogel samples were recorded using an XploRA PLUS Raman spectrometer (HORIBA Scientific) with an operating wavelength of 532 nm (7.6 mW). The dried aerogels were measured to confirm the crystallinity and crystal phases. The aging process of the gel was analyzed to identify crystallization processes. Therefore, an *in-situ* Raman probe was placed at a defined distance to the wet gel in an oven at 50 °C (Figure 4.1-2). The gel was rotated to prevent localized crystallization by the Raman laser and to receive average intensity values of the entire gel. The *in-situ* measurement was performed during the complete aging process of seven days or longer. For each data point, two single measurements of 30 minutes each were taken and the obtained signals accumulated to avoid peaks from cosmic radiation. The data was baseline corrected and analyzed using the LabSpec6 software (Horiba, Version 6.6.1.11).



Figure 4.1-2: Experimental setup for *in-situ* Raman measurements of wet gels.

4.1.8 Nuclear Magnetic Resonance Spectroscopy (NMR)

The ^1H -NMR measurements were performed using a Magritek Spinsolve 80 Ultra instrument. NMR measurements were performed to determine changes in the chemical structure of the used precursor molecules in different solvents. For *in-situ* measurements the samples were analyzed in intervals of 15 s. No deuterated solvent was used.

4.2 Electronic Properties

4.2.1 X-ray Photoelectron Spectroscopy (XPS)

XPS analysis was performed by the Interdisciplinary Center for Analytics on the Nanoscale (ICAN, University of Duisburg-Essen, North Rhine-Westphalia, Germany) to determine the elemental composition of the aerogels and the oxidation state of titanium. Measurements were conducted on a ULVAC-PHI VersaProbe II system using monochromatic Al $K\alpha$ radiation with a photon energy of 1486.7 eV. The instrument was equipped with an Ar^+ and electron neutralizer for charge compensation to ensure stable measurements. C1s signal was set to 284.8 eV for the spectrum correction.

4.2.2 Ultraviolet Photoelectron Spectroscopy (UPS)

UPS analysis was performed by the Interdisciplinary Center for Analytics on the Nanoscale (ICAN, University of Duisburg-Essen, North Rhine-Westphalia, Germany) to determine the VB maximum and to analyze electronic states, such as mid-gap states. Measurements were conducted on a ULVAC-PHI VersaProbe II System using He $I\alpha=21.22$ eV. The C1s signal from XPS measurements, which was set to 284.8 eV, was also used for UPS spectrum correction.

4.2.3 Ultraviolet–Visible Diffuse Reflectance Spectroscopy (UV–Vis DRS)

UV–Vis DRS was performed by Anja Hofmann of the University of Bayreuth to determine the absorption range of the material and the band gap. A PerkinElmer Lambda 750 UV/vis/Near-infrared spectrometer, equipped with a Praying-Mantis mirror unit from Harrick, was used to record the diffuse reflectance of the aerogel powders with a step size of 1 nm. The used white standard was a Spectralon pellet. The spectra were converted into absorption spectra using the Kubelka-Munk function. Tauc plots were used to estimate the band gaps.

4.3 Photocatalytic Activity

4.3.1 Photocatalytic Hydrogen Evolution

The photocatalytic experiments for hydrogen evolution were performed by Anja Hofmann of the University of Bayreuth. The following description of the experimental procedure is taken from the respective publication (Rose *et al.*).^[195] For all photocatalytic experiments, ultrapure water with TOC = 2 ppb was used. The experiments were conducted with a 300 W Xe lamp in a top-irradiated glass reaction vessel. Measurements were all performed at 20 °C (ECO RE 1050G (Lauda) thermostat) under stirring. The system was flushed with argon 5.0 before the measurements to remove residual air. Detection of the evolved hydrogen was performed every 11 minutes using a GC2014 gas chromatograph from Shimadzu, equipped with a shin carbon ST column (Restek) and a thermal conductivity detector, using argon 5.0 as the carrier gas. The argon 5.0 flow rate for the measurements was set to 25 mL·min⁻¹ with a Bronkhorst mass flow controller. The hydrogen evolution experiments with Pt photo deposition were carried out with 100 mg aerogel sample dispersed in a mixture of 135 mL water and 15 mL methanol. The dispersion was irradiated for 100 minutes without co-catalyst. The lamp was turned off to wait until no hydrogen evolution was detected anymore; then, an aqueous solution of hexachloridoplatinate (IV) hydrate (H₂PtCl₆) was added *via* rubber sealing without opening the reactor to reach a loading of 0.0076 μmol·m⁻². The lamp was turned on again after the hydrogen evolution peak was observed, and the sample was irradiated for another 100 minutes. Afterwards, the lamp was turned off, and it was left to rest until the hydrogen evolution was zero. A certain amount of H₂PtCl₆ was added to the calcined aerogel dispersion to reach the same loading amount of 0.1 wt.% Pt as for the as-synthesized aerogel sample. The dispersions of the calcined aerogel samples were irradiated again for 100 minutes, the lamp was turned off, and the measurements were stopped after no hydrogen evolution was detected. Photographs of all dispersions were taken before the measurement and after each irradiation step. In a second experiment the reaction parameters were kept identical to the hydrogen evolution experiments. The argon 5.0 flow rate was set to 100 mL·min⁻¹, and the hydrogen gas evolution was detected online using a mass spectrometer (Hiden HPR-20 Q/C) every 13 s. The samples were irradiated for 100 min, and it was left to rest until no hydrogen evolution from that irradiation was detected anymore (this time was set to zero). Then, 0.1 wt. % Pt as precursor was added to the dispersion *via* a rubber sealing without opening the reactor, and it was left to rest until no hydrogen evolution in the dark was detected anymore.

4.3.2 Photocatalytic Nitrogen Reduction

The photocatalytic experiments for nitrogen reduction were performed at the University of Bayreuth. The following description of the experimental procedure is taken from the respective publication (Rose *et al.*).^[195] For the nitrogen reduction reaction, 100 mg of the as-synthesized aerogel were dispersed in 150 mL of 2.5 mol·L⁻¹ aqueous methanol solution. The dispersion was irradiated for 100 minutes under the same conditions as for the absorbance detection measurements; the argon flow rate was set to 50 mL·min⁻¹. After the irradiation under argon flow, the carrier gas was switched to N₂. The flow rate was set to 50 mL·min⁻¹ N₂ for seven hours for the nitrogen reduction reaction in the dark. Afterwards, a salicylate test was performed to determine the yield of NH₃ quantitatively.

5 Results

5.1 Synthesis Procedure and Gelation Behavior of TiO₂ Wet Gels

5.1.1 Gelation and Shrinkage Behavior

The TiO₂ gels are synthesized as described in 3.1. with the performed variations of different synthesis parameters. The reactants have a direct impact on the rate of the hydrolysis and condensation reaction and thus on the gelation process, particle and pore size. The titanium-based precursor generally reacts strongly with water forming undesired precipitates of titanium-oxo and -hydroxo species. ^[99] Different chemical reaction conditions influence the structures which are obtained from Ti alkoxide precursors, *e.g.* colloidal particles (sol), precipitates or gels. ^[104] It is therefore very important to employ such reaction conditions to control the reactions so that gels are obtained. As mentioned in chapter 3, different amounts and types of solvents (with different steric hindrance), as well as solvent mixtures, are used in the synthesis to investigate the reaction kinetics. The amount of HCl is also varied, which can on the one hand catalyze the hydrolysis reaction, on the other hand can form complexes with chloride ions influencing the reaction kinetics and gel formation. The amount of water was varied, since the amount determines the hydrolysis level, that is important for further condensation reactions to form a 3D network. Also, the condensation reaction continues during aging of the gels, due to Ostwald ripening and rearrangements. This leads to changes in the gel and shrinkage. Therefore, it is important to investigate the impact of the synthesis parameter on the gelation kinetics, especially the gelation time and the shrinkage behavior, as it is crucial to finally controlling this process.

5.1.1.1 EtOH Solvent-Based Gels

After mixing TTIP and EtOH the sol appeared to be transparent. The reaction is performed in relatively high amount of solvent, compared to literature. ^[79] The usage of excess EtOH and TTIP as precursor leads to a ligand exchange of the alkyl groups. This was investigated by *in-situ* ¹H-NMR, compare chapter 9.9 in Figure 9.9-1 to Figure 9.9-4., showing a shift in peaks that can be assigned to the exchange of *OiPr* to *OEt* groups at the TTIP precursor. Few minutes after the addition of acid, the reaction mixture changed occasionally to a cloudy appearance, and precipitation of small white particles occurred, which dissolved again after the dropwise addition of water in a last step. The precipitate could be isolated leaving the suspension for a few months, while reducing the amount of solvent slowly. The precipitates were analyzed using

XRD, as shown in the subchapter 5.2.5.4. The precipitates were only found for low acid amounts and did not occur for increasing amount of acid. After 20 minutes, the water was added, which induced the gelation.

Figure 5.1-1 shows the gelation time of EtOH solvent-based gels (Equivalents solvent:TTIP:water 26:1:4) dependent on the HCl:TTIP ratio used during the synthesis. The gelation time increases from less than five minutes for very low TTIP:HCl molar ratios up to 45 minutes for high TTIP:HCl molar ratios (E1 to E6, cf. Table 9.2-1). At very high HCl amounts gelation does not occur and a sol remains. Sample E4.1 to E6.1 were synthesized with an increased amount of acid compared to E1 and increased amount of water compared to the respective samples E4, E5, and E6. The samples E4.1 to E6.1 show an opposite trend for the gelation time to the samples E4 to E6. Shorter gelation times are observed for E4.1 to E6.1 compared to sample E4 to E6, similar to sample E1 and E2.

The shrinkage behavior of the EtOH solvent-based gels is depicted in Figure 5.1-1. The size of the formed wet gel before and after aging was considered for characterizing the shrinkage behavior. For low acid amounts used during the synthesis (E1 to E2, cf. Table 9.2-1) the shrinkage varies between 10 and 15 %. The shrinkage increases up to 33 % for sample E3.

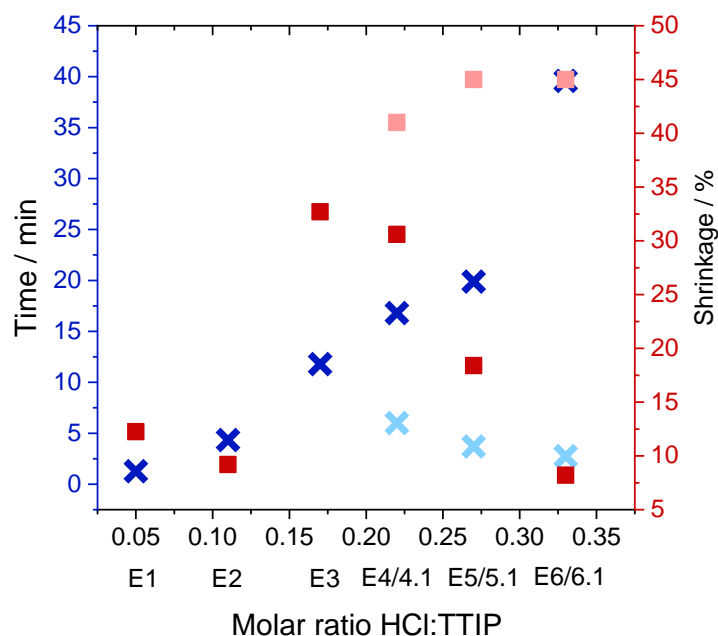


Figure 5.1-1: Gelation time and shrinkage of E1 to E6 (dark blue/red symbols; TTIP:EtOH:H₂O 1:26:4) and E4.1 to E6.1 (light blue/red symbols; TTIP:EtOH:H₂O 1:26:8-12) dependent on HCl:TTIP ratios.

For higher acid amounts (E4 to E6, cf. Table 9.2-1) the shrinkage decreases again to the initial value comparable to the sample E2. The shrinkage is much higher, up to 45 %, for samples E4.1 to E6.1 with increased HCl:TTIP and water:TTIP ratios used during the synthesis (cf. Table 9.2-1).

5.1.1.2 *i*PrOH Solvent-Based Gels

The reaction proceeds similar for *i*PrOH solvent-based gels compared to EtOH as solvent. The reaction mixture stayed completely clear during the synthesis. However, the water could not be added directly to the reaction mixture, due to very fast inhomogeneous gelation. Therefore, the water was dissolved in part of the *i*PrOH to prevent premature gelation.

Preliminary experiments were performed to optimize the amount of solvent and water. The *i*PrOH:TTIP ratio was changed from 30:1 to 45:1. Solvent molecules can coordinate to the precursor and prevent quick agglomeration of formed particles.^[99] The solvent is therefore important to control the gelation. The gelation times and shrinkage behavior dependent on the acid amount is shown in Figure 9.3-1 and Figure 9.3-2 for different solvent:TTIP ratios. The results show that a higher solvent content (solvent:TTIP 30:1 → 45:1) leads to longer gelation times. However, the differences in gelation time are quite small for large TTIP:HCl molar ratios of 0.17:1 to 0.27:1. At smaller TTIP:HCl molar ratios of 0.05:1 to 0.11:1 the differences in gelation time are larger. A solvent:TTIP ratio of 35:1 was chosen as optimum for further experiments.

For the hydrolysis of TTIP, four equivalents H₂O are required to achieve complete hydrolysis. In preliminary experiments, the amount of water was therefore varied from two, four and eight equivalents of water to investigate the impact on gel formation. Figure 9.3-2 shows the gelation time and shrinkage of these samples. No gelation is observed for H₂O:TTIP ratios of 2:1 at low and high HCl amounts (HCl:TTIP: 0.05:1 to 0.22:1). Instable gels and thus incomplete gelation is observed for H₂O:TTIP ratios of 4:1 at low HCl amounts (HCl:TTIP 0.05:1). For increasing HCl:TTIP ratio up to 0.22:1 the gelation time becomes shorter at a molar ratio for H₂O:TTIP of 4:1. A higher molar ratio of H₂O:TTIP of 8:1 leads to stable gels and the gelation time varies between 10 and 30 minutes – but no clear correlation between molar ratio HCl/TTIP and gelation time is observed. The shrinkage of the samples increases with the amount of water for all gelled samples (Figure 9.3-2).

Figure 5.1-2 shows the gelation time of *i*PrOH solvent-based gels (Equivalents: solvent:TTIP:water 35:1:4) dependent on the HCl:TTIP ratio used during the synthesis.

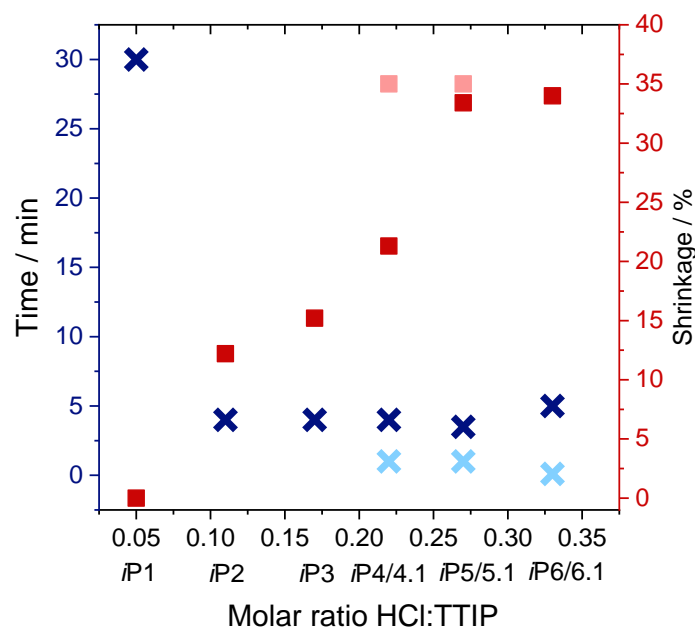


Figure 5.1-2: Gelation time and shrinkage of *iP1* to *iP6* (dark blue/red symbols; TTIP:*iPrOH*:H₂O 1:35:4) and *iP4.1* to *iP6.1* (light blue/red symbols; TTIP:*iPrOH*:H₂O 1:35:8-12) dependent on HCl:TTIP ratios.

The gelation behavior of *iPrOH* and EtOH solvent-based gels show huge differences. The gelation time of *iPrOH* solvent-based gels is very high (30 minutes) for a very low TTIP:HCl molar ratio of 0.05:1 (*iP1*, cf. Table 9.2-2). The gelation is reduced to approx. five minutes for a TTIP:HCl molar ratio of >0.11:1 (*iP2*-*iP6*, cf. Table 9.2-2).

Samples *iP4.1* to *iP6.1* were synthesized with an increased amount of acid compared to *iP1* and an increased amount of water compared to the respective samples *iP4* to *iP6*. For sample *iP4.1* to *iP6.1* the amount of water was simultaneously increased to the amount of acid, showing gelation times less than five minutes. For *iP6.1* the gelation occurred instantly, so that due to the non-controllable gelation an inhomogeneous gel was obtained, which was not further analyzed.

The shrinkage of the gels *iP1* to *iP6* increases from 0 % up to 35 % with increasing amount of acid. This was also observed for solvent:TTIP ratios of 30:1 to 45:1 (see appendix/Figure 9.3-1). The shrinkage behavior does not change dependent on the solvent amount. The samples *iP4.1* and *iP5.1* exhibit a similar shrinkage behavior, but it is much higher for *iP4.1* compared to *iP4* with less amount of water. For *iP5.1* the shrinkage is similar to *iP5*.

5.1.1.3 Mixed Solvent-Based Gels

Mixed solvent-based gels, which mainly based on *i*PrOH as solvent exhibit very short gelation times, as shown in Figure 5.1-3. For E-*i*P1 (EtOH:*i*PrOH 1:10) the gelation occurred instantly so that an inhomogeneous gel resulted, which was not further analyzed, due to the non-controllable gelation. The gelation time can be extended with increasing the amount of EtOH up to a 1:1 mixture of EtOH:*i*PrOH. Above 1:1 EtOH:*i*PrOH mixtures the gelation time varies between 2.5 and 6.5 minutes. The samples E-*i*P2 to E-*i*P4 with excess of *i*PrOH exhibit a nearly constant shrinkage at approx. 18 to 19 %. Similar values were found for 1:1 molar ratio of EtOH:*i*PrOH (E-*i*P5). For the samples E-*i*P6 to E-*i*P9 with excess of EtOH the shrinkage is lower but varies without any trend in the range of 10 to 16 %.

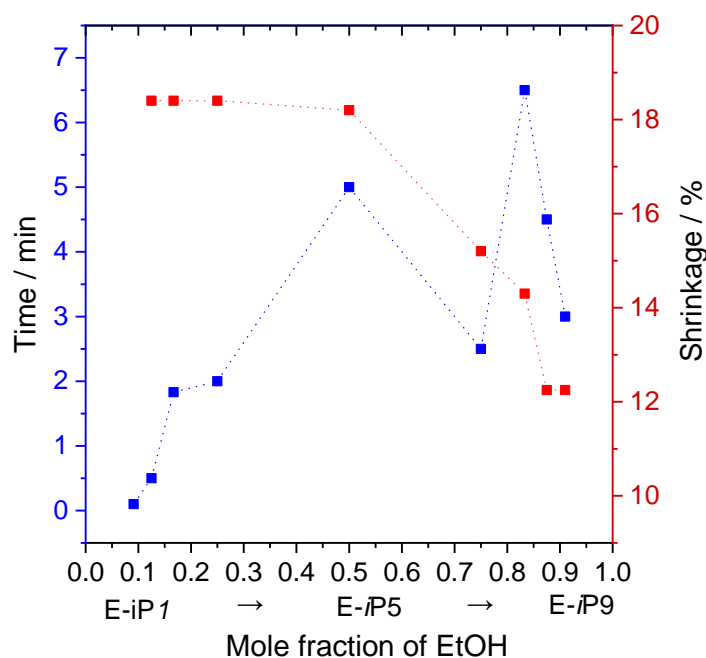


Figure 5.1-3: Gelation time and shrinkage of mixed solvent-based aerogels E-*i*P1 to E-*i*P9 dependent on the mole fraction of EtOH/(EtOH+*i*PrOH).

5.2 Structural Properties of TiO₂ Aerogel

5.2.1 Appearance of TiO₂ Aerogels

The appearance of the synthesized wet gels gives a first indication on the structure before the gel is dried under supercritical conditions. The appearance of the dried TiO₂ gels ranges from transparent to opaque and powder-like to monolithic. This depends on the crosslinking process, formation of porous structures, and the strength of the gel.

5.2.1.1 EtOH Solvent-Based Gels and Aerogels

The gel samples E1 to E6 were synthesized in an EtOH solvent-based synthesis route with increasing HCl:TTIP ratio from E1 to E6 (cf. Table 9.2-1) and are shown in Figure 5.2-2. The gels are translucent for low acid amounts used during the synthesis (sample E1) and turned opaque with increasing the amount of acid during the synthesis. The gels become less transparent during the aging process. Aging was actually performed to strengthen the gel structure. However, the gels E4 to E6 with high HCl:TTIP ratio appeared to be quite instable after aging, leading to a slurry-like appearance for gel sample E6. This is shown in Figure 5.2-2 for sample E6. The sample displayed nearly no shrinkage during aging.

The resulting supercritically dried aerogels appear to be very brittle leading to many smaller fragmentation (Figure 5.2-1). The aerogel samples E1 and E2 appeared to be transparent, while with increasing amount of acid used during the synthesis, the resulting aerogels turn opaque, as observed for the wet gels. For high acid amounts the aerogels exhibited a powder-like appearance.



Figure 5.2-2: Images of wet gels showing the appearance of the gels after aging with increasing acid amount from E1 to E6.

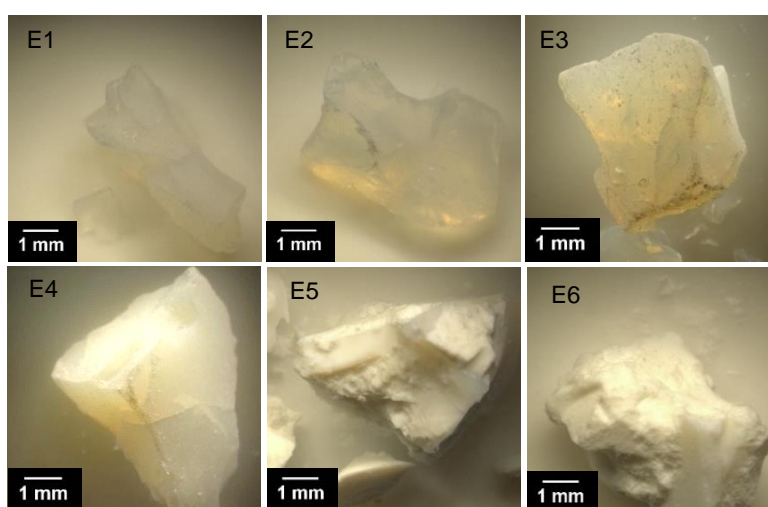


Figure 5.2-1: Optical microscope images of supercritically dried aerogels showing the appearance of the aerogels with increasing acid amount from E1 to E6.

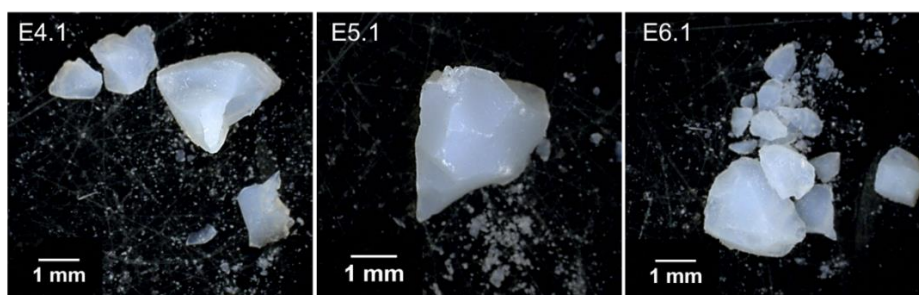


Figure 5.2-3: Optical microscope images of supercritically dried aerogels showing the appearance of the aerogels with increasing amount of acid and water from E4.1 to E6.1.

The aerogels E4.1 to E6.1 were synthesized with the EtOH solvent-based synthesis route, but contained high acid and water amounts. Small fragments were found for the aerogel samples E4.1 to E6.1 shown in Figure 5.2-3. Because of the higher water content, the stability and transparency of the aerogels E4.1 to E6.1 were generally higher compared to the aerogel samples E4 to E6, as shown in Figure 5.2-1 and Figure 5.2-3.

5.2.1.2 *i*PrOH Solvent-Based Aerogels

The *i*PrOH solvent-based gels (*i*P1 to *i*P6) were transparent directly after the gelation but turned cloudy after few minutes. With increasing HCl content the cloudy appearance occurred quicker. The gels *i*P1 to *i*P6 are shown in Figure 5.2-4. They appear to be less transparent compared to E1 to E6. The amount of acid used in the synthesis increases from *i*P1 to *i*P6 and the appearance of the gels turned from translucent to opaque.



Figure 5.2-4: Images of wet gels showing the appearance of the gels after aging with increasing acid amount from *i*P1 to *i*P6.



Figure 5.2-6: Images of wet gels showing the appearance of the gel *iP5* (HCl:TTIP 0.27:1) aged for one to seven days respectively.

In Figure 5.2-6 the changes due to the aging time are shown for sample *iP5*. After one day of aging, the sample exhibits many cracks. The shrinkage process starts slowly after two days. After four to five days the shrinkage rate increased until the sample was taken out of the furnace after seven days.

The supercritically dried aerogels synthesized with the *iPrOH* solvent-based synthesis route are shown in Figure 5.2-5. The aerogels show a similar translucent to opaque appearance like the wet gels in Figure 5.2-4. The aerogels appear to be brittle leading to many small fragments, similar to EtOH-based aerogels. With increasing amount of acid used during the synthesis, the aerogels turn into powder-like aerogels with some larger fragments. Since changes in the appearance were observed also for the samples E4.1 to E6.1 with increased water and acid

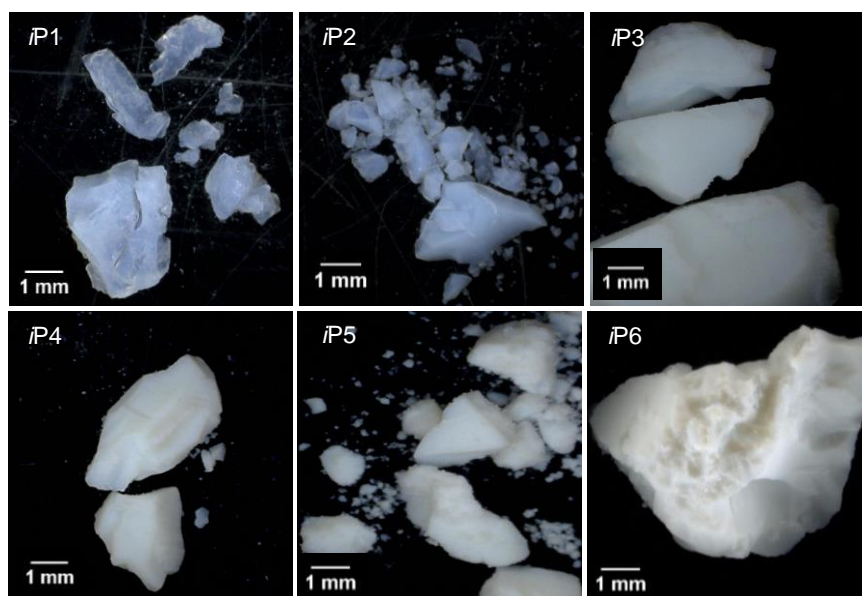


Figure 5.2-5: Optical microscope images of supercritically dried aerogels showing the appearance of the aerogels with increasing acid amount from *iP1* to *iP6*.

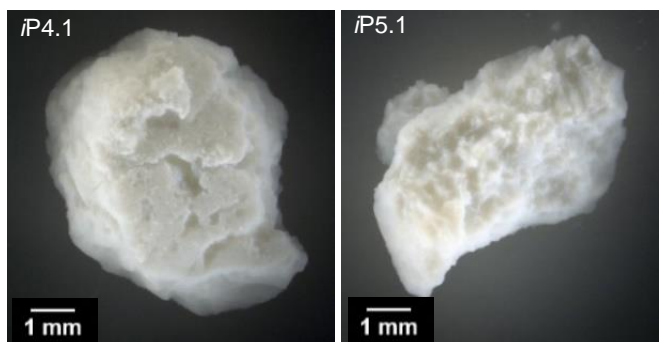


Figure 5.2-7: Optical microscope images of supercritically dried aerogels showing the appearance of the aerogels with increasing amount of acid and water from *iP4.1* to *iP5.1*.

amount used during the synthesis, it was expected that also sample *iP4.1* and *iP5.1* show differences. However, the stability and transparency of the aerogels *iP4.1* and *iP5.1* didn't change for an increased water and acid content used during the synthesis, as shown in Figure 5.2-7.

5.2.1.3 Mixed Solvent-Based Aerogels

The aerogels E-*iP1* to E-*iP9* appeared to be opaque. As an example, E-*iP5* (1:1) is shown in comparison to the aerogels E2 and *iP2* which were synthesized in pure EtOH and pure *iPrOH*, respectively (Figure 5.2-8). The aerogels made from EtOH are more transparent compared to the mixed solvent-based and the *iPrOH* solvent-based aerogels. However, the structural integrity seems to be influenced by the mixture of solvents. The sample E-*iP5* showed a monolithic structure in contrast to all other synthesized aerogels, which exhibited fragmentation.

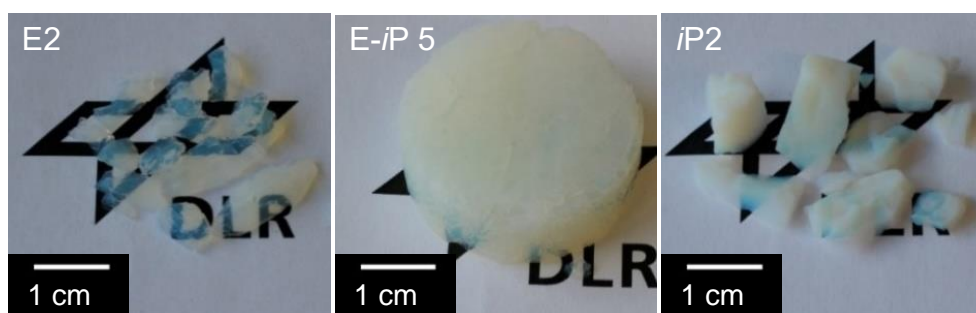


Figure 5.2-8: Images of supercritically dried aerogels, showing the structural integrity and transparency of the aerogels samples E2 (left), E-*iP5* (middle) and *iP2* (right).

5.2.1.4 Calcined Aerogels

The aerogels were calcined at different temperatures in air. The aerogels show a light brown color after calcination at 300 °C in air for 10 hours, as shown in Figure 5.2-9. Further increase in calcination temperature lead to white aerogels. Shorter calcination times between two and four hours in air at 300 °C result in dark brown aerogels, whereas calcination in vacuum show even darker aerogels with a brownish-black color.



Figure 5.2-9: Optical microscope images showing the appearance of aerogel sample E2 calcined at 300, 400 and 500 °C for 10 hours (h) in air (A).

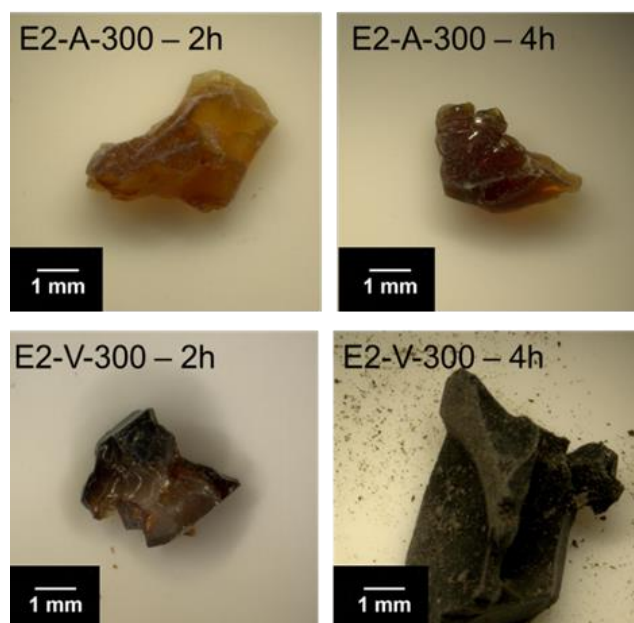


Figure 5.2-10: Optical microscope images showing the appearance of aerogel sample E2 calcined at 300 °C for two and four hours (h) in air (A) and vacuum (V).

5.2.2 Surface and Pore Characteristics

Nitrogen physisorption experiments were performed to determine the surface area, pore volume and pore size distribution of the aerogel samples. These values are important for the catalytic activity of the aerogel. The surface area influences the adsorption of reactants for catalytic reactions, since the surface area determines the amount of adsorbed species. The pore volume and pore size distribution determine which size of reactant molecule can access the catalytic aerogel structure. In the synthesis, the selected solvent, amount of acid and water, as well as the calcination treatments have an impact on the aerogel structure and therefore alter the pore structure.

5.2.2.1 EtOH Solvent-Based Aerogels

The physisorption isotherms of the EtOH solvent-based TiO₂ aerogels E1 to E6 are presented in Figure 5.2-11. The isotherm shape and hysteresis loops are classified according to the IUPAC recommendations.^[196] For sample E1 to E3 with low acid:TTIP molar ratios (0.05:1, 0.11:1, 0.17:1) the isotherm exhibits a type IVa character with the H1 hysteresis loop. The saturation plateau of the N₂ adsorption branch as well as the steep and narrow hysteresis loop indicate a mesoporous material with a narrow pore size distribution. Further, with increasing acid:TTIP ratio the hysteresis is shifted to lower relative pressures ($p/p^0 < 0.7$), indicating less accessible pores of the shape of, *e.g.* ink bottles with small bottlenecks. For sample E4 to E6 with higher

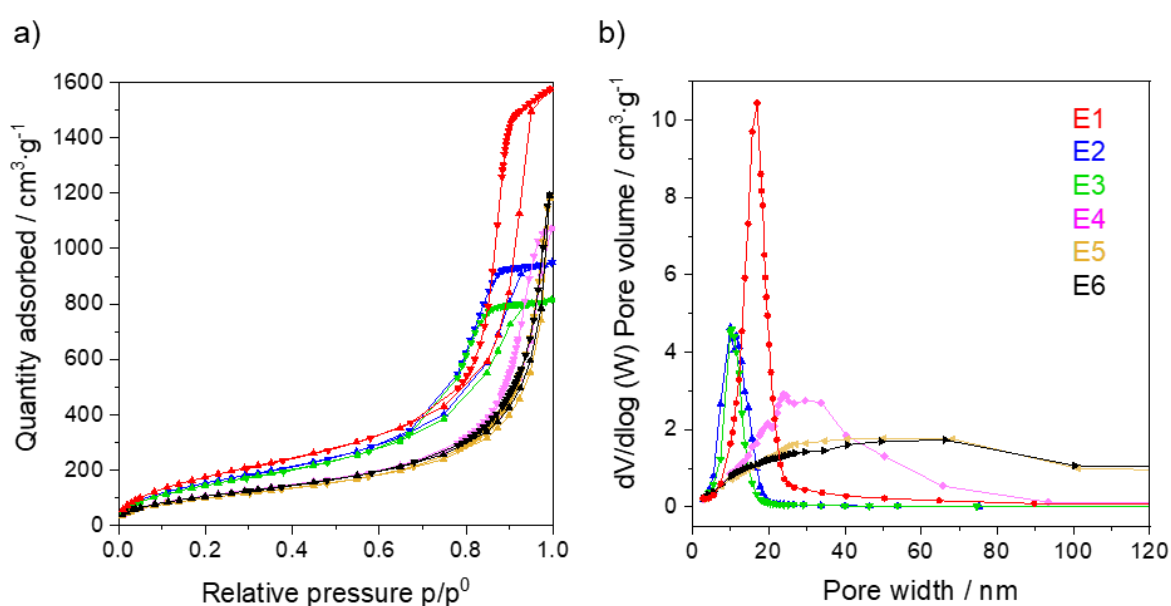


Figure 5.2-11: a) Physisorption isotherms and b) pore size distribution of aerogel samples E1 to E6. The amount of acid in the synthesis increases from E1 to E6.

acid:TTIP molar ratios ($>0.17:1$) the isotherms exhibit a combination of type IVa and II character. The steep ending of the isotherm at high relative pressure ($p/p^0 > 0.7$) and the very narrow hysteresis loop indicate meso- and macropores. The plateau at the ending of the adsorption path is missing. The hysteresis loops show a steep ending and close at higher relative pressures, indicating readily accessible pores. This is consistent with the pore size distribution shown in Figure 5.2-11. A narrow pore size distribution was obtained for low acid amounts for sample E1, E2, and E3, while high acid amounts during the synthesis lead to very broad pore size distributions for the samples E4 to E6.

In Figure 5.2-12 the isotherms and pore size distributions of EtOH solvent-based aerogels E4 to E6 with increased HCl:TTIP ratio ($>0.22:1$) are shown in comparison to the aerogels E4.1 to E6.1 with simultaneously increased water content. Interestingly, the aerogels E4 to E6 with high HCl:TTIP ratio but low water:TTIP ratio exhibit a broad pore size distribution, whereas a high HCl:TTIP ratio and high water:TTIP ratio lead to narrow pore size distribution. Even for very high HCl:TTIP ratios, the broadening effect of the pore size distribution can be compensated to achieve a narrow pore size distribution by simply increasing the water amount simultaneously to the acid amount during the synthesis.

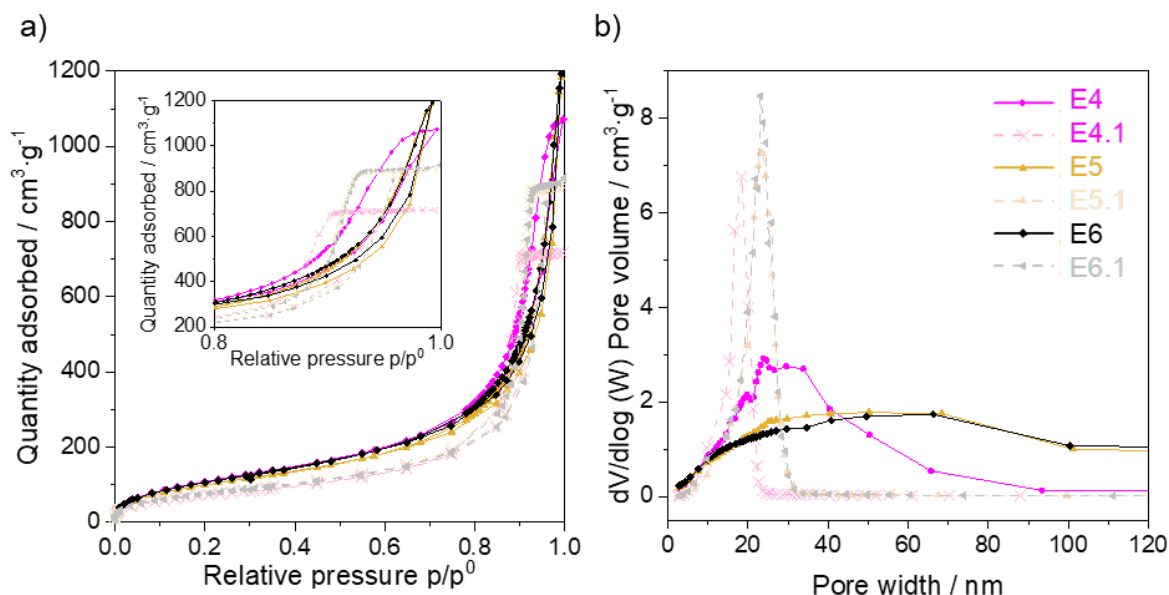


Figure 5.2-12: a) Physisorption isotherms and b) pore size distribution of aerogel sample E4 to E6 and E4.1 to E6.1. The amount of acid used in the synthesis increases from E4 to E6 and E4.1 to E6.1. The amount of water used in the synthesis increases from E4.1 to E6.1 and is higher compared to that of the respective samples E4, E5, and E6.

Table 5.2-1: Physisorption results of aerogels E1 to E6 and E4.1 to E6.1.

Sample	$S_{\text{BET}} / \text{m}^2 \cdot \text{g}^{-1}$	$V_{\text{P}} / \text{cm}^3 \cdot \text{g}^{-1}$	BJH value / nm
E1	692 ± 33	2.4 ± 0.2	17 ± 1.5
E2	600 ± 29	1.5 ± 0.1	11 ± 0.9
E3	568 ± 27	1.3 ± 0.1	10 ± 0.9
E4	416 ± 20	1.7 ± 0.2	24 ± 2.1
E4.1	269 ± 13	1.1 ± 0.1	18 ± 1.5
E5	383 ± 18	1.8 ± 0.2	40 ± 3.5
E5.1	290 ± 14	1.4 ± 0.1	23 ± 2.0
E6	410 ± 20	1.9 ± 0.2	66 ± 5.7
E6.1	289 ± 14	1.4 ± 0.1	23 ± 2.0

The physisorption results are summarized in Table 5.2-1. The EtOH solvent-based TiO₂ aerogel E1 exhibits the highest specific surface area and pore volume of $692 \text{ m}^2 \cdot \text{g}^{-1}$ and $2.4 \text{ cm}^3 \cdot \text{g}^{-1}$, respectively. For E2 the surface area decreased to about $600 \text{ m}^2 \cdot \text{g}^{-1}$, however, the pore volume decreased more drastically from 2.4 to $1.5 \text{ cm}^3 \cdot \text{g}^{-1}$. This trend is continued for E3 to E6, that the surface area and pore volume decrease with increasing amount of acid. The surface areas and pore volumes of the aerogels E4.1, E5.1 and E6.1 with high HCl:TTIP and high water:TTIP ratio are generally lower compared to the respective values of aerogel samples E4, E5, and E6 with high HCl:TTIP but low water:TTIP ratio. The BJH maximum values obtained from the pore size distribution shifts to larger pore sizes (10 to 66 nm) for the samples E2 to E6 with increasing acid amount used during the synthesis. The sample E1 does not fit in this trend and shows a BJH value of 17 nm. The samples E4.1, E5.1 and E6.1 exhibit BJH values between 18 to 23 nm similar to the sample E1. The series of EtOH solvent-based aerogels was synthesized using absolute EtOH. Due to availability, some aerogel samples of E2 (basis for calcined samples) were synthesized using denatured/technical grade EtOH. This led to an increase in pore volume, surface area, and BJH value compared to the sample E2 synthesized with absolute EtOH. The respective comparison of physisorption data is shown in the appendix in Figure 9.5-1.

5.2.2.2 *i*PrOH Solvent-Based Aerogels

Preliminary experiments were performed to optimize the amount of solvent and water to maximize the BET surface area of *i*PrOH solvent-based aerogels. Different solvent:TTIP molar ratios from 30:1 to 45:1 were investigated. The results are shown in the appendix in Figure 9.3-3 and show that the highest values of the BET surface area and pore volume can be achieved

for a solvent:TTIP molar ratio of 35:1. The surface area further depends on the amount of acid, which is shown in the following for the aerogel sample with optimized solvent:TTIP molar ratio of 35:1. No clear dependence of the BJH pore size distribution on the solvent amount was found. Between HCl:TTIP ratios of 0.11:1 to 0.22:1 the pore size decreases slightly with increasing solvent content. However, for larger HCl:TTIP ratios very similar BJH values were found at different solvent amounts (Figure 9.3-3). Also, the amount of water was therefore varied between two, four and eight equivalents of water to find the optimum. The surface area and pore volume showed slightly higher values for eight equivalents of water compared to four equivalents of water. However, the gelation time is much shorter for eight equivalents of water making the synthesis less controllable. Therefore, four equivalents of water were chosen as optimum for further experiments.

The physisorption isotherms of the *i*PrOH solvent-based TiO₂ aerogels *i*P1 to *i*P6 (solvent:TTIP:H₂O 35:1:4) are presented in Figure 5.2-13. For low acid/TTIP molar ratios (0.05:1) the isotherm exhibits a type IVa character with the H1 hysteresis loop according to the IUPAC classifications [196], indicating a mesoporous material. For higher acid/TTIP molar ratios (>0.11:1) the isotherms exhibit type IVa/II character indicating meso- and macropores, similar to EtOH solvent-based aerogels. The plateau at the end of the adsorption path is missing.

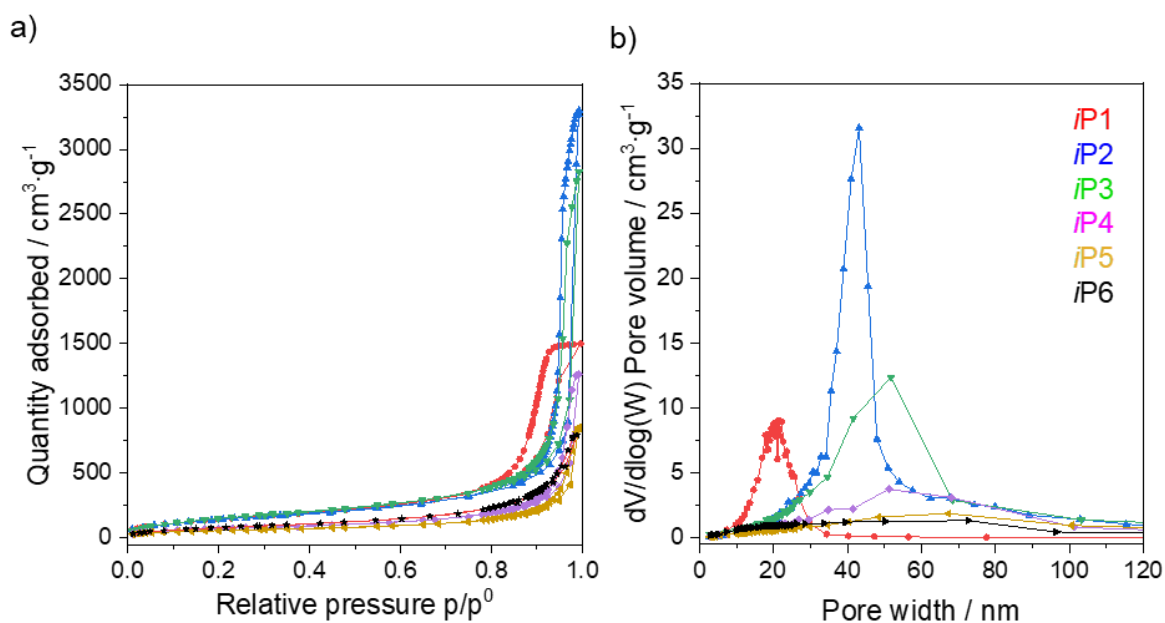


Figure 5.2-13: a) Physisorption isotherms and b) pore size distribution of the aerogel samples *i*P1 to *i*P6. The amount of acid in the synthesis increases from *i*P1 to *i*P6.

The hysteresis loop shows a steep ending (at $p/p^0 \approx 0.99$) and closes at higher relative pressures (at $p/p^0 \approx 0.7$), indicating readily accessible pores. The pore sizes increase with increasing acid amount, as depicted in the pore size distribution in Figure 5.2-13. In Figure 5.2-14a and b the isotherms and pore size distributions of *i*PrOH solvent-based aerogels *i*P4 to *i*P5 with increased acid amount are shown in comparison to the aerogels *i*P4.1 to *i*P5.1 with simultaneously increased water addition. The samples *i*P4.1 to *i*P5.1 behave very similarly in physisorption experiments to the samples *i*P4 to *i*P5.

The physisorption results are summarized in Table 5.2-2. The *i*PrOH solvent-based TiO₂ aerogel *i*P1 exhibits a high specific surface area and a pore volume of $554 \text{ m}^2 \cdot \text{g}^{-1}$ and $2.5 \text{ cm}^3 \cdot \text{g}^{-1}$, respectively which is similar to the findings of sample E2. The high surface area and large pore volume are achieved by the mesopores of average size of 20 nm. For *i*P2 and *i*P3 the specific surface area is similar to *i*P1, while the pore volume increased drastically. This is achieved by the combined meso- and macroporous structure with an average pore size of 43 nm and 52 nm, respectively. The samples *i*P4 to *i*P6 show smaller pore volumes and the surface area varies between 211 and $207 \text{ m}^2 \cdot \text{g}^{-1}$ which is less compared to *i*P1 and *i*P3.

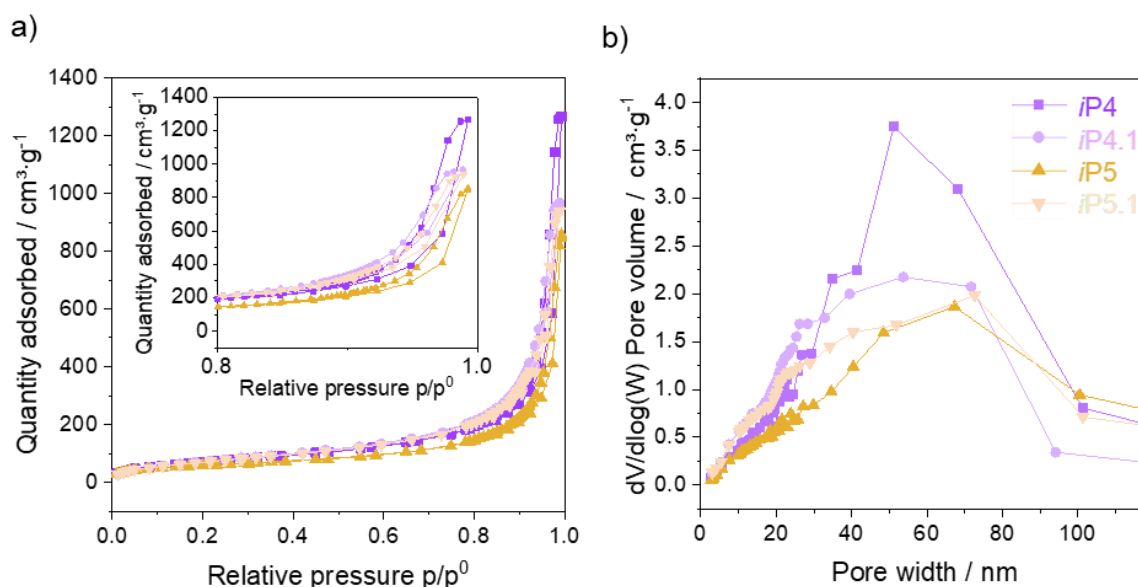


Figure 5.2-14: a) Physisorption isotherms and b) pore size distribution of aerogel sample *i*P4 to *i*P5 and *i*P4.1 to *i*P5.1. The amount of acid used in the synthesis increases from *i*P4 to *i*P5 and *i*P4.1 to *i*P5.1. The amount of water used in the synthesis increases from *i*P4.1 to *i*P5.1 and is higher compared to that of the respective samples *i*P4 and *i*P5.

Table 5.2-2: Physisorption results of aerogels *iP1* to *iP6* and *iP4.1* to *iP5.1*

Sample	$S_{\text{BET}} / \text{m}^2 \cdot \text{g}^{-1}$	$V_{\text{P}} / \text{cm}^3 \cdot \text{g}^{-1}$	BJH value / nm
<i>iP1</i>	554 ± 26	2.3 ± 0.2	20 ± 1.7
<i>iP2</i>	536 ± 26	5.1 ± 0.5	43 ± 3.7
<i>iP3</i>	586 ± 28	4.4 ± 0.4	52 ± 4.5
<i>iP4</i>	266 ± 13	2.0 ± 0.2	51 ± 4.4
<i>iP4.1</i>	280 ± 13	1.5 ± 0.1	54 ± 4.6
<i>iP5</i>	211 ± 10	1.3 ± 0.1	67 ± 5.8
<i>iP5.1</i>	271 ± 13	1.5 ± 0.1	71 ± 6.1
<i>iP6</i>	307 ± 15	1.2 ± 0.1	72 ± 6.2

The aging process and its impact on the specific surface area and pore volume were further analyzed for sample *iP5*, which showed a high crystallinity (see chapter 5.2.5). This sample was chosen because of the large shrinkage during aging. As stated in the synthesis section, the gels are aged for seven days to strengthen the gel network. The sample *iP5* was therefore aged between one and seven days respectively and the reactions were stopped by removing the sample from the oven and exchanging the liquid immediately with fresh solvent. The development of the surface area and pore volume is shown in Figure 5.2-15. The surface area and pore volume stay nearly constant for the first two days of aging before the values decrease steadily.

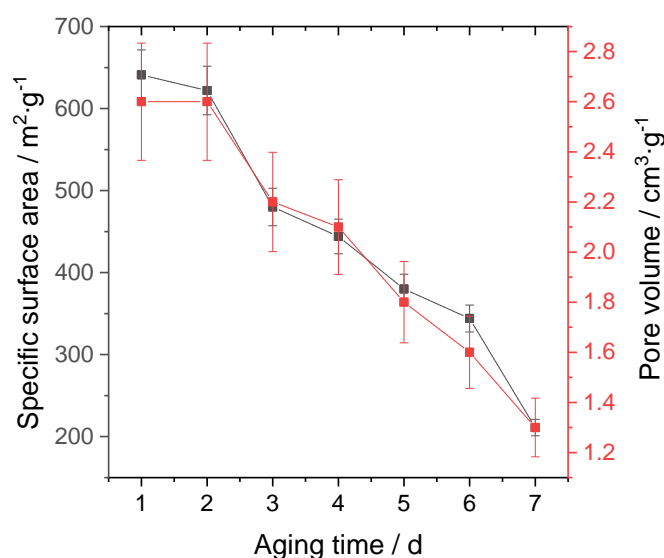


Figure 5.2-15: Surface area and pore volume of the aerogel sample *iP5* (HCl:TTIP 0.27:1) aged between one and seven days, respectively.

5.2.2.3 Mixed Solvent-Based Aerogels

The physisorption isotherms of the mixed solvent-based TiO₂ aerogels E-*i*P2 to E-*i*P9 are presented in Figure 5.2-16. The aerogels were synthesized using absolute EtOH. The samples E-*i*P2 to E-*i*P4, mainly containing *i*PrOH, show similar isotherms which fit to a type IVa/II isotherm.^[196] The plateau at the ending of the adsorption branch of the isotherms is missing, as previously observed for *i*PrOH solvent-based aerogels. The pore size distribution in Figure 5.2-16 shows a slight decrease in pore sizes from 23 nm to 17 nm with increasing EtOH content in *i*PrOH dominated aerogels. The samples E-*i*P6 to E-*i*P9, mainly containing EtOH, show almost identical isotherms which fit to a type IVa isotherm.^[196] Also, the pore size distributions are almost identical. The pores are slightly smaller for EtOH dominated aerogels (15 to 18 nm) compared to *i*PrOH dominated aerogels (17 to 23 nm). The pore size distributions of the pure *i*PrOH solvent-based aerogel *i*P2 and pure EtOH solvent-based aerogel E2 are shown in Figure 5.2-16 for comparison. The mixed solvent-based aerogels have pore sizes between the two extreme values of E2 and *i*P2. The sample E-*i*P5 with the same amount of *i*PrOH and EtOH exhibits a type IVa isotherm, but the adsorbed amount of N₂ is much higher compared to the other EtOH dominated samples. Also, the hysteresis loop is shifted to higher pressures, indicating larger pores than the other EtOH dominated samples.^[196] The pore size of E-*i*P5 about 26 nm lies in between the pure *i*PrOH solvent-based aerogel *i*P2 (45 nm) and pure EtOH solvent-based aerogel E2 (11 nm).

In Figure 5.2-17a comparison of the surface area and pore volume is shown for the mixed solvent-based aerogels and the extreme values of E2 and *i*P2 dependent on the mole fraction of EtOH. The *i*PrOH dominated aerogels exhibit slightly higher surface areas between 640 and 660 m²·g⁻¹ compared to the pure *i*PrOH solvent-based aerogel *i*P2 (540 m²·g⁻¹). The surface area drops below 600 m²·g⁻¹ for a 1:1 EtOH- *i*PrOH mixture but increases again for EtOH dominated aerogels to values between 610 and 660 m²·g⁻¹. However, the values vary and do not obey any trend. The *i*PrOH dominated aerogels and the 1:1 EtOH-*i*PrOH mixture exhibit much higher pore volumes compared to EtOH dominated and pure EtOH solvent-based aerogels.

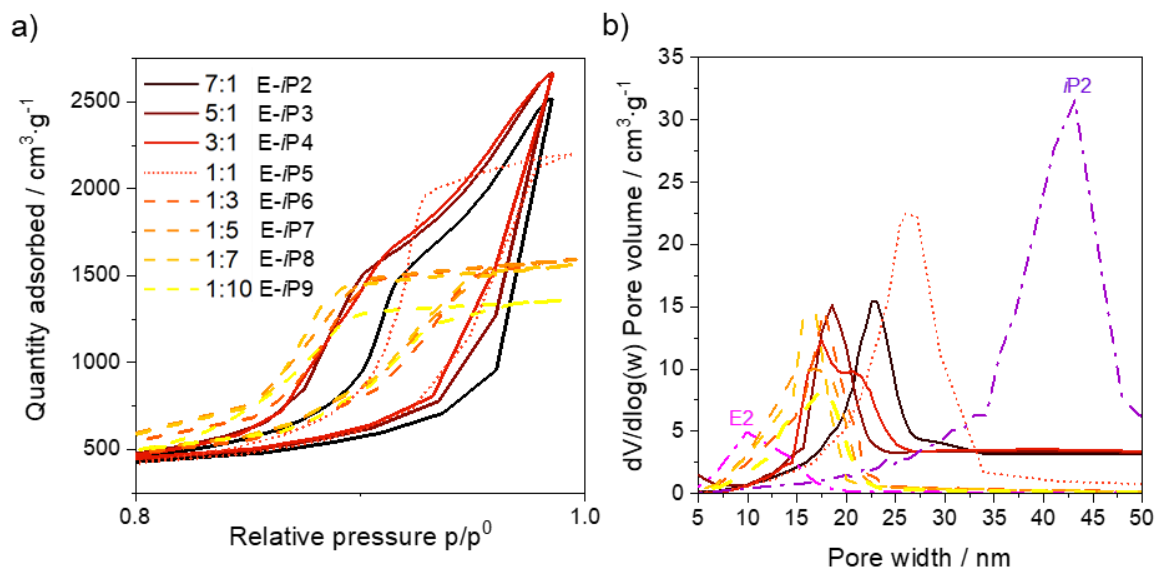


Figure 5.2-16: a) Physisorption isotherms and b) pore size distribution of mixed solvent-based aerogels E-*i*P2 to E-*i*P9 in comparison to pore size distributions of *i*P2 and E2. The dashed lines represent the aerogel samples with excess of EtOH. The solid lines represent the aerogel samples with excess of *i*PrOH.

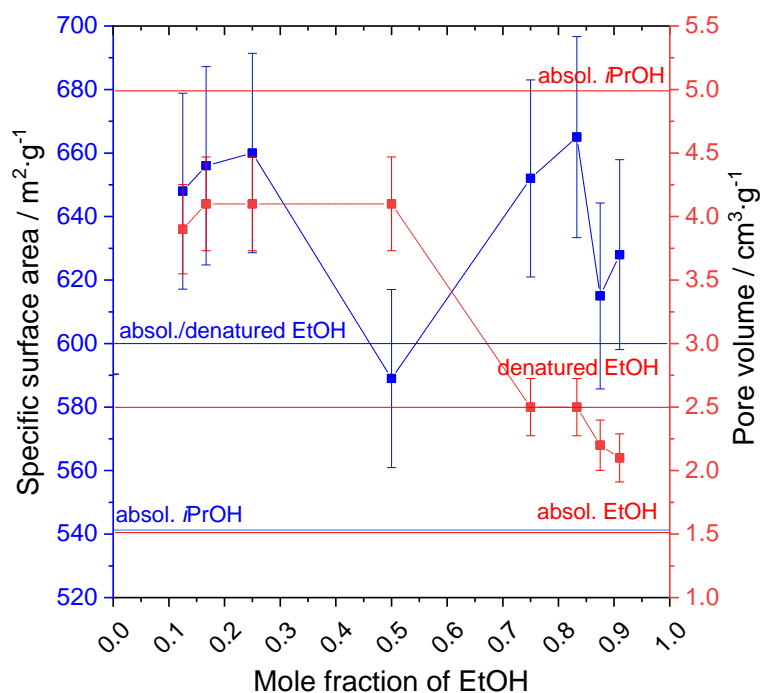


Figure 5.2-17: Surface area and pore volume of mixed solvent-based aerogels E-*i*P2 to E-*i*P9 dependent on the mole fraction of EtOH/EtOH+*i*PrOH. Reference lines indicate the values for the surface area and pore volume of E2 and *i*P2 for pure solvents.

5.2.2.4 Calcined Aerogels

After calcination of the aerogels in air for 10 hours the pore size distribution is slightly narrower, and the average pore size shifts to larger pores (20 to 25 nm) compared to the non-calcined sample E2. This can also be observed at the position of the hysteresis loops, which occur at a higher relative pressure and in a narrower pressure range for higher calcination temperatures. The surface area as well as the pore volume decrease for the calcined TiO₂ aerogel at 300 °C. The surface area and pore volume show a further decrease for the TiO₂ aerogels calcined at 400 and 500 °C, respectively (Table 5.2-3).

The results of the calcined samples E2-A-300-2/4 and E2-V-300-2/4 in Figure 5.2-19 are not comparable to data of the calcined aerogels shown in Figure 5.2-18 regarding the pore volume and pore size distribution. This is due to the usage of denatured EtOH for the samples E2-A-300/400/500-10, whereas for the other samples absolute EtOH was used for synthesis. The usage of different purities of EtOH leads to different pore volumes and pore sizes but no differences in surface area. A comparison of the used solvents is shown in chapter 9.5 in the appendix.

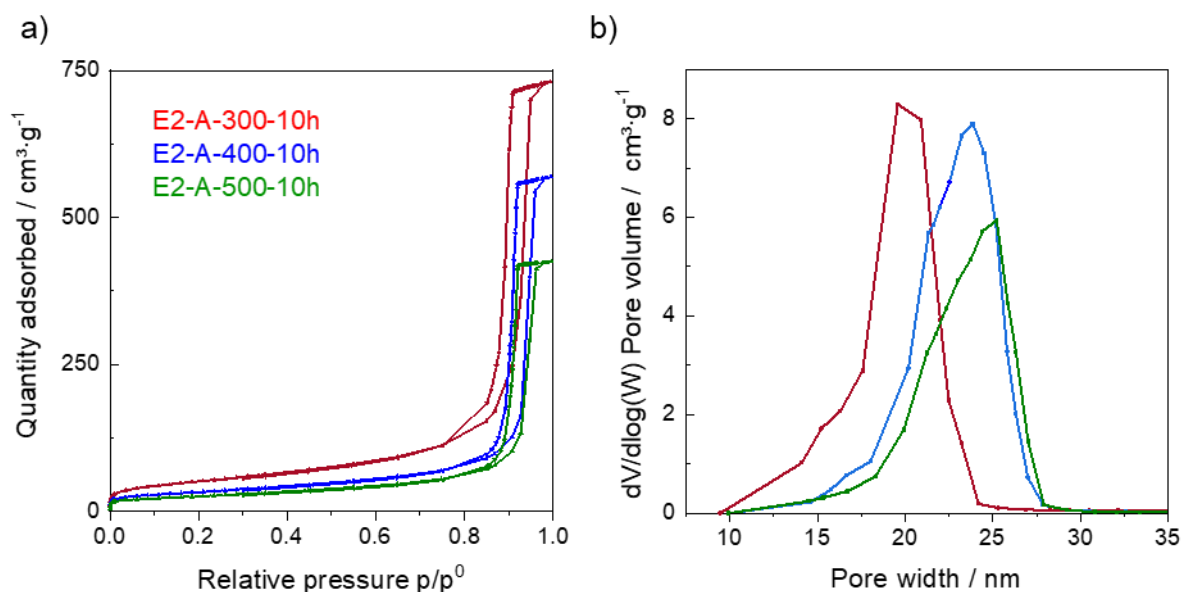


Figure 5.2-18: a) Physisorption isotherms and b) pore size distribution of calcined aerogel E2 (based on denatured EtOH) for 10 hours (h) at 300 °C (red), 400 °C (blue), 500 °C (green) in air (A). Reprinted (adapted) with permission from A. Rose *et al.* Photocatalytic Activity and Electron Storage Capability of TiO₂ Aerogels with an Adjustable Surface Area. ACS Applied Energy Materials, 2022. 5(12): p. 14966-14978. Copyright 2022 American Chemical Society.

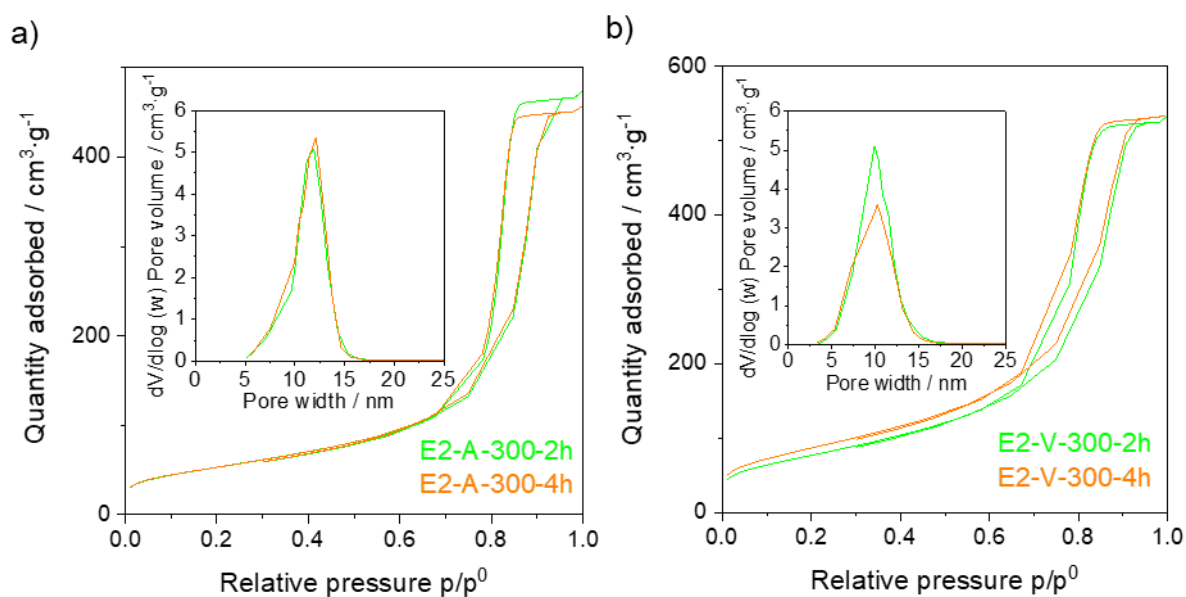


Figure 5.2-19: Physisorption isotherms and pore size distribution of calcined aerogels E2 (based on absol. EtOH) at a) 300°C in air (A) for two hours (green) and four hours (orange), b) 300 °C in vacuum (V) for two hours (green) and four hours (orange).

Shorter calcination times between two to four hours at 300 °C in air lead to an increase in pore sizes to 13 nm compared to E2 (11 nm). The surface area decreases significantly for longer calcination times, and the pore volume decreases accordingly. Interestingly, calcination in vacuum between two and four hours at 300 °C shows no change in pore size distribution. The surface area and pore volume also decrease compared to the untreated sample E2, but in much lesser extent compared to calcination in air.

Table 5.2-3: Physisorption results of calcined aerogel.

Sample	$S_{\text{BET}} / \text{m}^2 \cdot \text{g}^{-1}$	$V_{\text{P}} / \text{cm}^3 \cdot \text{g}^{-1}$	BJH value / nm
E2-A-300-10	184 ± 9	1.1 ± 0.10	20 ± 1.7
E2-A-400-10	118 ± 6	0.9 ± 0.08	24 ± 2.1
E2-A-500-10	92 ± 4	0.7 ± 0.06	25 ± 2.2
E2-A-300-2	122 ± 6	0.73 ± 0.07	13 ± 1.1
E2-A-300-4	191 ± 9	0.71 ± 0.06	13 ± 1.1
E2-V-300-2	281 ± 13	0.82 ± 0.07	10 ± 0.9
E2-V-300-4	316 ± 15	0.83 ± 0.07	10 ± 0.9

5.2.3 Density and Porosity

Aerogels generally exhibit low envelope densities which include the pores of the measured volume. The skeletal density describes the density of the solid particles and closed pores, excluding the open pores. The porosity can be calculated from these two measured density values. However, a certain mechanical strength is required to determine the envelope density, which is not the case for the synthesized aerogels. Another approach was chosen to determine the porosity using the skeletal density and the pore volume, which is additionally measured by physisorption experiments. The porosity is an important structural property of aerogels and might be crucial for potential applications.

5.2.3.1 EtOH Solvent-Based Aerogels

The skeletal densities of the aerogel samples E1 to E6 are shown in Table 5.2-4. No trend dependent on the acid content could be observed for the skeletal density and the porosity values of sample E1 to E6. The porosity varies between 77 and 83 %. The samples E4.1, E5.1 and E6.1 were synthesized with an increased amount of acid compared to E1 and increased amount of water compared to the respective samples E4, E5, and E6. The skeletal density of these samples is slightly lower, compared to E1 to E5. Also, the porosity decreases for these samples slightly to 72 to 78 %.

Table 5.2-4: Skeletal density and porosity values of aerogels E1 to E6 and E4.1 to E6.1.

Sample	Skeletal density / $\text{g}\cdot\text{cm}^{-3}$	Porosity / %
E1	2.202 ± 0.003	84.1 ± 1.4
E2	2.620 ± 0.003	79.7 ± 1.6
E3	2.613 ± 0.002	77.3 ± 1.8
E4	2.660 ± 0.006	81.9 ± 1.5
E4.1	2.319 ± 0.002	71.8 ± 2.0
E5	2.638 ± 0.004	82.6 ± 1.5
E5.1	2.506 ± 0.001	77.8 ± 1.7
E6	2.489 ± 0.005	82.5 ± 1.5
E6.1	2.516 ± 0.002	77.9 ± 1.7

5.2.3.2 *i*PrOH Solvent-Based Aerogels

The skeletal densities of the samples *i*P1 to *i*P6 are shown in Table 5.2-5, which are found to be slightly lower compared to EtOH solvent-based samples. The skeletal density increases with increasing amount of acid, whereas the porosity is decreasing. The calculated porosity for the

Table 5.2-5: Skeletal density and porosity values of aerogels *iP1* to *iP6* and *iP4.1* to *iP5.1*.

Sample	Skeletal density / g·cm ⁻³	Porosity / %
<i>iP1</i>	1.814 ± 0.004	80.7 ± 1.6
<i>iP2</i>	1.895 ± 0.009	90.6 ± 0.9
<i>iP3</i>	1.976 ± 0.004	89.7 ± 0.9
<i>iP4</i>	2.174 ± 0.002	81.3 ± 1.5
<i>iP4.1</i>	2.646 ± 0.008	79.9 ± 1.7
<i>iP5</i>	2.433 ± 0.003	76.0 ± 1.9
<i>iP5.1</i>	2.679 ± 0.008	80.1 ± 1.6
<i>iP6</i>	2.456 ± 0.005	74.7 ± 1.93

aerogel sample *iP1* is similar to the aerogel sample E1 but for sample *iP2* to *iP3* the porosity values are higher compared to the respective EtOH solvent-based aerogels. The highest porosity value is found for sample *iP2* with 91 %. The samples *iP4.1* and *iP5.1*, which were synthesized with an increased amount of water and acid, exhibit slightly higher density values and also higher porosities. Different solvent:TTIP ratios at constant acid and water content had no significant impact on the skeletal density or the porosity, and values between 91 and 93 % porosity were found (Table 9.3-1). At higher water content with a water:TTIP molar ratio of 8:1 at constant solvent content did not result in significant differences in density values. The porosity decreases with increasing acid amount (Table 9.3-2).

5.2.3.3 Mixed Solvent-Based Aerogels

For the mixed solvent-based aerogels only three exemplary aerogel samples are shown in Table 5.2-6. The skeletal density increases with decreasing content of *iPrOH* in the solvent used for the synthesis of the samples. The porosity is higher compared to the aerogels which were synthesized with EtOH only.

Table 5.2-6: Skeletal density and porosity values of mixed solvent-based aerogels E-*iP4* to E-*iP5*.

Sample	Skeletal density / g·cm ⁻³	Porosity / %
E- <i>iP4</i> (1:3)	2.073 ± 0.006	90.8 ± 0.9
E- <i>iP5</i> (1:1)	2.216 ± 0.005	90.6 ± 0.9
E- <i>iP6</i> (3:1)	2.419 ± 0.006	90.3 ± 0.9

5.2.3.4 Calcined Aerogels

The calcined aerogels in Table 5.2-7 exhibit higher skeletal densities compared to the non-calcined aerogels. The skeletal density increases with the calcination temperature in air, whereas the porosity decreases. The calcined samples E2-A-300-10, E2-A-400-10 and E2-A-500-10 were synthesized using denatured EtOH and calcined for ten hours, resulting in higher pore volume compared to samples prepared with absolute EtOH. The porosity values cannot be compared to E2-A-300-2/4 and E2-V-300-2/4, because the samples were synthesized using different purity grades of EtOH (chapter 9.5) leading to different pore volumes. Since the pore volume from physisorption results was used for calculating the porosity, the porosity values are affected. The increase of calcination time in air from two to four hours affects the skeletal density and causes a slight increase, however there is no impact on the porosity. The variation of calcination time from two to four hours at the same temperature of 300 °C resulted in nearly unchanged skeletal density and porosity.

Table 5.2-7: Skeletal density and porosity values of calcined aerogels.

Sample	Skeletal density / g·cm ⁻³	Porosity / %
E2-A-300-10	3.292 ± 0.009	78.4 ± 1.7
E2-A-400-10	3.477 ± 0.009	75.8 ± 1.9
E2-A-500-10	3.690 ± 0.009	72.1 ± 2.1
E2-A-300-2	3.195 ± 0.010	70.0 ± 2.2
E2-A-300-4	3.324 ± 0.011	70.2 ± 2.2
E2-V-300-2	3.004 ± 0.008	71.1 ± 2.1
E2-V-300-4	3.065 ± 0.014	71.8 ± 2.1

5.2.4 Morphology

The aerogels were analyzed using SEM to determine the morphology, such as particle sizes, overall porosity, and homogeneity of the aerogel structure. In physisorption experiments macro- and mesopores are identified and the pore structure determined. Using SEM larger pores can be detected to get an impression of the size and shape of macropores. Also, the homogeneity and porosity of the network as well as possible aggregation can be shown using SEM. TEM is important to characterize the particle size and determine crystalline phases.

5.2.4.1 SEM

EtOH Solvent-Based Aerogels

Figure 5.2-20 shows SEM images of the EtOH solvent-based TiO₂ aerogels E1 to E6 at low (2.000x) and high (100.000x) magnification. The fractured samples exhibit smooth surfaces that is demonstrated by low magnification SEM images. The aerogels E1 to E3 exhibit a homogeneous pore structure with small, interconnected particles whereas the aerogels E4 to E6 exhibit macropores, demonstrated by the high magnification SEM images. For higher amount of acid used during the synthesis, the pore size is increased.

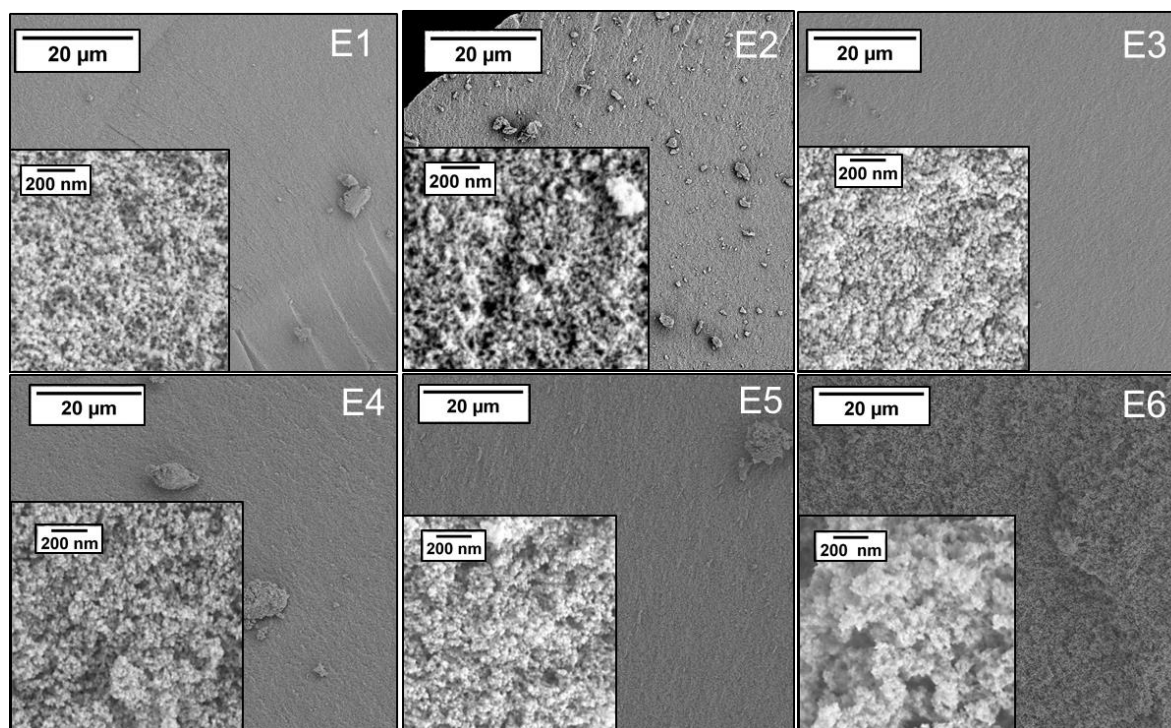


Figure 5.2-20: SEM images of aerogel samples E1 to E6. The images were taken at low (2.000x) and high (100.000x) magnification shown as inset. The amount of acid in the synthesis increases from E1 to E6.

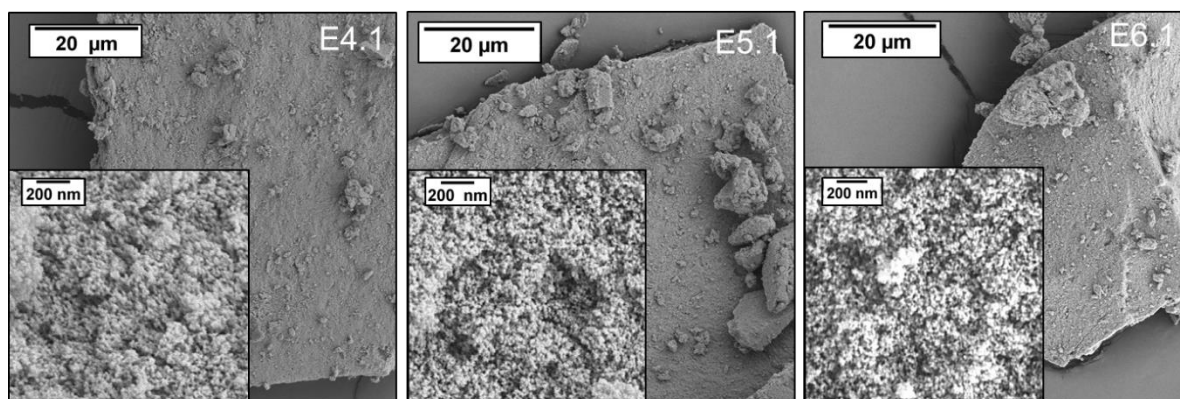


Figure 5.2-21: SEM images of aerogel sample E4.1 to E6.1. The images were taken at low (2.000x) and high (100.000x) magnification shown as inset. The amount of acid used in the synthesis increases from E4.1 to E6.1. The amount of water used in the synthesis increases from E4.1 to E6.1 and is higher compared to the respective samples E4, E5, and E6.

Figure 5.2-21 shows the SEM images of the EtOH solvent-based TiO₂ aerogels E4.1 to E6.1 which were synthesized with high acid and water amount. Also, low (2.000x) and high (100.000x) magnification images are shown. In comparison to aerogels E4 to E6, which were synthesized with increased acid amount but comparatively low water amount, the aerogels E4.1 to E6.1 show small interconnected particles with uniform open porous structure, comparable to that of sample E1 and E2. The simultaneous increase of water content seems to compensate the pore enlarging effect of the acid observed for the samples E4 to E6. The particle size is too small (< 50 nm) to be evaluated quantitatively by SEM.

*i*PrOH Solvent-Based Aerogels

Figure 5.2-22 shows the SEM images of the *i*PrOH solvent-based TiO₂ aerogels *i*P1 to *i*P6 at low (2.000x) and high (100.000x) magnification. The aerogels show all a smooth surface similar to the EtOH solvent-based aerogels. The high-magnification SEM image of *i*P1 and *i*P2 show small, interconnected particles forming an open porous structure, similar to that of the aerogels E1 to E3. The high-magnification SEM images of *i*P3 to *i*P6 reveal the macroporous structure of the aerogels, comparable to that of the aerogel samples E4 to E6. The acid concentration alters the pore size and shape. In Figure 5.2-23 the SEM images of *i*P4.1 and *i*P5.1 are shown. The samples were synthesized similarly to the samples E4.1 to E6.1 with increased water and acid equivalents. However, due to instant and inhomogeneous gelation the sample *i*P6.1 was not further analyzed.

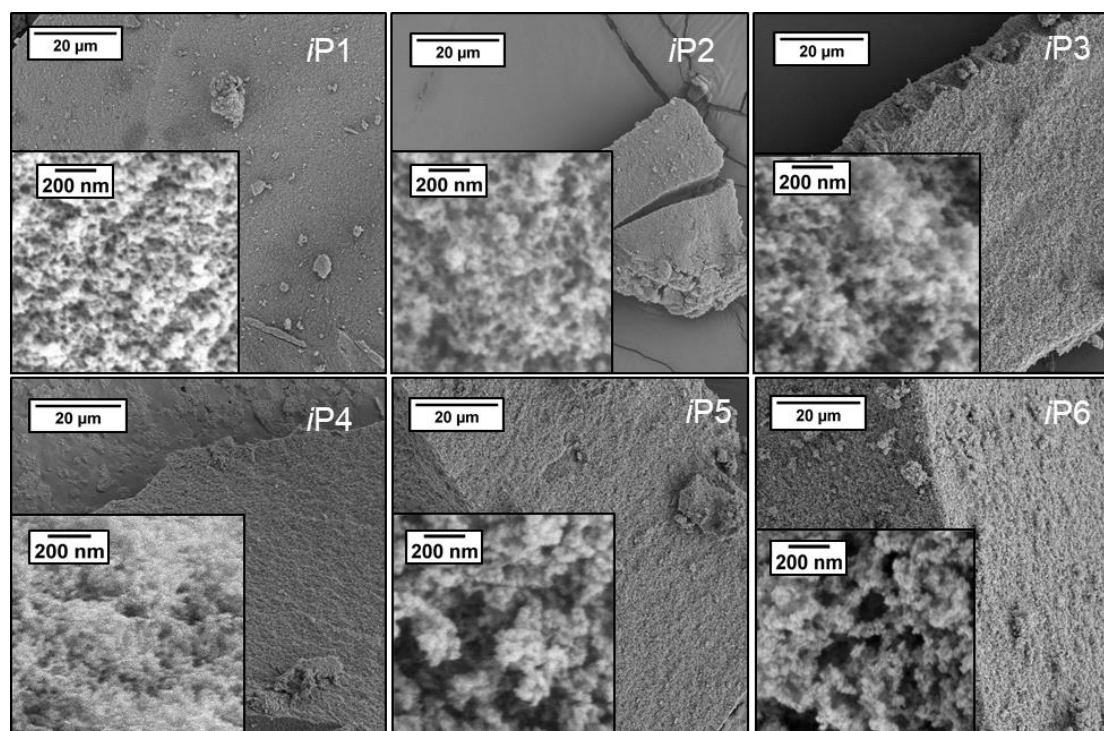


Figure 5.2-22: SEM images of aerogel sample *iP1* to *iP6*. The images were taken at low (2.000x) and high (100.000x) magnification shown as inset. The amount of acid in the synthesis increases from *iP1* to *iP6*.

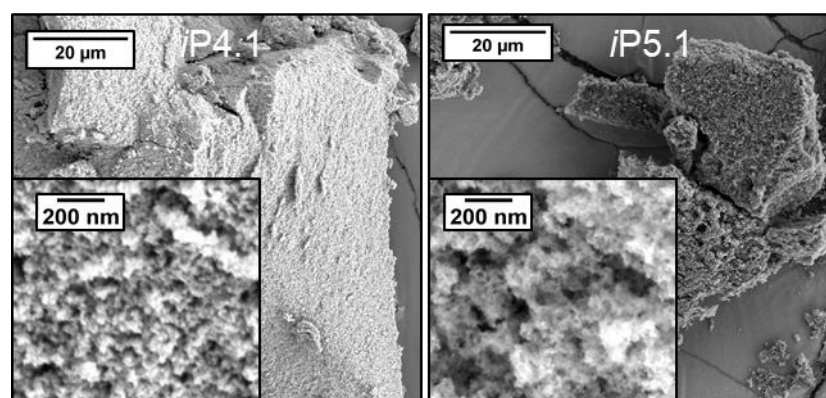


Figure 5.2-23: SEM images of aerogel sample *iP4.1* and *iP5.1*. The images were taken at low (2.000x) and high (100.000x) magnification shown as inset. The amount of acid used in the synthesis increases from *iP4.1* to *iP5.1*. The amount of water used in the synthesis increases from *iP4.1* to *iP5.1* as well and is higher than for the respective samples *iP4* and *iP5*.

For obtaining exceptionally high magnifications for estimating the diameter of the aerogel particles, a tiny amount of aerogel powder of sample *iP2* and *iP5* was dropped on a silicon wafer as sample holder and sputtered for a few seconds to fixate the powder on the wafer surface. The SEM images at very high magnification (250.000x) are shown in Figure 5.2-24. The measured particle diameters were 23 ± 4 nm for *iP2* and 28 ± 4 nm for *iP5*.

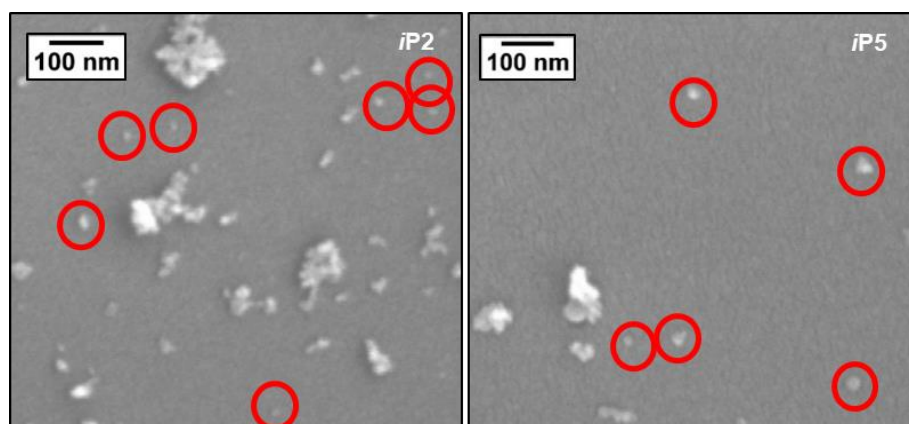


Figure 5.2-24: SEM images of aerogel sample *iP2* (HCl:TTIP 0.11:1) and *iP5* (HCl:TTIP 0.27:1) on a Si single crystal at 250.000x magnification. The red highlighted particles were used for particle size estimation.

This slight difference indicates that the increase in acid amount not just changes the pore structure, but also the particle size of the aerogel. However, this method is inaccurate as the resolution of the microscope is not good enough to assure that only one single particle is exposed for the measurement. Other methods (TEM and SAXS) were used to further examine the particles size in the wet gel and the aerogel.

Mixed Solvent-Based Aerogels

The mixed solvent-based aerogels exhibited all similar morphology. As an example, the SEM image of E-*iP5* is shown. The pore structure is similar to that of sample E2, however, some slightly larger pores are observed.

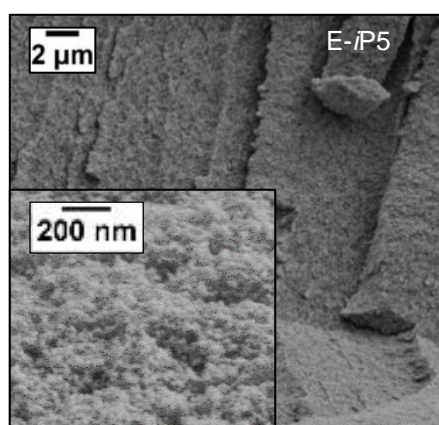


Figure 5.2-25: SEM image of mixed solvent-based aerogel E-*iP5*. The images were taken at low (2.000x) and high (100.000x) magnification shown as inset.

Calcined Aerogels

Figure 5.2-26 shows the SEM images of TiO₂ aerogels which were calcined at 300, 400, and 500 °C, respectively. The images show a very smooth uniform surface of the samples similar to that of E1 to E5. Fewer and larger voids between the particles appear with increasing the calcination temperature. The particles also become larger and are arranged more densely, forming some aggregates. Shorter calcination times between two and four hours in air or vacuum at 300 °C leads to slightly denser appearance of the aerogels compared to the non-calcined aerogel E2, but no larger aggregates were observed (cf. Figure 5.2-27).

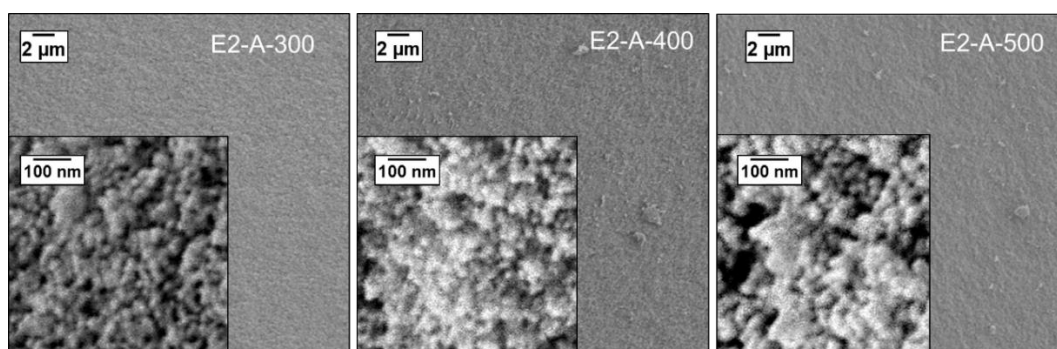


Figure 5.2-26: SEM images of aerogels calcined for 10 hours in air (A) at 300, 400, 500 °C, respectively. The images were taken at low (2.000x) and high (100.000x) magnification shown as inset.

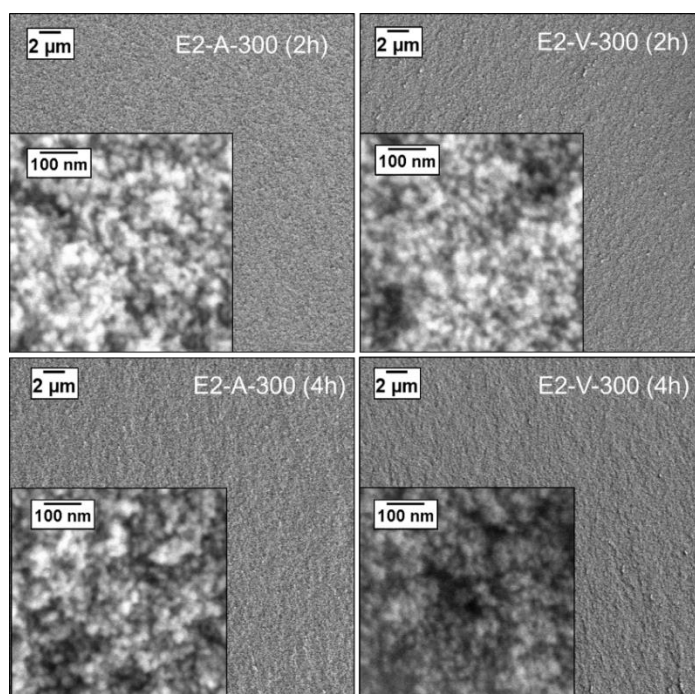


Figure 5.2-27: SEM images of aerogels calcined at 300 °C for two and four hours (h) in air (A) and vacuum (V), respectively. The images were taken at low (2.000x) and high (100.000x) magnification shown as inset.

5.2.4.2 TEM

EtOH Solvent-Based Aerogels

TEM images were taken of the TiO₂ aerogel E2 to further investigate the particle size and possible crystalline parts of the aerogel. The aerogel sample was crushed a few minutes in a mortar to achieve thin layers for TEM analysis, but not to destroy the porous structure. Figure 5.2-28a-d shows TEM images of the aerogel E2 sample at different magnifications. However, the aerogel clusters (Figure 5.2-28a) have still a larger size, and it is difficult to achieve thin parts of the 3D connected structure. Therefore, the particle size is still difficult to determine from the TEM images. Amorphous particles and nanocrystals were observed, which are interconnected (Figure 5.2-28d). Also, the porous structure was observed (Figure 5.2-28d).

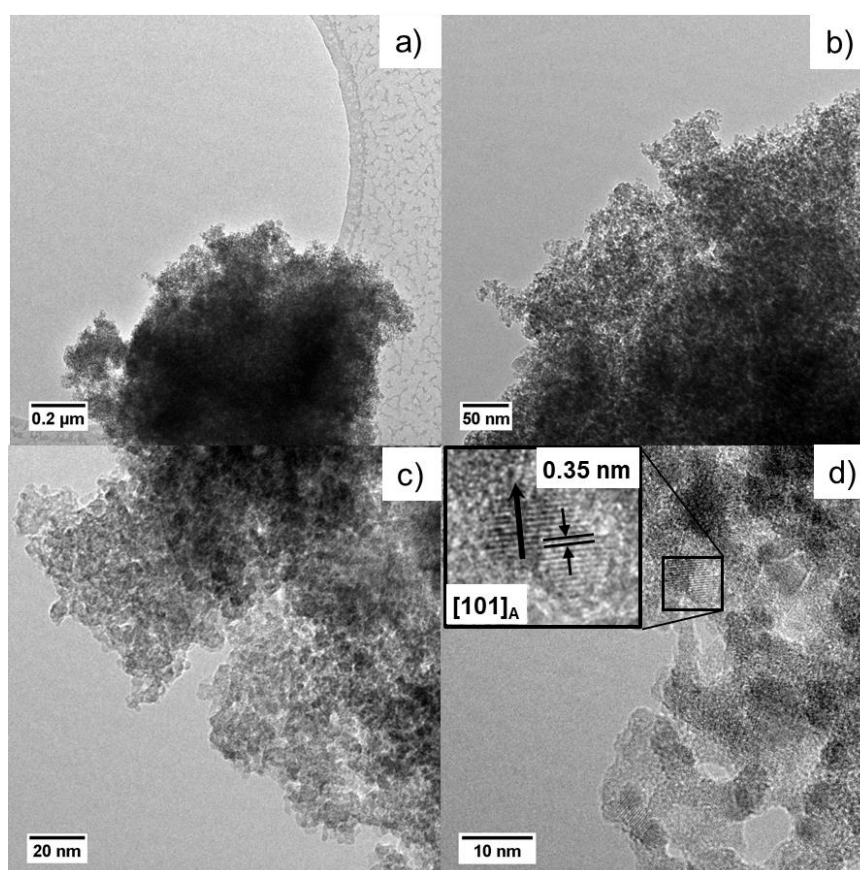


Figure 5.2-28: TEM images of E2 (HCl:TTIP 0.11:1) at a) 12.000x, b) 39.000x, c) 115.000x, and d) 295.000x magnification. The inset is a local enlargement of the TiO₂ nanocrystal. Reprinted (adapted) with permission from A. Rose *et al.* Photocatalytic Activity and Electron Storage Capability of TiO₂ Aerogels with an Adjustable Surface Area. ACS Applied Energy Materials, 2022, 5(12): p. 14966-14978 Copyright 2022 American Chemical Society.

The inset in Figure 5.2-28d shows the d-spacing which was measured to be 0.35 nm for the observed nanocrystals and fits to the (101) anatase lattice plane distance¹. The crystallite size can be estimated to be below 5 nm.

*i*PrOH Solvent-Based Aerogels

In Figure 5.2-29a-c TEM images of the sample *i*P2 are shown at different magnifications. Similar to E2, amorphous particles and nanocrystals were observed, as well as the porous aerogel structure (Figure 5.2-29b). However, compared to E2 much more crystalline parts were found, indicating a higher crystalline content. The inset in Figure 5.2-29c shows the d-spacing which was measured to be 0.35 nm and 0.175 nm for the observed nanocrystals.

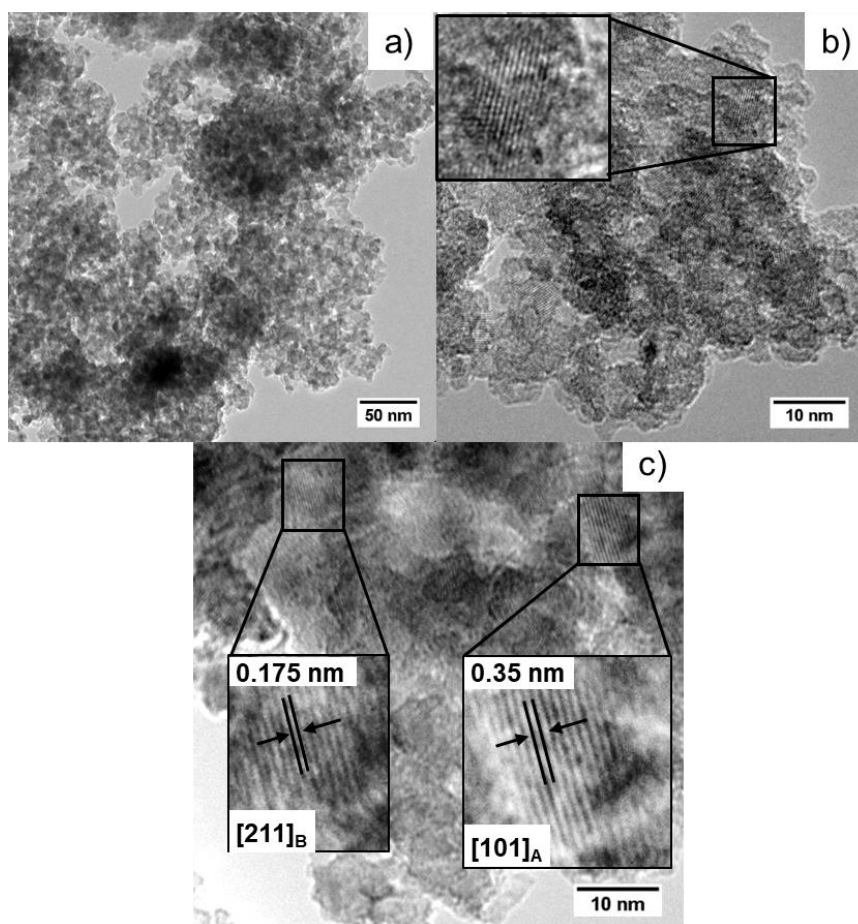


Figure 5.2-29: TEM images of *i*P2 (HCl:TTIP 0.11:1) at a) 49.000x b) 295.000x c) 295.000x magnification. The insets are local enlargements of the TiO₂ nanocrystals.

¹ Lattice plane distances were obtained from Crystallography Open Database (COD) 1010942 using the Diamond software (Crystal Impact GbR Version 4.6.8)

The lattice plane distance of 0.35 nm fits to the (101) anatase lattice plane distance² and 0.175 nm fits to the (211) lattice plane distance of the orthorhombic brookite³. Many reflections of brookite are overlapping with these of anatase. The crystallite size can be estimated to be below 5 nm. However, the particles size can only be roughly determined between 5 to 10 nm with some smaller and larger particles. Due to the thickness of the analyzed aerogel cluster and high particle connectivity the measurement of a single particle from the cluster is very difficult.

To qualitatively visualize the crystalline content of the aerogel sample, a TEM dark field (DF) image of sample *iP2* was taken. Therefore, the lens aperture of the transmission microscope was centered at the diffraction ring associated with anatase (101) reflection of TiO₂ aerogel. With this technique, anatase crystals can be visualized which lie in a suitable orientation to the beam. The DF-image is shown in Figure 5.2-30. The white flashing dots are corresponding to crystalline anatase parts in the aerogel. The image shows the uniform distribution of crystals in the aerogel structure. It is assumed that the crystals are embedded and interconnected with the remaining amorphous TiO₂ structure.

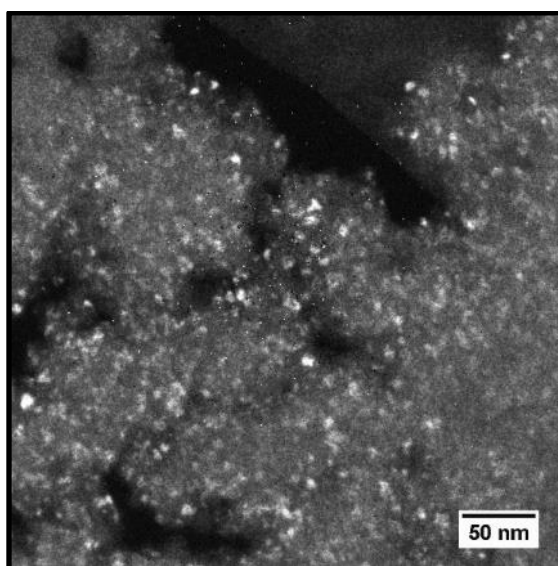


Figure 5.2-30: TEM DF-image of sample *iP2* (HCl:TTIP 0.11:1) at 49.000x magnification. Lens aperture was centered at diffraction ring associated with anatase (101) reflection of TiO₂ aerogel. White dots are the corresponding crystalline parts.

² Lattice plane distances were obtained from COD 1010942 using the Diamond software (Crystal Impact GbR, Version 4.6.8)

³ Lattice plane distances were obtained from COD 9004137 using the Diamond software (Crystal Impact GbR, Version 4.6.8)

In Figure 5.2-31a-d TEM images of the sample *iP5* are shown at different magnifications. A very high amount of nanocrystals was observed, as well as the porous aerogel structure (Figure 5.2-31c-d). Anatase and brookite were found similar to that of sample *iP2*. In Figure 5.2-32a-f high magnification images of sample *iP5* are shown. Due to a thin area of the aerogel cluster the particle size can be determined more accurately compared to the previous samples. The particle size varies from 20 to 66 nm (Figure 5.2-32c-d,f). Also smaller particles below 20 nm are present, as shown in Figure 5.2-31b-d. Especially in Figure 5.2-31a and Figure 5.2-32c the differently sized particles are observed. The surfaces of the smaller particles (20 to 30 nm, Figure 5.2-32c) appear to be very smooth. However, for larger particles sizes (33 to 66 nm, Figure 5.2-32d), the surfaces exhibit structures indicating local stresses originating presumably from crystallization processes or phase transitions. In Figure 5.2-32c-e different contrasts (dark stripes) were observed besides the thin lattice planes (red arrows in Figure 5.2-32c-e). These dark stripes look like a typical Moiré pattern as found in literature due to overlay of two crystals. [197, 198]

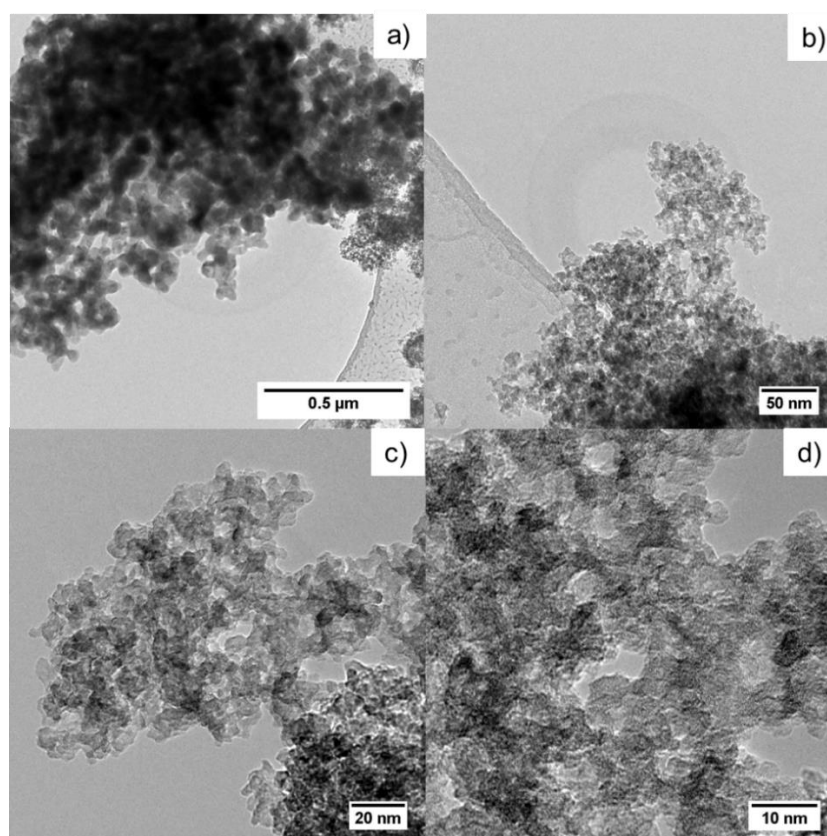


Figure 5.2-31: TEM images of *iP5* (HCl:TTIP 0.27:1) at magnification of a) 12.000x, b) 49.000x, c) 115.000x, and d) 245.000x, respectively.

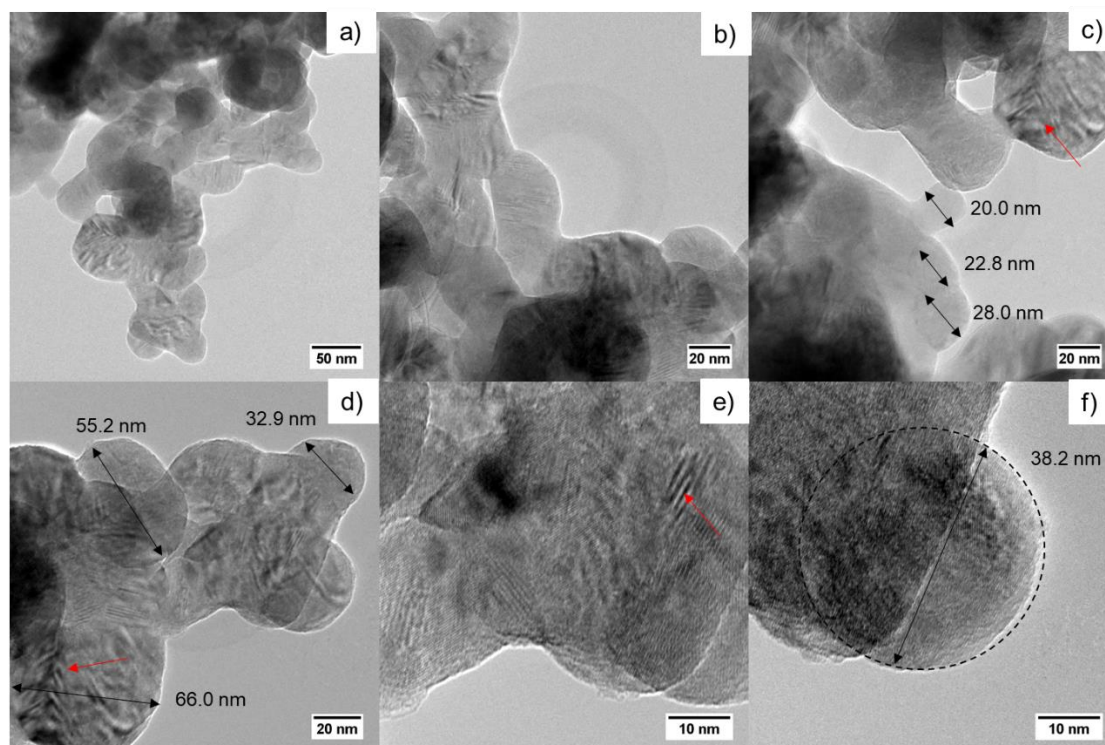


Figure 5.2-32: TEM lattice plane images of iP5 (HCl:TTIP 0.27:1) at magnification of a) 49.000x, b) 98.000x, c) 98.000x, d) 115.000x e) 245.000x showing Moiré pattern, and f) 245.000x.

5.2.5 Crystallinity and Phase Formation of Aerogels

Crystallinity is crucial for photocatalytic processes, as it influences the band structure and increase the charge carrier mobility. Using X-ray diffraction (XRD) the aerogels are analyzed to identify the present crystalline phases qualitatively. The quantitative phase analysis is performed by Rietveld refinement.

5.2.5.1 EtOH Solvent-Based Aerogels

The diffractograms of the aerogel samples E1 to E6 are shown in Figure 5.2-33a. Very broad reflections are observed for sample E1 which was synthesized with a very low acid:TTIP ratio (0.05:1), indicating an amorphous structure of the aerogel sample E1. The samples E2 to E6 with increasing acid:TTIP ratio (0.11:1 to 0.33:1) show broad but distinct reflections, indicating a nanocrystalline structure for these samples. The reflections coincide with the main reflections of TiO₂ anatase (PDF-21-1272).

The diffractograms of the aerogel samples E4 to E6 are shown in Figure 5.2-33b compared to the diffractograms of the aerogel samples E4.1 to E6.1. Samples E4.1 to E6.1 were synthesized with an increasing water:TTIP ratio (8:1 to 12:1) compared to sample E4, E5, and E6 (4:1).

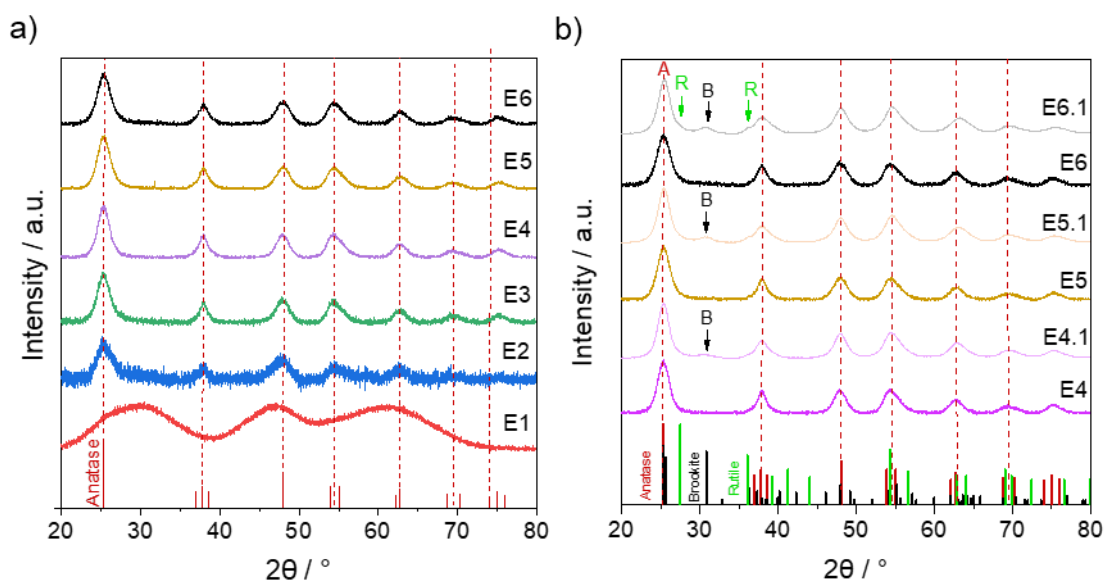


Figure 5.2-33: Diffractograms of aerogel samples a) E1 to E6 and b) E4.1 to E6.1 together with E4 to E6 for comparison, with reference reflection positions of anatase (red), brookite (black), and rutile (green). Normalized data related to the highest signal. The amount of acid in the synthesis increases from E1 to E6. The amount of acid and water in the synthesis increases from E4.1 to E6.1. A= Anatase, B = Brookite, R = Rutile.

For the samples E4 to E6 the reflections can be assigned to anatase, whereas for the samples E4.1 to E6.1 also brookite is found as second phase. At very high acid:TTIP (0.33:1) and water:TTIP (12:1) ratios, very small amounts of rutile (PDF 21-1276) can be detected. Rietveld analysis using an internal standard revealed that the crystallinity increases with the amount of acid used during the synthesis. The results are summarized in Table 5.2-8.

Table 5.2-8: Results of Rietveld refinement of aerogel samples E1 to E6 and E4.1 to E6.1. A = Anatase, B = Brookite, R = Rutile.

Sample	Crystallinity / wt. %	Phase content / wt. %	Crystallite size / nm
E1	amorphous	-	-
E2	10 (18) ± 0.3	A	4.4 ± 0.09 (A)
E3	62 ± 0.3	A	4.2 ± 0.05(A)
E4	74 ± 0.4	A	4.3 ± 0.04 (A)
E4.1	100 ± 4	62 ± 0.5 (A)+38 ± 4.3(B)	4.6 ± 0.05 (A), 2.0 ± 0.13 (B)
E5	78 ± 0.5	A	3.9 ± 0.040(A)
E5.1	100 ± 3	62 ± 0.5 (A)+38 ± 3.4(B)	4.2 ± 0.05 (A), 2.4 ± 0.14 (B)
E6	84 ± 0.5	A	3.6 ± 0.04(A)
E6.1	100 ± 3	57 ± 0.6 (A)+42 ± 3.3 (B)+ 1 ± 0.1(R)	4.2 ± 0.05(A), 2.5 ± 0.12 (B), 15.5 ± 2.64 (R)

The determined crystallinity of the aerogel samples is below 10 wt.% or amorphous for very low acid:TTIP ratios (below 0.11:1). A certain level of acid content (approx. acid:TTIP ratio >0.11:1) must be exceeded to achieve crystalline phases. Anatase is the main phase besides brookite, but the anatase:brookite ratio does not change below approx. 3:2. However, a crystallinity of 84 wt.% can be achieved as a maximum for the aerogel sample E6. With the high water:TTIP ratio used for the samples E4.1 to E6.1 not only different phases can be achieved compared to samples E4 to E6, also the crystallinity of these samples is increased up to 100 wt.%. The crystallite size of anatase varies between approx. 3.6 to 4.6 nm for the samples E2 to E6. The identified brookite crystallites for the samples E4.1 to E6.1 are much smaller (approx. 2.0 to 2.4 nm) compared to anatase, whereas the rutile crystallites (approx. 15.5 nm) appear to be very large in comparison to the anatase and brookite crystallites.

5.2.5.2 *i*PrOH Solvent-Based Aerogels

The diffractograms of the aerogels *i*P1 to *i*P6 are shown in Figure 5.2-34a. Similar to the aerogel sample E1, very broad reflections are observed for the aerogel sample *i*P1, which is therefore completely amorphous. Aerogel samples *i*P2 to *i*P6 show very broad but also distinct reflections, similar to E2 to E6, indicating a semi-crystalline structure for *i*P2 to *i*P3, due to the shoulder of the amorphous halo at $2\Theta=30^\circ$, whereas the sample *i*P4 to *i*P6 show a higher crystallinity, due to missing amorphous halos. The reflections of the samples *i*P2 to *i*P3 coincide with the main reflections of anatase TiO₂ (PDF-21-1272), whereas the reflections of sample *i*P4 to *i*P6 coincide with main reflections of anatase and brookite (PDF-15-0875).

Brookite is identified for acid:TTIP ratios above 0.22:1, up to a maximum anatase:brookite ratio of 3:2. However, the most intense brookite reflections at 2Θ below 35° are overlapping with the anatase reflections and with the amorphous halo, so that brookite might be present, but cannot be identified using XRD. Brookite could therefore not be considered for the Rietveld refinement for the samples *i*P1 to *i*P3. The TEM d-spacing measurements indicate the presence of brookite already for low acid:TTIP ratios of 0.11:1 in sample *i*P2. Further analytical methods, such as Raman spectroscopy, are applied to verify the formed phases.

The diffractograms of the aerogel samples *i*P4 to *i*P6 are shown in Figure 5.2-34b compared to the diffractograms of the aerogel samples *i*P4.1 and *i*P5.1. Samples *i*P4.1 and *i*P5.1 were synthesized with an increasing water:TTIP ratio (8:1 to 12:1), compared to sample *i*P4, *i*P5, and *i*P6 (4:1). No changes are observed for the reflection of the samples *i*P4, *i*P5, *i*P6, *i*P4.1 and *i*P5.1, which can be assigned to anatase and brookite.

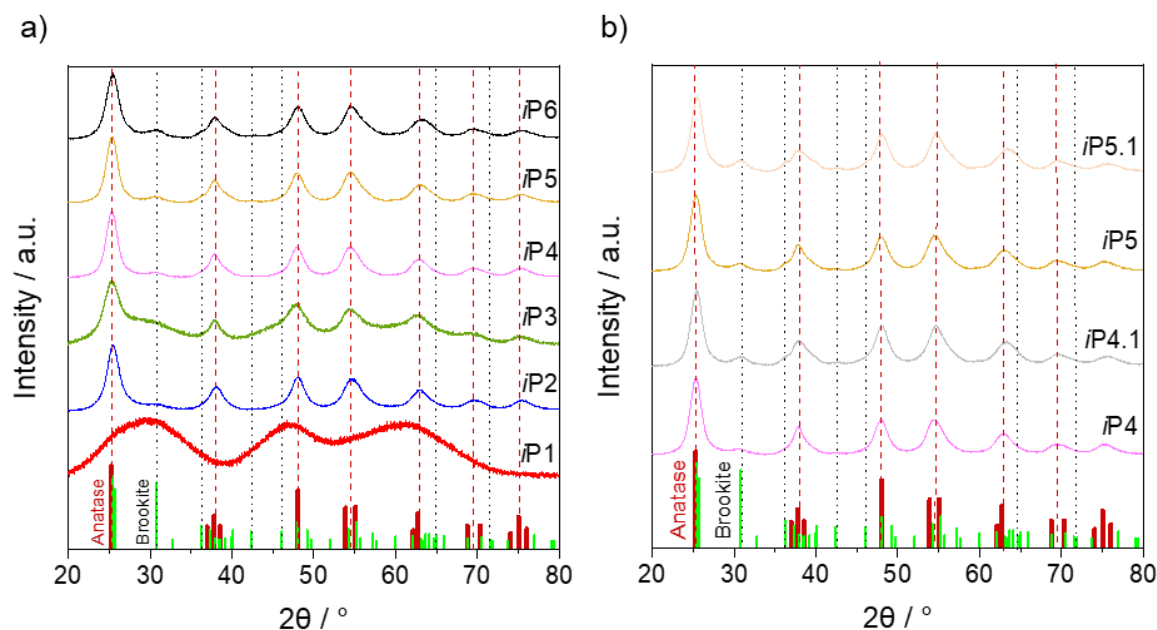


Figure 5.2-34: Diffractograms of aerogel samples a) *iP1* to *iP6* and b) *iP4.1* and *iP5.1* together with *iP4* and *iP5* for comparison, with reference reflection positions of anatase (red), and brookite (black). Normalized data related to the highest signal. The amount of acid in the synthesis increases from *iP1* to *iP6*. The amount of acid and water in the synthesis increases from *iP4.1* and *iP5.1*.

The degree of crystallinity was determined with Rietveld refinement using an internal standard and the results are summarized in Table 5.2-9. The crystallinity increases with the amount of acid used during the synthesis, as observed for the EtOH solvent-based aerogels. Also, a certain level of acid content (acid:TTIP ratio > 0.11:1) must be exceeded to achieve a crystallinity

Table 5.2-9: Results of Rietveld refinement of aerogel samples *iP1* to *iP6* and *iP4.1* to *iP5.1*. A = Anatase, B = Brookite.

Sample	Crystallinity / wt. %	Phase content / wt. %	Crystallite size / nm
<i>iP1</i>	amorphous	-	-
<i>iP2</i>	44 ± 0.4	A	4.3 ± 0.05 (A)
<i>iP3</i>	54 ± 1	A	5.4 ± 0.09 (A)
<i>iP4</i>	94 ± 5	64 ± 0.6 (A)+36 ± 4.6 (B)	5.4 ± 0.07 (A), 2.2 ± 0.13 (B)
<i>iP4.1</i>	100 ± 3	58 ± 0.6 (A)+42 ± 3.4 (B)	5.0 ± 0.07 (A), 2.8 ± 0.14 (B)
<i>iP5</i>	94 ± 3	61 ± 0.4 (A)+39 ± 2.8 (B)	5.3 ± 0.05 (A), 2.4 ± 0.13 (B)
<i>iP5.1</i>	100 ± 2	58 ± 0.7 (A)+42 ± 2.3 (B)	4.7 ± 0.07 (A), 3.1 ± 0.13 (B)
<i>iP6</i>	100 ± 4	58 ± 1.7 (A)+42 ± 2 (B)	4.2 ± 0.06 (A), 2.5 ± 0.08 (B)

above 10 wt.% in the samples. Almost 100 wt.% crystallinity is achieved for *i*PrOH solvent-based aerogels for the samples *i*P4 to *i*P6, whereas for EtOH solvent-based aerogels with similar acid:TTIP ratios for the samples E4 to E6 only approx. 70 to 80 wt.% crystallinity can be achieved. The samples *i*P4.1 to *i*P5.1 are completely crystalline and do not show any significant differences compared to the samples *i*P4 to *i*P5, according to the Rietveld analysis.

The crystallite size of anatase and brookite shown in Table 5.2-9 varies between 4.2 to 5.4 nm and 2.2 to 3.1 nm respectively. They are found to be slightly larger compared for *i*PrOH solvent-based aerogels compared to the EtOH solvent-based aerogels. The small crystallite size affects the peak width, that can also explain the observed broad reflections.

The solvent:TTIP ratio has no significant impact on the crystallinity nor on the crystalline phases. The data is shown in the appendix in Figure 9.3-5 and Figure 9.3-6. The aging process and progress of the increasing crystallinity of sample *i*P5 was further analyzed. The previous results in Table 5.2-9 showed a high crystallinity of 94 wt.% that can be achieved after seven days of aging and supercritical drying in CO₂. The sample *i*P5 was therefore aged between one and seven days, respectively and the reactions stopped by removing the sample from the oven and exchanging the liquid immediately with fresh solvent. After supercritical drying, XRD and Rietveld analysis were performed of these differently aged samples. The crystallinity dependent on the aging time is shown in Figure 5.2-35.

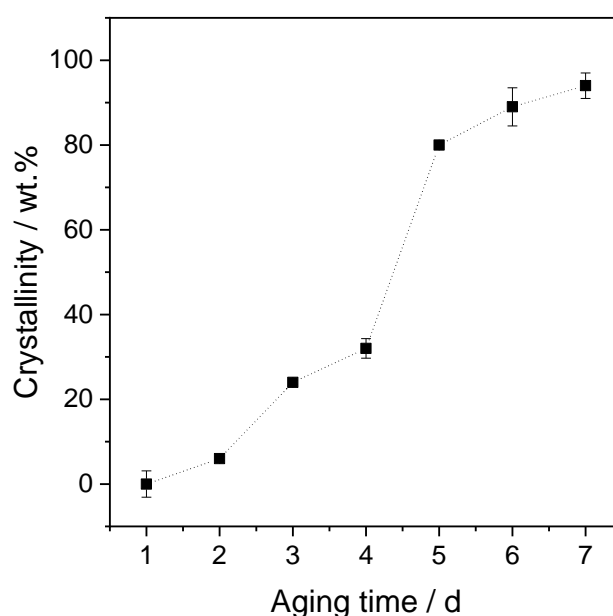


Figure 5.2-35: Crystallinity of the aerogel sample *i*P5 (HCl:TTIP 0.27:1) aged between one and seven days (d), respectively.

The results show that the sample *iP5* is amorphous after one day of aging. The crystallinity increases steadily up to 25 wt.% after four days of aging, then increases drastically to 80 wt.% between four and five days of aging and finally increases slowly further to above 90 wt.% after seven days aging.

5.2.5.3 Calcined Aerogels

Calcination of the sample E2 for 10 hours in air at 300, 400, and 500 °C, respectively leads to complete crystallization according to the Rietveld analysis in Table 5.2-10. The observed reflections in the diffractograms shown in Figure 5.2-36a can be assigned to TiO₂ anatase. The crystallite size increases from approx. 4 nm for the non-calcined sample E2 to 6.9, 9.5 and 12.9 nm for 300, 400 and 500 °C respectively. Especially, the diffractograms of the calcined aerogel at 500 °C exhibits well-defined and better-resolved reflections compared to the calcined aerogels at 300 and 400 °C, respectively. This can be related to the increase in crystallite size, since nanocrystals result in broad reflections.

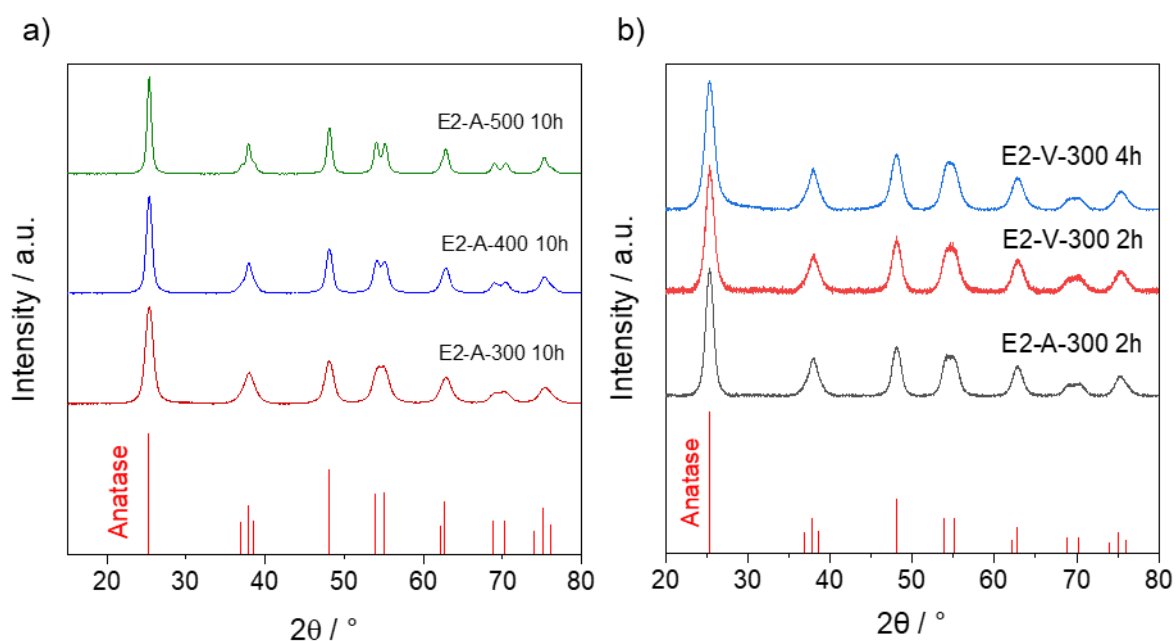


Figure 5.2-36: a) Diffractograms of calcined samples in air (A) for 10 hours at 300 to 500 °C and b) for two to four hours at 300 °C in air and vacuum with reference reflection positions of anatase (red). Normalized data related to the highest signal. Fig. 56 a) was reprinted (adapted) with permission from A. Rose *et al.* Photocatalytic Activity and Electron Storage Capability of TiO₂ Aerogels with an Adjustable Surface Area. ACS Applied Energy Materials, 2022. 5(12): p. 14966-14978. Copyright 2022 American Chemical Society.

Table 5.2-10: Results of Rietveld refinement of in air and vacuum calcined aerogels.
A = Anatase.

Sample	Crystallinity / wt.%	Phase content / wt.%	Crystallite size / nm
E2-A-300-10	100 ± 0.5	A	6.9 ± 0.05
E2-A-400-10	100 ± 0.4	A	9.5 ± 0.07
E2-A-500-10	100 ± 0.4	A	12.9 ± 0.08
E2-A-300-2	100 ± 0.6	A	5.7 ± 0.06
E2-A-300-4	100 ± 1.0	A	5.8 ± 0.13
E2-V-300-2	72 ± 0.6	A	5.6 ± 0.08
E2-V-300-4	67 ± 0.5	A	4.9 ± 0.07

The Rietveld analysis in Table 5.2-10 shows, that shorter calcination times for two to four hours at 300 °C in air also lead to complete crystallinity, but the crystallite size of anatase increases in a lesser extent compared to 10 hours calcination at 300 °C. The diffractograms in Figure 5.2-36b and the respective Rietveld results in Table 5.2-10 show that calcination in vacuum leads to semi-crystalline anatase aerogels with a remaining amorphous content of approx. 30 wt.%. The crystallite size increases slightly from 4.3 nm for the non-calcined aerogel E2 to values between 4.9 and 5.6 nm for the vacuum calcined samples. The crystallite growth is therefore prevented and much slower in vacuum compared to calcination in air.

5.2.5.4 Precipitates in Synthesis of E2

As previously mentioned in section 5.1.1.1, for gel formation TTIP and EtOH are mixed to a clear sol. A few minutes after the addition of acid, it changed occasionally to a cloudy appearance and small white precipitates occurred, which dissolved again after the addition of water in a last step. The precipitates were only found for low acid:TTIP ratios below 0.17:1 and did not occur for higher acid:TTIP ratios. The precipitate was isolated by reducing the amount of solvent slowly and the air-dried precipitates were analyzed using XRD. The diffractogram is shown in Figure 5.2-37a-c with different reference reflection positions for phase identification. An amorphous halo in the higher 2θ region was observed, which is quite unusual, that could be due to high scattering of the samples in the higher 2θ region. Besides the main reflections of anatase and brookite, a few reflections (24° , 26° , 40° and 51° 2θ), can be found which cannot be assigned to the typical TiO_2 phases. They could be assigned to Ti-Cl compounds found in the PDF 2 database.

Especially the reflections found at 24° , 26° and 51° 2θ could indicate a titanium oxide chloride hydrate with a similar formula of $\text{Ti}_2\text{O}_2\text{Cl}_4 \cdot 2\text{H}_2\text{O}$ / $\text{TiCl}_4 \cdot \text{TiO}_2 \cdot 2\text{H}_2\text{O}$ (PDF 21-1238) or

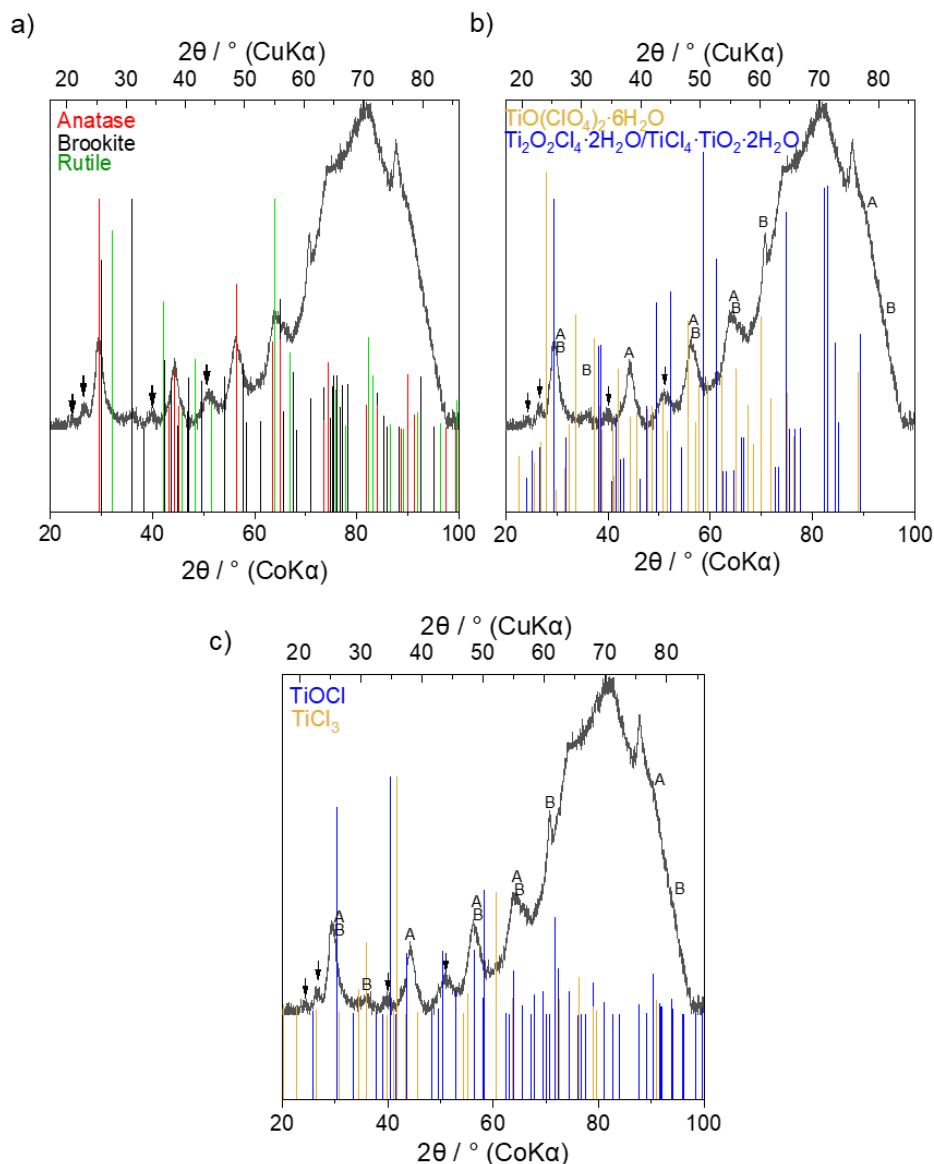


Figure 5.2-37: Diffractogram of precipitate occurring during the synthesis of E2 a) with reference reflection positions of anatase (red), brookite (black), rutile (green) b) with reference reflection positions of $\text{Ti}_2\text{O}_2\text{Cl}_4 \cdot 2\text{H}_2\text{O} / \text{TiCl}_4 \cdot \text{TiO}_2 \cdot 2\text{H}_2\text{O}$ (PDF 21-1238, blue) and $\text{TiO}(\text{ClO}_4)_2 \cdot 6\text{H}_2\text{O}$ (PDF 18-1410, yellow) c) with reference reflection positions of TiOCl (PDF 85-0654, blue) or TiCl_3 (PDF 29-1359, yellow).

$\text{TiO}(\text{ClO}_4)_2 \cdot 6\text{H}_2\text{O}$ (PDF 18-1410) supporting the assumption that several chloride ions coordinate to the titanium-based precursor after the addition of HCl. The reflection at $40^\circ 2\theta$ could fit to TiOCl (PDF 85-0654) or TiCl_3 (PDF 29-1359) from the database, also supporting the formation of Ti-Cl compounds. The change in the chemical structure of the precursor molecule influences the solubility, probably caused by coordination of chloride ions, leading to precipitation of the small particles.

5.2.6 Verification and Formation of Crystalline Phases

Raman spectroscopy was performed to identify and confirm possible crystalline phases in the wet gels and dried aerogels. It is a non-destructive method, which can be also used to analyze wet gels during synthesis or processing, such as precursor condensation or aging of the gels.

5.2.6.1 EtOH Solvent-Based Aerogels

Figure 5.2-38a shows the Raman spectra of TiO₂ aerogels E1 to E6. The Raman spectra of TiO₂ aerogel E1 and E2 with a low acid:TTIP ratio exhibit broad bands, indicating a high amorphous character. The bands are more pronounced compared to amorphous TiO₂ films reported in the literature. [199] This indicates a certain level of structural order of the material. Aerogel E3 to E6 with higher acid:TTIP ratio above 0.17:1 exhibit narrower Raman bands compared to that of the samples E1 and E2, which can clearly be assigned to anatase (141 cm⁻¹ (E_{g(1)}), 197 cm⁻¹ (E_{g(2)}), 398 cm⁻¹ (B_{1g(1)}), 515 cm⁻¹ (A_{1g}, B_{1g(2)}), and 640 cm⁻¹ (E_{g(3)})). [200-203]

No brookite can be identified in the detailed Raman spectra in Figure 5.2-38b that is in accordance with the XRD results.

Figure 5.2-39 shows the Raman spectra of the TiO₂ aerogels E4 to E6 (water:TTIP 4:1) and E4.1 to E6.1 (water:TTIP 8-12:1). The Raman bands of sample E4 to E6 can be clearly assigned to anatase, while for the samples E4.1 to E6.1 also brookite is identified (246 cm⁻¹ (A_{1g}),

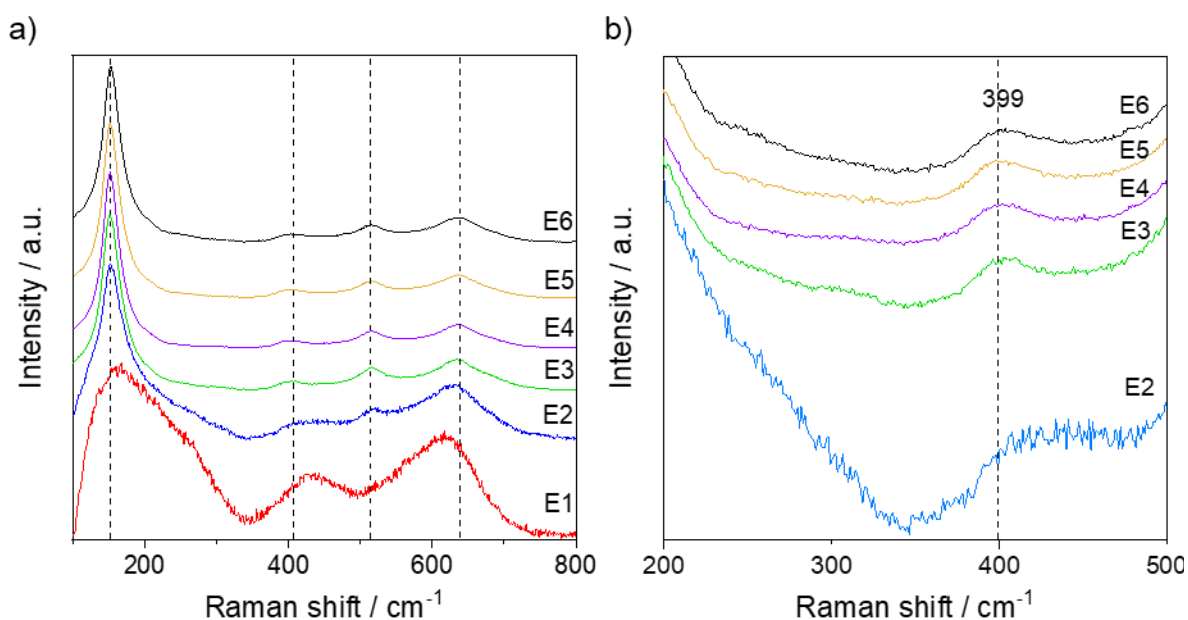


Figure 5.2-38: Raman spectra of aerogel samples E1 to E6 and detailed Raman spectra 200-500 cm⁻¹ of E2 to E6. Normalized data related to the highest signal. The amount of acid during the synthesis was increased from E1 to E6.

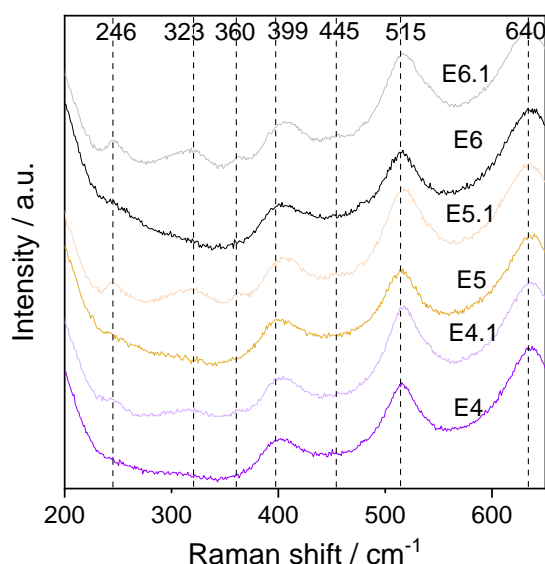


Figure 5.2-39: Raman spectra of aerogel samples E4.1 to E6.1 together with to E4 to E6 for comparison. Normalized data related to the highest signal. The amount of acid used in the synthesis increases from E4 to E6 and E4.1 to E6.1. The amount of water used in the synthesis increases from E4.1 to E6.1 and is higher compared to the respective samples E4, E5, and E6.

323 cm^{-1} (B_{1g}), 360 cm^{-1} (B_{2g}), 399 cm^{-1} (B_{2g}) and 455 cm^{-1} (B_{2g}).^[204-206] These results confirm the XRD results. No rutile could be found in the sample E6.1 for high acid:TTIP ratios above 0.33:1. However, the amount of rutile found in the sample E6.1 by XRD is very low and might not be detectable with Raman spectroscopy, since this method is less sensitive and area selective compared to XRD.

5.2.6.2 *i*PrOH Solvent-Based Aerogels

Figure 5.2-40a shows the Raman spectra of the TiO_2 aerogels *i*P1 to *i*P6. The Raman spectrum of the TiO_2 aerogel *i*P1 exhibits broad bands at 150.6 cm^{-1} ($E_{g(1)}$ band) and between 400 and 700 cm^{-1} . Especially, the band at 150.6 cm^{-1} is more distinctive compared to sample E1, indicating very low crystallinity of the sample *i*P1. Aerogel *i*P2 to *i*P6 exhibit narrower Raman bands compared to *i*P1, which can clearly be assigned to anatase (141 cm^{-1} ($E_{g(1)}$), 197 cm^{-1} ($E_{g(2)}$), 398 cm^{-1} ($B_{1g(1)}$), 515 cm^{-1} (A_{1g} , $B_{1g(2)}$), and 640 cm^{-1} ($E_{g(3)}$))^[200-203] and brookite (246 cm^{-1} (A_{1g}), 323 cm^{-1} (B_{1g}), 360 cm^{-1} (B_{2g}), 399 cm^{-1} (B_{2g}) and 455 cm^{-1} (B_{2g})).^[204-206] The bandwidth of the Raman bands decreases with increasing amount of acid used during the synthesis. This indicates that the broader bands reflect a high amorphous content of the samples. A higher level of crystallinity leads to more pronounced Raman bands for the crystalline TiO_2 aerogels (*i*P4 and *i*P5) compared to the semi-crystalline aerogel *i*P2. According to the detailed

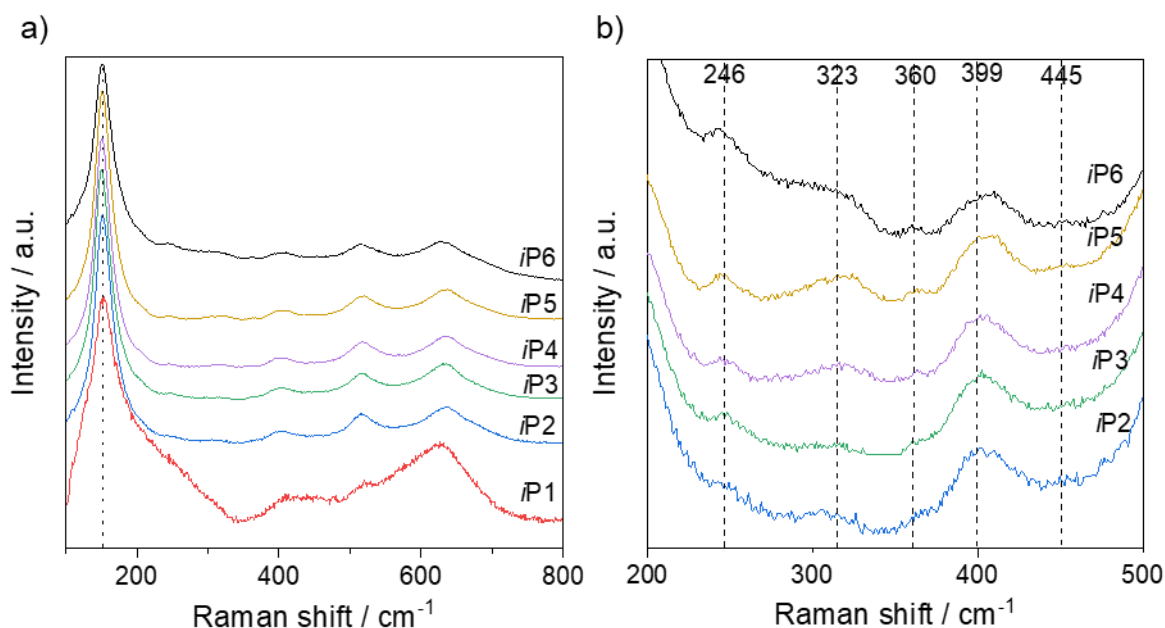


Figure 5.2-40: Raman spectra of aerogel sample *iP1* to *iP6* and detailed Raman spectra 200-500 cm^{-1} of *iP2* to *iP6*. Normalized data related to the highest signal. The amount of acid during the synthesis was increased from *iP1* to *iP6*.

Raman spectra in Figure 5.2-40b, the brookite formation in the samples *iP2* to *iP6* can be therefore verified by Raman microscopy. The intensity of the brookite bands increase with the acid content and confirm the XRD results. According to TEM d-spacing estimation and the Raman spectroscopy results, brookite is present in all semi- or completely crystalline *iPrOH*-based aerogels. HCl concentration leads to higher crystallinity and brookite formation. The samples *iP4.1* and *iP5.1* were not measured, since no other phases are observed in XRD analysis of these samples.

5.2.6.3 Calcined Aerogels

The calcined aerogels E2-A-300, E2-A-400 and E2-A-500 exhibit narrow Raman bands, similar to sample E3 to E6 with high acid:TTIP ratios and increased crystallinity. The identified bands can also be assigned to anatase with the same band positions found for EtOH solvent-based samples E3 to E6.

The bandwidth of the Raman bands decreases with increasing calcination temperature. Also, the maximum of the $E_{g(1)}$ bands shifts (blue shift) from 150.6 cm^{-1} of the non-calcined sample E2 to 141.3 cm^{-1} of the aerogel E2-A-500 calcined at $500 \text{ }^\circ\text{C}$.

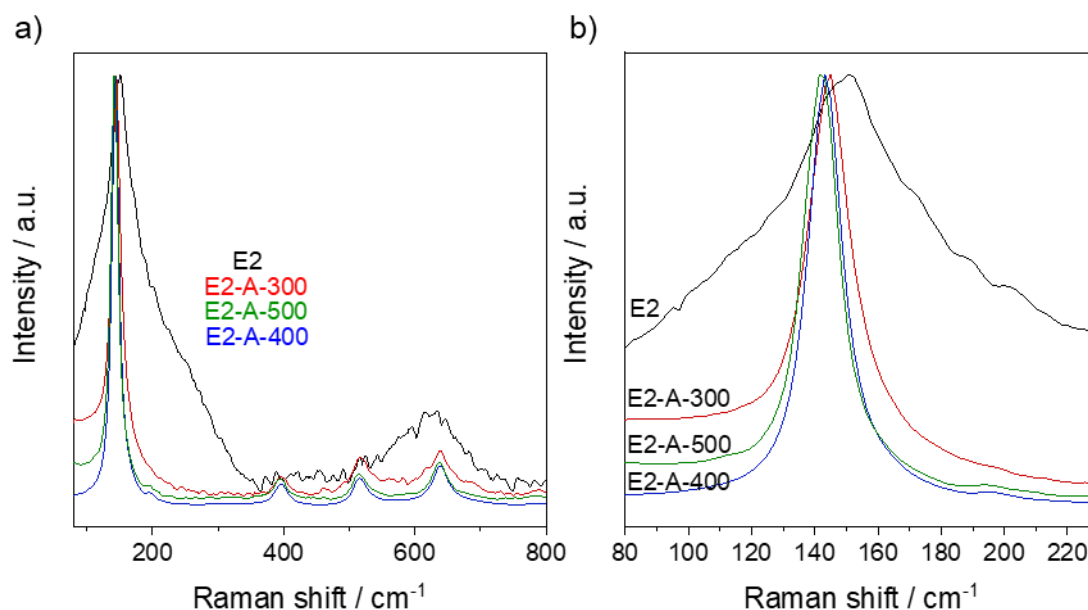


Figure 5.2-41: Raman spectra of calcined aerogels (10 hours in air (A), 300 to 500 °C) and detailed Raman spectra 80-230 cm⁻¹ of calcined aerogels. Normalized data related to the highest signal. Reprinted (adapted) with permission from A. Rose *et al.* Photocatalytic Activity and Electron Storage Capability of TiO₂ Aerogels with an Adjustable Surface Area. ACS Applied Energy Materials, 2022. 5(12): p. 14966-14978. Copyright 2022 American Chemical Society.

5.2.6.4 *In-situ* Raman Spectroscopy

The aging process of the wet gel samples E5 and *iP5* was analyzed via *in-situ* Raman spectroscopy to investigate the phase formation. Therefore, a special setup was required. The gels were prepared as usual and placed in plastic containers into the oven. The E_{g(1)} of anatase at 146 cm⁻¹ is used to monitor the phase formation during the aging process of sample E5, however the signal of this band is very low, due to the high solvent content in the wet gel. The Raman spectra over time are shown in Figure 5.2-42a. Between one and three days of aging no Raman signal was observed in the range of 140 to 150 cm⁻¹, so no anatase phase formation was detected in the wet gel during the first days of aging. An increase in intensity was observed between three and four days of aging indicating the formation of anatase.

The intensity of the E_{g(1)} of anatase is additionally plotted against the time in Figure 5.2-42b. An increase in intensity is observed starting from 80 hours that reflects the starting point of anatase crystallization.

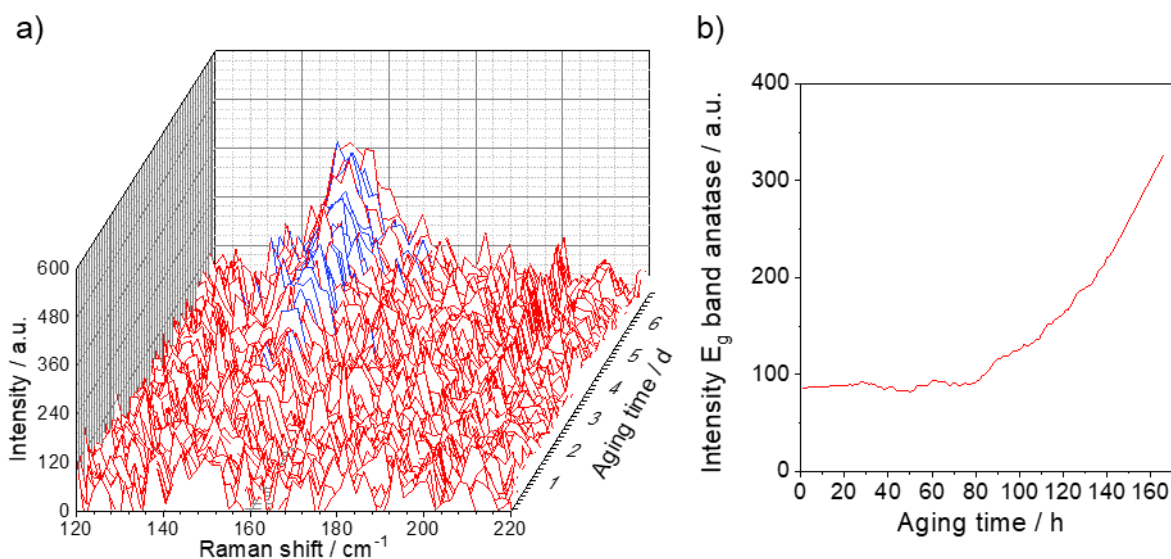


Figure 5.2-42: a) Raman spectra of the *in-situ* aging experiment of the wet gel E5 (HCl:TTIP 0.27:1) over time in the range of 120-220 cm⁻¹ and b) intensity of E_g band of anatase over time.

This experiment was also performed for the wet gel sample *iP5*. The Raman spectra over time are shown in Figure 5.2-43a. Also, the E_{g(1)} of anatase at 146 cm⁻¹ is used to monitor the phase formation. Between one and three days of aging no Raman signal was observed in the range of 140 to 150 cm⁻¹, similar to the sample E5, indicating no phase formation during this time of aging. An increase in intensity can be detected between three and four days of aging indicating the presence of anatase, similar to the sample E5. A starting point of crystallization is determined from the intensity change of the anatase band at 146 cm⁻¹, shown in Figure 5.2-43b.

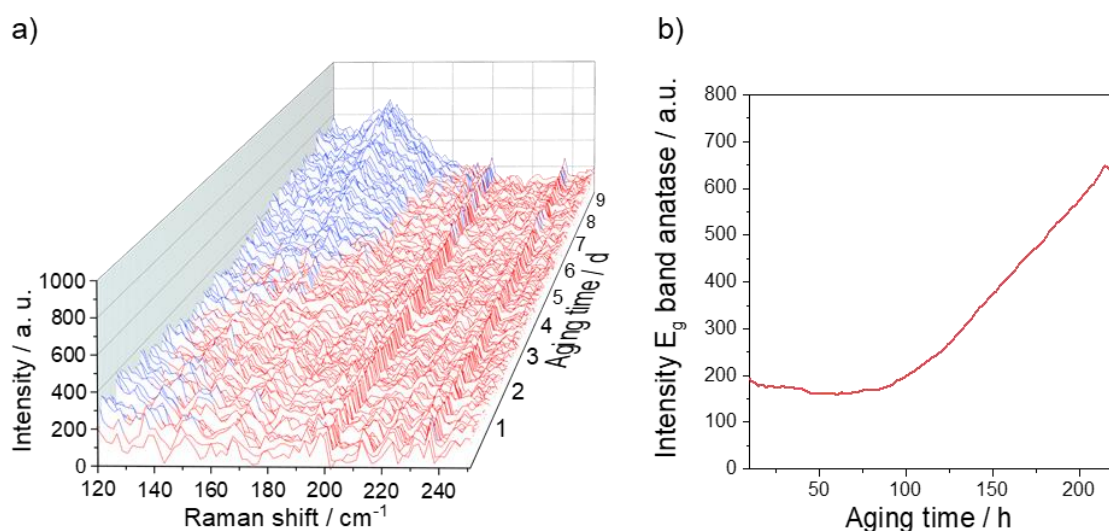


Figure 5.2-43: a) Raman spectra of the *in-situ* aging experiment of the wet gel of *iP5* (HCl:TTIP 0.27:1) over time in the range of 120-250 cm⁻¹ and b) intensity of E_g band of anatase over time.

An increase in intensity is observed starting from approx. 80 hours, similar to the sample E2. The aging was performed longer (nine days) for this sample. A slight flattening at the end of the curve was observed, that might indicate the end of the crystallization processes.

5.2.7 Crystallinity and Phase Formation of Wet Gels

In the previous chapter it was mentioned, that crystallinity is crucial for photocatalytic processes, especially the electron-hole pair generation. However, mostly dried TiO₂ nanostructures are tested for photocatalytic activity, as the drying or solvent removal approach during synthesis is most important for formation of crystalline phases. The wet gels and the aging process of the wet gels was therefore analyzed using synchrotron radiation for wide WAXS, to determine the starting point and degree of crystallization during aging. Additionally, the time-resolved formation and phase transitions can be determined.

5.2.7.1 EtOH Solvent-Based Wet Gels

Figure 5.2-44a shows the diffractograms of the EtOH solvent-based wet gels which were generated from the 2D diffraction images obtained from the WAXS detector after subtraction of the background. The wet gels E4 and E6 show broad but pronounced reflections which can be assigned to anatase. The wet gels are therefore partially crystalline before supercritical drying. The sample E3 shows also some reflections, which are less pronounced compared to E4 to E6. However, the samples E3 to E6 show a shoulder next to the (101) anatase reflection at $q=22 \text{ nm}^{-1}$, that can be assigned to the remaining amorphous content. Also, the reflections in the q -range between 30 to 45 nm^{-1} are very broad, which support the high amorphous content. The samples E1 and E2 show mainly very broad reflections typically found for amorphous nanomaterials. These results show the same trend as observed from XRD results of the dried aerogels, that the crystallinity increases with the amount of acid used during the synthesis.

The sample E5 was aged between one and seven days, respectively and the wet gels analyzed at the different aging stages. The results of the WAXS measurements are shown in Figure 5.2-44b.

Between one and two days of aging, the sample is mainly amorphous, since no distinctive reflections were observed. After three days of aging the reflections become more distinctive, indicating the starting point of crystallization to anatase at approx. three days of aging.

More pronounced reflections are found for longer aging times, so the crystallinity increases over time during the aging process.

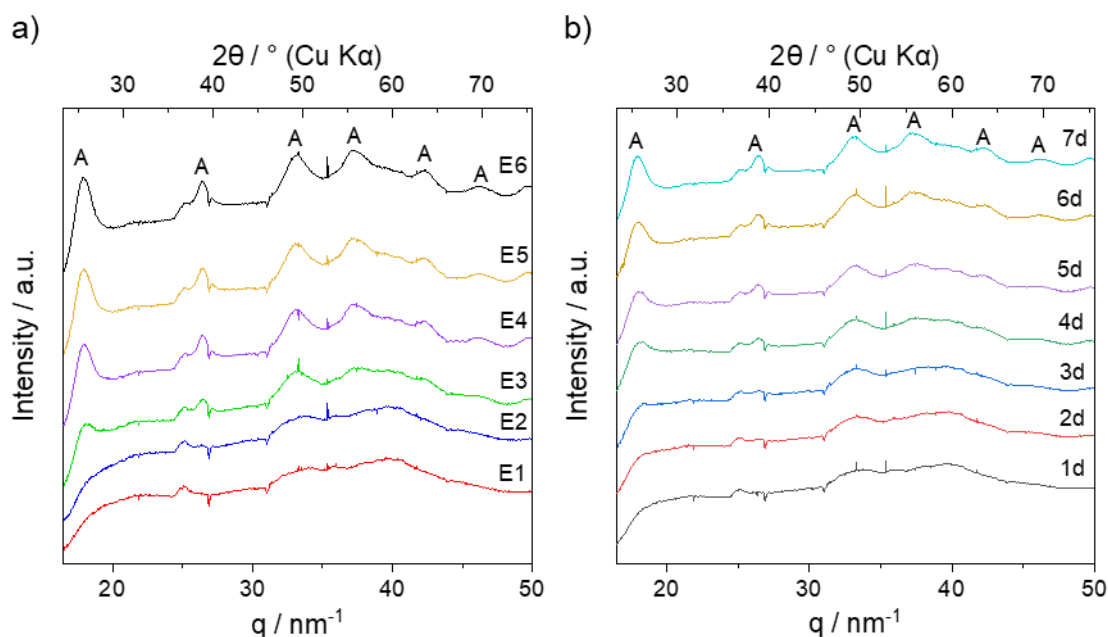


Figure 5.2-44: Diffractograms of a) the wet gels E1 to E6 based on synchrotron WAXS results and b) the *ex-situ* aging process (one to seven days) for the wet gel E5. The amount of acid during the synthesis was increased from E1 to E6. A = Anatase.

The quantification and determination of the amorphous content by Rietveld refinement was not possible for the sample E1 to E6, since a homogeneous distribution of the internal standard CeO_2 was required, which could not be achieved due to the long gelation times of these samples.

5.2.7.2 *i*PrOH Solvent-Based Wet Gels

Figure 5.2-45a shows the diffractograms of the *i*PrOH solvent-based wet gels. The sample *i*P1 shows similar broad reflections compared to sample E1 and E2, indicating a high amorphous content. Compared to the sample E2, the aerogel sample *i*P2 shows already more distinctive reflections, especially at low q values below 20 nm^{-1} . However, the reflections are still very broad indicating a high amorphous content. The reflections become more pronounced for *i*P3 which can be clearly assigned to anatase. There is a drastic change in the intensity of the reflection from sample *i*P3 to *i*P4. Well-defined reflections can be found for *i*P4, indicating a strong increase in crystallinity. Besides anatase, also reflections of brookite are identified at q -values of 22 nm^{-1} and 30 nm^{-1} . The brookite reflection at 22 nm^{-1} is overlapping with the broad halo of the remaining amorphous content, so that the presence of brookite can only be determined for sample *i*P4 to *i*P6. These results show the same trend as observed for XRD results of the dried aerogels, confirming that the crystallinity increases in the wet gel with the amount of acid used during the synthesis.

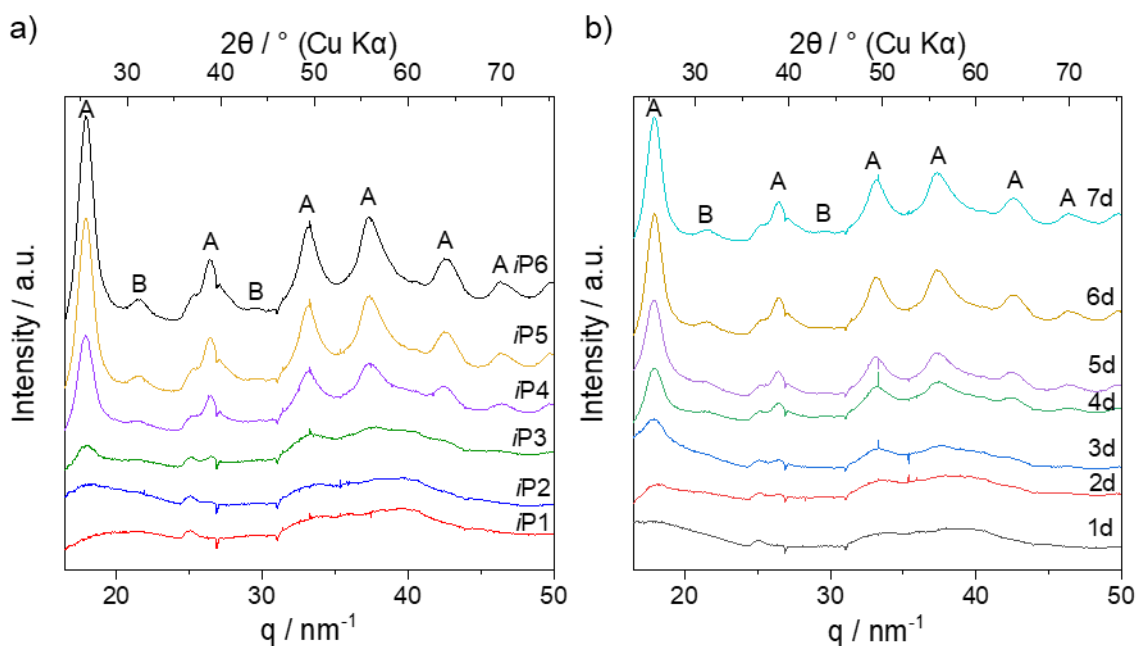


Figure 5.2-45: Diffractograms of a) the wet gels *iP1* to *iP6* based on synchrotron WAXS results and b) the *ex-situ* aging process (one to seven days) for the wet gel *iP5*. The amount of acid during the synthesis was increased from *iP1* to *iP6*. A = Anatase, B = Brookite.

The sample *iP5* was aged for one to seven days respectively and the wet gels analyzed at different aging stages, similarly to the investigations on sample E5 in Figure 5.2-44b. The results of the WAXS measurements are also shown in Figure 5.2-45b. Already after two days of aging the reflections became more distinctive, indicating the starting point of crystallization of anatase between two and three days of aging, which is observed to occur after a shorter aging time compared to the sample E5. The reflections become more pronounced for longer aging times, so the crystallinity increases over time. For sample *iP5*-3d, a shoulder next to the (101) anatase reflection at approx. $q=22 \text{ nm}^{-1}$ indicates remaining amorphous content, which is reduced for sample *iP5*-4d. A distinctive reflection appears at 22 nm^{-1} for the sample *iP5*-4d that fits to brookite, indicating that besides the crystallization to anatase, also crystallization to brookite occurs. However, the starting point of brookite crystallization is difficult to determine, due to overlapping reflections of the brookite reflections with the halo of the remaining amorphous content.

The *iPrOH* solvent-based gels were also synthesized with a certain amount of solid crystalline CeO_2 powder as internal standard. The gelation time of the *iPrOH* solvent-based gels is very short for all samples, that should prevent an inhomogeneous distribution of CeO_2 by

sedimentation of particles. A homogeneous distribution of CeO₂ in the wet gel and no interaction of CeO₂ with the gel network are assumed, however larger deviations in the obtained gels, due to the processing, are expected. The results of the samples *iP1* to *iP6* are shown in Table 5.2-11. The values of the obtained crystallinity and phase content show, that the sample *iP1* is completely amorphous and the crystallinity increases with the amount of acid, as observed previously. Up to sample *iP3* only anatase is used for the Rietveld refinement, due to overlapping reflections of brookite and the amorphous halo, that would otherwise lead to a poor fitting of the scattering curve. For *iP4* to *iP6* the brookite reflections were clearly observed in the diffractograms in Figure 5.2-45 and used for the Rietveld refinement. The determined ratios of anatase:brookite vary between 3.1:1 to 1.8:1 (Table 5.2-11) which deviate from the previously shown ratios obtained by XRD results. Also, the drop of crystallinity from sample *iP5* to *iP6* may be traced back to larger deviations because a solid internal standard was used in the wet gel and possible local inhomogeneities or deviations occurred due to processing of the gels.

The crystallinity and phase content are also determined for sample *iP5* at different aging stages. The results are summarized in Table 5.2-12. The results show an increasing crystallinity for longer aging times. Even after two days of aging some crystallinity can be measured. However, larger deviations are expected due to the processing of the wet, as mentioned above.

Table 5.2-11: Results of Rietveld refinement of wet gels *iP1*-*iP6* based on synchrotron WAXS results. A = Anatase, B=Brookite.

Sample	Crystallinity / wt.%	Phase content / wt.%
<i>iP1</i>	Amorphous	-
<i>iP2</i>	5 ± 3	A
<i>iP3</i>	32 ± 5	A
<i>iP4</i>	71 ± 7	46 ± 6 (A), 26 ± 3 (B)
<i>iP5</i>	100 ± 17	71 ± 15 (A), 29 ± 9 (B)
<i>iP6</i>	87 ± 10	65 ± 8 (A), 21 ± 5 (B)

Table 5.2-12: Results of Rietveld refinement of the *ex-situ* aging process (one to seven days) for the wet gel *iP5* based on synchrotron WAXS results. A=Anatase, B=Brookite.

Sample	Crystallinity / wt. %	Phase content / wt. %
<i>iP5</i> – 1d	5 ± 1	A
<i>iP5</i> – 2d	33 ± 8	A
<i>iP5</i> – 3d	34 ± 5	A
<i>iP5</i> – 4d	33 ± 3	30 ± 3(A), 3 ± 1 (B)
<i>iP5</i> – 5d	51 ± 4	36 ± 3 (A), 15 ± 3 (B)
<i>iP5</i> – 6d	97 ± 14	57 ± 11(A), 40 ± 9 (B)
<i>iP5</i> – 7d	100 ± 17	71 ± 15 (A), 29 ± 9 (B)

5.2.7.3 *In-situ* Analysis of Aging Process

The wet gel *iP5* was analyzed in an *in-situ* experiment to determine precisely the starting point of crystallization. The gel was pre-aged for 72 hours and further aged at 50 °C while measuring WAXS. The aging process was continued for 48 hours and measurements performed each 10 minutes. Figure 5.2-46a shows the diffractograms of the *iP5* wet gel dependent on the aging time which is generated from the 2D diffraction images obtained from the WAXS detector after subtraction of the background.

The results show that already after 72 hours aging pronounced reflections were observed, which can be assigned to anatase. The shoulder at the 101-anatase reflection, shown in more detail in Figure 5.2-46b, and the broad reflections in the q -range of 30 to 50 nm⁻¹, shown in more detail in Figure 5.2-46c, indicate a high remaining amorphous content after 72 hours. This shows that the starting point of crystallization of anatase is below 72 hours of aging at 50 °C. The reflections become more pronounced for longer aging times, confirming the increasing crystallinity.

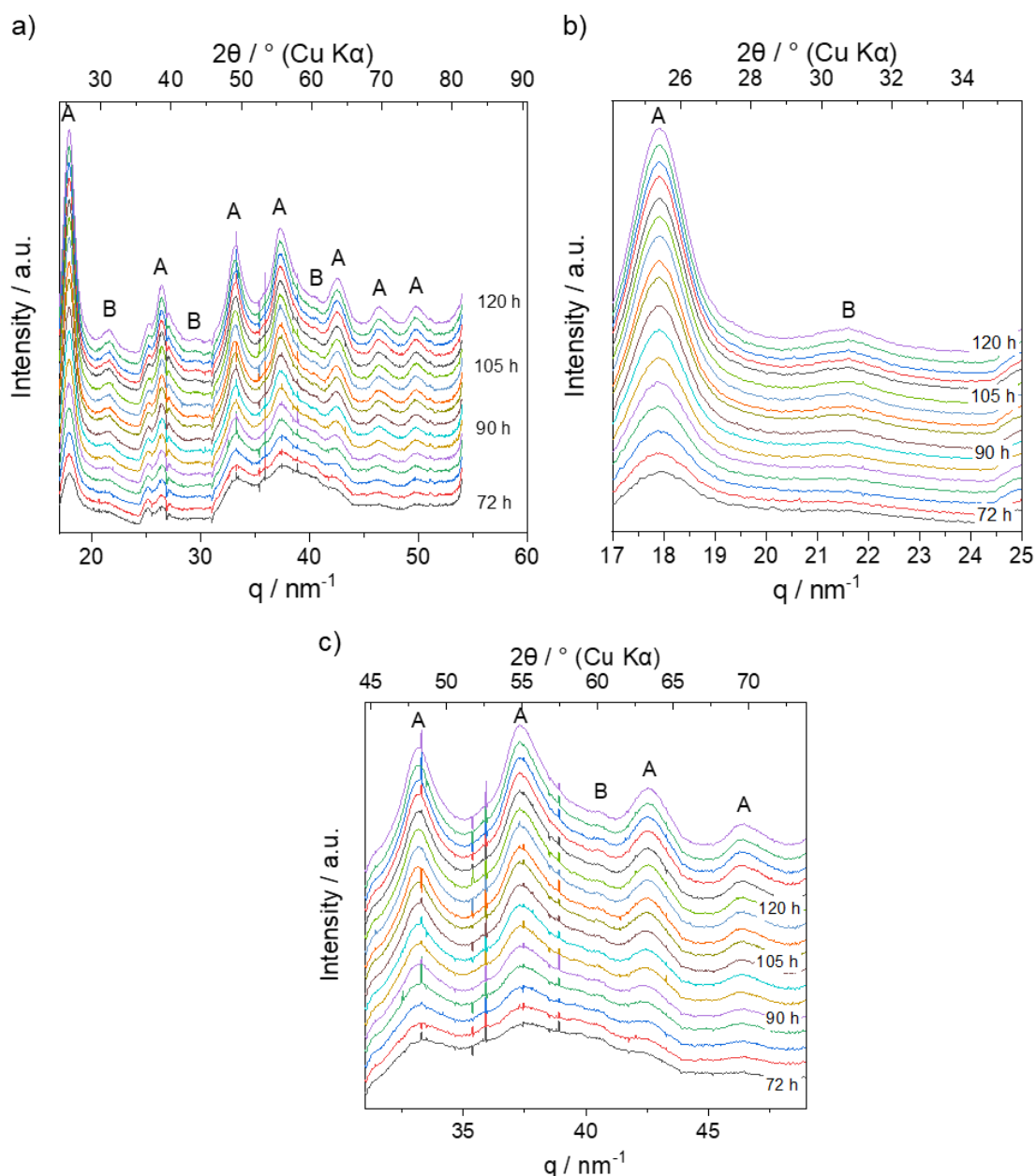


Figure 5.2-46: Diffractograms in the range of a) 17-60 nm^{-1} b) 17-25 nm^{-1} c) 32-48 nm^{-1} of the *in-situ* aging experiment of the wet gel iP5 based on synchrotron WAXS results. A = Anatase, B = Brookite.

In Figure 5.2-47a the intensity of the 101-anatase reflection at $q=18 \text{ nm}^{-1}$ is plotted against the aging time and demonstrates that the intensity of the anatase reflection increases steadily. As mentioned before the halo of the amorphous content is overlapping with the brookite reflection at $q=21.63 \text{ nm}^{-1}$. The intensities at $q=20.36 \text{ nm}^{-1}$ and $q=24.03 \text{ nm}^{-1}$ can be clearly assigned to amorphous content. These intensities observed at $q=20.36 \text{ nm}^{-1}$ and $q=24.03 \text{ nm}^{-1}$ were plotted against the time in Figure 5.2-47b, showing that the intensity representing the amorphous content decreases over time indicating a reduction of amorphous content. However, some larger

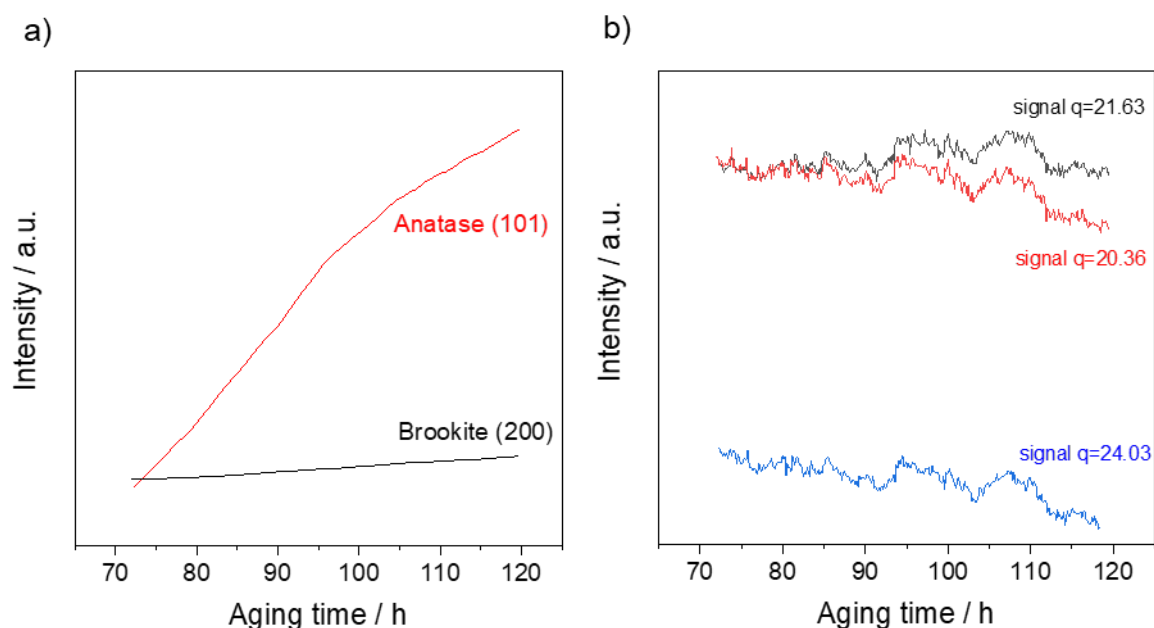


Figure 5.2-47: a) Intensity of anatase (101) reflection (red) and brookite (200) reflection (black) after subtraction of amorphous content over time during aging and b) intensity of brookite signal (black, $q=21.63 \text{ cm}^{-1}$) and signal of amorphous content (red, $q=20.36 \text{ cm}^{-1}$; blue, $q=24.03 \text{ cm}^{-1}$).

deviations in the decline of intensity values are observed at $q=95 \text{ nm}^{-1}$ and $q=110 \text{ nm}^{-1}$. During the *in-situ* measurements, the position where the beam hits the sample was changed approx. each 3.5 hours for statistical reasons that could lead to some deviations in the intensity progression.

The intensities of the amorphous content at $q=20.36 \text{ nm}^{-1}$ are subtracted from the intensities observed at $q=21.63 \text{ nm}^{-1}$ and plotted against the time, representing the formation of brookite. In Figure 5.2-47a the black curve shows that crystallization to brookite occurs also at 72 hours, but the slope of the increase of intensities is lower compared to the anatase intensities.

5.2.8 Analysis of the Nanostructure of Wet Gels

The nanostructure of the wet gels was analyzed using synchrotron radiation for SAXS experiments on the sample. This allows to determine the primary and secondary particle size of the wet gels, shape of particles as well as information on the formed flexible network by analyzing the Guinier and fractal region of the SAXS curves.

From the scattering curves the size of these clusters or aggregates was determined as well as the primary particle size. In the Guinier range for small q values the radius of gyration (R_G) was

calculated. Assuming uniform spheres, the corresponding cluster or aggregate diameter was calculated by the following equation:^[207]

$$diameter_{aggregate} = 2 \cdot r(radius) = \sqrt{\frac{5}{3}} \cdot R_G \quad \text{Eq. 7}$$

With an error of:

$$\Delta diameter_{aggregate} = \frac{2 \cdot \sqrt{5}}{\sqrt{3}} \cdot \Delta R_G \quad \text{Eq. 8}$$

The radius of gyration was calculated from the slope (a) of the linear curves in the Guinier plots using the following equation:^[207]

$$a(\text{slope}) = \frac{R_G^2}{3} \quad \text{Eq. 9}$$

With an error of:

$$\Delta R_G = \frac{\sqrt{3}}{2 \cdot \sqrt{a}} \cdot \Delta a \quad \text{Eq. 10}$$

The size of the primary particle was determined using the following equation:^[208]

$$diameter = \frac{\pi}{q_{\text{curve bend}}} \quad \text{Eq. 11}$$

The q values of curve bending are determined according to literature from the intersections between the linear fits, as indicated as an example in the following figure:^[208]

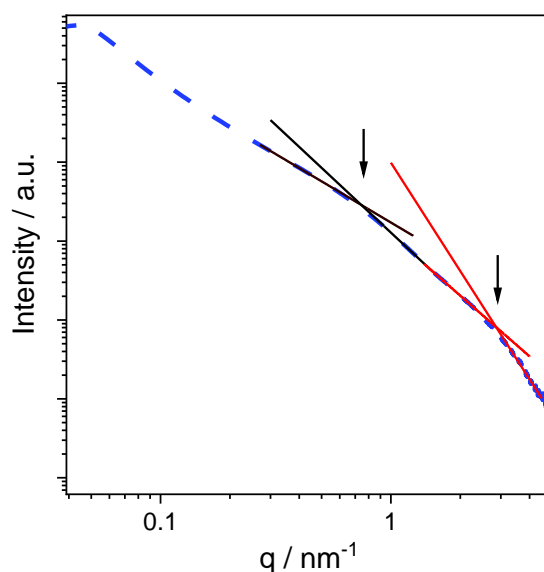


Figure 5.2-48: SAXS curve bending and evaluation as an example for determination of the primary particle size.

5.2.8.1 EtOH Solvent-Based Wet Gels

Figure 5.2-49 shows the logarithmic plots of the SAXS measurements of the wet gels E1 to E6. The Guinier plots are shown as inset in Figure 5.2-49, indicating particle aggregation for the sample E3 to E6, due to characteristic upturn at low q^2 , that is not found for the sample E1 and E2. In Table 5.2-13 the slope of the linear Guinier fits, the radius of gyration and the aggregate diameter is summarized.

The results show that the radius of gyration and aggregate diameter increases with the amount of acid used during the synthesis.

The SAXS curves generally indicate polydispersity, due to the absence of oscillating signals in the mid/higher q range. In the mid q range a large linear region was observed. This suggests that the wet gel network consists of fractal clusters, that is also supported by previous SEM and TEM results. The slope of the mid q range reveals a power-law exponent of -2 for sample E1 and E2, which is associated with a lamellar structure of the particles which is typically found for polymers. Sample E3 to E6 exhibits a more positive power law exponent of -1.7 to -1.8, indicating a slightly more cylindrical shape of particles.

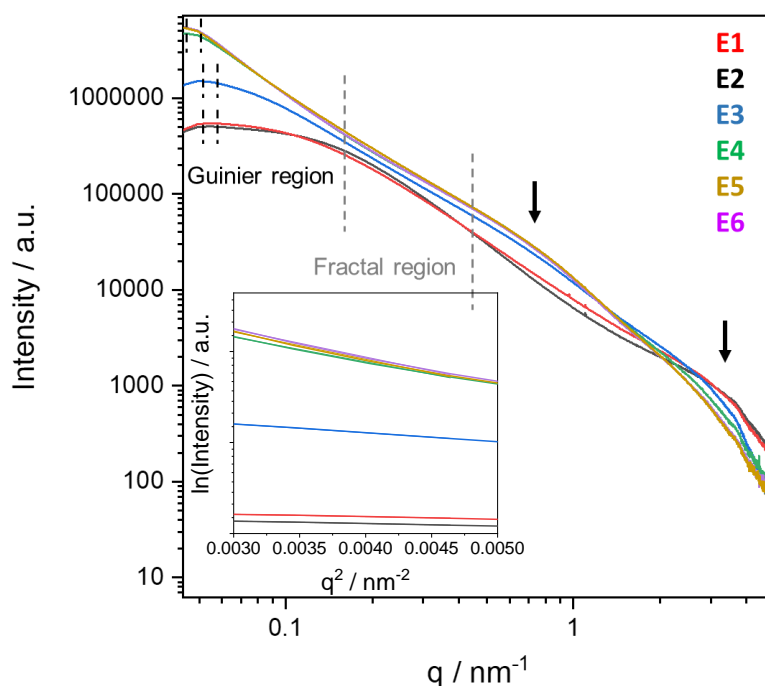


Figure 5.2-49: SAXS curves of wet gels E1 to E6. The amount of acid during the synthesis was increased from E1 to E6. The approximate ranges for the Guinier and fractal regions are shown with dashed lines and the curve bending marked with arrows. The Guinier plot is shown as an inset.

Table 5.2-13: Results of SAXS curve analysis of wet gels E1 to E6.

Sample	Slope Guinier region	R_G / nm	Secondary particle size / nm	Slope of fractal region	q value of curve bending / nm^{-1}	Primary particle size / nm
E1	-26.76 ± 1.22	9.0 ± 0.2	13.9 ± 0.5	-2.0 ± 0.01	3.36	0.93
E2	-25.63 ± 2.25	8.8 ± 0.4	13.6 ± 1.0	-1.9 ± 0.02	3.20	0.98
E3	-97.20 ± 2.19	17.1 ± 0.2	26.5 ± 0.5	-1.7 ± 0.04	3.20/0.70	0.98/4.50
E4	-272.33 ± 9.32	28.6 ± 0.5	44.3 ± 1.3	-1.7 ± 0.04	3.01/0.71	1.05/4.41
E5	-303.36 ± 12.03	30.2 ± 0.6	46.7 ± 1.5	-1.7 ± 0.04	2.88/0.75	1.09/4.22
E6	-300.33 ± 13.52	30.0 ± 0.7	46.5 ± 1.7	-1.8 ± 0.04	2.78/0.75	1.13/4.20

The SAXS curve bends at two different q values for sample E1 to E6 (black arrows in Figure 5.2-49). Generally, bending of the curve indicate a distribution of differently sized primary particles of the TTIP cluster which form in the initial phase of the hydrolysis and condensation reaction. For the gel E1 and E2 the curve bends at higher q values, while for E3 to E6 the curve additionally bends at lower q values. The determined q values of the curve bending at higher q values decrease slightly with increasing acid amount from 3.36 nm^{-1} to 2.78 nm^{-1} (E1 to E6). This leads to a calculated primary particle size which increases from 0.93 nm to 1.13 nm (Table 5.2-13). The second curve bending shifts slightly to higher q values from 0.70 nm^{-1} to 0.75 nm^{-1} with increasing amount of acid (E3 to E6) leading the values of the calculated particle size to decrease from 4.50 nm to 4.20 nm (Table 5.2-13). The samples E2 and E5 were additionally fitted as an example by Peter Staron from the Institute of Materials Physics of the Helmholtz-Zentrum Hereon. The particle size distributions are shown in the appendix Figure 9.6-1 and Figure 9.6-2 and match approximately with the previously estimated primary and secondary particle sizes from the scattering curve. They also support a broad distribution of differently sized particles.

In Figure 5.2-50a and b the Kratky and Porod-Debye plots are shown, respectively. The Kratky plot gives information about the stiffness of the gel network. The results show that all curves do not converge to the q axis supporting the flexibility of the gel network. For the gels E3 to E6 the values increase for larger q values. This indicates more flexibility due to longer chains in the network. Also, the gels E4 to E6 exhibit a bell-shaped peak at low q values. This additional peak indicates spherical and rigid aggregates in the gel network. The Porod-Debye plots in Figure 5.2-50b shows a lack of a plateau that indicates full flexibility of the gel network for the sample E1 to E6.

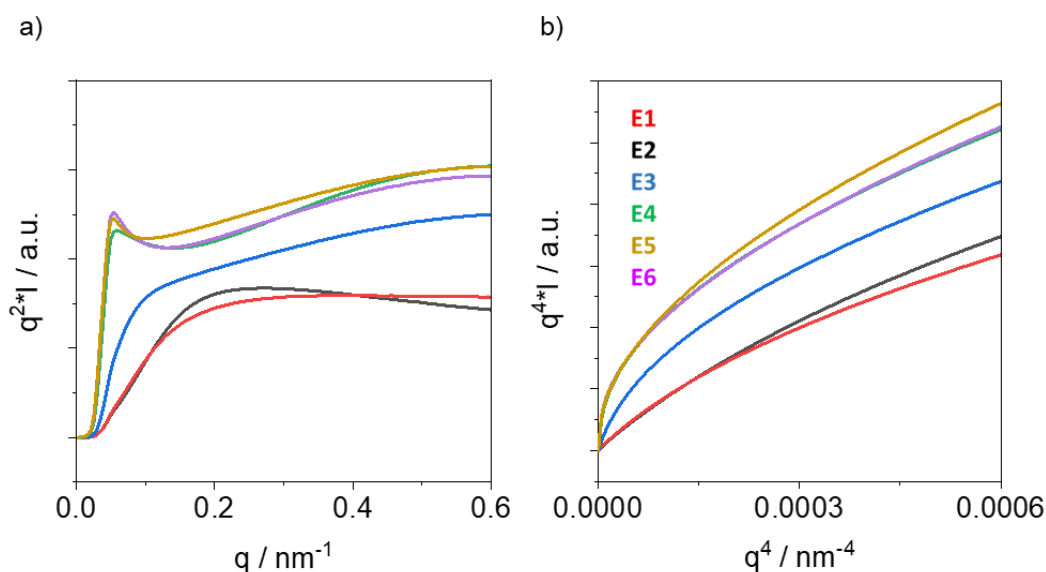


Figure 5.2-50: a) Kratky plot b) Debye-Porod plot of E1 to E6. The amount of acid during the synthesis was increased from E1 to E6.

Figure 5.2-51 shows the SAXS curves and the Guinier plots as inset of the wet gel E5 which was aged between one and seven days, respectively and measured at different stages of aging. The radius of gyration and secondary particle size increase for longer aging times.

The curves behave similar compared to sample E1 to E6. The linear region in the mid q range indicates fractal clusters. The slope of the mid q range was calculated and summarized in Table 5.2-14. A power-law exponent of approx. -2 was found for all samples, indicating a lamellar structure of the particles.

For E5 1-2d q values between 2.73 nm^{-1} to 3.01 nm^{-1} were determined resulting in a primary particle size between 1.02 nm and 1.15 nm. For E5 3-7d, the curve additionally bends at lower q values between 0.75 nm^{-1} and 1.13 nm^{-1} . This leads to a calculated particle size between 2.78 nm and 4.33 nm. It should be noted that the intensity of the curve bending at high q values decreases, while the intensity of the curve bending at low q values increases.

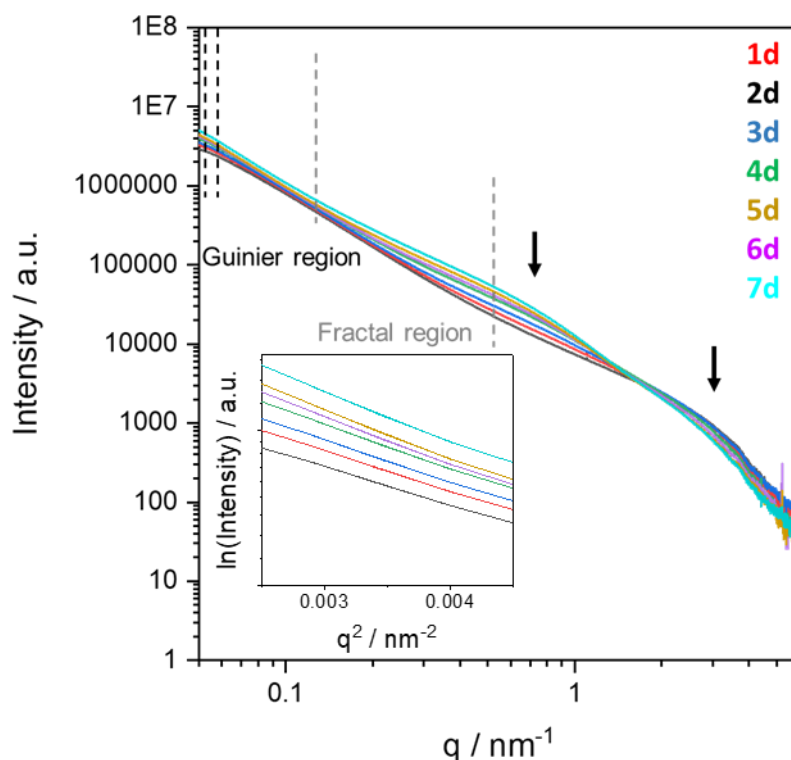


Figure 5.2-51: SAXS curves of wet gel E5 (HCl:TTIP 0.27:1) aged between one and seven days, respectively. The approximate ranges for the Guinier and fractal regions are shown with dashed lines and the curve bending marked with arrows. The Guinier plot is shown as an inset.

Table 5.2-14: Results of SAXS curve analysis of wet gel E5 (HCl:TTIP 0.27:1) aged between one and seven days, respectively.

Sample	Slope Guinier region	R_G / nm	Secondary particle size / nm	Slope of fractal region	q value of curve bending / nm^{-1}	Primary particle size / nm
E5-1d	-253.53 ± 3.94	27.6 ± 0.2	42.7 ± 0.6	-2.2 ± 0.02	2.87	1.10
E5-2d	-266.30 ± 4.70	28.3 ± 0.3	43.8 ± 0.6	-2.2 ± 0.03	2.73	1.15
E5-3d	-275.83 ± 6.01	28.8 ± 0.3	44.6 ± 0.8	-2.2 ± 0.03	2.97/1.13	1.06/2.78
E5-4d	-289.22 ± 7.10	29.5 ± 0.4	45.6 ± 0.9	-2.2 ± 0.04	3.01/0.91	1.02/3.46
E5-5d	-307.91 ± 8.59	30.4 ± 0.4	47.1 ± 1.1	-2.2 ± 0.04	2.92/0.75	1.07/4.17
E5-6d	-317.96 ± 9.78	30.9 ± 0.5	47.8 ± 1.2	-2.1 ± 0.04	2.99/0.73	1.05/4.33
E5-7d	-323.92 ± 10.62	31.2 ± 0.5	48.3 ± 1.3	-2.0 ± 0.04	2.88/0.75	1.09/4.22

5.2.8.2 *i*PrOH Solvent-Based Wet Gels

Figure 5.2-52 shows the SAXS curves of the *i*PrOH solvent-based wet gels *i*P1 to *i*P6 and Guinier plots as inset. The curves show similar behavior compared to the SAXS curves of the gels E1 to E6.

The radius of gyration and secondary particle size increases with the acid amount used during the synthesis of the gels. It should be noted that the radius of gyration is much higher for *i*P1 to *i*P3 compared to that of E1 to E3.

Fractal clusters are assumed for the gels *i*P1 to *i*P6, due to the linear curve progression and previous SEM and TEM results. The slope of the mid q range was calculated and summarized in Table 5.2-15. A power-law exponent of approx. -2 was found for all samples, indicating a lamellar structure of the particles.

Regarding the curve progression, a similar behavior was observed compared to the gels E1 to E6. For the gel *i*P1 to *i*P6, q values from the curve bending at high q values were determined which increase from 2.86 nm^{-1} to 3.11 nm^{-1} with the acid amount. This results in a decreasing primary particle size from 1.10 nm to 1.01 nm (Table 5.2-15).

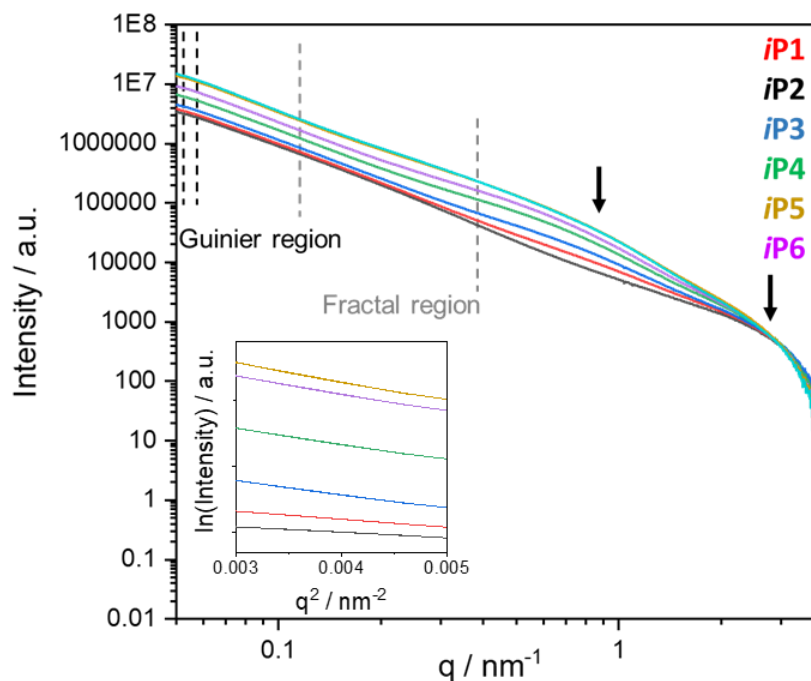


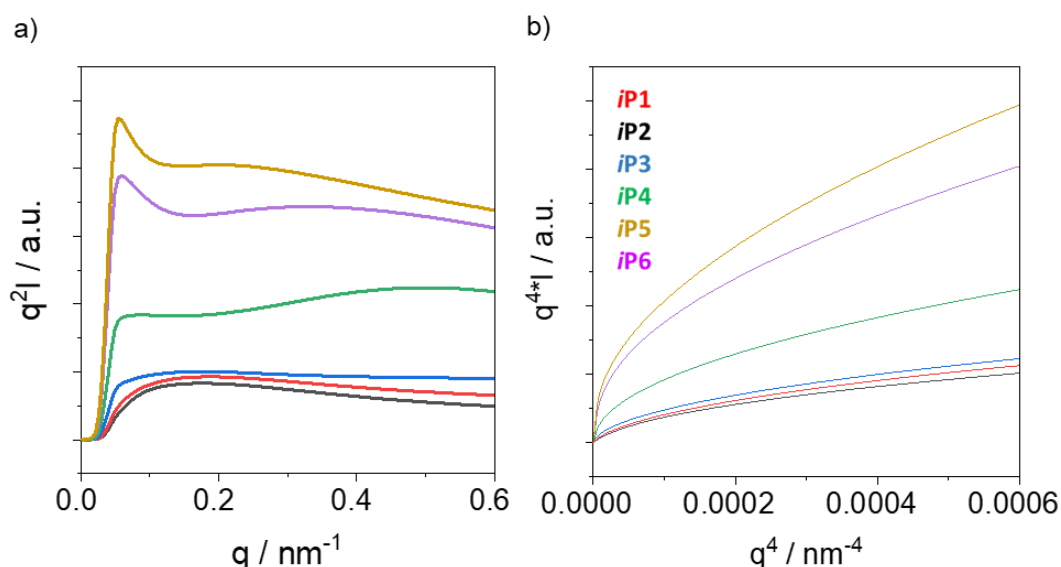
Figure 5.2-52: SAXS curves of wet gels *i*P1 to *i*P6. The amount of acid during the synthesis was increased from *i*P1 to *i*P6. The approximate ranges for the Guinier and fractal regions are shown with dashed lines and the curve bending marked with arrows. The Guinier plot is shown as an inset.

Table 5.2-15: Results of SAXS curve analysis of wet gels *iP1* to *iP6*.

Sample	Slope Guinier region	R_G / nm	Secondary particle size / nm	Slope of fractal region	q value of curve bending / nm^{-1}	Primary particle size / nm
<i>iP1</i>	-81.26 ± 2.94	15.6 ± 0.3	24.2 ± 0.7	-2.0 ± 0.02	2.86	1.10
<i>iP2</i>	-121.15 ± 1.23	19.1 ± 0.1	29.5 ± 0.3	-2.0 ± 0.02	2.89	1.09
<i>iP3</i>	-213.58 ± 5.46	25.3 ± 0.3	39.2 ± 0.8	-2.0 ± 0.01	2.92/0.71	1.08/4.41
<i>iP4</i>	-243.48 ± 7.05	27.0 ± 0.4	41.9 ± 1.0	-1.9 ± 0.01	2.96/0.63	1.06/5.00
<i>iP5</i>	-273.55 ± 7.82	28.6 ± 0.4	44.4 ± 1.1	-2.0 ± 0.01	2.99/0.73	1.05/4.29
<i>iP6</i>	-292.97 ± 9.57	29.6 ± 0.5	45.9 ± 1.3	-2.0 ± 0.01	3.11/0.88	1.01/3.56

However, the curves show a very steep decrease at high q values which is probably an artefact due to background subtraction (Figure 5.2-52). Therefore, the calculated values of the primary particle size at high q values might be inaccurate. For the gels *iP3* to *iP6*, the curve bends slightly at higher q values at 0.71 nm^{-1} to 0.88 nm^{-1} with increasing amount of acid, similar to E3 to E6. This results in decreasing values of the calculated particle size from 4.41 nm to 4.56 nm (Table 5.2-15).

In Figure 5.2-53a and b the Kratky and Porod-Debye plots are shown, respectively. The gels *iP1* to *iP3* show similar behavior compared to that of E1 to E2 indicating a flexible gel network. The gels *iP4* to *iP6* show similar to E3 to E6 increasing values for large q values.

Figure 5.2-53: Kratky plot (left) and Porod-Debye plot (right) of *iP1*-*iP6*.

This indicates more flexibility due to longer chains in the network. Also, a peak with increasing intensity was observed at low q values, similar to E4 to E6, indicating spherical and rigid aggregates in the gel network. The Porod-Debye plot in Figure 5.2-53 shows also a lack of a plateau, similar to the EtOH solvent-based samples, and supports the full flexibility of the gel network.

Figure 5.2-54 shows the SAXS curves and the Guinier plots as inset of the wet gel *iP5* which was aged between one and seven days, respectively and measured at different stages of aging. The radius of gyration and secondary particle size increase for longer aging times. The results are shown in Table 5.2-16. The curves behave similar compared to the samples *iP1* to *iP6*. The linear region in the mid q range indicates fractal clusters with a power-law exponent of approx. -2, indicating a lamellar structure of the particles. For *iP5* 1-2d q values between 2.92 nm^{-1} to 3.02 nm^{-1} were determined resulting in a primary particle size between 1.04 nm and 1.08 nm, which is similar to previous results of E5. For *iP5* 3-7d additional q values for the curve bending at lower q was determined between 0.67 nm^{-1} and 0.78 nm^{-1} . This leads to a calculated particle size between 4.00 nm and 4.76 nm.

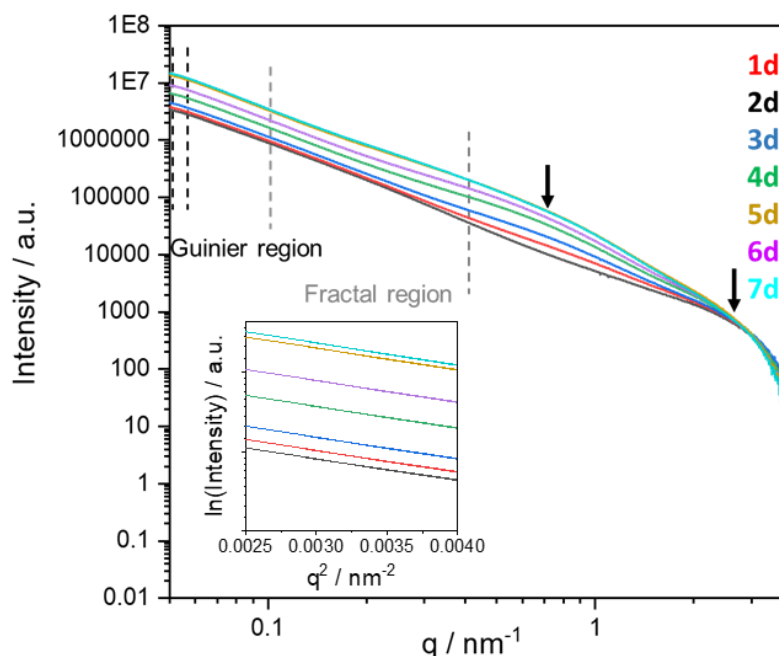


Figure 5.2-54: SAXS curves of wet gel *iP5* (HCl:TTIP 0.27:1) aged between one and seven days, respectively. The approximate ranges for the Guinier and fractal regions are shown with dashed lines and the curve bending marked with arrows. The Guinier plot is shown as an inset.

Table 5.2-16: Results of SAXS curve analysis of wet gel *iP5* (HCl:TTIP 0.27:1) aged between one and seven days, respectively.

Sample	Slope Guinier region	R_G / nm	Secondary particle size / nm	Slope of fractal region	q value of curve bending / nm^{-1}	Primary particle size / nm
<i>iP5</i> 1d	-257.80 ± 8.80	27.8 ± 0.5	43.1 ± 1.2	-2.2 ± 0.01	3.02	1.04
<i>iP5</i> 2d	-260.70 ± 9.17	28.0 ± 0.5	43.3 ± 1.3	-2.2 ± 0.01	2.94	1.07
<i>iP5</i> 3d	-261.79 ± 8.61	28.0 ± 0.5	43.4 ± 1.2	-2.2 ± 0.01	2.92/0.78	1.08/4.00
<i>iP5</i> 4d	-263.21 ± 8.54	28.1 ± 0.5	43.5 ± 1.2	-2.1 ± 0.01	2.92/0.66	1.08/4.76
<i>iP5</i> 5d	-265.24 ± 8.16	28.2 ± 0.4	43.7 ± 1.1	-2.1 ± 0.01	2.98/0.67	1.05/4.70
<i>iP5</i> 6d	-268.75 ± 7.34	28.4 ± 0.4	44.0 ± 1.0	-2.1 ± 0.01	3.01/0.74	1.04/4.22
<i>iP5</i> 7d	-273.56 ± 7.82	28.6 ± 0.4	44.4 ± 1.1	-2.1 ± 0.01	2.99/0.73	1.05/4.29

5.3 Chemical Composition

XPS analysis was performed to obtain the chemical composition of the synthesized aerogels and detect possible impurities in the sample. Also, the analysis of individual Ti2p spectra gives an indication of the oxidation states present in the samples.

5.3.1 EtOH and *iPrOH* Solvent-Based Aerogels

The EtOH solvent-based aerogels E2 and E5 and *iPrOH* solvent-based aerogels *iP2* and *iP5* were analyzed using XPS to obtain the chemical composition. Besides titanium (9.9 to 26.1 at.%) and oxygen (30.8 to 61.3 at.%), carbon (6.9 to 58.3 at.%) and chlorine (1.0 to 4.3 at.%) were found in the aerogels.

The XPS survey spectra and the individual spectra of Ti2p, C1s, Cl2p and O1s of E2 is shown in Figure 5.3-1 and Figure 5.3-2 as an example. The other spectra of sample E5, *iP2* and *iP5* are shown in the appendix in Figure 9.7-1 to Figure 9.7-3. For the samples E2 and E5 similar values of the Ti content (approx. 22 at.%), C content (approx. 17 to 22 at.%) and O content (approx. 51 to 57 at.%) were observed, whereas for sample *iP2* and *iP5* the compositions are shown in Table 5.3-2 and differ to a large extent, that could be due to inhomogeneities. In the Ti2p spectra asymmetric peaks are observed, which indicate small amounts of Ti^{3+} . The peaks were integrated and the percentage of Ti^{3+} and Ti^{4+} calculated, that is summarized in Table 5.3-1. The Ti^{3+} content is highest for E2 and decreases when *iPrOH* or high HCl:TTIP ratios are used during the synthesis. From the calculated Ti/O ratio it can be concluded that mainly

stoichiometric TiO_2 was formed. In Figure 5.3-3 a comparison of the $\text{Ti}2p$ signals for the samples E2, E5, *iP2* and *iP5* is shown. The aerogel sample *iP5* exhibits a narrower main peak and is less symmetric (showing less intensity at 457 eV). The broadening of the peaks may indicate a change in number of chemical bonds, sample condition (X-ray damage) or differential charging of the surface.

Impurities of nitrogen and C=O groups in the $\text{C}1s$ signal are found for sample E2, which could be assigned to remaining bitrex and methylethylketone (MEK) from denatured EtOH and are excluded in Table 5.3-2 and Table 5.3-1. The carbon content varies in the analyzed samples and originates from remaining ethyl/isopropyl groups in the structure from incomplete hydrolysis/condensation reactions. From the $\text{C}1s$ spectra (Figure 5.3-2) the carbon species were analyzed in more detail. The percentage of carbon species is shown in in Table 5.3-1. C-C and C-O signals were mainly found which originate from alcohol residues. The sample E2 contained significantly more C-O groups compared to the other samples. Surprisingly also signals for COOH were found in the $\text{C}1s$ spectra for all analyzed samples, that originates from adventitious carbon due to exposure to the atmosphere. The percentages of the carbon species are similar in the samples E5, *iP2* and *iP5*.

The chlorine content is higher in the EtOH solvent-based aerogels compared to the *iPrOH* solvent-based samples. Also, the chlorine content in the dried aerogels increases slightly from *iP2* to *iP5* and E2 to E5, which is in accordance with the used quantity of HCl during the synthesis. The chlorine signal in Figure 5.3-2 exhibits binding energies of 198.25 eV and 199.85 eV, which are shifted to lower values and related to metal chlorides. [209]

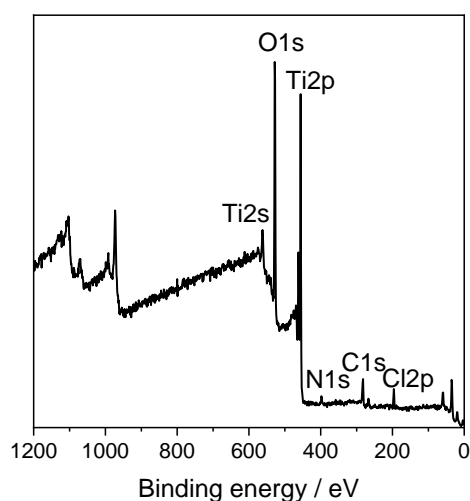


Figure 5.3-1: XPS survey spectra of the aerogel sample E2 (HCl:TTIP 0.11:1; based on denatured EtOH as solvent).

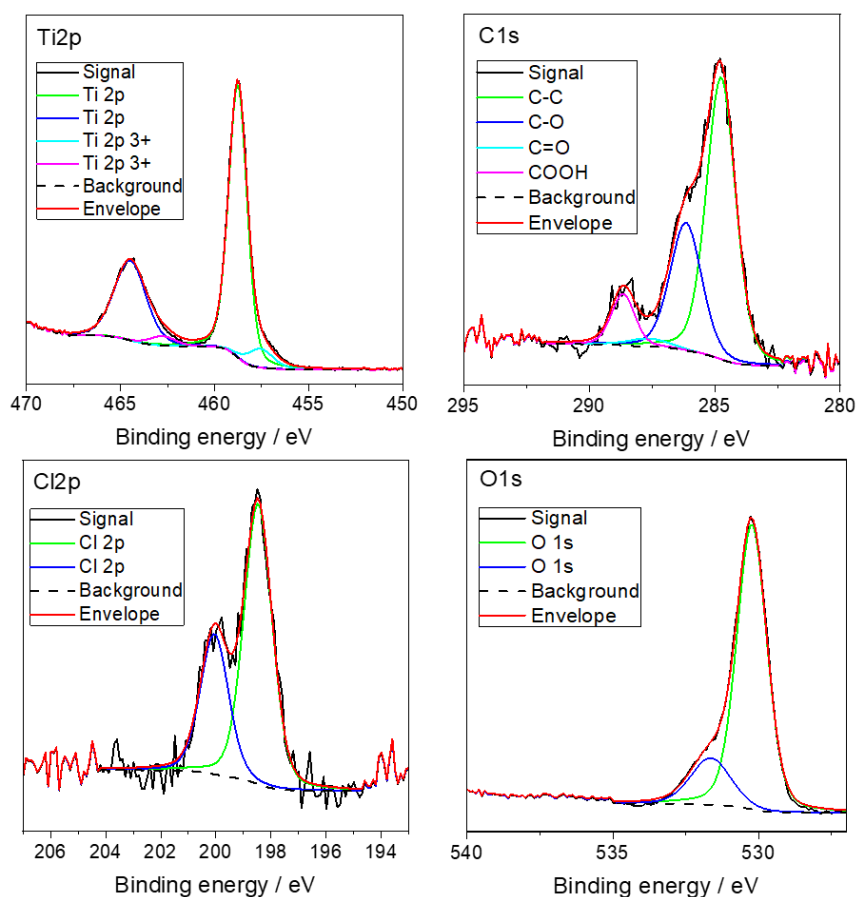


Figure 5.3-2: Ti2p, C1s, Cl2p, and O1s XPS spectra of the aerogel sample E2 (HCl:TTIP 0.11:1; based on denatured EtOH as solvent).

Table 5.3-2: Chemical composition of the aerogel samples E2 (HCl:TTIP 0.11:1), E5 (HCl:TTIP 0.27:1), *iP2* (HCl:TTIP 0.11:1), and *iP5* (HCl:TTIP 0.27:1).

Sample	Ti / at. %	C / at. %	O / at. %	Cl / at. %
E2	22.2	17.4	57.1	3.3
E5	22.4	21.8	51.4	4.3
<i>iP2</i>	9.9	58.3	30.8	1.0
<i>iP5</i>	26.1	6.9	61.3	4.0

Table 5.3-1: Oxidation states and carbon species of the aerogel samples E2 (HCl:TTIP 0.11:1), E5 (HCl:TTIP 0.27:1), *iP2* (HCl:TTIP 0.11:1), and *iP5* (HCl:TTIP 0.27:1).

Sample	Ti ³⁺	Ti ⁴⁺	C-C	C-O	COOH	Ti/O ratio
E2	8.8	91.2	61.1	29.9	9.0	0.49
E5	2.2	97.8	83.2	12.0	4.8	0.57
<i>iP2</i>	4.6	95.4	84.2	11.7	4.1	0.57
<i>iP5</i>	0.6	99.4	81.9	11.4	6.7	0.50

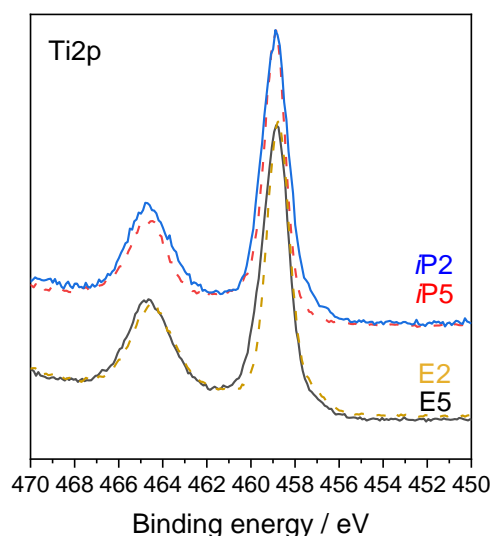


Figure 5.3-3: Ti2p XPS spectra of the aerogel samples E2 (HCl:TTIP 0.11:1), E5 (HCl:TTIP 0.27:1), *i*P2 (HCl:TTIP 0.11:1), and *i*P5 (HCl:TTIP 0.27:1).

5.3.2 Calcined Aerogels

The calcined aerogels E2-A-300 and E2-V-300 are analyzed using XPS to obtain the chemical composition and the results summarized in Table 5.3-3. From the calculated Ti/O ratio it can be concluded that stoichiometric TiO₂ is formed, similar to the non-calcined samples. The carbon content in both calcined samples is lower compared to non-calcined sample E2, indicating less remaining carbon residues after calcination. The observed amount of Ti³⁺ is lower for the air-calcined sample compared to the vacuum-calcined sample. However, both values are much lower compared to the non-calcined sample E2.

A narrower main peak in the Ti2p spectra is found for E2-A-300 which is less symmetric and showing less intensity at 457 eV and confirms the small amount of Ti³⁺ for sample E2-V-300.

Table 5.3-3: Chemical composition of calcined aerogel samples.

Sample	Ti / at.%	C / at.%	O / at.%	Cl / at.%
E2-A-300	25.3	14.3	59.2	1.2
E2-V-300	25.2	14.3	59.4	1.0

Table 5.3-4: Oxidation states and carbon species of calcined aerogel samples.

Sample	Ti ³⁺	Ti ⁴⁺	C-C	C-O	COOH	Ti/O ratio
E2-A-300	1.0	99.0	90.0	0.6	9.3	0.50
E2-V-300	2.4	97.6	91.5	0.9	7.6	0.50

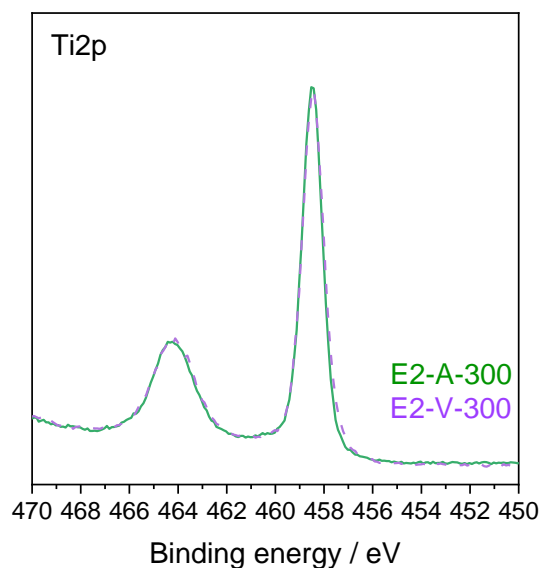


Figure 5.3-4: Ti2p XPS spectra of in air and vacuum calcined aerogel samples.

From the C1s spectra (Figure 9.7-4 and Figure 9.7-5) the carbon species were analyzed in more detail. The percentage of C-C of the calcined samples is higher compared to the non-calcined samples (Table 5.3-4). Also, the C-O signal almost disappears, indicating only few alcohol residues. The signals for COOH groups were observed in the C1s spectra also for the calcined samples in the same extent compared to the non-calcined samples. Similarly, to the non-calcined samples, the Cl was observed in the calcined samples, which is not removed during the calcination step at 300 °C. The chlorine signals are shifted to lower values and related to metal chlorides (Ti-Cl bonds).^[209]

5.4 Electronic Properties

Absorption spectra in diffuse reflectance are recorded to characterize the optical properties of the TiO₂ aerogels. They are converted to Kubelka-Munk spectra to determine the absorbance of the aerogels and to observe a possible shift from UV to vis light. Tauc plots are used to determine the bandgap of the aerogels.

5.4.1 Band gap and Position of Valence Band

The band gap of the aerogel sample E2 is estimated between 3.4 and 3.5 eV, whereas the sample E5, synthesized with a higher HCl amount, exhibits a band gap of 3.3 eV. The band gap of the vacuum-calcined aerogel is 3.4 eV, which is slightly higher than the band gap of the air-calcined aerogels of 3.2 to 3.3 eV, which was expected as it is a partially amorphous sample, compared to the completely crystalline air-calcined aerogels. The band gap becomes narrower with increasing calcination temperature.

The received data from UPS measurements are plotted on a logarithmic scale to determine the upper edge of the VB and identify mid-gap states. A logarithmic scale is reported in literature to give more realistic values for the VB maximum.^[210] A strong increase of the curve and therefore high density of electronic states (O2p) indicates where a tangent has to be applied, as shown in Figure 5.4-1. Logarithmic extrapolation leads to the VB edge value (relative to the Fermi level). A value of 2.8 eV for the VB maximum was determined for the aerogel sample E2. From the VB edge and the band gap the CB was calculated, which was found to be between -0.6 and -0.7 eV. The UPS results Figure 5.4-1 show occupied states in the band gap, so-called band gap states, for sample E2 which are associated with defect states in the sample such as Ti³⁺.

Table 5.4-1: Band gap values of the aerogel samples E2, E5 and calcined aerogels.

Sample	Indirect band gap / eV
E2	3.4-3.5
E5	3.3
E2-A-300 (2 h)	3.3
E2-A-300 (10 h)	3.3
E2-A-400 (10 h)	3.3
E2-A-500 (10 h)	3.2
E2-V-300 (2 h)	3.4

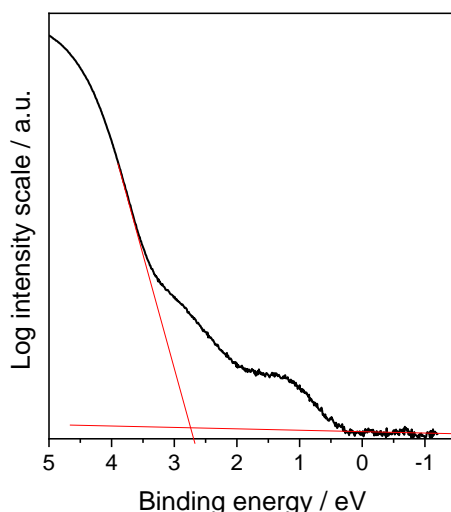


Figure 5.4-1: UPS spectrum of the aerogel sample E2 (HCl:TTIP 0.11:1) and extrapolation for the determination of the VB edge.

5.5 Photocatalytic Activity

The synthesized aerogel E2 and the calcined aerogels E2-A-300/400/500 were investigated in experiments for photocatalytic hydrogen generation, nitrogen reduction reaction to ammonia and electron storage capability as proof of concept. The experiments were performed to investigate the influence of the physicochemical properties of the aerogels on the electron storage capability and photocatalytic activity. The photocatalytic experiments were published in the respective publication listed in the appendix in chapter 9.12 (Rose *et al.*).^[195]

5.5.1 Photocatalytic Hydrogen Generation

The hydrogen evolution rates of the aerogel after deposition of the Pt co-catalyst increase with the calcination temperature as summarized in Table 5.5-1.

Table 5.5-1: Hydrogen evolution rates of the aerogel sample E2 and calcined aerogels. Reprinted (adapted) with permission from A. Rose *et al.* Photocatalytic Activity and Electron Storage Capability of TiO₂ Aerogels with an Adjustable Surface Area. ACS Applied Energy Materials, 2022. 5(12): p. 14966-14978. Copyright 2022 American Chemical Society.

Sample	Hydrogen evolution rate (with 0.1 wt.% Pt) / $\mu\text{mol h}^{-1}$
E2	25.5
E2-A-300-10h	176.5
E2-A-400-10h	279.2
E2-A-500-10h	331.8

Pt is added as co-catalyst to form a Schottky-junction, as explained in section 2.4.2 of the chapter ‘State of the art’. Without co-catalyst the hydrogen evolution rates are less than $10 \mu\text{mol}\cdot\text{h}^{-1}$ for the non-calcined and calcined aerogels, showing the same trend, that the hydrogen evolution rate increases with the calcination temperature (Figure 5.3-4).

5.5.2 Electron Storage Capability

Figure 5.5-1 shows the aerogel dispersions in the water-methanol mixture after irradiation with UV-light. Methanol is used as hole scavenger which reacts with photogenerated holes to prevent fast recombination of charge carriers. The aerogel samples were irradiated for 100 minutes without a co-catalyst. The color changed from a colorless to a bluish-colored dispersion after irradiation. The color of the dispersion indicates electrons which are stored in the aerogel material and formation of Ti^{3+} .

It was observed that the dispersion turned dark blue for the non-calcined aerogel E2 while the calcined aerogels (E2-A-300-10h, E2-A-400-10h, E2-A-500-10h) were less colored with increasing calcination temperature (Figure 5.5-1).

Figure 5.5-2a shows the time-dependent hydrogen evolution. The irradiation of UV-light and the co-catalyst addition are highlighted in the Figure 5.5-2a. The aerogels were irradiated for 100 minutes without co-catalyst, showing low hydrogen evolution rates.

The images in Figure 5.5-2a show the color of the dispersions before UV-light irradiation and the blueish color change after UV-light irradiation. The lamp was switched off after 100

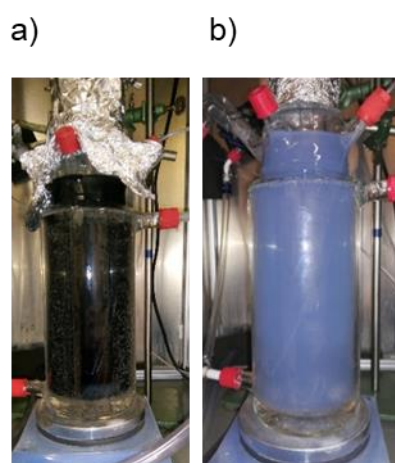


Figure 5.5-1: Coloration of different photocharged aerogel dispersions. a) The aerogels sample E2 with a dark blue color. b) The calcined aerogel E2-A-500-10h is shown in the right image with a light blue color.

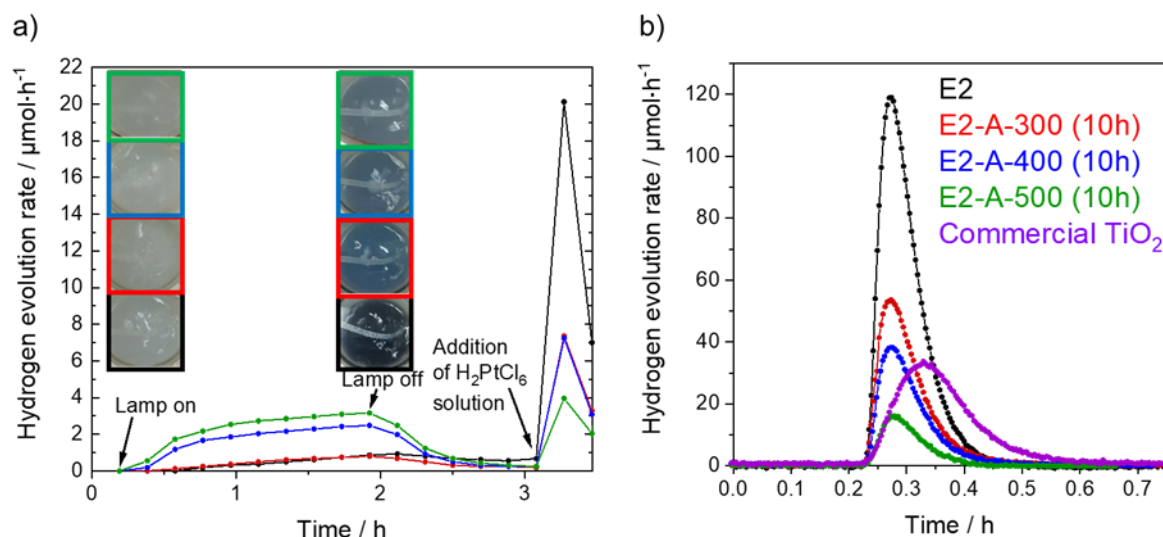


Figure 5.5-2: a) Hydrogen evolution rates over time and images of the dispersions before irradiation and after 100 min of irradiation of the calcined aerogels at 500, 400, and 300 °C and the as-synthesized sample E2 from top to bottom. b) Hydrogen evolution rates in the dark of the calcined aerogels, the as-synthesized aerogel E2, and the commercial anatase for comparison.^[195] Reprinted (adapted) with permission from A. Rose *et al.* Photocatalytic Activity and Electron Storage Capability of TiO_2 Aerogels with an Adjustable Surface Area. ACS Applied Energy Materials, 2022. 5(12): p. 14966-14978. Copyright 2022 American Chemical Society.

minutes and no hydrogen could be detected, due to the missing generation of electron-hole pairs. The coloration of the dispersion remained dark blueish for the aerogel sample E2 and light blueish for the calcined aerogels. Pt as co-catalyst was deposited on the aerogels by using a H_2PtCl_6 solution. After a few seconds, the coloration of the dispersion disappeared, while a sharp peak (after three hours in Figure 5.5-2) in the hydrogen evolution was observed without any further light irradiation. The peak in the hydrogen evolution rate was observed for the non-calcined aerogel E2 as well as for the calcined aerogels. However, the observed peaks were less intense with increasing calcination temperature of the calcined aerogels which were also less colored.

A second experiment was performed using the same experimental conditions but a mass spectrometer for high resolution of hydrogen detection. Figure 5.5-2b shows the hydrogen evolution of the aerogels after Pt addition, assuming that all Pt^{4+} of the H_2PtCl_6 solution was reduced to Pt^0 and that the remaining stored electrons were used only for the hydrogen evolution reaction. The dispersion with the aerogel sample was irradiated for 100 minutes. After switching off the lamp and achieving a stable baseline, the H_2PtCl_6 solution was added to achieve 0.1 wt.% Pt deposition on the aerogel. The experiment confirmed the previously

observed results in Figure 5.5-2a, that the highest peak in hydrogen evolution rates were observed for the aerogel sample E2. The hydrogen evolution rate decreases with increasing calcination temperature. For comparison, commercial anatase nanoparticles were also tested, which show similar hydrogen evolution rates to the aerogel sample calcined at 400 °C. However, the peak was retarded for the commercial anatase sample compared to that of the synthesized aerogels in this work.

5.5.3 Photocatalytic Reduction of Nitrogen to Ammonia

A similar experiment with the aerogel E2 was performed to study the reduction of nitrogen in the dark from stored photogenerated electrons to ammonia. The aerogel was irradiated with UV-light in a water-methanol mixture as explained above under argon to store electrons in the aerogel. The aerogel was irradiated with UV-light as explained for the hydrogen evolution experiments. The dispersion was flushed with nitrogen for seven hours as reaction time. Figure 5.5-3 shows the absorbance spectra of a salicylate test, which was performed afterwards to quantify the generated ammonia. In Figure 5.5-3 the peak can be assigned to ammonia, since

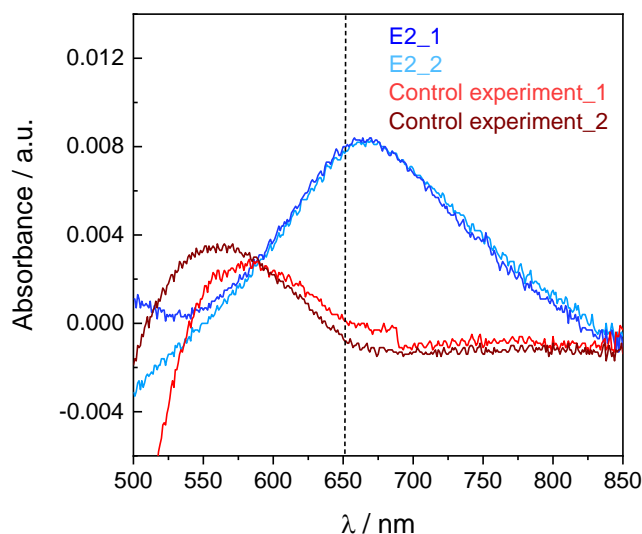


Figure 5.5-3: Absorbance spectra (dark and light blue) of the salicylate test of the solution after dark nitrogen reduction reaction with photocharged as-synthesized TiO₂ aerogel sample (E2) for quantitative determination of the obtained NH₃ concentration. Control experiments (brown/red) baseline before photocharging (nitrogen gas, dark, no photocharging yet) and identical measurement in argon gas. ^[195] Reprinted (adapted) with permission from A. Rose *et al.* Photocatalytic Activity and Electron Storage Capability of TiO₂ Aerogels with an Adjustable Surface Area. ACS Applied Energy Materials, 2022. 5(12): p. 14966-14978. Copyright 2022 American Chemical Society.

no signal was observed without flushing with N₂. In the experiment 5 μg·L⁻¹ ammonia could be achieved. Control experiments were performed to confirm the ammonia generation. A peak could be observed, which could be assigned to nitroprusside from the salicylate testing, which is not related to ammonia.

5.6 Mixed Metal Oxide and Doped Aerogels

On the basis of the developed TiO₂ aerogel synthesis different mixed-oxide and doped aerogels were synthesized and analyzed. The aim was to narrow the band gap for more efficient hydrogen evolution and absorption also in the vis region, as well as efficient charge carrier separation. V₂O₅-TiO₂ and SnO₂-TiO₂ aerogels were synthesized from liquid alkoxide precursors to simply modify the gel and adjust the metal oxide/Ti ratio. A homogeneous distribution of the additional metal oxide was expected, since only liquid precursors were used. The reaction was performed under nitrogen atmosphere to prevent premature hydrolysis and condensation, due to different hydrolysis reaction rates of the alkoxide precursors. Similar gelation behavior is observed for the V₂O₅-TiO₂ and SnO₂-TiO₂ gels, however they exhibit a yellow-brownish and yellow color respectively compared to the colorless TiO₂ gels. For the V₂O₅-TiO₂ gels the same synthesis procedure as for sample E2 was used with an adjusted amount of water (chapter 3.2.1). For SnO₂-TiO₂ gels the same synthesis procedure as for sample *i*P2 was used with adjusted amounts of solvent and water (chapter 3.2.1). The purchased SnTIP was already diluted in *i*PrOH due to low solubility in other solvents. Additionally, doped TiO₂ aerogels with small amounts (1 at.%) GO and MoS₂ were synthesized on the basis of sample E2 to investigate the properties and homogeneity of the doped aerogel with solid additives. The results are shown in the appendix in 9.10.

In Figure 9.10-1 the appearance of the mixed-oxide and doped aerogels is shown. The SnO₂-TiO₂ aerogel has a yellow translucent appearance with larger fragments, whereas the V₂O₅-TiO₂ aerogel has a brown translucent appearance. The MoS₂-TiO₂ and GO-TiO₂ aerogels appeared to be grey. However, the GO-TiO₂ aerogel exhibits some black spots visible in the aerogel, indicating inhomogeneities and larger GO aggregates in the sample. In the SEM images in Figure 9.10-2 smooth surfaces and a homogeneous pore structure for V₂O₅-TiO₂ and SnO₂-TiO₂ aerogels were observed, which indicate mesopores. For MoS₂-TiO₂ and GO-TiO₂ aerogels a few larger particles are found, which can originate from SEM sample preparation or larger aggregates from the dopants. The TEM images of V₂O₅-TiO₂ aerogel in Figure 9.10-3 confirms the mesoporous structure and shows particle sizes below 10 nm. Additionally, STEM mappings

were performed to investigate the distribution of vanadium and MoS₂ nanoparticles in the sample. The STEM mapping in Figure 9.10-4 confirms a homogeneous distribution of vanadium in the TiO₂ aerogel. The STEM mapping in Figure 9.10-5 shows also a homogeneous distribution of Mo and S in the aerogel, however only very small amounts are found.

The physisorption results are summarized in Table 9.10-1 and Figure 9.10-6. The SnO₂-TiO₂ aerogel exhibits a broad pore size distribution and large macropores with a BJH maximum of 83 nm. Larger pores and a higher surface area, compared to sample *iP2*, are observed, but having a smaller pore volume. The V₂O₅-TiO₂ aerogel shows a similar pore size distribution compared to sample E2 with a BJH maximum of 10 nm. The pore volume is found to be similar, but the surface area increased compared to sample E2. The MoS₂-TiO₂ and GO-TiO₂ aerogels show similar results to sample E2 but exhibit larger surface areas are observed, as well as an increased pore volume for the GO-TiO₂ aerogel, compared to sample E2.

In Figure 9.10-7 the diffractograms of the mixed-oxide and doped aerogels are presented. All samples were found to be amorphous. The GO-TiO₂ and V₂O₅-TiO₂ aerogels show slightly more pronounced broad reflections, which indicate a more ordered structure. However, the samples are mainly amorphous, that is evident from the amorphous halos. The MoS₂-TiO₂ aerogel exhibits some sharp reflections, which can be assigned to crystalline MoS₂ (PDF 37-1492).

In Table 9.10-2 and Table 9.10-3 the XPS results are summarized. The ratio of V/Ti and Sn/Ti is 0.04:1 and 0.06:1 respectively, whereas a molar ratio of 0.05:1 of the alkoxide precursors (VOIP:TTIP and SnTIP:TTIP) was initially used. This shows small deviations from the originally used amounts of precursor in the final aerogel. For the MoS₂-TiO₂ and GO-TiO₂ aerogels, 1 at.% of the dopant in relation to the TTIP precursor was used. Lower amounts of Mo/S are found in the final aerogel, also the Mo:S ratio does not fit to MoS₂. XPS can only detect elements on the surface (irradiation depth of a few nanometers) and is limited to the analyzed position of the sample, that could explain the Mo:S ratio, since MoS₂ could also be captured in pores surrounded by TiO₂. For the GO-TiO₂ aerogel, a C/Ti ratio of 1.14 was found compared to 0.78 for E2. This indicates an increased carbon content, that could originate from the added GO. Ti³⁺ is observed in the mixed-oxide and doped aerogel samples, with exception of the MoS₂-TiO₂ aerogel. The amount of Ti³⁺ increases in the following order *iP2*<SnO₂-TiO₂<V₂O₅-TiO₂<E2<GO-TiO₂.

Diffuse reflectance spectra were converted to Kubelka–Munk spectra and Tauc plots for band gap estimation. The Kubelka-Munk spectra of the GO-TiO₂ and SnO₂-TiO₂ aerogels show

similar behavior compared to the TiO₂ sample E2 regarding the absorption edge. From the respective Tauc plots, the band gaps for the GO-TiO₂ and SnO₂-TiO₂ aerogels are estimated, which were both 3.5 eV. The MoS₂-TiO₂ shows absorption in the vis range between 400 and 700 nm, besides the much stronger UV-light absorption. From the Tauc plots two values can be determined, which are 1.7 eV and 3.5 eV. The V-TiO₂ aerogel does not show a sharp absorption edge at 320 to 270 nm, but tailing up to 450 nm. Also, the band gap of 3.2 eV is narrower compared to the other mixed-oxides. In Figure 9.10-13 the UPS results are shown. The results show occupied states in the band gap for the SnO₂-TiO₂, V₂O₅-TiO₂ and GO-TiO₂ aerogel which correlate with the Ti³⁺ amount. For the MoS₂-TiO₂ aerogel no occupied states are found. The VB maximums were determined from logarithmic plots and the CB calculated from these values for the aerogels. The values of the CB and VB are summarized in Table 9.10-4. For the SnO₂-TiO₂ aerogel the most positive value for the VB edge of 3.4 eV is determined. The V-TiO₂ and GO-TiO₂ aerogels show values of 3.3 eV and 3.0 eV for the VB edge, respectively. The MoS₂-TiO₂ aerogel shows a less positive value of 1.6 eV for the VB edge. The calculated CB minimums are approx. -0.1 eV for the SnO₂-TiO₂, V₂O₅-TiO₂ and MoS₂-TiO₂ aerogel. For the GO-TiO₂ aerogel a more negative CB edge of approx. -0.5 eV is calculated.

6 Discussion

6.1 Impact of Synthesis Parameters on Gelation Kinetics and Shrinkage

6.1.1 Gelation Kinetics

6.1.1.1 Amount and Type of Solvent

In this work a novel synthesis route was developed to achieve (semi-)crystalline aerogels without calcination. The synthesis parameters play an important role in the gel formation and consequently on the structural properties and on the crystallinity, as elaborated in section 2.3.4 of the chapter ‘State of the art’. In this work, the gels were synthesized using two different solvents, EtOH and *i*PrOH. The solvents were used either alternatively as pure solvents or as a mix.

*i*PrOH solvent-based gels were prepared using *i*PrOH:TTIP molar ratios between 30:1 and 45:1 (Table 9.2-3 and Table 9.2-2). Since the precursor reacted quickly with water when dissolved in *i*PrOH, the precursor was added to only half of the solvent while the water for hydrolysis was diluted into the other half of the solvent. To the solution of precursor and solvent, HCl was added first and subsequently, after 20 minutes, the solvent with diluted water. By means of this procedure local inhomogeneous gelation was prevented. The high reactivity of the precursor was described in literature due to the similarity of the TTIP ligands and the used solvent. ^[21] The gelation time of the *i*PrOH solvent-based gels increased with the amount of solvent (see appendix in Figure 9.3-1), that was observed in preliminary results, indicating that the solvent works as an isolating layer on the TTIP by steric and electrostatic interactions, as described in literature for TiO₂ nanoparticle synthesis routes. ^[37] This leads to decreased reaction rates for the synthesized gels in this work. Smaller *i*PrOH:TTIP molar ratios than 30:1 were not used in this work due to quick gelation and low controllability of the synthesis.

Additionally, it is assumed that the high solvent content and low reaction temperature enhance the controllability of the hydrolysis and condensation reaction for achieving a uniform and defined pore size distribution. The precipitation of large particles was prevented in the developed synthesis by the chosen high organic solvent content and reducing the molecular interactions that leads to dilution of the system. In literature it was described that a high solvent content dilutes the system and reduces interactions, ^[106-108] but does not effectively prevent precipitation, when no acid is added. ^[211] However, less solvent was used in the synthesis procedures reported in literature compared to the developed synthesis in this dissertation. ^{[79, 88,}

110]

EtOH solvent-based gels were prepared using an EtOH:TTIP ratio at 26:1, as described in the synthesis procedure in section 3.1.1 of chapter ‘Synthesis of TiO₂ aerogels’. It is shown in ¹H-NMR data (appendix chapter 9.9) that a ligand exchange occurs at the TTIP precursor during the first few seconds of mixing, due to the excess of EtOH in the reaction mixture. The ligand exchange changes the gelation kinetics due to different alkoxy groups at the titanium-based precursor, which presumably changes from TTIP to TTE. Actually, the TTE precursor should be more reactive compared to the TTIP precursor, according to literature, due to the inductive effect of the alkyl group on the Ti atom. This effect is increasing with longer alkyl groups.^[43] Also the steric hindrance is increasing for longer alkyl groups that reduces the sensitivity to water.^[21] This is elaborated in section 2.3.3 of the chapter ‘State of the art’.

For very low HCl:TTIP ratios (0.05:1) the gelation time of the EtOH solvent-based gel is much shorter compared to the *i*PrOH solvent-based gel, confirming a higher reactivity of the formed titanium-based precursor in EtOH due to ligand exchange. For HCl:TTIP ratios of 0.11:1 the gelation times are similar for both *i*PrOH and EtOH solvent-based gels. The gelation time of the EtOH solvent-based gels increase with the amount of HCl used for the synthesis (Figure 5.1-1), whereas for *i*PrOH solvent-based gels the gelation time is much shorter (Figure 5.1-2). These findings show the opposite behavior for EtOH solvent-based gels as expected from literature. Actually, a higher amount of HCl causes a higher hydrolysis rate, due to high concentration of protons which catalyzes the hydrolysis reaction.^[103] The gelation rate should therefore increase for both used solvents with the HCl amount used during the synthesis. However, the two used solvents behave differently. This could indicate that chloride ions from the added HCl coordinate to the Ti atom. Chloride ions can act as complexing agents and decrease therefore the reaction rates, as well as separate hydrolysis and condensation reaction.^[41] When EtOH is used, the alkoxy ligand of the TTIP molecule changes from *Oi*Pr to *OEt* groups (appendix chapter 9.9). The steric hindrance is therefore reduced and more space for chloride ions is available to coordinate to the Ti atom of the precursor. Dependent on the number of chloride ions which coordinate to the Ti atom, fewer sites of the titanium-based precursor can therefore be hydrolyzed that lead to lower condensation reaction rates. This could be the case for EtOH solvent-based gels. With a high number of coordinated chloride ions to the Ti atom of the precursor, the gelation would be hindered and no 3D network can be formed. Therefore, at least three hydrolyzed groups which condense together would be required. If more than one or two chloride ions coordinate, the condensation reaction to form a 3D network becomes possible leading to a slurry-like appearance as observed for EtOH solvent-based gels

with high acid amounts (*e.g.* gel sample E6). It is also possible that to the 4-fold coordinated titanium-based precursor, chloride ions, solvent or water molecules are able to coordinate to the Ti atom, forming a 6-fold coordinated titanium-based precursor. A higher number of chloride ions could therefore coordinate to the Ti atom. However, this could also depend on the ligand strength and concentration in the reaction mixture. ^[212, 213]

It was observed during preliminary results, that EtOH solvent-based gels dissolved when they are washed in EtOH after gelation. This observation was also reported in literature by different researchers. ^[79, 214] Mir *et al.* reported that supercritical drying in CO₂ was not possible, as the gels dissolved in acetone or EtOH before placing the samples in the autoclave for drying. They explained this effect by weak bridging of hydrolyzed Ti oligomers which are destroyed when using acetone or EtOH. ^[214] Sadriyeh *et al.* also reported that gels dissolve in EtOH due to Ostwald ripening and a syneresis effect ^[79] Since the EtOH solvent-based gels dissolved in this work, this could mean that unreacted or uncondensed groups are present in the synthesized gels, which are quite instable directly after gelation, which require further reaction and stabilization during aging, justifying the long aging process of several days. However, during the aging process and further crosslinking reactions, shrinkage of the gel structure was observed (Figure 5.1-1). It is assumed that the liquid is forced out of the pores during aging due to a syneresis effect, as reported in literature, ^[215] that lead to stresses in the synthesized gels. These stresses can lead to cracks in the gel, which were observed in most synthesized gels, which in turn could also lead to dissolution of the gel in some cases. The solvent concentration increases at the outer surface of the gel during shrinkage, that could dissolve partially unreacted groups. The choice of solvent for the solvent exchange before supercritical drying and the time of aging before washing the gels is therefore very important to obtain stable TiO₂ gels. In this case, *i*PrOH was chosen as solvent for washing the gels to prevent their dissolution, that led to stable gels which could be supercritically dried in a next step.

The mixed solvent-based gels were synthesized with different EtOH-*i*PrOH molar ratios, keeping the molar ratio of solvent:TTIP constant at 26:1. The EtOH was added to the TTIP precursor and *i*PrOH in a second step after mixing. The water was added dropwise to the reaction mixture in all cases leading to homogeneous gels. The mixed solvent-based gels exhibited extended gelation times from few seconds to five minutes with increasing EtOH content (Figure 5.1-3). For gel sample E2 (pure EtOH) and *i*P2 (pure *i*PrOH) gelation times lower than five minutes were observed for the same HCl:TTIP ratio of 0.11:1 (Figure 5.1-1 and

Figure 5.1-2). The short gelation times and therefore high reaction rates of mixed solvent-based gels with high *i*PrOH fractions in Figure 5.1-3 originate from the high similarity of the precursor and the used solvent. Due to the very short gelation times observed when using *i*PrOH, mixed solvent-based aerogels with very high *i*PrOH fractions (*e.g.* *i*PrOH:EtOH 10:1), led to inhomogeneous gelation. Even the addition of water pre-diluted in half of the solvent didn't result in any improvement, that is probably due to the relatively low solvent:TTIP molar ratio of 26:1. The observed gelation times are very short for low EtOH mole fractions (Figure 5.1-3) and are extended only up to a molar ratio of EtOH: *i*PrOH of 1:1. The results presented above indicate that added EtOH molecules seem to act as additional spacer between the TTIP molecules, which have an isolating effect and therefore reduce the reaction rate.

As described in literature, the exchange of *Oi*Pr to OEt groups should increase the reaction rate due to higher reactivity of TTE. ^[43] However, in the *i*PrOH dominated gels of this work, it is expected that mainly *Oi*Pr groups are present at the titanium-based precursor. Some local exchange of *Oi*Pr to OEt groups, up to the sample with an EtOH:*i*PrOH ratio of 1:1 (gel sample E-*i*P5), might be possible, since EtOH was added first to the TITP precursor.

It is assumed that the majority of ligands are exchanged to OEt at the used Ti precursor, if EtOH is present in excess. The gelation time for EtOH mole fraction above 0.5 was observed to vary between 2.5 and 7 minutes and could be explained by the excess of EtOH and exchange of alkoxy groups that changes the reactivity. The inconsistent gelation time could be explained by the *i*PrOH in the solvent mixtures even for high EtOH mole fractions.

6.1.1.2 Amount of HCl

Main difference of the novel synthesis compared to the gel synthesis in the literature is the targeted addition of conc. HCl in a first step and stirring for a few minutes. In the synthesis procedure elaborated in section 3.1.1 in the chapter 'Synthesis of TiO₂ aerogels', clear gels are formed for the EtOH solvent-based route. There is no precipitation after adding water to the acidic sol, independent on the amount of water. However, if no acid is added to the system, this leads to rapid precipitation of white particles similar to standard sol-gel synthesis routes for TiO₂ nanoparticles in the literature. ^[49, 216] For synthesis under acidic conditions, mainly HNO₃ was used in literature. ^[25, 76, 79, 216] The acid and water were basically added in one step, leading to simultaneous hydrolysis and condensation reaction. ^[25, 76] In the novel HCl-supported synthesis route described in this dissertation, conc. HCl was used. HCl as strong acid, controls the acidic conditions, but exhibits a small amount of water since it is 37 wt.% aqueous conc.

HCl. By adding HCl in a first step, as performed in this work, a clear sol is obtained. HCl slows down the particle growth and prevents precipitation of titanium hydroxide particles.^[43] It is suggested that the small amount of water leads to premature hydrolysis of precursor molecules, before the final water addition after 20 minutes in a last step. The water addition in the last step of at least four equivalents relative to TTIP leads to a quick hydrolysis caused by the high amount of water and presumably delayed condensation reaction of due to high proton concentration caused by the acid. The TTIP precursor molecules could be partially hydrolyzed and condensed after the addition of acid, because of the very low amount of water added with the conc. aqueous HCl (37 wt.%). With increasing amount of HCl in the TiO₂ gel synthesis, consequently the amount of water slightly increases. This could lead to differently sized titanium oxo clusters which could change the reaction kinetics and pore formation. In literature, TTIP cluster sizes could be adjusted with very small amounts of water,^[217] that support the assumption.

Also, the used amount of HCl used in in this work is quite high compared to literature and is probably responsible for inhibiting the precipitation besides the high solvent content.^[110] It was described in literature that the presence of acid can prevent precipitation and fast condensation of hydrolyzed particles, due to an increased proton concentration that in turn lead to fast hydrolysis reactions.^[211] The gelation rate should be therefore lower. However, the gelation time for the EtOH and *i*PrOH solvent-based aerogels show different behavior with increasing acid content used during the synthesis, indicating different gelation kinetics with high proton concentrations.

Supported by XRD and XPS (section 5.2.5.4 and 5.3.1), it is assumed that chloride ions coordinate to the precursor and that the titanium-based precursor exchanges its alkoxy ligands according to the used solvent. However, the coordination of chloride ions is expected to require more time. During the synthesis of the EtOH solvent-based gel E2, a fine white solid precipitated a few minutes after the addition of acid, which dissolved completely after addition of water after 20 minutes. The precipitates and the final aerogel contained Ti-Cl compounds (cf. Figure 5.2-37 and Figure 5.3-2). The stirring of all reactants for at least 20 minutes is assumed to be required, to achieve an equilibrium for the coordination of chloride ions to the titanium-based precursor. However, chloride ions coordinated at the titanium-based precursor could be removed by water molecules during hydrolysis and condensation reactions, after adding high water amounts after 20 minutes stirring.

The gelation time of EtOH solvent-based gels increase with the amount of HCl (Figure 5.1-1). At very high HCl amounts used in the reaction mixtures it was observed that gelation does not occur, and a liquid sol remains, similar to literature reports for very low pH values.^[43] The long gelation times could be explained by decreased condensation reaction rates due to the high proton concentration with increasing amount of acid used during the synthesis. This can lead to decreased interaction of protonated species according to literature.^[43] As explained before another explanation for the extended gelation times or the missing gelation could be the coordination of chloride ions to the Ti atom which can reduce the ability to form a 3D network. A higher HCl content is assumed to lead to a higher number of chloride ions to coordinate to the Ti atom reducing the condensation reaction rate.

Chloride ions were reported in literature to influence gelation kinetics by complex formation achieving transparent gels and to slow down sol-gel condensation reactions.^[214] Kignelman *et al.* reported that acetic acid as complexing ligand reduced the hydrolysis and condensation reaction.^[103] Generally, when TTIP is hydrolyzed, the hydrolysis rate is increased with the use of an acid. The TTIP gets protonated by eliminating the alcohol. When using complexing agents *e.g.* acetic acid, the overall reaction rate was reported to be lower.^[103] However, the wet gels and dried aerogels in this work were opaque for high HCl:TTIP ratios. This could be due to the observed broad pore size distribution for high HCl:TTIP ratios in EtOH and *i*PrOH solvent-based aerogels that is further discussed in section 6.2.2 of the chapter 'Discussion'.

The gelation time of *i*PrOH solvent-based gels was observed to become shorter with higher amount of HCl (Figure 5.1-2). Generally, the observed gelation times are quite short (less than 5 minutes), that was explained above (section 6.1.1.1 and 2.3.3), due to the high reactivity of alkoxide precursors and the similarity of TTIP and *i*PrOH.^[21]

In the case of *i*PrOH solvent-based gels in this work it is assumed to be more difficult to form complexes with chloride ions due to steric hindrance of *Oi*Pr groups, that could explain the shorter gelation times compared to the gelation times for EtOH solvent-based gels, which increase. For EtOH solvent-based gels it is suggested that it's easier to form complexes with chloride ions due to less steric hindrance of *OEt* groups. A higher number of coordinated chloride ions in the EtOH solvent-based synthesis could inhibit the condensation reaction leading to longer gelation times, whereas less complexation leads to shorter gelation time in the case of *i*PrOH solvent-based gels.

However, it needs to be distinguished between the effect of chloride ions and protons on the resulting network. It has been reported that inorganic acids accelerate the hydrolysis rate, which is then higher compared to the condensation reaction rate. ^[102, 103] High concentrations of protons are actually reported to slow down the condensation reaction rate. ^[43] This could also be the case for EtOH solvent-based gels, as explained above, however, this does not explain the short gelation times and therefore expected high condensation rates for *i*PrOH solvent-based gels.

The synthesized *i*PrOH solvent-based gels in this work were transparent directly after the gelation but turned cloudy after few minutes. This could be due to larger macropores leading to light scattering or a broad pore size distribution due to fast sol-gel condensation reactions. With increasing HCl content the cloudiness appears quicker, that is probably due to very fast condensation reaction, which goes in line with the very short gelation times (Figure 5.1-2). For very high acid amounts gelation occurred instantly, so that an inhomogeneous gel was obtained, that could not be analyzed. According to literature, for more transparent or translucent gels, small and equally sized mesopores and slow condensation reaction are required. ^[214]

6.1.1.3 Amount of Water

A high solvent:TTIP ratio of 45:1 was chosen to achieve extended gelation times even for high water:TTIP ratios to determine clear differences in gelation times. The gelation time was observed to increase with the solvent content in preliminary results (Figure 9.3-1), leading to homogeneous gels that could be analyzed. The preliminary results (chapter 9.3.1) confirmed that a water:TTIP ratio of 4:1 is necessary to achieve the required degree of hydrolyzed precursor molecules to form a stable 3D gel network, since for lower water:TTIP ratios instable gels were obtained. Shorter gelation times were therefore observed with high water:TTIP ratios (Figure 9.3-2) due to a high hydrolysis rate, compared to low water:TTIP ratios. The results in Figure 9.3-2 are in accordance with the literature, where a stoichiometric amount of water above two is observed to form a 3D gel network instead of nanoparticles or forming a clear sol without gelation. ^[211] The gelation times for gels with high water content (four and eight equivalents) were observed to be shorter if the HCl:TTIP ratio is increased from 0.05:1 to 0.11:1 (Figure 9.3-2). Also, for a high HCl:TTIP ratio of 0.22:1 similar short gelation times were found for the samples synthesized with different amounts of water (Figure 9.3-2). This demonstrates the catalyzing effect of the hydrolysis reaction due to HCl addition during the synthesis for *i*PrOH solvent-based gels.

As explained before, the gelation time increase for EtOH solvent-based gels, while for *i*PrOH solvent-based gels the gelation time becomes shorter, with increasing HCl:TTIP ratios. If the water:TTIP ratio is increased to ratios of 8:1 to 12:1 besides a high HCl:TTIP ratio between 0.22:1 and 0.33:1 for the samples E4.1 to E6.1 or *i*P4.1 and *i*P5.1, the gelation time becomes shorter for both solvents. This effect is more evident for EtOH solvent-based gels. Water molecules can also coordinate to the titanium-based precursor replacing chloride ions at the usage of high HCl amounts during the synthesis, that should increase the reaction rates. It was also reported in literature, that gelation is faster for high water:alkoxide ratios. ^[79, 211] A higher amount of water should lead to higher hydrolysis level. The condensation reaction, especially the oxolation reaction during formation of Ti-O-Ti bonds releases water, that could further initiate the hydrolysis of remaining unhydrolyzed groups. ^[37] This is described in more detail in section 2.3.3 of the chapter 'State of the art'.

6.1.2 Shrinkage

The results discussed in the sections 6.1.1.1 to 6.1.1.3 of the chapter 'Results' demonstrate the dependency of the reaction rates on the HCl:TTIP and water:TTIP ratios. Nearly all the synthesized gels show some shrinkage during the first hours after gelation (approx. 10 %). This is due to further reactions of Ti-OH and RO-Ti groups by alkoxolation and oxolation reactions. ^[37, 215] Most shrinkage occurred during aging of the wet gels at 50 °C (Figure 5.1-1 and Figure 5.1-2). It was reported in literature that slightly increased temperatures speed-up the shrinkage process, ^[211] supporting the high shrinkage of the aged gels.

The EtOH solvent-based gels show an increasing shrinkage behavior during aging up to a HCl:TTIP ratio of 0.17:1. The gels shrink less for high HCl:TTIP ratios of 0.33:1, that is demonstrated in the picture of the wet gel sample E6, which completely filled the test tube after the aging process (Figure 5.2-2). The high shrinkage up to HCl:TTIP ratios of 0.17:1 could be due to the increasing crystallinity of the gels. From WAXS experiments, it is evident, that the crystallization occurs during aging, that is further discussed in section 6.3. In contrast, the wet gel sample E6 exhibited a slurry-like appearance, so that no shrinkage behavior was observed due to the instable gel. Less condensation and crosslinking are assumed in the gel, that lead to instable gels, due to coordination of chloride ions, as explained before.

A higher HCl content used in the reaction mixture (cf. Table 9.2-2 and Figure 5.1-2) leads to higher shrinkage of the *i*PrOH solvent-based gels, that can be partially traced back to the

increasing crystallinity of the samples, since the shrinkage correlates with the crystallinity of the gels (Figure 5.2-6 Table 5.2-9). Crystallization begins between two and four days (and Figure 5.2-45), according to the WAXS results. Between four and seven days of aging high shrinkage was observed.

High water:TTIP ratios (8:1 to 12:1 > 4:1) lead to higher shrinkage of the samples, besides high HCl:TTIP ratios (cf. Table 9.2-1 and Table 9.2-2). The difference is more evident for EtOH solvent-based gels compared to *i*PrOH solvent-based gels (Figure 5.1-1 and Figure 5.1-2). A high amount of water leads to a high hydrolysis level of Ti(OR)₄ and therefore a high number of hydroxyl groups (Ti-OH), which can further react in condensation reactions. This could lead to more branching of the network, leading to a stronger network that pushes solvent out of the pores. This is supported by lower BJH maxima found for higher water contents (Figure 5.2-12 and Figure 9.3-4).

As depicted in Figure 9.3-1b the amount of solvent (*i*PrOH) used in the reaction mixture has no significant impact on the shrinkage behavior for different HCl:TTIP ratios.

Mixed solvent-based gels in Figure 5.1-3 with low EtOH fractions and excess of *i*PrOH exhibit higher shrinkage (approx. 18 %) compared to high EtOH fractions (approx. 12 %). With increasing EtOH mole fractions (above 0.5) the gels exhibit lower shrinkage. For comparison, pure EtOH solvent-based gels exhibited shrinkage below 10 % and pure *i*PrOH solvent-based gels showed shrinkage above 10 %. The shrinkage behavior of mixed solvent-based gels agrees with the observed shrinkage behavior of pure EtOH solvent-based (Figure 5.1-1) and pure *i*PrOH solvent-based gels (Figure 5.1-2) at a HCl:TTIP ratio of 0.11:1, that with the usage of *i*PrOH higher shrinkage occurs compared to EtOH. (Figure 5.1-3)

The shrinkage behavior of the wet gels during aging could be related to the steric hindrance of the precursor, which depends on the coordinated alkoxy ligands (O*i*Pr or OEt) and on the number of coordinated water as well as chloride ions to the Ti atom of the precursor. A higher number of coordinated chloride ions (which are smaller than alkyl groups/solvent molecules) lead to lower steric hindrance of the formed titanium-based precursor. ^[218, 219] Also, the crystallinity of *i*PrOH solvent-based aerogels is slightly higher for lower acid amounts (HCl:TTIP 0.11:1) and increases in a larger extent with the amount of acid used in the reaction mixture compared to EtOH solvent-based aerogels (cf. Table 5.2-8 and Table 5.2-9). That could explain higher shrinkage for *i*PrOH solvent-based gels.

The crystallization process occurs during aging, that is shown by *in-situ* Raman (Figure 5.2-42 and Figure 5.2-43) and *in-situ* WAXS experiments (Figure 5.2-44 and Figure 5.2-45). This is further discussed in chapter 6.3. It is suggested that the crystallization processes cause the shrinkage of the gels, especially for high TTIP:HCl ratios, due to the more ordered and denser arrangement of the Ti and O atoms due to crystallization. The increased crystallinity of *i*PrOH solvent-based aerogels could therefore lead to higher shrinkage compared to EtOH solvent-based aerogels. The higher crystallinity of *i*PrOH solvent-based gels is discussed in section 6.3.1 of the chapter ‘Discussion’.

6.1.3 Separation of Hydrolysis and Condensation Reaction

From the preliminary results in section 9.3 of the chapter ‘Appendix’ and further synthesized gels based on varying acid contents in section 5.1.1 of the chapter ‘Results’ the synthesis parameters were identified which give control about the gel formation. The separation and control of the hydrolysis and condensation reaction is important to achieve a homogeneous gel network. ^[103] If condensation reactions occur too fast and simultaneous to the hydrolysis reaction, the precursor might only partially be hydrolyzed and therefore the stability of the network is reduced, so that no 3D network can be formed. Without any presence of acid TiO₂ nanoparticles would precipitate. ^[31, 43, 99]

The decrease of the temperature to 0 °C, how it was performed in this work, reduces the general reaction rate. The addition of conc. HCl leads to an increased hydrolysis rate, whereas the condensation reaction is decreased with increasing amount of protons due to lower reactivity of hydrolyzed species and assumed complexation of chloride ions. Therefore, the hydrolysis and condensation reaction can be controlled separately in the developed synthesis route to achieve a homogeneous gel. The effect of coordinated and complexing chloride ions to reduce the condensation reaction was observed to differ for EtOH or *i*PrOH solvent-based gels, as the gelation times increase with the HCl content for EtOH solvent-based gels, whereas for *i*PrOH solvent-based gels the observed gelation times are shorter. The latter samples exhibit a limited control of the hydrolysis and condensation reaction rates, that is reflected in the pore size distribution from physisorption experiments, since the *i*PrOH solvent-based samples were opaque, exhibiting meso- and macropores, while EtOH solvent-based aerogels exhibited mesopores and were comparatively more transparent supporting a more homogeneous network formation (at HCl:TTIP ratio of 0.11:1). The physisorption results are discussed in section 6.2.2.

The addition of four to eight equivalents of water to the reaction mixture of *i*PrOH solvent-based gels increased the hydrolysis level, but also the condensation reaction rate, due to a very quick formation of many Ti-OH groups that condense quickly forming linked Ti-O-Ti bonds. In this case, the gelation is less controllable for *i*PrOH solvent-based gels. In contrast, for EtOH solvent-based gels, a high acid content (HCl:TTIP 0.22:1 to 0.33:1) led to long gelation times and broad pore size distributions. It is assumed that the high proton concentration makes the gelation controllable but dependent on the amount of chloride ions coordinated to the Ti center (more than two or three chloride ions), no homogeneous 3D network can be formed. However, a high water content (water:TTIP 8:1 to 12:1) besides a high acid content resulted in translucent gels with a narrow pore size distribution, indicating a homogeneous network formation even for short gelation times.

A higher solvent content (*e.g.* solvent:TTIP 35:1 to 45:1) decreases the condensation reaction rate, due to less collisions of Ti-OH groups and coordination of solvent molecules to the titanium-based precursor. The controllability of the reactions and gel formation is therefore increased.

6.2 Impact of Synthesis Parameters on Structural Properties

6.2.1 Appearance of Wet Gels and Aerogels

The EtOH solvent-based aerogels have generally a more transparent appearance compared to *i*PrOH solvent-based aerogels, as shown in the images of the wet gels and supercritically dried aerogels in Figure 5.2-2 to Figure 5.2-7. The *i*PrOH solvent-based aerogels have a translucent appearance for low amounts of acid and turn opaque in a similar trend compared to the EtOH solvent-based gels with increasing acid amount. The high transparency of EtOH solvent-based aerogels indicate small particle or pore sizes and a homogeneous pore size distribution. Less translucent aerogels indicate larger pores and a less homogenous pore size distribution which is evident from physisorption results (Figure 5.2-11). The slurry-like appearance for EtOH solvent-based gels with high acid content (sample E6) indicate that the precursor is not completely hydrolyzed or that a homogeneous 3D network cannot be formed.

The opaque appearance of the *i*PrOH solvent-based gels can be related to the very fast condensation reaction and the observed fast gelation time, as discussed in the previous section 6.1.1. According to literature, transparent or translucent gels require small mesopores and slow condensation reactions. ^[214] At a HCl:TTIP ratio of 0.11:1, the mesopores for *i*PrOH

solvent-based aerogels are larger and the samples exhibit a small fraction of macropores compared to EtOH solvent-based aerogels, which exhibited only mesopores, that could explain the non-transparent appearance of *i*PrOH solvent-based aerogels. Also, the secondary particle size in the wet gels is larger for *i*PrOH solvent-based gels compared to EtOH solvent-based gels, that is evident from SAXS results. The secondary particle size increases with the acid amount used in the reaction mixture, according to the SAXS results. *i*PrOH shows higher steric hindrance compared to EtOH, that could explain the larger pores. The introduction of HCl to the synthesis is suggested to cause chloride ions to coordinate to the Ti atoms, as elaborated in previous sections. The number of coordinated chloride ions therefore is expected to determine also the size of the titanium-based precursor, since chloride ions have a smaller ionic radius compared to the alkoxy ligands or solvent molecules. ^[218, 219] The titanium-based precursor showed to form differently sized clusters in literature. These clusters are found to be larger for TTIP compared to TTE. ^[43] As described previously, TTE forms if EtOH is added in excess to TTIP during the synthesis, due to ligand exchange (chapter 9.9). The addition of chloride ions to Ti atoms might change the size of these clusters dependent on the number of coordinated chloride ions and electrostatic attractive or repulsion forces.

The wet gels synthesized with low amounts of HCl exhibited a blueish color (samples E1, E2, *i*P1, *i*P2), that could be due to Rayleigh scattering at small particles or pores as well as due to structural defects *e.g.* Ti³⁺. ^[220] After drying, yellowish transparent or translucent aerogels were obtained. The color indicates the presence of alkoxy groups captured inside the pores, as reported in literature. ^[43]

The mixed solvent-based aerogel with an EtOH:*i*PrOH molar ratio of 1:1 exhibited a translucent and monolithic appearance after supercritical drying (Figure 5.2-8). This indicates that small and uniform pores are present. Also, the obtained monolith confirms a higher structural integrity and stability, since the other formed gels synthesized with pure EtOH, pure *i*PrOH, and other EtOH-*i*PrOH mixtures broke into fragments after supercritical drying. The order in which the EtOH and *i*PrOH is added to the titanium-based precursor could be important, since this step might influence which alkyl ligands coordinate to the titanium-based precursor. The ligand exchange from *Oi*Pr to *OEt* groups, confirmed by NMR measurements, is expected to change the reactivity of the precursor and therefore leads to a different network formation. It is assumed that only a few *OEt* groups are exchanged back to *Oi*Pr groups in the solvent molar ratio EtOH:*i*PrOH of 1:1, that stabilize the gel network. The EtOH solvent-based aerogels exhibit very small mesopores. With the introduction of some *Oi*Pr groups the pores would increase

slightly in size and could therefore compensate more stresses within the gel and stabilize the porous structure during supercritical drying. This is supported by physisorption results, which showed an increased pore size for the aerogel with a solvent molar ratio EtOH:*i*PrOH of 1:1, compared to the respective aerogel synthesized based on pure EtOH.

The calcined aerogels at 400 to 500 °C exhibited a white appearance (Figure 5.2-9), that is typical for crystalline TiO₂ powder. This indicates that no carbon residues are left in the material, since the brownish appearance of the calcined aerogel at 300 °C demonstrated a partial decomposition of carbon. The vacuum calcined aerogel at 300 °C exhibited a very dark black color but turned brownish when grinded, similar to the in air calcined aerogel at 300 °C (Figure 5.2-10). This color could be also due to thermally decomposing carbon residues, which remain in the aerogel. Also, it seemed that the dark color only appears on the surface of the aerogel fragments. This could indicate that the color stems from an amorphous layer on crystalline TiO₂ in core-shell structure as reported in literature.^[127]

6.2.2 Surface and Pore Characteristics

The specific surface area of the TiO₂ aerogel samples *i*P1, *i*P2, E1, and E2 (Table 5.2-1 and Table 5.2-2) is in the same range as reported elsewhere (466 to 733 m²·g⁻¹ for amorphous TiO₂ aerogels).^[25, 79, 80, 85] The supercritical drying process preserves the mesoporous structure of the synthesized TiO₂ aerogels, leading to the observed high values of the surface area and defined pore size distribution.^[10] The specific surface area is higher for EtOH solvent-based aerogels compared to *i*PrOH solvent-based aerogels (cf. Table 5.2-1 and Table 5.2-2). De Sario *et al.* reported that a higher precursor concentration (less solvent) led to a decrease in surface area.^[115] However, these observations could not be confirmed in this dissertation, since preliminary results based on different solvent:TTIP ratios (30:1 to 45:1) showed that the highest surface area could be obtained for a solvent:TTIP ratio of 35:1. Also, comparing the surface area of EtOH and *i*PrOH solvent-based aerogel, the differences cannot be assigned to the solvent:precursor ratio. The lower surface area for *i*PrOH solvent-based aerogels could be due to larger particles and pores for *i*PrOH, due to the ligand exchange of TTIP forming TTE, when EtOH is used (see chapter 6.1.1). Larger clusters of TTIP, compared to TTE, could lead to larger pores and pore volumes, due to steric hindrance. Large particles or pores contribute less to the surface area compared to small particles and pores.

It is assumed that HCl leads to many differently sized TTE or TTIP clusters dependent on the amount of HCl and therefore a varying number of coordinated chloride ions. The amount of chloride ions and the amount of water used during the synthesis is expected to determine the formed particle sizes which in turn affects the surface area. The specific surface area and pore volume decrease with increasing HCl content. Also, the pore sizes increase and the distribution becomes broader with increasing amount of HCl. This trend is observed for EtOH and *i*PrOH solvent-based aerogels (Figure 5.2-11 and Figure 5.2-13). However, the results of the aerogel sample E1 does not fit in this trend. This gel needs to be resynthesized and characterized again to check the results.

The results of the pore size distributions of EtOH and *i*PrOH solvent-based aerogels are in accordance with the optical appearance of the aerogels (cf. Figure 5.2-1 and Figure 5.2-5). The opaque appearance of the synthesized aerogels can be traced back to the broad pore size distribution when increasing the amount of acid used during the synthesis. When the pore size distribution is narrow the more translucent aerogels were observed, even with high amounts of acid (aerogel sample E4.1, Figure 5.2-3). In literature, a high transparency is generally related to small (smaller than the wavelength of vis light) and uniform pores in aerogels to minimize scattering. [221, 222]

The higher water amount used for the gel samples E4.1 to E6.1 could lead to a stronger condensation and crosslinking, as more groups are hydrolyzed. The high acid content slows down the condensation reaction, but at the same time a high hydrolysis rate is achieved, that could lead to a narrow pore size distribution. However, the gel samples *i*P4.1 and *i*P5.1 show a broad pore size distribution even at high HCl:TTIP and water:TTIP ratios, indicating fast hydrolysis and fast condensation reaction rates.

At very high acid amount, hydrolysis intermediates could be present which cannot condense due to the slowed condensation reaction in the case of EtOH solvent-based gels. This leads to a powder-like aerogel with a broad pore size distribution and macropores (aerogel sample E6, Figure 5.2-1 and Figure 5.2-11b). Also, differently formed molecules of the formula $Ti(OH)_{x-y}(Cl)_y$ after hydrolysis and coordination of chloride ions may lead to inhomogeneities during crosslinking, due to less condensing groups.

The decrease in surface area with increasing amount of acid could be due to the high degree of crystallinity. The reduced number of small mesopores could also explain the decreased surface area, as small pores contribute more to higher surface areas.

The aerogel sample *iP5* was aged between one and seven days, respectively and analyzed by physisorption measurements to investigate the impact of the aging on the physico-chemical properties, showing that the surface area and pore volume decrease steadily for longer aging times (Figure 5.2-15). Choi *et al.* reported that extended aging times between two and three days increased the pore volume and the pore size.^[25] These findings cannot be confirmed by the results of this work, since a decreasing pore volume was observed for sample *iP5* for extended aging times. Also, for low acid amounts, *e.g.* sample E2, very small mesopores were found even after the long aging process. The amount of acid and the type of solvent are found to have the greatest influence on the surface and pore structure. The observed crystallinity for the different aging steps in Figure 5.2-35 supports that the reduction of surface area and pore volume results from shrinkage and therefore from crystallization of the gel. Interestingly, the surface areas and pore volumes are still very high, compared to calcined TiO₂ aerogels reported in literature (102 to 157 m²·g⁻¹).^[79] The surface of the interconnected particles in the synthesized (semi-)crystalline aerogels is well accessible through the high porosity which is still maintained, confirmed by calculated porosity values from density measurements (cf. Table 5.2-4 and Table 5.2-5).

The surface area of the aerogel samples E4.1 to E6.1 seems to be independent of any change in HCl:TTIP ratio above 0.22:1 for high water amount, as the surface area is constant in the range of 269 to 290 m²·g⁻¹ (cf. Table 5.2-1) The pore volume and BJH value behave similarly. The similar values observed for the sample E4.1 to E6.1 could be due to the high crystallinity which remained unchanged at 100 wt.%.

The mixed solvent-based aerogels with low EtOH mole fractions exhibit higher values for the specific surface area compared to the aerogel samples E2 or *iP2*, whereas the pore volume lies in between the reference values of the aerogel samples E2 and *iP2* (Figure 5.2-17). Since EtOH was added first to the TTIP precursor it is assumed, that most *OiPr* groups are exchanged with *OEt* groups. After addition of *iPrOH* some *OEt* groups are exchanged back to *OiPr* groups. This could lead to a mixed particle-pore structure with small particles due to the *OEt* groups but also larger pores due to the *OiPr* groups, that make the surface of the particles better accessible for catalytic reactions. The pore sizes of the mixed solvent-based aerogels are between the two extremes of aerogels with pure EtOH (E2, 10 nm) and pure *iPrOH* (*iP2*, 50 nm) used in the synthesis, as shown in Figure 5.2-16. This indicates that a mixture of *OEt* and *OiPr* groups are attached to the Ti atom. For low EtOH mole fractions the pores are slightly larger compared to

high EtOH mole fractions as shown in the pore size distribution in Figure 5.2-16. This indicates that OEt group coordination at the Ti atom is dominant, but with increasing *i*PrOH amount the O*i*Pr groups are primarily coordinated to the Ti atom. The surface area varies between 610 and 660 m²·g⁻¹ for all mixed solvent-based aerogels, apart from the sample with the EtOH mole fraction of 0.5 of which the value for the surface area drops to lower values (590 m²·g⁻¹) (Figure 5.2-17). This aerogel sample with the EtOH mole fraction of 0.5 should be resynthesized and analyzed to verify the obtained value. The other mixed solvent-based aerogels exhibit slightly higher values for the surface area compared to the values obtained for the EtOH solvent-based aerogel E2 and to the *i*PrOH solvent-based aerogel *i*P2. The coordination of OEt groups to the titanium-based precursor lead to smaller pores according to the pore size distribution in Figure 5.2-16. Smaller pores contribute to a greater extent to a high surface area. The addition of even small amounts of EtOH to *i*PrOH dominated synthesis procedures can therefore increase the surface area.

The pore volume varies for high EtOH mole fractions but show a decreasing trend and approaching to reference values of E2, due to domination of OEt groups at the Ti atom (Figure 5.2-17).

The aerogel sample with the EtOH mole fraction of 0.5 exhibited a monolithic shape. The order of solvent addition to the titanium-based precursor might be affecting which solvent molecules dominantly coordinate to the titanium-based precursor. The ligand exchange from O*i*Pr to OEt groups was mentioned previously with excess of EtOH, leading to different reactivity of the precursor and therefore different network formation. Since EtOH is added to TTIP before the addition of the second solvent (*i*PrOH), it is assumed that only a few OEt groups are exchanged back to O*i*Pr groups, that stabilize the gel network. The EtOH solvent-based aerogels exhibit very small mesopores (Figure 5.2-16). With the introduction of some O*i*Pr groups the pores would grow slightly in size and could therefore compensate the stress within the gel and stabilize the porous structure during supercritical drying that could explain the monolith formation (Figure 5.2-8).

In addition to the BJH pore size distribution, the pore shape can be estimated from the behavior of adsorption and desorption branches of the physisorption isotherms. The BJH values for EtOH solvent-based aerogels for low amounts of acid (samples E1 to E3) are smaller compared to *i*PrOH solvent-based aerogels (samples *i*P1 to *i*P3) (cf. Table 5.2-1 and Table 5.2-2). The

isotherms for samples E1 to E3 show that the hysteresis closes at lower pressures, indicating ink-bottle shaped pores, whereas for samples *iP1* to *iP3* the hysteresis closes at higher pressures, indicating slit/cylinder shaped pores (Figure 5.2-11a and Figure 5.2-13a). For mixed solvent-based aerogels, the hysteresis also closes at higher pressures (Figure 5.2-16a). This indicates that EtOH causes the formation of very small necks that might be disadvantageous for the accessibility of reactants to the surface. Closed pores might also be present, which are not detectible with physisorption measurements.

In literature, TiO₂ aerogels are reported to be mainly amorphous and exhibit high specific surface areas. [25, 79, 80, 85] However, the synthesized aerogels in this work were partially or completely crystalline and exhibited higher values for the specific surface area compared to the crystalline aerogels calcined at 300 °C in the literature (102 to 157 m²·g⁻¹) or the calcined aerogels in this work (see section 5.2.2.4 of the chapter ‘Results’). [79] Therefore the theoretical specific surface area is calculated for completely crystalline anatase and brookite nanoparticles with crystallite sizes of 4 to 6 nm and 2 to 3 nm respectively, which were found in the present crystalline aerogels (cf. Table 5.2-8 and Table 5.2-9). The results showed that surface areas between 387 and 258 m²·g⁻¹ for anatase⁴ and between 484 and 726 m²·g⁻¹ for brookite⁵ can be achieved. For mixed anatase-brookite nanoparticles a theoretical specific surface area of approx. 440 m²·g⁻¹ (60 wt.% anatase and 40 wt.% brookite) is calculated. These theoretical values are compared to the experimental values of completely crystalline aerogels (cf. Table 5.2-8 and Table 5.2-9). The aerogel samples E4.1 to E6.1, with anatase and brookite crystals, exhibited surface areas between 269 and 290 m²·g⁻¹ and the aerogel samples *iP4* to *iP6*, also with anatase and brookite crystals, between 211 and 307 m²·g⁻¹ (cf. Table 5.2-1 and Table 5.2-2). The experimental values of the surface area fit into the range of the theoretical ones of anatase, but are slightly lower compared to the theoretical value of anatase-brookite mixed phase nanoparticles. This could be due to the loss of some surface area caused by connecting points of the particles in the network. Also, the crystalline aerogels exhibited some larger aggregates, that was shown from SAXS data (Figure 5.2-50 and Figure 5.2-53) and some remaining carbon residues, which could contribute to or reduce the surface area (cf. Table 5.3-2). This was neglected for the calculation and comparison to theoretical values. The

⁴ Anatase density (ρ)=3.88 g·cm⁻³, mass (m)= $\rho \cdot 4/3 \cdot \pi \cdot (0.5 \cdot d)^3$, d =crystallite size; Surface area (A)= $4 \cdot \pi \cdot r^2$

⁵ Brookite density (ρ)=4.13 g·cm⁻³, mass (m)= $\rho \cdot 4/3 \cdot \pi \cdot (0.5 \cdot d)^3$; d =crystallite size; Surface area (A)= $4 \cdot \pi \cdot r^2$

advantage of aerogels is that the 3D porous network makes the surface area of the particles and crystallites almost completely accessible in contrast to agglomerated crystalline nanoparticles.

The calcination of the aerogels in air led to a decrease in surface area and pore volume, as well as in an increase of the pore size with increasing temperature. This is in accordance with the results reported in literature for calcined aerogel samples. [76, 79] The increase in pore size could be explained by the small pores that fuse together forming larger pores. The calcination in air leads also to sintering of the TiO₂ aerogel and decomposition of organic residues. The sintering leads to a decreasing porosity and formation of larger particles or aggregates for calcination at 500 °C, as shown in SEM images (cf. Table 5.2-7 and Figure 5.2-26). Therefore, the specific surface area decreases due to lower porosity and larger particles.

The calcination in vacuum at 300 °C for two and four hours leads to a decrease in specific surface area and pore volume but to a lower extent compared to calcination in air (cf. Table 5.2-3). Interestingly, the pore size does not increase compared to air calcination. The oxygen deficient atmosphere during the vacuum heat-treatment could lead to less sintering in the sample, supported by SEM images (Figure 5.2-26 and Figure 5.2-27). Calcination in vacuum should not remove all carbon, since the carbon cannot be oxidized, as it is the case for calcination in air. Residual carbon on the particle surface can hinder recrystallization processes and pore fusion, as it blocks a part of the open surface sites. The isotherm of the non-calcined aerogel sample E2 revealed ink-bottle pores with smaller necks (Figure 5.2-11). Closed pores could be present which open during the calcination in vacuum or enlarge the necks of the pores, that could explain the unchanged pore size distribution of the vacuum calcined aerogels at 300 °C. In contrast to that, the calcination in air leads to sintering while the pores fuse together to form larger pores. The results also show that the calcination temperature determines the extent of surface area and porosity reduction, since there are neglectable changes for calcination durations between two and four hours in air and in vacuum.

6.2.3 Morphology and Particles Size

The porosity of the aerogels sample E1 to E6 varies between 77 and 83 % (Table 5.2-4), which is similar to values found for EtOH solvent-based aerogels from the literature. The literature values were also calculated from the measured skeletal density and pore volume. [223] The porosity values of the aerogel sample E1 to E3 show a decreasing trend with increasing amount

of acid (Table 5.2-4). However, the samples E4 to E6 do not obey this trend that could be due to the similarity in surface area and pore volume of these samples, evident from the physisorption results (cf. Table 5.2-1).

A similar behavior was observed for the *i*PrOH solvent-based aerogels (Table 5.2-5). The porosity values clearly decrease from aerogel sample *i*P1 to *i*P6 with increasing amount of acid used during the synthesis. The decreasing porosity can be explained by a denser arrangement due to crystallization of the aerogels, since the crystallinity increases from sample *i*P1 to *i*P6 (cf. Table 5.2-9). The porosity values calculated for *i*PrOH solvent-based aerogels are higher than that of EtOH solvent-based aerogels, for low HCl:TTIP ratios of 0.11:1 to 0.17:1. This could be related to the macropores and high pore volumes found for *i*PrOH solvent-based aerogels, since the porosity was calculated on the basis of the accumulated pore volume from physisorption results. The SEM images of the aerogels confirm, that the porosity is still available even for high crystallinities achieved with higher acid amounts used during the synthesis. The formation and larger proportion of macropores could explain the drop in the surface area and pore volume (cf. Table 5.2-1 and Table 5.2-2; Figure 5.2-20 and Figure 5.2-22). In contrast, calcined aerogels exhibit lower porosity values compared to crystalline aerogels synthesized with the HCl supported route, since sintering occurs during calcination (cf. Figure 5.2-26). The drop of the pore volume of crystalline aerogels synthesized with the HCl supported route is probably due to a shift of the pore size to very large macropores, which cannot be measured with N₂ physisorption measurements.

For *i*PrOH solvent-based aerogels a slightly higher solvent:TTIP ratio was used for the synthesis (35:1) compared to EtOH solvent-based aerogels (26:1), due to quick gelation. As shown in preliminary results, the solvent:TTIP ratio has no significant impact on the porosity (cf. Table 9.3-1 in the appendix).

From the SEM images it is evident that the porous structure is still present, but the fraction of macropores increases (Figure 5.2-20 and Figure 5.2-22). The porosity values decrease slightly with the amount of water for EtOH solvent-based aerogels (aerogel samples E4.1 to E6.1, cf. Table 5.2-4). With a high amount of water, a higher hydrolysis level is expected and therefore more connection points for the network can be formed and consequently less aggregation. This is also observed in the SEM images (Figure 5.2-21). Higher porosity values were therefore expected. However, the aerogel samples E4.1 to E6.1 were found to be completely crystalline compared to the respective samples E4 to E6 which exhibit a maximum crystallinity of 80 wt.% (cf. Table 5.2-8). This difference in crystallinity can lead to the observed lower porosity values

of the aerogel sample E4.1 to E6.1. A simultaneous increase of water and acid seem to compensate the pore enlarging effect due to the increased acid amount, so that mesopores could be achieved besides a high crystallinity.

The mixed solvent-based aerogels exhibit a higher calculated porosity of approx. 91 % compared to pure EtOH and pure *i*PrOH solvent-based aerogels (cf. Table 5.2-6). The higher porosity could be achieved due to small particles which stem from the expected formation of TTE precursor, due to ligand exchange, and slightly larger pores, due to some additional OiPr groups at the titanium-based precursor, as explained in chapter 6.2.2.

The calcination at 300 to 500 °C in air leads to a decrease in porosity with increasing temperature. Calcination of aerogels leads to a decrease in surface area and pore volume, but also to a loss of porosity, as the microstructure gets denser and larger particles appear, as confirmed by SEM images (Figure 5.2-26). However, the calculated porosity values cannot be compared to the non-calcined aerogel sample E2, due to the usage of denatured EtOH for these calcined aerogels, which alters the pore volume, as indicated in the appendix (cf. Figure 9.5-1). The usage of denatured EtOH, compared to absolute EtOH, led to a similar surface area, but larger pore size and pore volume. These observations are assigned to the additives in denatured EtOH as shown in Table 9.1-1.

The synthesis of samples E2-300-A and E2-300-V are based on the usage of absolute EtOH as solvent and can be compared to the non-calcined aerogel sample E2. In both cases the porosity decreases to 70 and 71 % respectively from 80 % for the aerogel sample E2 (cf. Table 5.2-4 and Table 5.2-7). These results show that the porosity is reduced to a larger extent for calcined samples compared to the non-calcined aerogels which were synthesized with high amounts of HCl. In both cases, with calcination and with the HCl-supported synthesis route, a high crystallinity was achieved (cf. Table 5.2-8 and Table 5.2-10).

The scattering curves (Figure 5.2-49 to Figure 5.2-54) show a curve progression and power-law exponent of the mid *q*-range typically found for aerogels, indicating a lamellar shape of the connected particles of the 3D gel network.^[208, 224] This supports a fractal structure of the TiO₂ aerogels, that is also evident from SEM and TEM images as shown in Figure 6.2-1. Also, the scattering curves bend at two different *q*-values, that can be associated with differently sized particles.

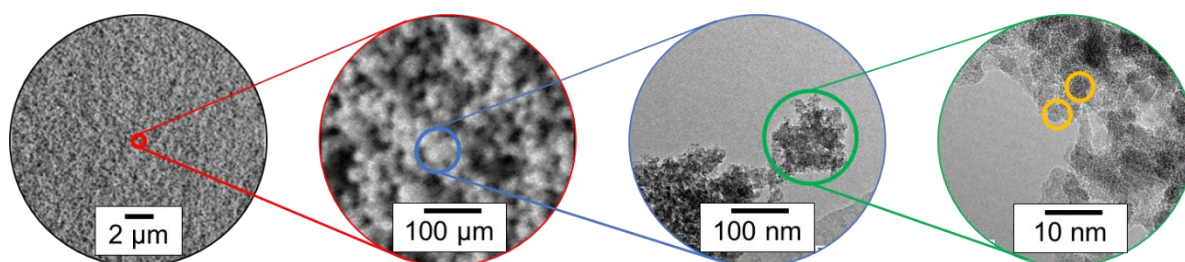


Figure 6.2-1: Scheme of fractal structures of aerogel sample E2 based on SEM and TEM images.

From the high magnification SEM images in Figure 5.2-24, it can be assumed that the secondary particle or aggregate sizes increase with increasing acid content from 23 to 32 nm for aerogel samples *iP2* and *iP5*. Slightly larger values for the aggregate/secondary particle size were found from SAXS data in the wet gel. For wet gel samples *iP2* and *iP5* secondary particles sizes are 29.5 nm and 44.4 nm respectively, assuming spherical particles (cf. Table 5.2-15). This could indicate slight shrinkage during the supercritical drying process. However, TEM images indicate a varying particle size between 20 and 60 nm for the aerogel sample *iP5* (Figure 5.2-31 and Figure 5.2-32). The particle size from TEM images could not be determined for all samples, since many particles were lying on top of each other, due to the interconnected structure and therefore only very few isolated particles were available for measurement.

In Figure 6.2-2 the relationship between solvent, acid amount and primary/secondary particle size is shown, based on the SAXS, physisorption and SEM results, which are described and discussed in the following.

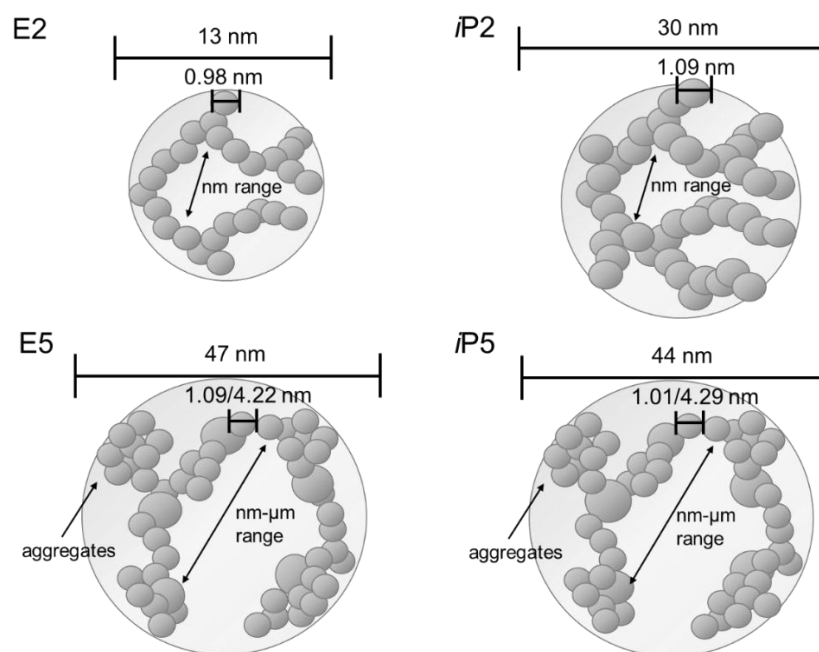


Figure 6.2-2: Scheme of possible 3D network of the aerogel sample E2, E5, *iP2* and *iP5*, showing the relationship between solvent, acid amount and its impact on the particle size.

The SAXS results showed that the Guinier radius/secondary particle size increases with the amount of acid for EtOH and *iPrOH* solvent-based wet gels (cf. Table 5.2-13 and Table 5.2-15). This indicates that a higher content of chloride ions leads to larger aggregates which are formed in the aerogel. However, it needs to be mentioned that the Guinier approximation is only valid for $q \cdot R_g < 2$. The calculated Guinier radii for high acid contents are near this limitation and might be inaccurate. For the wet gel samples E1 to E3 the Guinier radii are smaller compared to the wet gel samples *iP1* to *iP3*, that could support the assumptions that TTE forms smaller clusters but also that more chloride ions coordinate to the titanium-based precursor instead of alkoxy groups that would lead to smaller precursor molecules. The aging of E5 and *iP5* shows that the Guinier radius/secondary particle size only slightly increases during aging, indicating that further condensation to larger particles occurs. It is assumed that the high acid content and protonated species inhibit particle growth, so that the particle size remains small in the nano range below 70 nm. The primary particle size was found to increase from 0.93 to 1.13 nm for EtOH and decrease slightly from 1.10 nm to 1.01 nm for *iPrOH* solvent-based gels (cf. Table 5.2-13 and Table 5.2-15). The primary particle size seems to be slightly smaller when EtOH is used as solvent compared to TTIP in *iPrOH*. This could be due to a smaller cluster size. According to literature the TTIP cluster size in solution is approx. 1 nm.^[43] The literature value fits to the measured results of the primary particle size. Also, different precursor cluster sizes

were observed in literature dependent if TTIP or TTE was used. For TTIP 11 to 12 Ti atoms in the clusters were reported whereas for TTE only five to seven Ti atoms were reported, that causes slightly smaller cluster sizes.^[43, 225] This could explain the slight difference in primary particle size obtained from the SAXS results when using EtOH and *i*PrOH as solvent in combination with TTIP, due to the expected and previously explained ligand exchange from *Oi*Pr to OEt groups. The increase in size of the primary particles of the EtOH solvent-based gels with the acid amount (cf. Table 5.2-13) could be due to the small amount of water which is added with the aqueous conc. HCl solution. In literature, it was observed that partly hydrolyzed and condensed TTIP precursor can be achieved with very low amounts of water. The size of the titanium oxo cluster could therefore be adjusted with the added water.^[217] With an increasing amount of conc. HCl (37 wt.%) to the reaction mixture, the amount of water is slightly increased, too. But the total amount of water is very low in the reaction mixture at this point so that the precursor gets partly hydrolyzed and condensed on a very low level, that could therefore lead to different cluster sizes for the gel samples E1 to E6.

The pH value had no impact on the cluster size in water-based systems according to the literature.^[43] It can be assumed that the amount of water and the type of precursor play a major role for the primary particle size. The primary particle size for the wet gel sample E5 at different aging times showed no significant changes, but varying values between 1.02 nm and 1.15 nm (cf Table 5.2-14). For the wet gel *i*P5 primary particle sizes between 1.04 and 1.08 nm could be found at different aging times (cf. Table 5.2-16). Since no significant differences in primary particle size were found for EtOH or *i*PrOH solvent-based gels at high acid amounts, the impact of the water amount on the precursor cluster size might be larger than the impact of the different cluster sizes due to the precursor ligands (TTE or TTIP).

The decrease in size of the primary particles of the *i*PrOH solvent-based gels with increasing acid amount could be also due to the small amount of water which is added with the aqueous conc. HCl solution. However, the change in the particle size is very small, that could be due to the untypical strong decrease at high q values of the scattering curves and therefore inaccurate determination of the primary particle size. Probably too much background was subtracted of the scattering curves. But even without background subtraction a strong decrease at high q values is observed in the original measurements for all *i*PrOH solvent-based gels. Ideally, the measurements need to be repeated.

The particle sizes observed between 4.20 nm and 4.50 nm for EtOH solvent-based gels and 4.00 nm to 4.76 nm for *i*PrOH solvent-based gels (cf. Table 5.2-13 and Table 5.2-15) occurred

only for higher amounts of acid, that lead to higher crystallinity of the gels according to the WAXS and XRD results (cf. Table 5.2-8, Table 5.2-9, Table 5.2-13, Table 5.2-11). The sizes of the particles obtained from SAXS measurements fit to the determined crystallite size of anatase by the Rietveld refinement. This is supported by the SAXS experiments of the aging of wet gels E5 and *i*P5 (Table 5.2-14 and Table 5.2-16). The second curve bending at low q values of the scattering curves, and therefore particle sizes between 2.78 and 4.76 nm, was only observed after three days of aging demonstrating the starting point of crystallization. The fitting of the SAXS curves would give more detailed information on the particle size distribution. The curves of the wet gel samples E2 and E5 were fitted as an example (Figure 9.6-1 and Figure 9.6-2) and the resulting particle size distribution confirms the previous findings and evaluation of the SAXS curves. The results of the curve fits also show, that differently sized particles are present in the gel. The scattering curves of the other samples need to be analyzed and fitted but is out of the scope of this work. Also, the final aerogels could be investigated by SAXS to identify the differences in wet gels and supercritically dried aerogels and therefore the impact of the drying process on the pore and particle structure could be studied. It needs to be considered that the pores also contribute to the scattering curves. In literature, it was reported that for type-IV nitrogen adsorption behavior the pore sizes determined in physisorption experiments correspond to calculated pore size distributions from SAXS data.^[226] The pores and particles in a gel are not comparable with a diluted solution of particles, so that it might not be possible to distinguish between particles or pores for the determined particle sizes of a distribution (or the values determined in this work from the scattering curve). This needs to be further investigated.

From the Kratky- and Porod-Debye-plots (Figure 5.2-50 and Figure 5.2-53) it can be concluded that the flexibility and disorder of the network increases with the amount of acid. The observed trend of the curve shape for increasing amount of acid is similar for EtOH and *i*PrOH solvent-based gels. Similar curve shapes were reported for other gels and protein folding.^[227-229] The increased flexibility and disorder of the gel network at high HCl amounts, used during the synthesis, could be due to a lower condensation level and a lower possibility to form a 3D network. Longer chains and less connecting points as well as an inhomogeneous crosslinking of chains make the network more flexible and increase the disorder. Therefore, some compacter and some looser parts could be present in the gel network. The Kratky plots of gels with high acid content exhibit also a distinct peak at low q values before reaching a plateau. The plateau indicates full flexibility of the network, but the additional peak indicates spherical rigid

aggregates or particles in the network which are much denser compared to the other parts of the gel. This curve shape was reported in literature for polymers with compact chain conformations, [229] supporting the assumption that larger aggregates are occasionally formed for higher HCl amounts for EtOH and *i*PrOH solvent-based aerogel.

6.3 Impact of Synthesis Parameters on Crystallinity and Phase Content

6.3.1 Crystallinity

The XRD results revealed that the crystallinity of the supercritically dried aerogels increases with the acid content for both used solvents during the synthesis, EtOH and *i*PrOH (Figure 5.2-33 and Figure 5.2-34). The *i*PrOH solvent-based aerogels exhibited complete crystallinity for a high acid content, whereas for EtOH solvent-based aerogels a maximum of 84 wt.% crystallinity could be achieved (cf. Table 5.2-8 and Table 5.2-9). The high crystallinity was also confirmed by TEM results, where many crystallites, lying on top of each other (Moiré pattern), could be identified (Figure 5.2-31 and Figure 5.2-32). Also, the structured surface of the particles indicates crystalline phases and phase transitions. Compared to literature, other reported aerogels were mainly amorphous. [25, 85] Some occasional anatase crystallites in TiO₂ aerogels were observed in non-calcined aerogels when using HNO₃, in literature. However the degree of crystallinity is rarely determined and reported in literature. [85, 223] The observation of very few crystallites in a mainly amorphous structure is because of the increased tendency for TiO₂ to form crystalline phases compared to silica, as elaborated in section 2.3.3 of the chapter ‘State of the art’. Ti is mostly 6-fold coordinated and the [TiO₆] units are connected by edge sharing. The degree of freedom is lower for the long-range ordered octahedra compared to corner-shared [SiO₄] tetrahedron. [100] The synchrotron WAXS and *in-situ* Raman results showed, that already in the wet gel the crystallization starts leading to high degrees of crystallinity (Figure 5.2-42, Figure 5.2-43, Figure 5.2-44, Figure 5.2-45). It is important to consider the solvent-removal approach or drying process of synthesized TiO₂ materials, such as for TiO₂ nanoparticles or gels synthesized using the sol-gel process. In literature, crystallization is mainly described to occur during drying at room temperature, during calcination of TiO₂ powder at higher temperatures or supercritical drying in solvents at high temperatures and pressures, as explained in more detail in section 2.1.3 of the chapter ‘State of the art’. However, this leads to an overestimation of crystallinity of the as-prepared (non-dried) sample. [37] For the wet gel sample *i*P5, the *in-situ* Raman results show an increase in intensity of the anatase band between three and four days of aging (Figure 5.2-43b). However, this

method is less sensitive compared to XRD and therefore might be inaccurate for determining the exact crystallization starting point. On the contrary, the performed synchrotron WAXS experiments exhibit a very high accuracy and resolution, due to the high sample-to-detector distance and the high beam energy of 75 keV and therefore a high photon flux. These results show that already after two days distinctive reflections appear in the diffractograms in Figure 5.2-45 and Figure 5.2-46, but the main crystallization occurs between three and six days. This fits to the high shrinkage that was observed for the wet gel *iP5*, caused by the denser arrangement due to crystallization (Figure 5.1-2).

Different solvent:TTIP ratios (30:1 to 45:1) used for the synthesis of the aerogel samples *iP7.1* to *iP7.5*, *iP8.1* to *iP8.5* and *iP9.1* to *iP9.5* had no significant impact on the crystallinity showing that the precursor concentration plays no significant role for the crystallization process (Figure 9.3-5 and Figure 9.3-6).

For the dried and wet gel EtOH solvent-based sample E5 similar trends for the crystallinity and crystallization starting point were found from *in-situ* Raman and XRD/WAXS results (Figure 5.2-42, Figure 5.2-44, Figure 5.2-33). However, the crystallinity increases slower with the amount of acid compared to *iP5* (cf. Table 5.2-9 and Table 5.2-8), that leads to an overall lower crystallinity in the wet gel and supercritically dried aerogel when EtOH is used as solvent (cf. Table 5.2-8). The type of solvent and solvent viscosity might influence the nucleation and growth of crystallites and therefore the crystallization process. ^[230]

A comparison of the WAXS diffractograms and Rietveld results of the wet gel and supercritically dried aerogel sample *iP5* shows, that after gel aging between one and seven days, respectively, the achieved crystallinity is similar in the wet gels and dried aerogels, indicating that the supercritical drying process has no significant impact on the crystallization or nucleation process as well as on the achieved final crystallinity of the aerogel samples (cf. Table 5.2-9, Table 5.2-12, Figure 5.2-35). The nucleation and main crystallization of the gels occur in the wet sample during aging.

In TEM analysis, much more crystalline parts could be identified for the aerogel sample *iP2* compared to E2, which were both synthesized using the same HCl:TTIP ratio of 0.11:1 (cf. Table 9.2-1 and Table 9.2-2). The crystallites were homogeneously distributed, as shown in the DF-TEM image in Figure 5.2-30. The higher crystallinity achieved for the *iPrOH* solvent-based aerogels might be caused by large particles leading to more collisions favoring nucleation, which form during condensation reaction of the TTIP precursor cluster, which should be larger compared to the assumed TTE cluster (by ligand exchange) in EtOH solvent-based reactions

(cf. Table 5.2-8 and Table 5.2-9). Also, the higher reactivity found for *i*PrOH solvent-based gels could be a reason for the stronger tendency to crystallize, due to increased stresses in the gel that favors the rearrangement of the TiO₂ octahedra. ^[112]

The SAXS data showed that only for a low acid amount used during the synthesis, the secondary particle size is smaller for EtOH compared to *i*PrOH solvent-based wet gels. For a higher acid amount, the secondary particle size is similar for EtOH and *i*PrOH solvent-based wet gels (cf. Table 5.2-13 and Table 5.2-15). Generally, the secondary particle size increases with the amount of acid. However, the analysis of primary particle size and the determined bends of the SAXS curves are quite inaccurate, as explained above. Smaller details and changes in the primary particle size might not be detected for the assumed formation of TTE and TTIP clusters and their respective sizes. The fitting of SAXS curves and particle size distribution would give more information on the aerogel structure to determine subtle differences in the particle sizes in the nano range. However, the strong decrease at high *q* values for scattering curves in Figure 5.2-52 makes the curve fitting difficult and only up to *q* values before the steep curve ending. Very small particles might therefore not be detected.

The EtOH solvent-based aerogels which were synthesized with an increased amount of acid and water (samples E4.1 to E6.1, cf. Table 9.2-1) exhibited complete crystallinity compared to EtOH solvent-based aerogels with lower amount of water (samples E4 to E6, cf. Table 9.2-1). Also, brookite was identified besides anatase in the aerogel samples E4.1 to E6.1 with weight fractions of 62 wt.% anatase and 38 wt.% brookite (Table 5.2-8). An increased water content, used during the synthesis to initiate the hydrolysis reaction, could lead to more hydroxyl groups (Ti-OH) on the surface of the particles which form the gel network and therefore create more interfacial forces that could lead to a reinforced rearrangement of octahedra during aging of the wet gels and therefore higher crystallinity.

The Raman spectra confirm the increasing crystallinity with the HCl amount used during the synthesis for the EtOH solvent-based and *i*PrOH solvent-based aerogels (Figure 5.2-38 to Figure 5.2-40). For a low HCl amount used during the synthesis, very broad bands were found while for increasing amounts the bands appeared to be more distinctive and can be assigned to anatase and brookite. Comparing the amorphous aerogel sample E1 and *i*P1, the Raman bands are more pronounced for sample *i*P1, demonstrating the higher tendency of *i*PrOH solvent-based aerogels to crystallize or rearrange to higher structural order.

The calcination of the aerogel sample E2 at 300 °C in air led to completely crystalline samples (Table 5.2-10). The Rietveld refinement showed that calcination at 300 °C for two hours is enough to completely crystallize the aerogel. Longer calcination times show no difference in crystallinity but an increase in crystallite size with increasing temperature and reduction of carbon content due to oxidation. Longer exposure times at higher temperatures alter the microstructure due to stronger sintering and crystal growth, that was evident from SEM images and Rietveld results (Figure 5.2-26, Table 5.2-10). In contrast, the calcination in vacuum led to lower crystallinity compared to the calcination in air (Table 5.2-10). Also, the crystallite size is smaller for the vacuum treated sample compared to air calcination. This indicates that the nucleation and crystal growth is hindered in vacuum conditions. It is expected that the remaining carbon from the gel synthesis cannot be removed by calcination of the aerogels in vacuum as easily as in the case of air calcination, due to less oxidation of the carbon. Residual carbon on the particle surface probably hinders the crystallization processes and pore fusion, as it blocks a part of the open surface sites.

6.3.2 Crystallite Size and Crystal Growth

The anatase crystallite size of all non-calcined aerogel samples, based on usage of EtOH and *i*PrOH as solvent during the synthesis, are similar between 4 and 5 nm, whereas the brookite crystallite size is approx. 2 to 3 nm (Table 5.2-8 and Table 5.2-9). The values are constant for different reaction conditions (HCl:TTIP or water:TTIP ratios). The observed small crystallite size can be explained by the large amount of solvent. Small crystals tend to agglomerate to larger particles and to decrease surface area, according to literature.^[231] The solvent allows crystals to grow but prevents aggregation.^[106, 108] From the *in-situ* WAXS results of the wet gel sample *i*P5 it is shown that the starting point of crystallization is below 72 hours of aging (Figure 5.2-46). The intensity of the reflections in the diffractograms for anatase and brookite increase both from the beginning of the *in-situ* measurement (Figure 5.2-47). This indicates that anatase and brookite formation occurs simultaneously and disagrees a suggested phase transformation from anatase to brookite by the dissolution-precipitation mechanism in literature.^[48] The *in-situ* WAXS experiments show, that the intensity of the anatase reflection increases faster compared to the brookite reflection. This indicates that anatase formation occurs more likely and that the brookite crystals grow much slower compared to anatase. This is supported by the smaller crystallite size of the found brookite crystals compared to anatase (Table 5.2-8 and Table 5.2-9).

The Raman spectra confirm the small crystallite size for the EtOH and *i*PrOH solvent-based aerogels determined from XRD results (cf. Table 5.2-8 and Table 5.2-9; Figure 5.2-38, Figure 5.2-40). Swamy *et al.* reported broad Raman bands for small crystallite sizes of 4 nm and narrow bands for crystallite sizes of 20 nm.^[203] Thus, the nanosized crystals of 4 nm found for the aerogel samples E2 to E6 and *i*P2 to *i*P6 explain the observed broad Raman bands in Figure 5.2-38 and Figure 5.2-40. The bands of the aerogel samples E5 and *i*P5 are broader compared to calcined aerogel samples which exhibited a larger crystallite size even for comparable crystallinity (Figure 5.2-41). Kelly *et al.* reported a band shift (blue shift) and band broadening for small crystallite sizes compared to large crystallite sizes.^[202] This blue shift, observed in literature, can also be observed especially for the calcined aerogel samples in Figure 5.2-41. The $E_{g(1)}$ bands shifts (blue shift) from 150.6 cm^{-1} of the non-calcined sample E2 to 141.3 cm^{-1} of the sample E2-A-500-10h that matches the increase in crystallite size.

6.3.3 Crystallization Process and Phase Content

Besides the achieved degree of crystallinity, which varies for EtOH and *i*PrOH solvent-based aerogels dependent on different synthesis parameters, also different phases are formed. In this section the origin of the differently formed phases is discussed as well as different crystallization approaches.

From the XRD diffractograms of the aerogels in Figure 5.2-33 only anatase was identified for EtOH solvent-based aerogels (samples E1 to E6), independent on the used amount of acid during the synthesis. The TEM results and measurement of d-spacing of the aerogel sample E2 confirmed the formation of anatase crystals (Figure 5.2-28). Whereas, anatase and brookite were identified, if the water content was increased simultaneously to the acid content for the aerogel sample E4.1 to E6.1 (Figure 5.2-33). If *i*PrOH is used, brookite was found in most samples with an increased amount of acid (sample *i*P4 to *i*P6, Table 5.2-9), as well as for an increased amount of water (sample *i*P4.1 to *i*P6.1, Table 5.2-9). The presence of brookite and anatase crystals was confirmed by TEM analysis (Figure 5.2-29) and Raman spectroscopy (Figure 5.2-40). From d-spacing measurements of the present crystallites, anatase and brookite was identified already for the aerogel sample *i*P2, which was synthesized with low acid concentrations (cf. Table 9.2-2). In XRD results brookite was only found for increased acid concentrations, however, the main brookite reflections overlap with the anatase reflections and broad reflections of the remaining amorphous content that makes it difficult to determine

brookite from XRD results in semi-crystalline TiO₂ aerogels, *e.g.* *iP2* or *iP3* with amorphous halos (Figure 5.2-34).

The phase content varies between 58 and 64 wt.% anatase and between 36 and 42 wt.% brookite. The brookite fraction increases slightly with the acid content. Similar anatase and brookite weight fractions of 65.2 and 34.8 wt.% respectively, were found in literature for a xerogel dried at 100 °C in air. ^[49] For the in air and vacuum calcined samples of this work, only anatase was identified, which is the expected phase below calcination temperatures of 500 °C, since the transition to rutile occurs at higher temperatures above 700 °C, according to literature and explained in more detail in section 2.1.2 of the chapter ‘State of the art’. ^[30]

Brookite was observed in literature for calcined TiO₂ nanoparticles, which were synthesized *e.g.* by precipitation, followed by peptization and a calcination step. ^[232] The Ostwald’s Rule of Stages ^[233] might also be applicable to the synthesis procedure developed in this work, so that the formation of the metastable anatase and brookite phases is kinetically favored during the extensive aging process at 50 °C performed in this work, instead of rutile.

Anatase is thermodynamically favored for small crystal sizes (smaller than 11 nm), ^[36, 203] that could be a reason for the present phases in the synthesized aerogels. In the present work crystallite sizes below 10 nm were found, that would support the formation of anatase and brookite instead of rutile (Table 5.2-8 and Table 5.2-9). Anatase can also transform to brookite dependent on the initial particle size, as it determines the thermodynamic phase stability for nanocrystalline systems. ^[35] From the SAXS curves in Figure 5.2-49 and Figure 5.2-52 no significant differences in the primary particle size are found for an increasing acid amount used to synthesize the gels. However, the pore size is larger for *iPrOH* solvent-based aerogels compared to *EtOH* solvent-based aerogels. A dependency of the phase formation on the surface area was also described in literature. ^[35] However, from the obtained results, it is unlikely that the surface area or pore size affects the phase formation. Anatase and brookite were found in *iPrOH* solvent-based aerogels with broad pore size distributions and mainly macropores. For some *EtOH* solvent-based aerogels with narrow pore size distributions and mesopores (E4.1 to E6.1, Figure 5.2-33) also anatase and brookite were observed. Therefore, no clear dependency of the pore size on the obtained phase was observed from these samples. However, the amount of solvent or fluid that infiltrates the pores in the wet gels is different for small mesopores compared to large macropores. The solvent plays an important role in the formation of different phases of the aerogels as shown in the different XRD results in Figure 5.2-33 and Figure 5.2-34. The adsorption of solvent molecules to the particle surface in the pores could be therefore

different, due to the pore size that could affect the nucleation and phase formation. This needs to be studied in further experiments.

The choice of solvent, the amount of water, and the amount of acid used to synthesize the gels were identified to be crucial for crystallization of the wet gels. Therefore, there are three variables in the synthesis and aging process that might change the crystallization conditions and thus lead to different phase content of the gels: the amount of coordinated chloride ions, the amount of protons and the amount of water in the gel. The used solvent affects the mentioned variables, *e.g.* the coordination of chloride ions due to different steric hindrance. *OrPr* groups bound to the titanium-based precursor exhibit a higher steric hindrance compared to *OEt* groups. This could enable more chloride ions to coordinate to the Ti atom at high HCl concentrations in the reaction mixture. As described previously, Ti(OR)_4 can interact by vacant d-orbitals with Lewis bases or with compounds, which have a lone pair of electrons. This results in titanium with higher coordination number.^[99, 102] Since Ti is able to form complexes which are 5- or 6-fold coordinated, a few chloride ions could coordinate.^[99, 100] Chloride ions exhibit more than one lone pair that makes the coordination and formation of different complexes with bridging chloride ions possible.^[212, 213] These different complexes could serve as templates for the formation of different phases.^[40] In this work, the coordination of chloride ions to the titanium-based precursor is assumed, since Ti-Cl compounds were identified in XRD and XPS measurements (Figure 5.2-37 and Figure 5.3-2). As mentioned in chapter 5.2.5.4, during synthesis of EtOH solvent-based aerogels, a white precipitate is formed several minutes after the addition of HCl to the reaction mixture (TTIP and solvent). This precipitate was further analyzed using XRD (Figure 5.2-37). The reflections in the diffractogram fit to a titanium hydroxido chlorido complex, besides anatase and brookite, that suggests the formation of a similar complex compared to the literature for the appearing precipitates during the synthesis (literature reference reflections positions and PDF numbers are shown in Figure 5.2-37). The precipitates dissolved again after the dropwise addition of water, that led to a change in polarity and a possible change in the complex structure due to the additional water molecules. Also, the XPS measurements revealed the presence of titanium chlorides in the Cl2p XPS spectrum (Figure 5.3-2). Two peaks appear for the XPS Cl2p spectrum due to the spin-orbit splitting.^[234] Cao *et al.* assigned the two signals in the Cl2p XPS spectrum to Ti-Cl and Ti-Cl-Ti bonds, respectively, due to physical adsorption on the surface and the introduction of Cl into the TiO_2 lattice at the place of oxygen.^[209] Cl introduction into the TiO_2 lattice was also reported

elsewhere. ^[235-237] For this work it is suggested that a complex is formed due to the HCl addition by coordination of chloride ions to the Ti atom that serves as template for different phases. The adsorption of chloride ions on the surface of the TiO₂ particles is expected during the gel synthesis, but also the introduction of Cl into the TiO₂ lattice due to the crystallization based on the complexes. This is supported by the UV-vis absorption spectrum of the aerogel sample E5 (HCl:TTIP 0.27:1) compared to the aerogel sample E2 (HCl:TTIP 0.11:1) in Figure 9.8-1 that shows a tailing absorption edge and a slightly elevated curve in the vis range, indicating a small shift of the absorption to the UV-vis range, that could be due to Cl doping. This shift in the UV-vis absorption spectrum was also reported in literature. ^[237] On the basis of literature reports, two possible structures of this intermediate titanium hydroxido chlorido complexes are proposed and shown in Figure 6.3-1, similar to the proposed complex structure of Pottier *et al.* ^[40] and Wu *et al.* ^[213]. The complex structure investigated by Wu *et al.* was reported on the basis of reactions between TiCl₄ and Ti(O*i*Pr)Cl₃ with *i*PrOH and crystallizes in the orthorhombic space group Pbc_a, similar to brookite. ^[206, 213] Larger clusters of these structures (with Ti-Cl-Ti; Cl as bridging ligand) and (partially) hydrolyzed species also might be possible to occur in the synthesis of the TiO₂ aerogels in this work. Cl could be introduced by physical adsorption on the surface or at the place of hydroxyl groups. The alkoxy ligands could also be exchanged by other ligands (*e.g.* H₂O) or (partially) hydrolyzed before coordination of the chloride ions due to steric reasons.

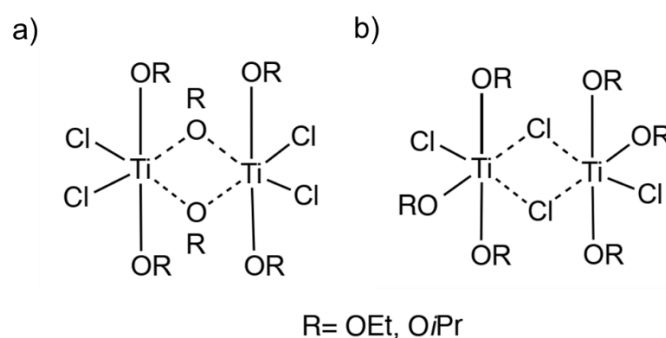


Figure 6.3-1: Possible intermediate titanium hydroxido chlorido complex a) a dimer of two pentacoordinated titanium atoms, connected by two alkoxy bridges and each coordinated to two chlorido ligands, b) two titanium atoms with Cl as bridging ligand.

It is expected that a different number of chloride ions coordinate to the Ti atom dependent on the used solvent, due to steric hindrance. With lower steric hindrance of the OEt groups at the titanium-based precursor (using TTIP and EtOH), a higher number of chloride ions is assumed to coordinate to the Ti atom. The coordination of chloride ions is also dependent on the ligand strength and ligand concentration in the reaction mixture. ^[212, 213] A higher number of coordinated chloride ions instead of OEt groups would lead to less hydrolysable groups at the precursor and therefore a lower ability to form of a 3D network. Instead longer chains rather than crosslinking of the condensed precursor is expected. This supports the previous findings. The EtOH solvent-based wet gel E6 (HCl:TTIP 0.33:1) exhibited a slurry-like appearance after aging instead of a stable monolith (wet gel) as observed for the aerogel sample E2 (HCl:TTIP 0.11:1) with lower acid amounts (Figure 5.2-2). The dried aerogel E6 exhibits a more powder-like white appearance, supporting the theory that a higher number of chloride ions are coordinated to the titanium atom, which affects the gelation and crosslinking of the 3D network (Figure 5.2-1). The complexing effect of chloride ions can reduce the condensation reaction similar to reports from literature, ^[103] which is generally favorable to separate and control the hydrolysis reaction, but leads also to extended gelation times for EtOH solvent-based gels with increasing amount of chloride ions/HCl in the system, as observed in this work (Figure 5.1-1). The assumption of a hindered condensation reaction due to coordination of chloride ions is supported by the SAXS results, especially in the Kratky plots, which show an increasing flexibility of the network with the acid amount used for synthesis (Figure 5.2-50). This supports a lower condensation level and lower possibility to form a 3D network, due to complexing chloride ions. Longer chains and less connecting points of the chains are assumed which make the network more flexible. Also, the very broad pore size distribution in Figure 5.2-11b for high HCl:TTIP ratios indicates that a varying number of chloride ions is coordinated to the Ti atoms that lead to changed condensation reactions and therefore an inhomogeneous network. Besides chloride ions, solvent and water molecules can coordinate to the Ti atom, that changes the behavior of the formation of precursor clusters. ^[99] As reported in literature, the precursor cluster size of TTE is smaller compared to TTIP. ^[43] With the introduction of chloride ions or coordination of other solvent or water molecules the size of the molecules would change and therefore the pore size. This could explain that the pore size distribution of EtOH solvent-based aerogels gets broader with increasing HCl content in the synthesis and that the aerogels exhibit an opaque appearance with increasing acid amount (Figure 5.2-11 and Figure 5.2-1).

Pottier *et al.* suggested different complexes as precursor which form on a water-based synthesis using TiCl_4 and NaCl .^[40] They suggested $[\text{Ti}(\text{CH}_2\text{Cl}_3(\text{OH}_2)]^-$ and $[\text{Ti}(\text{OH})_2\text{Cl}_4]^{2-}$ which form at higher chloride content and lead to anatase. Brookite formation was traced back to the formation of the following complex $[\text{Ti}(\text{OH})_2\text{Cl}_2(\text{OH}_2)_2]^0$. The presence of helper ions such as NaOH ,^[39] other alkali ions,^[41] pH during hydrothermal processes^[42] or chloride ions^[40] have been reported to support brookite formation based on titanium(IV) precursor, such as TiCl_4 in an aqueous synthesis. The suggested complexes by Pottier *et al.* support that for EtOH solvent-based aerogels only anatase is formed, probably due to a higher number of coordinated chloride ions, whereas for *i*PrOH a lower number of chloride ion can coordinate due to higher steric hindrance, that leads to brookite formation. This is supported by short gelation times observed in this work for *i*PrOH solvent-based gels, whereas for EtOH based gels the gelation time increases with the acid amount and therefore condensation reaction is slower (Figure 5.1-1 and Figure 5.1-2).

The number and conformation (cis or trans) of coordinated chloride ions at the titanium-based precursor could favor the arrangement of edge sharing octahedra, leading to anatase or favor the arrangement of edge and corner sharing octahedra, leading to brookite. This could be affected by the used solvent and the steric hindrance and therefore possible different conformation of coordinated chloride ions. This is exemplary shown in Figure 6.3-2.

The XPS results show a higher percentage of chlorine for EtOH solvent-based aerogels than for *i*PrOH solvent-based aerogels as well as for higher HCl amounts used in both synthesis procedures (*i*PrOH and EtOH solvent-based), supporting different complex formation (cf. Table 5.3-2). The percentage of Cl content is much lower compared to the found Ti percentage. The proposed reaction mechanism of Pottier *et al.* suggested that the chloride ions are eliminated in further steps of the condensation reaction under release of HCl.^[40] This could indicate that a similar reaction mechanism is present in the developed synthesis, eliminating most of the chloride ions, but leaving a few chloride residues. However, it is not clear, if the stated complex can be formed and if the proposed mechanism is valid in the case of the developed synthesis route, since by Pottier *et al.* used TiCl_4 in their study. The hydrolysis and condensation reactions of metal salts in aqueous solutions are more complex compared to alkoxide reactions.^[238] Further analytical studies are required to reveal the structure of the formed complexes in the developed synthesis. It is also not clear if only the chloride ions from HCl influence the reactions, since the amount of protons increase with the amount of HCl.

The formation of crystalline structures from chloride precursors was also suggested in literature by the partial charge model and change in pH value, ^[238] which is the second variable in the proposed synthesis of this dissertation. Complexes such as $[\text{Ti}(\text{OH})_x(\text{OH}_2)_{6-x}]^{(4-x)+}$ undergo hydrolysis and condensation reactions forming agglomerates and finally crystalline structures. ^[21] Different steric hindrance and polarity lead to different complexes, which were regarded responsible for different phases. Different pH values in water-based systems or different concentration of protons in solvent-based systems could therefore lead to anatase, rutile, or brookite. However, some researchers reported rutile formation for low pH values or high proton concentrations, whereas higher pH values or low proton concentrations lead to anatase. Others reported for TiO_2 nanoparticles, which were synthesized by precipitation approach from TiCl_4 and further calcination for two hours at $450\text{ }^\circ\text{C}$, that brookite formed at pH values from 6 to 2, with increasing brookite fraction at lower pH values. ^[206] Li *et al.* reported anatase and brookite formation at high HCl:Ti ratios. ^[28] These observations fit to the *i*PrOH solvent-based aerogels in this dissertation, since an increasing weight fraction of brookite was found for higher amount of HCl. For very high amounts HCl even small amounts of rutile were found (cf. Table 5.2-9). The amount of protons could be equivalent to the pH value, however differences are expected as the synthesis procedures reported in literature are water-based in contrast to the solvent-based synthesis procedure in this work.

The observed crystallization of the EtOH and *i*PrOH solvent-based gels with increasing acid content (Figure 5.2-44 and Figure 5.2-45), could be explained by another crystallization mechanism which was proposed by Nikannen *et al.* They developed a two-step synthesis of TiO_2 powder synthesized from TTBT, *i*PrOH and water. The precipitated powder was exposed to different HNO_3 /water mixtures at $50\text{ }^\circ\text{C}$, dried at $50\text{ }^\circ\text{C}$ and calcined. They suggested that the protons of the acid charge the surface of the precipitates, leading to increased repulsion forces. They assumed that a rearrangement of the octahedra occurs while aging the particles, due to weak bonds of amorphous precipitates. They stated that, higher repulsion forces can be achieved with more protons, thus more acid to separate octahedra. During aging, the octahedra condense again together (corner and edge sharing), so that anatase or other crystal structures are formed. ^[31, 239] This approach could be applicable to the aging process of the TiO_2 gels in this dissertation.

The third variable, which affects the crystallization process, is water added to the reaction mixture in the last step of the reaction. An increased amount of water simultaneously to

increased acid content, led to anatase and brookite formation also for the EtOH solvent-based aerogels. Whereas for low amounts of water only anatase formation was observed (Table 5.2-8). This agrees to the observations from literature, where in solvothermal processes for low H₂O:Ti ratios anatase was favored, whereas for high water contents brookite was found as by-phase, due to formation of the previously mentioned complex as precursor. [28] This supports the assumption that the complex formation is different for the aerogel samples E4 to E6 compared to the aerogel samples E4.1 to E6.1. A high amount of water in the reaction mixture could lead to coordination of water molecules to Ti atoms and therefore fewer coordinated chloride ions. This would lead to faster condensation reaction and higher condensation level, supported by the shorter gelation times and increased stability for the samples E4.1, E5.1 and E6.1 compared to E4, E5 and E6, as described in section 5.1.1.1 of the chapter ‘Results’.

Nikannen *et al.* showed in a different study that a high amount of water during synthesis led to crystalline anatase-brookite powder. [240] Benčina *et al.* observed a similar effect of water during a hydrothermal treatment. Amorphous TiO₂ was exposed to water vapor leading to rearrangement of octahedra to anatase. [48] They suggested a dissolution–precipitation mechanism, where water vapor helps to rearrange of octahedra and leads finally to nucleation and crystal growth. [48]. This supports, that brookite was found for the aerogel samples E4.1 to E6.1 when using high acid and water contents, whereas for high acid contents and stoichiometric water content (samples E2 to E6) only anatase can be found.

However, the crystallization mechanisms reported in literature only refer to TiO₂ nanoparticles. It is expected to be different for aerogels than for nanoparticles, as they have a chemically connected 3D structure and the aerogels are not exposed to high temperatures and pressures compared to calcination or hydrothermal processes. The aerogels are not ambiently dried, that already leads to crystalline phases.

The crystallization mechanism occurring during gel aging in this work cannot completely be accredited to one of the proposed reaction mechanisms for TiO₂ nanoparticles in the literature explained in this section. It is believed that the crystallization mechanism and phase formation is a mixture of complex formation with chloride ions and water acting as template or intermediate precursor for the respective phases. The influence of protons is equally important which initiate the crystallization during aging, since the crystallization process starts not directly in the beginning of the reaction after complex formation but between two and three

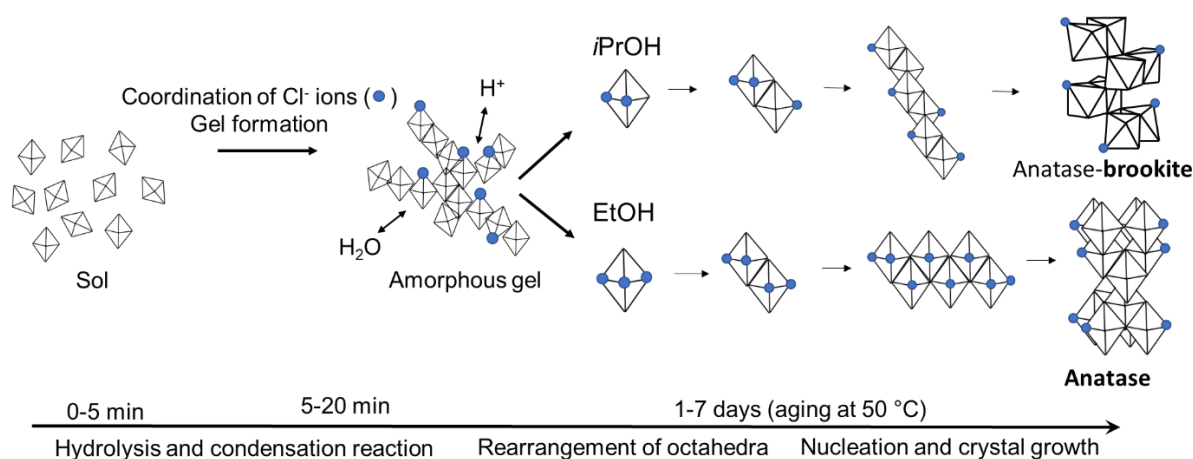


Figure 6.3-2: Crystallization process for the formation of anatase and anatase-brookite aerogels.

days of aging. The protons presumably have an effect on the rearrangement of the octahedra for nucleation. These processes are schematically shown in Figure 6.3-2. The temperature during aging of the developed synthesis procedure of 50 °C also might play an important role to accelerate the rearrangement of octahedra and the crystallization process. Since the crystallization takes a few days, it is assumed that the rearrangement of octahedra, and therefore nucleation as well as crystal growth, occurs slower for the solid wet gel in solvent which are 3D connected, compared to single nanoparticles.

As show in *in-situ* WAXS experiments of the wet gel sample *iP5*, crystallization occurs slowly during the extensive aging process at 50 °C for seven days (Figure 5.2-46) and could therefore induce rearrangements in the TiO₂ lattice and support the formation of metastable phases, such as brookite. Very slow reaction rates or slow precipitation of TiO₂ nanoparticles were reported to support the formation of brookite, according to literature.^[40]

The SAXS results, especially the Kratky and Porod-Debye plots, support that the gels with high acid content show a higher ability to crystallize, since a higher flexibility of the network was observed with increasing acid amount used during the synthesis. With a higher flexibility in the network it is assumed that it is easier to rearrange the octahedra, as for less flexible gels with lower HCl amount used during the synthesis.

The crystallization process therefore depends on an interplay of aging time, chloride content, protons, solvent and water to adjust the crystallinity and phases, as summarized in the flow chart in Figure 6.3-3. This is an important tool to selectively control the crystallinity by the aging time and chloride ions/protons. The achieved phases can be controlled by the used

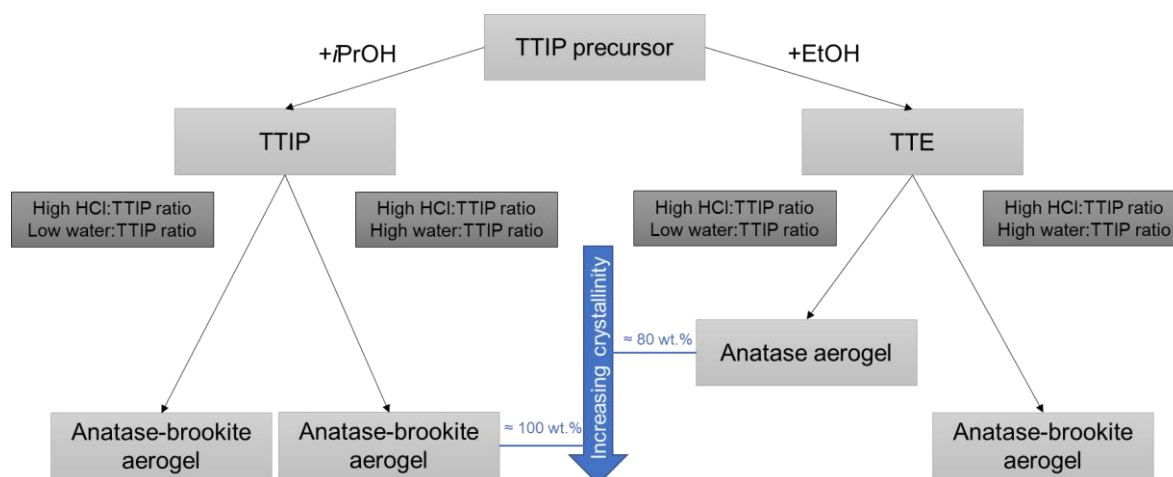


Figure 6.3-3: Flow chart of the formation of anatase or anatase-brookite aerogel dependent on different reaction conditions.

solvent, amount of water and HCl. Meso- or macroporous TiO_2 aerogels can therefore be adapted in terms of specific phases required for the targeted application.

The synthesis should be investigated with a different acid to separate the effects of chloride ions and protons. The choice of acid was reported to have an impact on the phase which is formed during calcination of TiO_2 nanoparticles. Calcination of TiO_2 nanoparticles synthesized with HCl was reported to lead to the rutile phase.^[51, 52] The rutile phase is not favored for photocatalytic applications, due to less photocatalytic activity compared to anatase. However, from the results it cannot be confirmed that rutile is generally formed with usage of HCl, since rutile was found in only one sample in very low concentration. Hu *et al.* reported that HCl for synthesizing TiO_2 nanoparticles, could be responsible for brookite formation by complex formation and therefore slow condensation reaction.^[40, 206] HNO_3 is widely used in literature in combination with TTIP, however, HNO_3 has an oxidizing effect, which is unfavorable for determining the effect of protons and chloride ions. *E.g.* NaCl or TiCl_4 could be used to increase the chloride content without changing the concentration of protons. Alternatively, HBr could be used as acid during the synthesis. Bromide ions are larger compared to chloride ions and might not be able to coordinate to titanium-based precursors, caused by steric hindrance of alkoxy groups.^[219] Therefore, only the effect of protons without complexing ligands could be investigated.

6.4 Chemical and Electronic Properties and Structural Defects

6.4.1 Chemical Composition

The two peaks of the Ti2p XPS spectra of the aerogel samples E2, E5, *iP2* and *iP5* can be assigned to $2p_{3/2}$ and $2p_{1/2}$ of Ti^{4+} in TiO_2 (Figure 5.3-3). The peak of the aerogel sample *iP2* is broader and asymmetric compared to the aerogel sample *iP5*, that supports the contribution of Ti^{3+} . The peaks of the aerogel sample E2 are shifted to slightly lower energies, also indicating Ti^{3+} . A shift and asymmetric peak was also reported in literature for the presence of Ti^{3+} .^[241] Chlorine can be found in all samples, with higher percentage in EtOH solvent-based aerogels compared to *iPrOH* solvent-based aerogels (Table 5.3-2). In the aerogel sample E5 and *iP5*, the chlorine content is higher when a high amount of acid was used during synthesis. It is actually expected that with higher concentration of chloride ions in the reaction mixture, the more chloride ions can coordinate. The observed difference in chlorine content could be due to less chloride ions that can coordinate to TTIP compared to the expected TTE precursor (formed due to ligand exchange), due to steric hindrance. It is expected that most of the chloride ions are eliminated in the form of HCl during condensation reactions of TTIP or crystallization according to the suggested reaction mechanism of Pottier *et al.*,^[40] however a small residue might be left. An inhomogeneous distribution of chloride ions in the gel could lead to deviations in the measured values of the Cl XPS signal. The chlorine signal is also shifted to lower values indicating metal chlorides. In literature the Cl signals at 197.92 eV and 200.03 eV were reported in Cl-doped TiO_2 for Ti-Cl and Ti-Cl-Ti bonds, respectively. The Ti-Cl signal at 197.92 eV was associated with physically adsorbed chloride ions on the TiO_2 surface, whereas the Ti-Cl-Ti signal at 200.03 eV was associated with doped Cl into the TiO_2 lattice at the place of lattice oxygen.^[209] The signals from literature fit to the found Cl signals in this work (Figure 5.3-2). The physically adsorbed chloride ions could be left over from the synthesis, that could not be removed by the washing process. The other Cl signal could indicate that a small amount of the chloride ions is incorporated into the TiO_2 lattice and might contribute to the crystallization process of TiO_2 , as reported by Pottier *et al.*^[40]. The basic TiO_2 structure at the particle surface is shown schematically in Figure 6.4-1, besides, defective structures with oxygen vacancies, chloride ions adsorbed on the surface and incorporated into the lattice are shown.

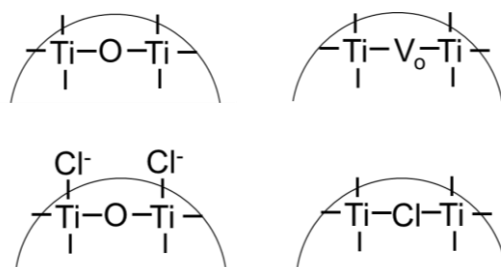


Figure 6.4-1: Scheme of basic TiO₂ structures at particle surfaces, TiO₂ structures with an oxygen vacancy, TiO₂ with adsorbed chloride ions on the surface and TiO₂ with Cl at the place of lattice oxygen.

The chloride ions (181 pm) are larger compared to O²⁻ (126 pm) in the TiO₂ lattice. [219, 242] Therefore, it might be difficult to stabilize and incorporate chlorine in the TiO₂ lattice. Chlorine could also be embedded in the gaps or channels formed between the octahedra in anatase and brookite crystal structures. However, there are a few reports in literature that investigated the incorporation of chloride ions into the TiO₂ lattice. [209, 235-237] Cl-doped TiO₂ was reported in literature to reduce the bandgap to 3.0 eV and shift the absorption to the vis range. [237] This is further discussed in section 6.4.3. The introduction of chloride ions into the TiO₂ lattice by substitution of O²⁻, could be a reason for the observed amount of Ti³⁺ found in the Ti XPS spectrum. However, the Cl content found in the aerogel samples E2, E5, *i*P2 and *i*P5 does not correlate with the amount of Ti³⁺. This is also further discussed section 6.4.3.

The presence of Ti-Cl bonds is supported by XRD results of precipitates, which occurred during the synthesis of the gel sample E2. Some reflections in the diffractogram, as indicated in Figure 5.2-37, cannot be assigned to typical TiO₂ phases, but could fit to Ti-Cl compounds, *e.g.* titanium chlorides or titanium oxide chloride hydrates according to literature (for reference see PDF number in Figure 5.2-37).

The chlorine content is reduced for calcined samples, that could indicate that the Cl is partially removed by calcination in air or vacuum (Table 5.3-3). The oxygen spectrum shows mainly two oxygen species, at 530.24 eV and 531.7 eV (Figure 5.3-2). In some samples (see appendix Figure 9.7-1 to Figure 9.7-3) a third oxygen signal occurs at 533 eV. The binding energy of at 530.24 eV was expected and can be assigned to the Ti⁴⁺-O framework, according to literature. [209] The binding energy at 531.7 eV can be associated with Ti-O-C-R from carbon residues of the alkoxide precursors or Ti-OH. [243] This binding energy was also reported for Ti surrounding oxygen regions which exhibit oxygen vacancies. [209, 244] The binding energy at 533 eV was also reported in literature with surface OH groups. [209, 244] Ti-OH is strongly bound to surface defects, and therefore associated with oxygen vacancies and Ti³⁺. [245] Physically

adsorbed water is removed in ultra-high vacuum conditions of XPS measurements and should not be visible in the measurements.

The observed carbon in the XPS spectra originates from precursor residues (Figure 5.3-2). The carbon content in the aerogel samples E2 is reduced from 17.4 at.% to 14.3 at.%, due to thermally decomposed carbon by calcination. The C1s signal also contain adventitious carbon, with typical contamination of C-C, C-O-C, and O-C=O components, since the aerogel has been exposed to the atmosphere.^[246] The COOH content does not change after calcination, that could indicate a thin layer of adventitious carbon causing the COOH signal, since no carboxyl groups are expected in the sample (Table 5.3-1, Table 5.3-4).

In the aerogel sample *i*P2 a higher percentage of carbon was found compared to aerogel sample E2 (Table 5.3-1). A slightly higher carbon content is expected, due to longer alkyl chains of the *Oi*Pr groups in the solvent residues of *i*PrOH solvent-based aerogels compared to the *OEt* groups in EtOH solvent-based aerogels. The large deviations between the two aerogel samples could also stem from inhomogeneities and localized higher occurrence of carbon residues, since XPS measurements give only information about few nanometers depth from the surface. In the aerogel sample *i*P5 the carbon content is much lower compared to aerogel sample E5, supporting the assumption that in the *i*PrOH solvent-based aerogels a higher amount of inhomogeneities is present (Table 5.3-1).

6.4.2 Electronic Properties

As explained in the section 2.4.2 of the chapter ‘The state of the art’, the band gaps play an important role for the generation of electron-hole pairs and determine the light absorption. A small band gap is therefore favorable. The band gap values of the aerogel sample E2 are between 3.4 and 3.5 eV and are slightly larger than the band gap of the calcined aerogels of 3.2 to 3.3 eV, which was expected as the aerogel sample E2 is a partially amorphous sample (Table 5.4-1). The band gap is reduced with increasing calcination temperature, due to anatase crystallization and therefore a more defined band structure compared to diffuse band structures in amorphous materials.^[247, 248] The estimated band gaps are in correspondence with the reported literature values for anatase TiO₂ powders and aerogels, with values ranging from 3.0 to 3.2 eV.^[249] The band gap of the non-calcined aerogel sample E5 is comparable to the aerogel calcined in air at 300 °C. This shows that also without calcination a higher crystallinity and an appropriate band gap can be achieved. For all calcined aerogels, only one sharp absorption edge at 340 to 375 nm occurs in the UV-vis spectra (Figure 9.8-2), indicating only anatase and no

second phase is formed. For the vacuum calcined aerogel (Figure 9.8-3), the absorption is slightly increased at higher wavelengths in the vis range compared to the other calcined aerogels. However, the light absorption is decreased compared to non-calcined aerogel sample E2, that could be due to less light reflection in the aerogel, due to the dark color and organic residues in the pores. The band gap of the vacuum calcined aerogel is wider compared to defect rich black TiO₂ reported in literature. [127] This agrees with the low amount of Ti³⁺ found in XPS measurements (Figure 5.3-2). Also, the Ti/O ratio indicates stoichiometric TiO₂. For Ti³⁺ rich anatase a band gap of 2.9 eV was reported, whereas for bulk TiO₂ 3.2 eV is reported in literature. The narrower band gap was observed in combination with the formation of an amorphous shell around the crystals. [127] The black appearance of the synthesized aerogels in this work can therefore not be assigned to structural defects *e.g.* Ti³⁺ or oxygen vacancies. The dark appearance is rather likely due to partial decomposition of organic residues.

The Cl-doping in the TiO₂ lattice was reported by Filippatos *et al.* to reduce the bandgap to values of 3.0 eV. [237] The reduction of the band gap value from 3.5/3.4 eV to 3.3 eV is accredited to the higher crystallinity of the aerogel sample E5, compared to aerogel sample E2 (Figure 9.8-1). The UV-vis spectrum in Figure 9.8-1 of the aerogel sample E5 shows a tailing absorption edge and a slightly elevated curve at higher wavelengths, compared to the spectrum of the aerogel sample E2, indicating a slightly increased absorption in the vis range for the aerogel sample E5.

From the determined band gap and VB maximum of the aerogel sample E2, the CB minimum was estimated to be approx. between -0.6 eV to -0.7 eV (section 5.4.1). This fits to values found in literature. [249] A VB maximum of 2.8 eV and CB minimum between -0.6 and -0.7 eV would fit to enable the half reactions for hydrogen evolution and nitrogen reduction to ammonia. However, the wide band gap only enables the material to absorb UV-light, so that doping of the aerogel would be necessary to achieve a narrower band gap and also to efficiently absorb vis-light.

6.4.3 Structural Defects and Ti³⁺ Defect Analysis

As discussed in section 6.4.1, the XPS results indicate the presence of Ti³⁺ in the aerogel samples E1, E5, *i*P1 and *i*P5. The highest Ti³⁺ content is found for E1 and decreases for higher acid content used during the synthesis. The aerogel sample *i*P2 showed lower Ti³⁺ content compared to E2 (Table 5.3-1).

The amount of Ti^{3+} decreased for the calcined aerogel samples E2-A-300 and E2-V-300 but in less extent for the vacuum treated aerogel (Table 5.3-4). The presence of Ti^{3+} is associated with defects such as oxygen vacancies, ^[245] as illustrated in Figure 6.4-2 for the anatase crystal structure. Defects can be advantageous for photocatalytic reactions, as defects can act as catalytic sites, if these defects are found on the surface. ^[155]

It was actually expected that the Ti^{3+} content increases in the synthesized aerogels samples which were calcined in the vacuum conditions, due to the oxygen deficiency during calcination and therefore loss of oxygen from the surface of TiO_2 . In literature, calcination in air (above 500 K) was reported to introduce Ti^{3+} and that Ti^{3+} forms due to thermal decomposition of organic residues. ^[251-253] However, higher temperatures are probably required in the vacuum treatment to form Ti^{3+} , than used in this work for the aerogel sample E2-V-300-2h and E2-V-300-4h. For the air calcined samples, the bulk defects are probably reduced due to the calcination, ^[155] but no more surface defects are introduced, since the photocatalytic activity increased with the calcination temperature, further discussed in section 6.5. Bulk defects can act as recombination centers for electron hole pairs and decrease the photocatalytic activity. ^[155]

The vacuum calcination at higher temperatures above 600 °C can create Ti^{3+} in TiO_2 samples, according to literature. Lower temperatures between 50 and 300 °C were reported to already create amounts of Ti^{3+} . Guillemot *et al.* reported a peak area ratio of $\text{Ti}^{3+}/\text{Ti}^{4+}$ of <3 % at 323 K for eight hours annealing in vacuum, whereas a peak area ratio of $\text{Ti}^{3+}/\text{Ti}^{4+}$ of 21 % at 573 K for eight hours was found. This supports the very small amount of Ti^{3+} which was found for the vacuum calcined sample in this work, which was calcined only for two and four hours at 300 °C, respectively. ^[241] The temperature of 300 °C used for the aerogel samples E2-V-300-2h and E2-V-300-4h is probably too low to create Ti^{3+} , but higher temperatures would damage the porous aerogel structure, due to sintering. It was also pointed out by Guillemot *et al.* that for

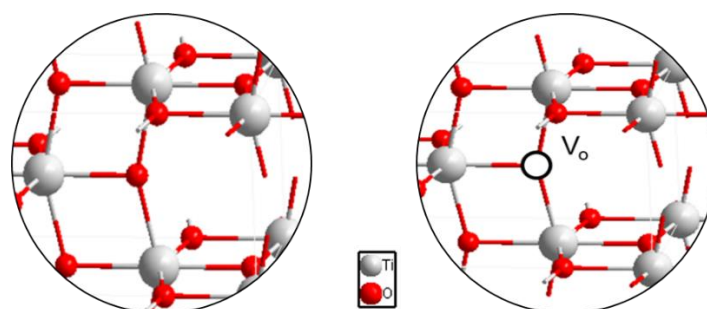


Figure 6.4-2: TiO_2 anatase crystal structure with and without oxygen vacancy (V_o). Images of unit cells of anatase generated with Diamond Version 4.6.8. ^[250]

porous samples the Ti^{3+} to Ti^{4+} ratio might be different compared to TiO_2 flat surfaces, since XPS analyzes only 3 to 5 nm in depth of a sample. If surface porosity (*e.g.* micropores) is present, the signal of outer layer atoms is changed while the inner layer atoms remains constant. ^[241] For the synthesized aerogels, primary particles and crystallite sizes are found in range of 1 to 5 nm from SAXS and XRD experiments (*cf.* Table 5.2-8 and Table 5.2-13). The pores exhibited sizes larger than 10 nm (mesopores) up to the macroporous range. The small particles or crystallites of the aerogel network are expected to be completely penetrated by the X-rays due to the small particle and crystallite size. However, the high meso- and macroporosity and consequently the large distances between small particles in the 3D aerogel network, could lead to deviations in the obtained measurement results. The actual $\text{Ti}^{3+}/\text{Ti}^{4+}$ ratio might be changed in the TiO_2 aerogel due to the high number of structural surface defects and high porosity, as reported in literature. ^[241]

The stability of Ti^{3+} in TiO_2 created by vacuum annealing was reported by Guillemot *et al.* to be one week under laboratory atmospheric conditions. ^[241] In synthesized aerogels of this work it seems that Ti^{3+} is much more stable compared to literature reports, since the measurements were performed a few weeks after the supercritical drying step.

The origin of the Ti^{3+} formation in the synthesized aerogels could be due to the formation of crystalline phases and rearrangement of octahedra during aging. In literature it was reported that diffusion and bonding to Ti of ions *e.g.* Na^+ or Ca^{2+} cause a shift of oxygen atoms and Ti-O bond shortening that enables the reduction of Ti^{4+} to Ti^{3+} . ^[244, 254] The coordination of chloride ions to the Ti atom could represent a similar case and reason for the Ti^{3+} formation. The substitution of oxygen (two negative charges) with chloride ions (one negative charge), *e.g.* in the anatase crystal structure, could cause Ti^{3+} due to charge compensation. However, it was reported in literature that the oxidation state of the Ti atom could remain Ti^{4+} if Cl is bound on the surface of the particles ($\text{TiO}_{2-x}\text{Cl}_{2x}$). ^[235]

The O1s XPS spectra of the aerogels exhibit a signal at 530.24 eV which is associated with the Ti^{4+} -O network (Figure 5.3-2, Figure 9.6-1, Figure 9.7-1 to Figure 9.7-5). An additional peak occurs at 531.64 eV that could be assigned to surface adsorbed hydroxyl groups which are not removed by the low vacuum during XPS measurements. Ti-OH is associated with surface defects of anatase. ^[245] Also, the gel samples E1, E2, *iP1*, and *iP2* have a blueish appearance, which probably stems from Rayleigh scattering at the small particles and pores but could also indicate small amounts of Ti^{3+} created during the synthesis (Figure 5.2-2 and Figure 5.2-4). These results support that surface defects are created in the aerogels.

According to Ganharul *et al.*, Ti^{3+} is mainly formed in anatase and is less likely formed in other polymorphs, *e.g.* compared to rutile, due to the lower vacancy formation energy in anatase crystals. [244] This supports that structural defects are more probable for anatase. The *i*PrOH solvent-based aerogels exhibited a lower Ti^{3+} amount compared to EtOH solvent-based aerogels (Table 5.3-1). The lower Ti^{3+} amount found for the aerogel sample *i*P5 could be explained by the high brookite fraction, since defects are more likely in anatase, according to literature. [244] The UPS spectrum of the aerogel sample E2 in Figure 5.4-1 shows occupied states between the Fermi energy and the VB edge indicating mid-gap energy levels, which are associated with Ti^{3+} defects, according to literature. [244] The presence of mid-gap states for the aerogel sample E2 confirms the Ti^{3+} found in XPS measurements. The presence of Ti^{3+} defects is highly favorable in the aerogels, as they shift the absorption also to vis light instead of UV-light. [137] However, in the absorption spectrum in diffuse reflection of the aerogel sample E2 no shift to vis light was observed, indicating that the Ti^{3+} concentration is too low to shift the absorption edge. Defects can also act as electron-hole traps to prevent charge carrier recombination and therefore increase the photocatalytic activity and electron storage capability (extended lifetime of the charges). [128] Electron paramagnetic resonance (EPR) experiments would be required to prove Ti^{3+} in the samples. Ar^+ and electrons were used for charge neutralization during XPS and UPS measurements, however it is unlikely that the measurement condition caused the formation of Ti^{3+} . Generally, Ar^+ bombardment with much higher acceleration voltages are only able to reduce Ti^{4+} to Ti^{3+} . [255]

6.5 Evaluation of TiO_2 Aerogel as Catalyst for Photocatalytic Applications

The results show that the TiO_2 aerogel is basically suitable for photocatalytic hydrogen generation (Figure 5.5-2). As shown in the publication by Rose *et al.*, [195] without co-catalyst the TiO_2 shows hydrogen evolution rates of less than $10 \mu\text{mol}\cdot\text{h}^{-1}$ which is due to the overpotential of unmodified TiO_2 (Table 5.5-1). [126] The sample E2-A-500 shows the highest hydrogen evolution rate up to $3.2 \mu\text{mol}\cdot\text{h}^{-1}$ without co-catalyst, which is found to be higher for a comparable calcined samples with a surface area of $85 \text{ m}^2\cdot\text{g}^{-1}$ measured at even higher temperatures of $30 \text{ }^\circ\text{C}$. [76]

After the addition of co-catalyst, the hydrogen evolution rate increases with the calcination temperature. The increasing calcination temperature leads to higher crystallinity confirmed by XRD (*cf.* Table 5.2-8 and Table 5.2-10), that increases the charge carrier mobility. Amal *et al.*

investigated WO₃ photoelectrodes and showed that higher calcination temperatures lead to an enhanced crystallinity and better charge mobility that in turn leads to higher photocatalytic hydrogen evolution. [256]

Also, the aerogel microstructure seems to influence the photocatalytic activity. Since the TiO₂ particles are chemically linked in the 3D aerogel network, the charge carrier separation seems to be enhanced due to the wide distribution of charge carriers in the aerogel. With calcination at higher temperatures and thus sintering, the interconnection of the TiO₂ nanocrystals seems to further improve the charge carrier separation. [76] The enhanced hydrogen evolution rate could also be due to a reduced amount of bulk defects in the calcined aerogels. Calcination can reduce the number of bulk defects, which can serve as recombination centers. The reduction of bulk defects leads to an increase in the diffusion length of charge carriers, so that they migrate faster to the surface where they can react. A reduced bulk to surface defect ratio can enhance the photocatalytic activity for TiO₂ nanocrystals, as reported by Kong *et al.* The reduced bulk to surface defect ratio was achieved by calcination. [155]

The observed hydrogen evolution rate of 332 $\mu\text{mol}\cdot\text{h}^{-1}$ is very high for the used low amount of co-catalyst of 0.1 wt.% (Table 5.5-1). In literature, hydrogen evolution rates of 16.4 $\mu\text{mol}\cdot\text{h}^{-1}$ and 720 $\mu\text{mol}\cdot\text{h}^{-1}$ were obtained for a 0.5 wt.% Pt-loaded TiO₂ aerogel (at 30 °C) and 1 wt.% loaded TiO₂ aerogel, respectively. [76, 257]

The calcined aerogel sample E2-A-500 exhibits the highest hydrogen evolution rate (Table 5.5-1). In contrast, the non-calcined aerogel sample E2 exhibits the highest electron storage capability (Figure 5.5-2). These differences can be related to the structural properties of the synthesized aerogels. The aerogel sample E2 exhibits a higher surface area compared to the calcined aerogels (Table 5.2-1 and Table 5.2-3). Also, the non-calcined aerogel sample shows the most intense dark color of the dispersion after UV irradiation, compared to the calcined aerogels (Figure 5.5-2). The color is related to the amount of stored electrons [158] and shows that in the non-calcined aerogel sample E2 most electrons can be stored. Ikeda *et al.* associated the amount of accumulated electrons with the number of defects, [258] since electrons can be trapped in defects *e.g.* surface defects such as oxygen vacancies in TiO₂. From XPS and UPS measurements in Figure 5.3-2 and Figure 5.4-1 it is shown that the aerogel E2 exhibits Ti³⁺ and mid-gap states which are associated with defects *e.g.* oxygen vacancies, as explained in more detail in section 6.4.3. The amount of Ti³⁺ is reduced for calcined samples and therefore less defects where electrons can be trapped. The combination of the high surface area of E2 and the

high number of defects leads to the high amount of stored photocharged electrons. Since the calcined aerogels exhibit a lower surface area and lower amount of Ti^{3+} (cf. Table 5.2-1, Table 5.2-3, Table 5.3-1, Table 5.3-4), less surface defects are assumed that lead to lower storage capability. The calcination process seems to reduce the amount of surface and bulk defects that reduces the capability to store electrons, but improves the charge carrier separation and hydrogen evolution, that was shown by Rose *et al.* [195] Since electrons are stored in the non-calcined aerogel sample E2, less electrons are available for the generation of hydrogen under UV-light. This is evident from the dark color of the dispersion in Figure 5.5-2 and can explain the low hydrogen evolution values without co-catalyst.

After addition of the co-catalyst, a sharp peak of hydrogen evolution rate was observed and a discoloration of the dispersion. This can be related to the stored electrons in the aerogel sample E2. After addition of the H_2PtCl_6 solution, metallic Pt clusters are formed, caused by the reduction of H_2PtCl_6 due to the stored electrons. These Pt nanoparticles are expected on the surface of the TiO_2 aerogel, forming a Schottky contact between Pt and TiO_2 . The remaining stored electrons in the aerogel are then transferred to the Pt metal particles. The Pt nanoparticles act as co-catalyst and the transferred electrons are applied to reduce protons to hydrogen. The hydrogen evolution is therefore increased, that is visible from the sharp peak in Figure 5.5-2a. [195] The intensity of this peak can be related to the amount of stored electron. This hydrogen evolution rate peak is highest for E2 and decreases with increasing calcination temperature (Figure 5.5-2a).

This experiment was repeated and after irradiation the co-catalyst was added in the dark (Figure 5.5-2b). The dispersions decolorized after addition to H_2PtCl_6 , based on the assumption that all Pt^{4+} is reduced to Pt^0 and the remaining stored electrons transferred to the formed metallic Pt particles, where they are used for the hydrogen evolution and no stored electrons are left in the material. This indicates that Pt as co-catalyst prevents the storage of electrons in surface defect states, since they are all transferred to the Pt nanoparticles for further reactions. An increase in the calcination temperature and therefore a decrease in surface area results in a decreased amount of stored electrons and therefore a lower hydrogen evolution rate peak for the calcined samples compared to the non-calcined aerogel sample E2. Since the capability to store electrons is reduced for lower surface areas, it is believed that electrons are trapped in surface defects and not in bulk defects. [195] The calcination leads to a reduction of bulk defects, according to literature, which can act as recombination centers. [155] In the case of the calcined aerogels the hydrogen evolution rate increases, that support the fact that bulk defects are reduced. Also, the

presence of surface defects in the non-calcined aerogel sample E2 is evident from XPS and UPS experiments, as described previously. The surface defects present in the aerogel samples act as charge carrier traps, but also offers adsorption sites for the used methanol as a hole scavenger.^[155]

The stored photogenerated electrons were also used to reduce nitrogen to ammonia in the dark. The results show, that with the aerogel E2 it is generally possible to generate hydrogen and ammonia. This is also supported by the determined VB and CB edges which theoretically enable the mentioned photocatalytic processes.

6.6 Towards Mixed Metal Oxide and Doped TiO₂ Aerogels

The developed sol-gel synthesis is a good way to introduce dopants or metal oxides into the TiO₂ gel. The adjustability of the doped metal oxide fraction is very simple, when using alkoxides. This was supported by XPS results, showing similar contents of the doped metal in the final aerogel compared to the used precursor amount (cf. Table 9.10-2 and chapter 3.2). The metal atom from the additional alkoxide precursor (SnIP and VOIP) is incorporated into the network and presumably chemically linked to the TiO₂ network. The STEM mapping shows a homogeneous distribution of V and Ti in the aerogel (Figure 9.10-4). Solid dopants *e.g.* chlorides or in this case GO and MoS₂ are less favorable, due to less adjustability during synthesis. Metal chlorides or GO/MoS₂ might be washed out of the wet TiO₂ gel during solvent exchange or supercritical drying. Supported by XPS the amount of Mo and S in the sample was very low, indicating that most got washed out. However, Mo and S are both found in the STEM mapping, which are homogeneously distributed (Figure 9.10-5 and Table 9.10-2). This works probably only for very small nanoparticles, such as the used nanosized MoS₂. GO sheets are normally exfoliated in water and could exhibit larger aggregates when dispersed in solvent.^[259] More inhomogeneities and larger aggregates are present and visible in the sample with the bare eye (Figure 9.10-1).

The addition of a solid dopant or an additional alkoxide precursors negatively influences the crystallinity (Figure 9.10-7). The aerogels were completely amorphous whereas the aerogel without dopants was semi-crystalline (Figure 5.2-33). The addition of dopants seems to disturb the crystallization process during aging.

Besides the negative impact on the crystallinity, the addition of dopants had a positive effect on the pore structure (Figure 9.10-6 and Table 9.10-1). The specific surface increased compared to undoped TiO₂ aerogel, since the surface area of *e.g.* additional nanoparticles of MoS₂ or GO

sheets contribute to the overall surface area. The pore volume increased for solid dopants such as GO, which served as spacer between the pores, and also led to slight increase in pore size. Further, no change in the pore size was observed for the V_2O_5 - TiO_2 aerogel. This shows that the additional liquid VOIP precursor only has very small impact on the pore structure, but contribute to a higher surface area due to additional nanostructures. The addition of the SnTIP precursor led to a slightly decreased pore volume compared to pure TiO_2 aerogel. A similar surface area but very broad pore size distribution was observed, that is also evident from the SEM image (Figure 9.10-2), which is probably due to different reactivity of the two precursors, that led to aggregation of particles during the synthesis. The SnTIP precursor was pre-diluted in *i*PrOH when purchased. For *i*PrOH solvent-based aerogels, large mesopores and macropores are observed that could explain the larger pores for the SnO_2 - TiO_2 aerogel.

The XPS results showed a positive effect on the structural defects and amount of Ti^{3+} (Table 9.10-3). Apart from MoS_2 - TiO_2 , Ti^{3+} was found in all samples with increasing amount of the following order: *i*P2 < SnO_2 - TiO_2 < V_2O_5 - TiO_2 < E2 < GO- TiO_2 (cf. Table 9.10-3 and Table 5.3-1). The low Ti^{3+} amount found in SnO_2 - TiO_2 is similar to *i*P2, for the *i*PrOH solvent-based aerogels. For the other samples, which were EtOH solvent-based, the Ti^{3+} amount is higher. The highest amount was found for GO, probably due to structural reasons of the thin GO sheets, but which have a diameter in the μm -range. The solvent dependency of the Ti^{3+} formation and influence of dopants need to be further investigated.

The very low dopant amount was sufficient to alter the electronic properties (Table 9.10-4). The band gaps of MoS_2 - TiO_2 and V_2O_5 - TiO_2 are reduced compared to the undoped TiO_2 aerogel. The addition of MoS_2 nanoparticle lead to successful narrowing of the band gap and shifts the light absorption to the vis range (Figure 9.10-12). The reduction is due to the introduction of energy level (S2p) to the TiO_2 VB. ^[143, 144] It is expected that grain boundaries of the MoS_2 and TiO_2 led to the changed electronic properties, since two values (for MoS_2 and TiO_2) for the band gap can be extracted from the Tauc plot (Figure 9.10-12). For GO no change in band gap was observed. This is probably caused by too large aggregates of GO or not sufficiently exfoliated GO, which filled the pores but were not connected to the TiO_2 aerogel. Also, the V_2O_5 - TiO_2 aerogel showed a smaller band gap of 3.2 eV compared to amorphous TiO_2 (3.4 to 3.5 eV). In this case, it is expected that V is introduced and chemically connected in 3D network, since only one value for the band gap can be extracted from the Tauc plot. The brownish color and XPS results indicated the formation of V_2O_5 that is reported in literature with band gaps of 2.8 eV (Figure 9.10-1), that could explain the smaller band gap. ^[120] The

Kubelka Munk plot show a curve tailing instead of a sharp edge in Figure 9.10-12, indicating that the absorption is slightly shifted to 450 nm.

The VB edge of SnO₂-TiO₂ showed the most positive value and also a wide band gap of 3.5 eV, that was expected, due to the wide band gap of SnO₂ (Figure 9.10-13 and Table 9.10-4).^[175]

However, the charge separation is expected to be improved in this sample, that needs to be studied in electron storage experiments in the future. The VB edges determined for V₂O₅-TiO₂ and GO-TiO₂ showed more positive values compared to pure TiO₂ (Figure 9.10-13 and Table 9.10-4, Table 5.4-1). That could be due to the diffuse VB structure of amorphous V₂O₅-TiO₂ and agglomerated GO that shifted the VB to more positive values. Nevertheless, the calculated CB position should be suitable for all candidates to photocatalytically generate hydrogen. The impact on the photocatalytic activity needs to be studied in the future.

7 Summary and Outlook

The aim of this work was to develop a simple sol-gel synthesis route to achieve (semi-)crystalline TiO₂ aerogels for photocatalytic applications. Since photocatalytic processes highly depend on the properties, *e.g.* crystallinity and surface area, the adjustability of these properties by synthesis parameters is very important. Therefore, different synthesis parameters, *e.g.* amount of acid, type and amount of solvent, and amount of water were varied. These parameters were expected to change the gelation kinetics due to changing hydrolysis level and proton concentration as well as steric hindrance. This in turn influenced the structural properties and the crystallization processes of the typically amorphous aerogel, *e.g.* by chloride ions of the HCl as complexing agent, and was compared to calcined aerogels. Besides the structural properties, the crystallization process and formation of different phases in the gels was investigated by means of *in-situ* WAXS and Raman experiments. The chemical and electronic properties were analyzed regarding the application of the synthesized aerogel as photocatalyst, which was tested in proof-of-concept trials. Based on the developed synthesis route, mixed metal oxide and doped metal oxide aerogels were synthesized and characterized considering the usage in photocatalytic processes.

The results showed that only with a few synthesis parameters, the aerogel properties can be selectively controlled and adjusted according to the application. These aerogel properties include the surface area, pore size distribution, crystallinity and crystal phase, and the appearance, as summarized in Figure 6.6-1.

The choice of solvent had a direct impact on the pore size distribution of the aerogel. Dependent on the application a certain pore size for reactants might be required. Using the TTIP precursor in EtOH in the synthesis, mesoporous aerogels could be achieved, while in *i*PrOH, meso- and macroporous aerogels were obtained, due to TTIP ligand exchange and steric reasons. The aerogels were very homogenous exhibiting a narrow pore size distribution. The smaller pores for EtOH solvent-based aerogels had a direct impact on the surface area, which increased, compared to *i*PrOH solvent-based aerogels. The different pore sizes also influenced the appearance of the aerogels, which changed from transparent for EtOH to translucent for *i*PrOH. Mixtures of the two solvents seemed to stabilize the aerogel structure, so that a monolithic shape could be achieved with higher mechanical strength. The pore size could be adapted with solvent mixtures.

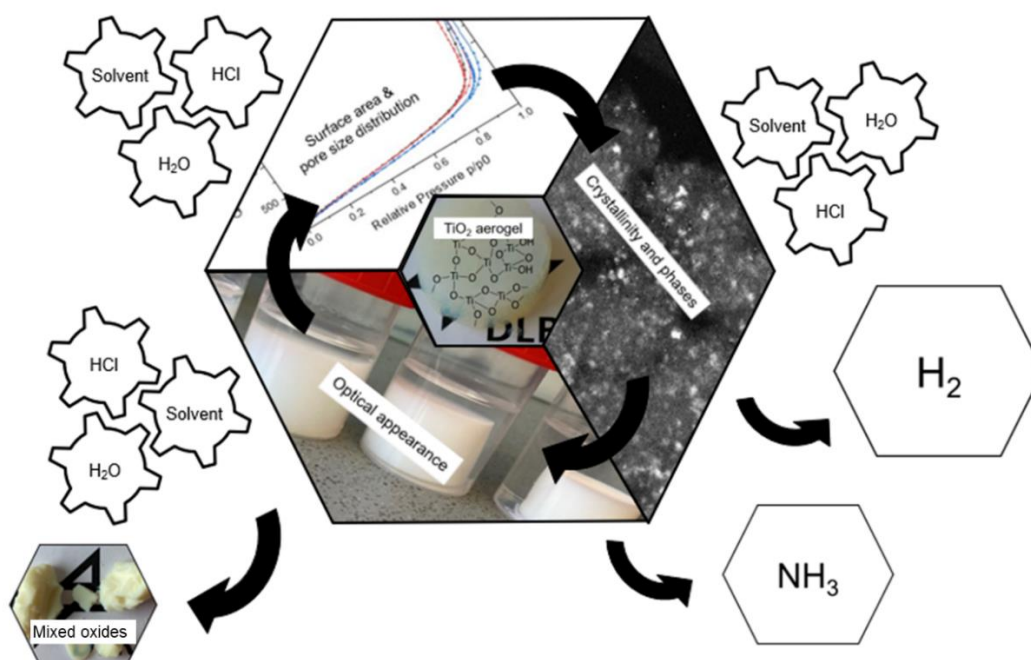


Figure 6.6-1: Scheme of the developed tunable synthesis route with influencing synthesis parameters to control aerogel properties and the potential applications.

HCl had a significant impact on the surface area and pore size distribution. Compared to the usage of different solvents, which increased the size of the mesopores, the increase in HCl leads to macropores and broadens the pore size distribution. The surface area and pore volume decreased. This could be related on the one hand to the reduced condensation reaction rate, due to a high proton concentration. The hydrolysis and condensation reaction could be successfully separated in the HCl-supported synthesis route. On the other hand, this could be related to the crystallization of the amorphous gels. The crystallization process was proven by *in-situ* WAXS and Raman measurements to occur during aging of the wet gel. The chloride ions and the aging process at acidic aqueous conditions at slightly elevated temperatures (50 °C) were assumed to be responsible for crystallization. Since the crystallization occurs during aging, already the wet gel can be further used in liquid systems in photocatalytic applications, *e.g.* as thin gel layers, without further supercritical drying. This needs to be tested in the future in an appropriate experimental setup. Also, it might be advantageous to adjust the ratio of amorphous to crystalline content. The ratio can be controlled by varying the aging time to achieve a selective and precise crystallinity from completely amorphous to 100 wt.% crystallinity. Chloride ions from the HCl are assumed to coordinate differently to the TTIP precursor dependent on the steric hindrance of the TTIP ligands leading to intermediate complexes, which act as template

for the formation of either anatase or mixtures of anatase and brookite. Cl was found to be introduced into the TiO₂ crystal structure, supported by XRD and XPS results. In the case of *i*PrOH solvent-based systems completely crystalline aerogels with nanocrystalline anatase and brookite were obtained, while EtOH solvent-based systems led to semi-crystalline aerogels with up to 80 wt.% nanocrystalline anatase. The broad pore size distribution at high acid amounts could be prevented by increasing the amount of water for EtOH solvent-based systems. Fully crystalline and translucent mesoporous anatase-brookite aerogels could be achieved. The effect of chloride ions and protons on the achieved crystallinity needs to be further investigated to identify its impact separately. This helps to gain more information about the crystallization mechanism in the wet gels and the resulting dominating phases.

Compared to the classical calcination process, the achieved crystallinity in the wet gel, as effect of the aging process and the chloride ions, shows some advantages. The calcination of the TiO₂ aerogels at 300 to 500 °C in air leads to much lower specific surface areas in the crystalline aerogels compared to the HCl-supported synthesis route without calcination. The calcination process leads to sintering and therefore reduction of porosity but slightly larger mesopores. Also, an increase in crystallite size could be observed. With high HCl amounts and the gel aging process route a high degree of crystallinity could be achieved without any sintering and therefore minor loss of porosity compared to the calcination process route. However, this alternative process led to macropores and some larger aggregates, so that the final aerogel is less homogeneous regarding the pore size compared to the calcined ones. Also, mainly anatase and brookite nanocrystals grow simultaneously during the aging process. The crystallite size didn't seem to be affected by the higher amounts of acid or the aging process and remained below 5 nm. The calcination of TiO₂ aerogels typically leads only to the anatase phase and an increase in crystallite size.

The band gap and its position are crucial for the absorption of light and determines the feasibility of photocatalytic reactions. The semi-crystalline aerogel exhibited a broad band gap, but could be reduced in the completely crystalline aerogels applying both ways, the calcination and the HCl-supported synthesis route. Concerning the structural properties, the HCl-supported synthesis route mostly resulted in broad pore size distributions, while narrow pore size distributions were obtained for calcined samples, only with a shift of the BJH peak maximum to a larger pore size. High amounts of water besides the increase of acid lead to completely

crystalline anatase-brookite aerogels with a narrow pore size distribution based on EtOH as solvent.

The gel structure and pore network formation are depending on the initial gelation process in the HCl-supported synthesis route, which is controlled by hydrolysis and condensation reaction rates, based on the concentration of chloride ions and protons, by different amount of HCl added during the synthesis. Besides the achieved higher crystallinity with increasing acid amount, the primary and secondary particle size increases, that was shown with TEM, SEM and SAXS experiments. The gel structure had a disordered arrangement of particle chains and a more flexible network (before drying) with large and dense aggregates for increasing acid amounts, whereas for low amounts of acid a very homogeneous dense gel network was found. This was supported by physisorption experiments. The differences in the gel network could be related to altered reaction kinetics and less condensed network for very high acid contents. With increasing acid content, the hydrolysis and condensation reaction could be separated and controlled efficiently. A high number of protons catalyze the hydrolysis reaction, but hydrolyzed species hinder the condensation reaction. Also, the coordination of chloride ions to the Ti atom is assumed to prevent condensation and the network formation, leading to network with large aggregates and inhomogeneous pore size distribution. The particle and cluster growth during (pre-)hydrolysis after acid addition and the condensation reaction after water addition could be further analyzed by dynamic light scattering (DLS). The particles and gel network properties are relevant for the crystallization of the material, since a more flexible and less stable structure is more vulnerable to rearrangement of TiO₂ octahedra and crystallization. The HCl-supported synthesis route of nanocrystalline aerogels offers great potential with adjusting processing parameters with respect to requirements for several applications *e.g.* tailoring the surface area and pore size distribution dependent on the reactant size and adsorption behavior. An example is the photocatalytic decontamination of waste water from larger heavy metal compounds. Large surface areas offer many sites to capture metal ions. The pores size and open porosity is crucial to maintain efficient diffusion pathways and determines the permeation or capture and removal of metal ions. ^[260] The adjustability of the new developed synthesis and the resulting aerogel properties are much more flexible compared to calcination of TiO₂ aerogels to achieve crystalline materials.

The photocatalytic experiments showed that the hydrogen evolution was higher compared to literature for the TiO₂ aerogel in combination with a co-catalyst. The calcined completely crystalline aerogels produced more hydrogen compared to the semi-crystalline (10 wt.%

anatase) aerogel. This shows that the photoinduced generation of electron-hole pairs is dependent on the crystallinity of the aerogel. The semi-crystalline (10 wt.% anatase) aerogel showed exceptional properties in storing photogenerated electrons in the aerogel structure over several hours, which could be further used on demand for N₂ reduction to ammonia.

The aerogel exhibited high number of structural defects and Ti³⁺, associated with oxygen vacancies, which could not be achieved by vacuum thermal treatment without damage of the porous structure. The observed Ti³⁺ in XPS results should be confirmed by EPR in further experiments. These results demonstrate the wide range of potential application of the developed TiO₂ aerogels.

The further developed mixed metal oxide and doped metal oxide aerogels were successfully synthesized by simple modification of the developed one-pot gel synthesis. Homogeneous distributions of the second metal oxide or dopant were achieved, independent on the physical state (solid or liquid) of the additive or precursor. However, solid additives might be more easily removed from the pores due to the applied solvent exchange after aging of the gels. The capture of the solid additives and incorporation into the gel needs to be improved. Solid state NMR could help to study the aerogel structure and reveal *e.g.* Sn-O-Ti or V-O-Ti bonds. Further structural analysis revealed, that a defined pore size distribution was achieved for the combination of two alkoxide precursors when EtOH is used as solvent, but also depends on the differences in reactivity and moisture sensitivity of the selected precursor. The surface area and pore volume were slightly influenced positively by the additional introduced materials, however the aerogels stayed completely amorphous. The impact of an increase in HCl needs to be investigated and its effect on the crystallinity. Especially, in the case of V₂O₅-TiO₂, it was observed in literature, that vanadium alkoxides lead to oxides with lower valences than V⁵⁺, dependent on the amount of acid, [261] that could be interesting in further reducing the band gap. From the calculated band gap positions, theoretically all mixed metal oxide and doped metal oxide aerogels should be able to photocatalytically generate hydrogen, however only MoS₂-TiO₂ and V₂O₅-TiO₂ show a reduced band gap, so that also vis-light can be absorbed. The ability of charge separation and hydrogen generation needs to be tested for the mixed metal oxide and doped metal oxide aerogels as well as the anatase and anatase-brookite aerogels based on the HCl-supported synthesis route compared to calcined TiO₂ aerogels in the future. Since the pore size is different for calcined aerogels and the crystalline aerogels based on the new HCl-supported synthesis route, the impact of the pore size on the photocatalytic activity needs to be studied.

8 References

1. 2023, A. ZEROe - *Towards the world's first hydrogen-powered commercial aircraft*. 2023 03.05.2023]; Available from: <https://www.airbus.com/en/innovation/zero-emission-journey/hydrogen/zeroe>.
2. Deutschen, B.d. and L.e.V. (BDL). *Analyse der Klimaschutzinstrumente im Luftverkehr zur CO₂-Reduktion*. October 2022 [cited 2023 03.05.2023]; Available from: <https://www.bdl.aero/de/publikation/analyse-der-klimaschutzinstrumente-im-luftverkehr-zur-co2-reduktion/>.
3. (IEA), I.E.A. *The Future of Hydrogen*. License: CC BY 4.0 2019 [cited 2023 03.05.2023]; Available from: <https://www.iea.org/reports/the-future-of-hydrogen>.
4. Airbus. *The green hydrogen ecosystem for aviation, explained*. 17 June 2021 [cited 2023 03.05.2023]; Available from: <https://www.airbus.com/en/newsroom/news/2021-06-the-green-hydrogen-ecosystem-for-aviation-explained>.
5. Wang, Y., et al., *PEM Fuel cell and electrolysis cell technologies and hydrogen infrastructure development – a review*. Energy & Environmental Science, 2022. **15**(6): p. 2288-2328.
6. Kim, E.-J., et al., *Stabilizing role of Mo in TiO₂-MoO_x supported Ir catalyst toward oxygen evolution reaction*. Applied Catalysis B: Environmental, 2021. **280**: p. 119433.
7. Zaleska-Medynska, A., *Metal oxide-based photocatalysis: fundamentals and prospects for application*. 2018: Elsevier.
8. Maeda, K., et al., *Photocatalyst releasing hydrogen from water*. Nature, 2006. **440**(7082): p. 295-295.
9. DECHEMA, G.f.C.T.u.B.e.V. *Herstellung von Wasserstoff_Photokatalyse*. 2023 [cited 2023 04.05.2023]; Available from: https://dechema.de/processnet_media/FG+Chemische+Reaktionstechnik/Chemische+Energieforschung/Herstellung+von+Wasserstoff_Photokatalyse.pdf.
10. Hüsing, N. and U. Schubert, *Aerogels—airy materials: chemistry, structure, and properties*. Angewandte Chemie International Edition, 1998. **37**(1-2): p. 22-45.
11. Zhang, Z., et al., *Role of Particle Size in Nanocrystalline TiO₂-Based Photocatalysts*. The Journal of Physical Chemistry B, 1998. **102**(52): p. 10871-10878.
12. Ovenstone, J., *Preparation of novel titania photocatalysts with high activity*. Journal of Materials Science, 2001. **36**(6): p. 1325-1329.
13. Tian, G., et al., *Preparation and Characterization of Stable Biphasic TiO₂ Photocatalyst with High Crystallinity, Large Surface Area, and Enhanced Photoactivity*. The Journal of Physical Chemistry C, 2008. **112**(8): p. 3083-3089.
14. Haider, A.J., Z.N. Jameel, and I.H. Al-Hussaini, *Review on: titanium dioxide applications*. Energy Procedia, 2019. **157**: p. 17-29.
15. (BfR), B.f.R. *Titandioxid - gibt es gesundheitliche Risiken?* 2021 01.05.2023]; Available from: https://www.bfr.bund.de/de/titandioxid___gibt_es_gesundheitliche_risiken_-240812.html.
16. (efsa), E.B.f.L. *Titandioxid: E171 gilt bei Verwendung als Lebensmittelzusatzstoff nicht mehr als sicher*. 2021 [cited 2023 01.05.2023]; Available from: <https://www.efsa.europa.eu/de/news/titanium-dioxide-e171-no-longer-considered-safe-when-used-food-additive>.
17. (BVL), B.f.V.u.L. *Verbot von Titandioxid in Lebensmitteln*. 05.08.2022 [cited 2023 01.05.2023]; Available from:

- https://www.bvl.bund.de/SharedDocs/Pressemitteilungen/01_lebensmittel/2022/2022_PM_Titandioxid.html.
18. Sugimoto, T., X. Zhou, and A. Muramatsu, *Synthesis of Uniform Anatase TiO₂ Nanoparticles by Gel–Sol Method: I. Solution Chemistry of Ti(OH)_n(4–n)⁺ Complexes*. Journal of Colloid and Interface Science, 2002. **252**(2): p. 339-346.
 19. Huang, F., et al., *Electrospinning amorphous SiO₂-TiO₂ and TiO₂ nanofibers using sol-gel chemistry and its thermal conversion into anatase and rutile*. Ceramics International, 2018. **44**(5): p. 4577-4585.
 20. Wu, J.-J. and C.-C. Yu, *Aligned TiO₂ nanorods and nanowalls*. The Journal of Physical Chemistry B, 2004. **108**(11): p. 3377-3379.
 21. Golobostanfard, M.R. and H. Abdizadeh, *Effect of mixed solvent on structural, morphological, and optoelectrical properties of spin-coated TiO₂ thin films*. Ceramics International, 2012. **38**(7): p. 5843-5851.
 22. Elghniji, K., et al., *Synthesis and characterization of Fe³⁺ doped TiO₂ nanoparticles and films and their performance for photocurrent response under UV illumination*. Journal of Alloys and Compounds, 2012. **541**: p. 421-427.
 23. Baia, L., et al., *Synthesis and nanostructural characterization of TiO₂ aerogels for photovoltaic devices*. Thin Solid Films, 2006. **511-512**: p. 512-516.
 24. Bernardes, J.C., et al., *Novel modified nonalkoxide sol–gel synthesis of multiphase high surface area TiO₂ aerogels for photocatalysis*. Journal of Sol-Gel Science and Technology, 2020. **94**(2): p. 425-434.
 25. Choi, H., et al., *Synthesis of high surface area TiO₂ aerogel support with Pt nanoparticle catalyst and CO oxidation study*. Catalysis Letters, 2018. **148**(5): p. 1504-1513.
 26. Bhosale, M.G., et al., *Sol–gel method synthesized Ce-doped TiO₂ visible light photocatalyst for degradation of organic pollutants*. Applied Organometallic Chemistry, 2022. **36**(4): p. e6586.
 27. Li, J.-G., T. Ishigaki, and X. Sun, *Anatase, brookite, and rutile nanocrystals via redox reactions under mild hydrothermal conditions: phase-selective synthesis and physicochemical properties*. The Journal of Physical Chemistry C, 2007. **111**(13): p. 4969-4976.
 28. Li, G. and K.A. Gray, *Preparation of mixed-phase titanium dioxide nanocomposites via solvothermal processing*. Chemistry of Materials, 2007. **19**(5): p. 1143-1146.
 29. Alsaiari, M.A., et al., *Growth of amorphous, anatase and rutile phase TiO₂ thin films on Pt/TiO₂/SiO₂/Si (SSTOP) substrate for resistive random access memory (ReRAM) device application*. Ceramics International, 2020. **46**(10): p. 16310-16320.
 30. Haggerty, J.E.S., et al., *High-fraction brookite films from amorphous precursors*. Scientific Reports, 2017. **7**(1): p. 15232.
 31. Gopal, M., W.J. Moberly Chan, and L.C. De Jonghe, *Room temperature synthesis of crystalline metal oxides*. Journal of Materials Science, 1997. **32**(22): p. 6001-6008.
 32. Allen, N.S., et al., *The effect of crystalline phase (anatase, brookite and rutile) and size on the photocatalytic activity of calcined polymorphic titanium dioxide (TiO₂)*. Polymer Degradation and Stability, 2018. **150**: p. 31-36.
 33. Zhang, Y., et al., *Titanate and titania nanostructured materials for environmental and energy applications: a review*. RSC Advances, 2015. **5**(97): p. 79479-79510.
 34. Di Paola, A., M. Bellardita, and L. Palmisano, *Brookite, the Least Known TiO₂ Photocatalyst*. Catalysts, 2013. **3**(1): p. 36-73.
 35. Zhang, H. and J.F. Banfield, *Understanding Polymorphic Phase Transformation Behavior during Growth of Nanocrystalline Aggregates: Insights from TiO₂*. The Journal of Physical Chemistry B, 2000. **104**(15): p. 3481-3487.

36. Ranade, M., et al., *Energetics of nanocrystalline TiO₂*. Proceedings of the National Academy of Sciences, 2002. **99**(suppl_2): p. 6476-6481.
37. Kignelman, G. and W. Thielemans, *Meta-analysis of TiO₂ nanoparticle synthesis strategies to assess the impact of key reaction parameters on their crystallinity*. Journal of Materials Science, 2021. **56**(10): p. 5975-5994.
38. Mahy, J.G., et al., *Eco-Friendly Colloidal Aqueous Sol-Gel Process for TiO₂ Synthesis: The Peptization Method to Obtain Crystalline and Photoactive Materials at Low Temperature*. Catalysts, 2021. **11**(7): p. 768.
39. Keesmann, I., *Zur hydrothermalen synthese von brookit*. Zeitschrift für anorganische und allgemeine Chemie, 1966. **346**(1-2): p. 30-43.
40. Pottier, A., et al., *Synthesis of brookite TiO₂ nanoparticles by thermolysis of TiCl₄ in strongly acidic aqueous media*. Journal of Materials Chemistry, 2001. **11**(4): p. 1116-1121.
41. Cargnello, M., T.R. Gordon, and C.B. Murray, *Solution-phase synthesis of titanium dioxide nanoparticles and nanocrystals*. Chemical reviews, 2014. **114**(19): p. 9319-9345.
42. Lin, H., et al., *Synthesis of High-Quality Brookite TiO₂ Single-Crystalline Nanosheets with Specific Facets Exposed: Tuning Catalysts from Inert to Highly Reactive*. Journal of the American Chemical Society, 2012. **134**(20): p. 8328-8331.
43. Simonsen, M.E. and E.G. Sjøgaard, *Sol-gel reactions of titanium alkoxides and water: influence of pH and alkoxy group on cluster formation and properties of the resulting products*. Journal of sol-gel science and technology, 2010. **53**(3): p. 485-497.
44. Iarikov, D.D., P. Hacıoğlu, and S. Ted Oyama, *Chapter 3 - Amorphous Silica Membranes for H₂ Separation Prepared by Chemical Vapor Deposition on Hollow Fiber Supports*, in *Membrane Science and Technology*, S.T. Oyama and S.M. Stagg-Williams, Editors. 2011, Elsevier. p. 61-77.
45. Matijevic, E., *Monodispersed metal (hydrous) oxides - a fascinating field of colloid science*. Accounts of Chemical Research, 1981. **14**(1): p. 22-29.
46. Símonarson, G., et al., *Evolution of the Polymorph Selectivity of Titania Formation under Acidic and Low-Temperature Conditions*. ACS Omega, 2019. **4**(3): p. 5750-5757.
47. Yin, H., et al., *Hydrothermal synthesis of nanosized anatase and rutile TiO₂ using amorphous phase TiO₂*. Journal of Materials Chemistry, 2001. **11**(6): p. 1694-1703.
48. Benčina, M., et al., *Crystallized TiO₂ Nanosurfaces in Biomedical Applications*. Nanomaterials, 2020. **10**(6): p. 1121.
49. Moussaoui, R., et al., *Sol-gel synthesis of highly TiO₂ aerogel photocatalyst via high temperature supercritical drying*. Journal of Saudi Chemical Society, 2017. **21**(6): p. 751-760.
50. Kong, Y., X.-D. Shen, and S. Cui, *Direct synthesis of anatase TiO₂ aerogel resistant to high temperature under supercritical ethanol*. Materials Letters, 2014. **117**: p. 192-194.
51. Isley, S.L. and R.L. Penn, *Relative Brookite and Anatase Content in Sol-Gel-Synthesized Titanium Dioxide Nanoparticles*. The Journal of Physical Chemistry B, 2006. **110**(31): p. 15134-15139.
52. Hidalgo, M.C., et al., *Hydrothermal preparation of highly photoactive TiO₂ nanoparticles*. Catalysis Today, 2007. **129**(1): p. 50-58.
53. Hu, Y., H.L. Tsai, and C.L. Huang, *Effect of brookite phase on the anatase-rutile transition in titania nanoparticles*. Journal of the European Ceramic Society, 2003. **23**(5): p. 691-696.
54. Cihlar, J., et al., *Influence of LA/Ti molar ratio on the complex synthesis of anatase/brookite nanoparticles and their hydrogen production*. International Journal of Hydrogen Energy, 2021. **46**(12): p. 8578-8593.

-
55. Nachit, W., et al., *Photocatalytic activity of anatase-brookite TiO₂ nanoparticles synthesized by sol gel method at low temperature*. *Optical Materials*, 2022. **129**: p. 112256.
 56. Song, K.C. and S.E. Pratsinis, *Control of phase and pore structure of titania powders using HCl and NH₄OH catalysts*. *Journal of the American Ceramic Society*, 2001. **84**(1): p. 92-98.
 57. Tobaldi, D., et al., *Influence of sol counter-ions on the visible light induced photocatalytic behaviour of TiO₂ nanoparticles*. *Catalysis Science & Technology*, 2014. **4**(7): p. 2134-2146.
 58. Assaker, K., et al., *Water-Catalyzed Low-Temperature Transformation from Amorphous to Semi-Crystalline Phase of Ordered Mesoporous Titania Framework*. *ACS Sustainable Chemistry & Engineering*, 2014. **2**(2): p. 120-125.
 59. Kistler, S.S., *Coherent expanded aerogels and jellies*. *Nature*, 1931. **127**(3211): p. 741-741.
 60. McNaught, A.D. and A. Wilkinson, *Compendium of chemical terminology*. 2nd ed. (the "Gold Book") ed. IUPAC. Vol. 1669. 1997, Oxford: Blackwell Science Oxford.
 61. Pierre, A.C., *History of Aerogels*, in *Aerogels Handbook*, M.A. Aegerter, N. Leventis, and M.M. Koebel, Editors. 2011, Springer New York: New York, NY. p. 3-18.
 62. Smirnova, I. and P. Gurikov, *Aerogel production: Current status, research directions, and future opportunities*. *The Journal of Supercritical Fluids*, 2018. **134**: p. 228-233.
 63. Du, A., et al., *A Special Material or a New State of Matter: A Review and Reconsideration of the Aerogel*. *Materials*, 2013. **6**(3): p. 941-968.
 64. Luna, A.L., et al., *Monolithic metal-containing TiO₂ aerogels assembled from crystalline pre-formed nanoparticles as efficient photocatalysts for H₂ generation*. *Applied Catalysis B: Environmental*, 2020. **267**: p. 118660.
 65. Abbas, Q., et al., *Structural tuneability and electrochemical energy storage applications of resorcinol-formaldehyde-based carbon aerogels*. *International Journal of Energy Research*, 2022. **46**(5): p. 5478-5502.
 66. Qiu, J., et al., *Facile Preparation of Cellulose Aerogels with Controllable Pore Structure*. *Nanomaterials*, 2023. **13**(3): p. 613.
 67. Zhao, Y., Y. Li, and R. Zhang, *Silica aerogels having high flexibility and hydrophobicity prepared by sol-gel method*. *Ceramics International*, 2018. **44**(17): p. 21262-21268.
 68. Lamy-Mendes, A., et al., *Progress in silica aerogel-containing materials for buildings' thermal insulation*. *Construction and Building Materials*, 2021. **286**: p. 122815.
 69. Malakooti, S., et al., *Sound insulation properties in low-density, mechanically strong and ductile nanoporous polyurea aerogels*. *Journal of Non-Crystalline Solids*, 2017. **476**: p. 36-45.
 70. Li, X., et al., *A flexible silica aerogel with good thermal and acoustic insulation prepared via water solvent system*. *Journal of Sol-Gel Science and Technology*, 2019. **92**: p. 652-661.
 71. Zverev, A.Y., *Noise control mechanisms of inside aircraft*. *Acoustical Physics*, 2016. **62**(4): p. 478-482.
 72. Ko, E. and H. Kim, *Preparation of chitosan aerogel crosslinked in chemical and ionic ways by non-acid condition for wound dressing*. *International Journal of Biological Macromolecules*, 2020. **164**: p. 2177-2185.
 73. García-González, C.A., M. Alnaief, and I. Smirnova, *Polysaccharide-based aerogels—Promising biodegradable carriers for drug delivery systems*. *Carbohydrate Polymers*, 2011. **86**(4): p. 1425-1438.
-

74. Mirzaeian, M. and P.J. Hall, *Preparation of controlled porosity carbon aerogels for energy storage in rechargeable lithium oxygen batteries*. *Electrochimica Acta*, 2009. **54**(28): p. 7444-7451.
75. Li, J., et al., *Studies on preparation and performances of carbon aerogel electrodes for the application of supercapacitor*. *Journal of Power Sources*, 2006. **158**(1): p. 784-788.
76. Lin, C.-C., et al., *Titania and Pt/titania aerogels as superior mesoporous structures for photocatalytic water splitting*. *Journal of Materials Chemistry*, 2011. **21**(34): p. 12668-12674.
77. Fujisima, A. and K. Honda, *Photolysis-decomposition of water at surface of an irradiated semiconduction*. *Nature*, 1972. **238**: p. 37-38.
78. Teichner, S.J., et al., *Inorganic oxide aerogels*. *Advances in Colloid and Interface Science*, 1976. **5**(3): p. 245-273.
79. Sadriyeh, S. and R. Malekfar, *The effects of hydrolysis level on structural properties of titania aerogels*. *Journal of Non-Crystalline Solids*, 2017. **457**: p. 175-179.
80. Schäfer, H., B. Milow, and L. Ratke, *Synthesis of inorganic aerogels via rapid gelation using chloride precursors*. *RSC advances*, 2013. **3**(35): p. 15263-15272.
81. Bernardes, J.C., et al., *Enhancing the optical transparency of TiO₂ aerogels with high surface area through water-based synthesis*. *Optical Materials*, 2020. **109**: p. 110359.
82. GmbH, S.-A.C. *SAFETY DATA SHEET Propylene oxide*. 15.04.2023 03.05.2023]; Version 6.9:[Available from: <https://www.sigmaaldrich.com/DE/en/sds/aldrich/82320>.
83. Kwon, J., et al., *Gas-Phase Nitrogen Doping of Monolithic TiO₂ Nanoparticle-Based Aerogels for Efficient Visible Light-Driven Photocatalytic H₂ Production*. *ACS Applied Materials & Interfaces*, 2021. **13**(45): p. 53691-53701.
84. Štengl, V., et al., *Titania aerogel prepared by low temperature supercritical drying*. *Microporous and mesoporous materials*, 2006. **91**(1-3): p. 1-6.
85. Lermontov, S., et al., *An approach for highly transparent titania aerogels preparation*. *Materials Letters*, 2018. **215**: p. 19-22.
86. Qingge, F., et al., *Synthesis and structural characteristics of high surface area TiO₂ aerogels by ultrasonic-assisted sol-gel method*. *Nanotechnology*, 2018. **29**(7): p. 075702.
87. Kolen'ko, Y.V., et al., *Photocatalytic activity of sol-gel derived titania converted into nanocrystalline powders by supercritical drying*. *Journal of Photochemistry and Photobiology A: Chemistry*, 2005. **172**(1): p. 19-26.
88. Doneliene, J., et al., *Effect of Precursor Nature and Sol-Gel Synthesis Conditions on TiO₂ Aerogel's Structure*. *Molecules*, 2021. **26**(16): p. 5090.
89. Guerrero-Araque, D., et al., *SnO₂-TiO₂ structures and the effect of CuO, CoO metal oxide on photocatalytic hydrogen production*. *Journal of Chemical Technology & Biotechnology*, 2017. **92**(7): p. 1531-1539.
90. Ozouf, G. and C. Beauger, *Niobium-and antimony-doped tin dioxide aerogels as new catalyst supports for PEM fuel cells*. *Journal of Materials Science*, 2016. **51**: p. 5305-5320.
91. Baumann, T.F., et al., *Facile synthesis of a crystalline, high-surface-area SnO₂ aerogel*. *Advanced Materials*, 2005. **17**(12): p. 1546-1548.
92. Dong, W. and B. Dunn, *Sol-gel synthesis of monolithic molybdenum oxide aerogels and xerogels*. *Journal of Materials Chemistry*, 1998. **8**(3): p. 665-670.
93. Livage, J., *Sol-gel chemistry and electrochemical properties of vanadium oxide gels*. *Solid State Ionics*, 1996. **86-88**: p. 935-942.
94. Beauger, C., et al., *Doped TiO₂ aerogels as alternative catalyst supports for proton exchange membrane fuel cells: A comparative study of Nb, V and Ta dopants*. *Microporous and Mesoporous Materials*, 2016. **232**: p. 109-118.

95. Wang, L., et al., *Improving the activity and stability of Ir catalysts for PEM electrolyzer anodes by SnO₂: Sb aerogel supports: does V addition play an active role in electrocatalysis?* Journal of Materials Chemistry A, 2017. **5**(7): p. 3172-3178.
96. Sasikala, R., et al., *Highly dispersed phase of SnO₂ on TiO₂ nanoparticles synthesized by polyol-mediated route: photocatalytic activity for hydrogen generation.* International Journal of Hydrogen Energy, 2009. **34**(9): p. 3621-3630.
97. Ramírez-Ortega, D., et al., *Energetic states in SnO₂-TiO₂ structures and their impact on interfacial charge transfer process.* Journal of Materials Science, 2017. **52**(1): p. 260-275.
98. Dong, W. and B. Dunn, *Sol-gel synthesis and characterization of molybdenum oxide gels.* Journal of Non-Crystalline Solids, 1998. **225**: p. 135-140.
99. Schubert, U., *Chemical modification of titanium alkoxides for sol-gel processing.* Journal of Materials Chemistry, 2005. **15**(35-36): p. 3701-3715.
100. Schubert, U., *Ein Vergleich der Chemie von Silicium und Titan: Wie ähnlich können Haupt-und Nebengruppen-Elemente sein?* Chemie in unserer Zeit, 2020. **54**(2): p. 84-92.
101. Pierre, A.C., *Introduction to sol-gel processing.* 2020: Springer Nature.
102. Livage, J., M. Henry, and C. Sanchez, *Sol-gel chemistry of transition metal oxides.* Progress in Solid State Chemistry, 1988. **18**(4): p. 259-341.
103. Kignelman, G. and W. Thielemans, *Synergistic effects of acetic acid and nitric acid in water-based sol-gel synthesis of crystalline TiO₂ nanoparticles at 25° C.* Journal of Materials Science, 2021. **56**(30): p. 16877-16886.
104. Cristoni, S., et al., *Electrospray ionization in the study of the polycondensation of Ti (O-*i*-C₃H₇)₄ and Ti (O-*n*-C₄H₉)₄.* Rapid Communications in Mass Spectrometry, 2000. **14**(8): p. 662-668.
105. Danks, A.E., S.R. Hall, and Z. Schnepf, *The evolution of 'sol-gel' chemistry as a technique for materials synthesis.* Materials Horizons, 2016. **3**(2): p. 91-112.
106. Matter, F., A.L. Luna, and M. Niederberger, *From colloidal dispersions to aerogels: How to master nanoparticle gelation.* Nano Today, 2020. **30**: p. 100827.
107. Niederberger, M., *Nonaqueous Sol-Gel Routes to Metal Oxide Nanoparticles.* Accounts of Chemical Research, 2007. **40**(9): p. 793-800.
108. Schubert, U., *Chemistry and fundamentals of the sol-gel process.* The Sol-Gel Handbook, 2015: p. 1-28.
109. Marchisio, D.L., et al., *Effect of Mixing and Other Operating Parameters in Sol-Gel Processes.* Industrial & Engineering Chemistry Research, 2008. **47**(19): p. 7202-7210.
110. Boujday, S., et al., *Photocatalytic and electronic properties of TiO₂ powders elaborated by sol-gel route and supercritical drying.* Solar Energy Materials and Solar Cells, 2004. **83**(4): p. 421-433.
111. Niu, T., et al., *Synthesis of Monolithic TiO₂ Aerogels With Relatively Low Shrinkage and Improved Formability Assisted by CTAB.* Frontiers in Materials, 2021. **8**.
112. Hu, L., et al., *Effects of solvent on properties of sol-gel-derived TiO₂ coating films.* Thin Solid Films, 1992. **219**(1): p. 18-23.
113. Dong, Y., W. Zhang, and Y. Tao, *CTAB modified TiO₂ supported on HZSM-5 zeolite for enhanced photocatalytic degradation of azophloxine.* Journal of Materials Research and Technology, 2020. **9**(4): p. 9403-9411.
114. Wu, W., et al., *Preparation and photocatalytic activity analysis of nanometer TiO₂ modified by surfactant.* Nanomaterials and Nanotechnology, 2018. **8**: p. 1847980418781973.

115. DeSario, P.A., et al., *Correlating Changes in Electron Lifetime and Mobility on Photocatalytic Activity at Network-Modified TiO₂ Aerogels*. The Journal of Physical Chemistry C, 2015. **119**(31): p. 17529-17538.
116. Gao, L. and Q. Zhang, *Effects of amorphous contents and particle size on the photocatalytic properties of TiO₂ nanoparticles*. Scripta Materialia, 2001. **44**(8): p. 1195-1198.
117. Parayil, S.K., R.J. Psota, and R.T. Koodali, *Modulating the textural properties and photocatalytic hydrogen production activity of TiO₂ by high temperature supercritical drying*. International Journal of Hydrogen Energy, 2013. **38**(25): p. 10215-10225.
118. Hoffmann, M.R., et al., *Environmental applications of semiconductor photocatalysis*. Chemical reviews, 1995. **95**(1): p. 69-96.
119. Zada, A., et al., *Accelerating photocatalytic hydrogen production and pollutant degradation by functionalizing g-C₃N₄ with SnO₂*. Frontiers in Chemistry, 2020. **7**: p. 941.
120. Imtiaz, F., J. Rashid, and M. Xu, *Semiconductor Nanocomposites for Visible Light Photocatalysis of Water Pollutants*. 2019.
121. Liu, Y., et al., *Promoting Photogenerated Holes Utilization in Pore-Rich WO₃ Ultrathin Nanosheets for Efficient Oxygen-Evolving Photoanode*. Advanced Energy Materials, 2016. **6**(23): p. 1600437.
122. Wang, G., et al., *Hydrogen-Treated TiO₂ Nanowire Arrays for Photoelectrochemical Water Splitting*. Nano Letters, 2011. **11**(7): p. 3026-3033.
123. Benu, D.P., et al., *Macroemulsion-mediated synthesis of fibrous ZnO microrods and their surface morphology contribution to the high photocatalytic degradation rate*. New Journal of Chemistry, 2023. **47**(1): p. 428-442.
124. Sasidharan, S., et al., *Insight into the Fabrication and Characterization of Novel Heterojunctions of Fe₂O₃ and V₂O₅ with TiO₂ and Graphene Oxide for Enhanced Photocatalytic Hydrogen Evolution: A Comparison Study*. Industrial & Engineering Chemistry Research, 2022. **61**(7): p. 2714-2733.
125. Bratsch, S.G., *Standard Electrode Potentials and Temperature Coefficients in Water at 298.15 K*. Journal of Physical and Chemical Reference Data, 1989. **18**(1): p. 1-21.
126. Linsebigler, A.L., G. Lu, and J.T. Yates Jr, *Photocatalysis on TiO₂ surfaces: principles, mechanisms, and selected results*. Chemical reviews, 1995. **95**(3): p. 735-758.
127. Naldoni, A., et al., *Effect of nature and location of defects on bandgap narrowing in black TiO₂ nanoparticles*. Journal of the American Chemical Society, 2012. **134**(18): p. 7600-7603.
128. Vequizo, J.J.M., et al., *Trapping-induced enhancement of photocatalytic activity on brookite TiO₂ powders: comparison with anatase and rutile TiO₂ powders*. ACS Catalysis, 2017. **7**(4): p. 2644-2651.
129. Yeh, T.-F., et al., *Graphite Oxide with Different Oxygenated Levels for Hydrogen and Oxygen Production from Water under Illumination: The Band Positions of Graphite Oxide*. The Journal of Physical Chemistry C, 2011. **115**(45): p. 22587-22597.
130. Song, M., et al., *Structural Insight on Defect-Rich Tin Oxide for Smart Band Alignment Engineering and Tunable Visible-Light-Driven Hydrogen Evolution*. Inorganic Chemistry, 2020. **59**(5): p. 3181-3192.
131. Karunakaran, C. and S. Senthilvelan, *Photocatalysis with ZrO₂: oxidation of aniline*. Journal of Molecular Catalysis A: Chemical, 2005. **233**(1): p. 1-8.
132. Li, Y., et al., *Single-layer MoS₂ as an efficient photocatalyst*. Catalysis Science & Technology, 2013. **3**(9): p. 2214-2220.
133. Kudo, A. and Y. Miseki, *Heterogeneous photocatalyst materials for water splitting*. Chemical Society Reviews, 2009. **38**(1): p. 253-278.

-
134. Błędowski, M., et al., *Visible-light photocurrent response of TiO₂-polyheptazine hybrids: Evidence for interfacial charge-transfer absorption*. Physical chemistry chemical physics : PCCP, 2011. **13**: p. 21511-9.
 135. Zhang, J., et al., *New understanding of the difference of photocatalytic activity among anatase, rutile and brookite TiO₂*. Physical Chemistry Chemical Physics, 2014. **16**(38): p. 20382-20386.
 136. Apostolova, I., A. Apostolov, and J. Wesselinowa, *Band Gap Tuning in Transition Metal and Rare-Earth-Ion-Doped TiO₂, CeO₂, and SnO₂ Nanoparticles*. Nanomaterials, 2023. **13**(1): p. 145.
 137. Zhang, X., et al., *Defective Black TiO₂: Effects of Annealing Atmospheres and Urea Addition on the Properties and Photocatalytic Activities*. Nanomaterials, 2021. **11**(10): p. 2648.
 138. Yan, X., Y. Li, and T. Xia, *Black Titanium Dioxide Nanomaterials in Photocatalysis*. International Journal of Photoenergy, 2017. **2017**: p. 8529851.
 139. Bozheyev, F., et al., *Effect of Mo-doping in SnO₂ thin film photoanodes for water oxidation*. International Journal of Hydrogen Energy, 2020. **45**(58): p. 33448-33456.
 140. Yang, Q., et al., *Nanostructured heterogeneous photo-catalysts for hydrogen production and water splitting: A comprehensive insight*. Applied Materials Today, 2019. **17**: p. 159-182.
 141. Lee, S.S., et al., *Electrospun TiO₂/SnO₂ nanofibers with innovative structure and chemical properties for highly efficient photocatalytic H₂ generation*. International journal of hydrogen energy, 2012. **37**(14): p. 10575-10584.
 142. Hurum, D.C., et al., *Explaining the Enhanced Photocatalytic Activity of Degussa P25 Mixed-Phase TiO₂ Using EPR*. The Journal of Physical Chemistry B, 2003. **107**(19): p. 4545-4549.
 143. Nouri, A. and A. Fakhri, *Synthesis, characterization and photocatalytic applications of N-, S-, and C-doped SnO₂ nanoparticles under ultraviolet (UV) light illumination*. Spectrochimica Acta Part A: Molecular and Biomolecular Spectroscopy, 2015. **138**: p. 563-568.
 144. Zaleska, A., *Doped-TiO₂: a review*. Recent patents on engineering, 2008. **2**(3): p. 157-164.
 145. Fang, S., et al., *Photocatalytic hydrogen production over Rh-loaded TiO₂: what is the origin of hydrogen and how to achieve hydrogen production from water?* Applied Catalysis B: Environmental, 2020. **278**: p. 119316.
 146. Panayotov, D.A., et al., *Ultraviolet and Visible Photochemistry of Methanol at 3D Mesoporous Networks: TiO₂ and Au-TiO₂*. The Journal of Physical Chemistry C, 2013. **117**(29): p. 15035-15049.
 147. Khan, M.R., et al., *Schottky barrier and surface plasmonic resonance phenomena towards the photocatalytic reaction: study of their mechanisms to enhance photocatalytic activity*. Catalysis Science & Technology, 2015. **5**(5): p. 2522-2531.
 148. Nakata, K. and A. Fujishima, *TiO₂ photocatalysis: Design and applications*. Journal of Photochemistry and Photobiology C: Photochemistry Reviews, 2012. **13**(3): p. 169-189.
 149. Li, F., et al., *TiO₂-on-C₃N₄ double-shell microtubes: In-situ fabricated heterostructures toward enhanced photocatalytic hydrogen evolution*. Journal of colloid and interface science, 2020. **572**: p. 22-30.
 150. Su, T., et al., *Role of Interfaces in Two-Dimensional Photocatalyst for Water Splitting*. ACS Catalysis, 2018. **8**(3): p. 2253-2276.
 151. Wan, W., et al., *Monolithic aerogel photocatalysts: a review*. Journal of Materials Chemistry A, 2018. **6**(3): p. 754-775.
-

152. Kumar, A., et al., *Three-dimensional carbonaceous aerogels embedded with Rh-SrTiO₃ for enhanced hydrogen evolution triggered by efficient charge transfer and light absorption*. ACS Applied Energy Materials, 2020. **3**(12): p. 12134-12147.
153. Schneider, J., et al., *Understanding TiO₂ Photocatalysis: Mechanisms and Materials*. Chemical Reviews, 2014. **114**(19): p. 9919-9986.
154. Yan, J., et al., *Understanding the effect of surface/bulk defects on the photocatalytic activity of TiO₂: anatase versus rutile*. Physical Chemistry Chemical Physics, 2013. **15**(26): p. 10978-10988.
155. Kong, M., et al., *Tuning the Relative Concentration Ratio of Bulk Defects to Surface Defects in TiO₂ Nanocrystals Leads to High Photocatalytic Efficiency*. Journal of the American Chemical Society, 2011. **133**(41): p. 16414-16417.
156. Gordon, T.R., et al., *Nonaqueous Synthesis of TiO₂ Nanocrystals Using TiF₄ to Engineer Morphology, Oxygen Vacancy Concentration, and Photocatalytic Activity*. Journal of the American Chemical Society, 2012. **134**(15): p. 6751-6761.
157. Bahnemann, D., et al., *Flash photolysis observation of the absorption spectra of trapped positive holes and electrons in colloidal titanium dioxide*. The Journal of Physical Chemistry, 1984. **88**(4): p. 709-711.
158. Mohamed, H.H., et al., *Kinetic and Mechanistic Investigations of Multielectron Transfer Reactions Induced by Stored Electrons in TiO₂ Nanoparticles: A Stopped Flow Study*. The Journal of Physical Chemistry A, 2011. **115**(11): p. 2139-2147.
159. Tong, Z., et al., *Three-dimensional porous aerogel constructed by g-C₃N₄ and graphene oxide nanosheets with excellent visible-light photocatalytic performance*. ACS applied materials & interfaces, 2015. **7**(46): p. 25693-25701.
160. Li, G., Q. Chen, and J. Lan, *Facile synthesis, metastable phase induced morphological evolution and crystal ripening, and structure-dependent photocatalytic properties of 3D hierarchical anatase superstructures*. ACS Applied Materials & Interfaces, 2014. **6**(24): p. 22561-22568.
161. Morris Hotsenpiller, P.A., et al., *Orientation Dependence of Photochemical Reactions on TiO₂ Surfaces*. The Journal of Physical Chemistry B, 1998. **102**(17): p. 3216-3226.
162. Ren, L., et al., *Insights into the pivotal role of surface defects on anatase TiO₂ nanosheets with exposed {001} facets for enhanced photocatalytic activity*. Materials Research Bulletin, 2023. **164**: p. 112255.
163. Ghuman, K.K. and C.V. Singh, *Effect of doping on electronic structure and photocatalytic behavior of amorphous TiO₂*. Journal of Physics: Condensed Matter, 2013. **25**(47): p. 475501.
164. Kaur, K. and C.V. Singh, *Amorphous TiO₂ as a photocatalyst for hydrogen production: a DFT study of structural and electronic properties*. Energy Procedia, 2012. **29**: p. 291-299.
165. Monai, M., T. Montini, and P. Fornasiero, *Brookite: nothing new under the sun?* Catalysts, 2017. **7**(10): p. 304.
166. Wang, Y., et al., *Effect of morphology-induced interfacial defects on band location and enhanced photocatalytic dye degradation activity of TiO₂/Graphene aerogel*. Journal of Physics and Chemistry of Solids, 2022. **162**: p. 110448.
167. Torres-Rodríguez, J., et al., *Titania hybrid carbon spherogels for photocatalytic hydrogen evolution*. Carbon, 2023. **202**: p. 487-494.
168. Chu, J., et al., *Mixed Titanium Oxide Strategy for Enhanced Photocatalytic Hydrogen Evolution*. ACS Applied Materials & Interfaces, 2019. **11**(20): p. 18475-18482.
169. Reddy, N.L., et al., *One-pot synthesis of Cu-TiO₂/CuO nanocomposite: application to photocatalysis for enhanced H₂ production, dye degradation & detoxification of Cr (VI)*. International Journal of Hydrogen Energy, 2020. **45**(13): p. 7813-7828.

170. de Brito, J.F., et al., *Role of CuO in the modification of the photocatalytic water splitting behavior of TiO₂ nanotube thin films*. Applied Catalysis B: Environmental, 2018. **224**: p. 136-145.
171. Jiang, L., et al., *Significantly Enhanced Photocatalytic Hydrogen Evolution over Cu₂O Embedded on TiO₂ Aerogels under Simulated Solar Light Irradiation*. Journal of Materials Science Research and Reviews, 2021. **8**(3): p. 12-23.
172. Xia, Y., et al., *Oxygen-vacancy-assisted construction of Ce–TiO₂ aerogel for efficiently boosting photocatalytic CO₂ reduction without any sacrifice agent*. Ceramics International, 2023. **49**(4): p. 6100-6112.
173. Tang, Z., et al., *Fabrication of TiO₂ @MoS₂ heterostructures with improved visible light photocatalytic activity*. Colloids and Surfaces A: Physicochemical and Engineering Aspects, 2022. **642**: p. 128686.
174. Mkhaldid, I.A., et al., *Visible-light-induced V₂O₅ -TiO₂ photocatalysts with high photocatalytic ability for degradation of tetracycline*. Optical Materials, 2023. **135**: p. 113263.
175. Kim, T., et al., *Facile synthesis of SnO₂ aerogel/reduced graphene oxide nanocomposites via in situ annealing for the photocatalytic degradation of methyl orange*. Nanomaterials, 2019. **9**(3): p. 358.
176. Afuyoni, M., G. Nashed, and I.M. Nasser, *TiO₂ doped with SnO₂ and studying its structural and electrical properties*. Energy Procedia, 2011. **6**: p. 11-20.
177. Chen, L.-C., et al., *Properties of sol–gel SnO₂/TiO₂ electrodes and their photoelectrocatalytic activities under UV and visible light illumination*. Electrochimica Acta, 2009. **54**(4): p. 1304-1311.
178. Emran, K.M. and R.M. Alsahli, *Electrocatalytic Hydrogen Generation using Sn loaded TiO₂ Nanotubes*. International Journal of electrochemical science, 2021. **16**(6).
179. Zakrzewska, K., et al., *Microstructure and photoelectrochemical characterization of the TiO₂–SnO₂ system*. Thin Solid Films, 2005. **490**(1): p. 101-107.
180. Cheng, C., W. Ren, and H. Zhang, *3D TiO₂/SnO₂ hierarchically branched nanowires on transparent FTO substrate as photoanode for efficient water splitting*. Nano Energy, 2014. **5**: p. 132-138.
181. Li, X. and H. Zhu, *Two-dimensional MoS₂: Properties, preparation, and applications*. Journal of Materiomics, 2015. **1**(1): p. 33-44.
182. Li, Z., X. Meng, and Z. Zhang, *Recent development on MoS₂-based photocatalysis: A review*. Journal of Photochemistry and Photobiology C: Photochemistry Reviews, 2018. **35**: p. 39-55.
183. Li, Y.-Y., et al., *Heterostructured SnS₂/SnO₂ nanotubes with enhanced charge separation and excellent photocatalytic hydrogen production*. International Journal of Hydrogen Energy, 2018. **43**(31): p. 14121-14129.
184. Liu, C., et al., *Vertical single or few-layer MoS₂ nanosheets rooting into TiO₂ nanofibers for highly efficient photocatalytic hydrogen evolution*. Applied Catalysis B: Environmental, 2015. **164**: p. 1-9.
185. Zhang, Q., et al., *Multi-layered mesh-like MoS₂ hierarchical nanostructure fabricated on Ti foil: an efficient noble metal-free photocatalyst for visible-light-driven H₂ evolution from water*. Catalysis Communications, 2016. **82**: p. 7-10.
186. Yu-Cheng, C. and L. Yu-Wen, *MoS₂@ SnO₂ core-shell sub-microspheres for high efficient visible-light photodegradation and photocatalytic hydrogen production*. Materials Research Bulletin, 2020. **129**: p. 110912.
187. Rani, A., et al., *Visible light driven photocatalysis of organic dyes using SnO₂ decorated MoS₂ nanocomposites*. Chemical Physics Letters, 2020. **738**: p. 136874.

188. Afanasiev, P., *MoS₂ “inorganic fullerenes” combined with TiO₂ in water-methanol suspensions: Highly active hydrogen production photo catalysts operating via transfer of accumulated electrons*. International Journal of Hydrogen Energy, 2020. **45**(29): p. 14696-14712.
189. Paul, K.K., et al., *Strongly enhanced visible light photoelectrocatalytic hydrogen evolution reaction in an n-doped MoS₂/TiO₂(B) heterojunction by selective decoration of platinum nanoparticles at the MoS₂ edge sites*. Journal of Materials Chemistry A, 2018. **6**(45): p. 22681-22696.
190. Zhang, Y., et al., *C-doped hollow TiO₂ spheres: in situ synthesis, controlled shell thickness, and superior visible-light photocatalytic activity*. Applied Catalysis B: Environmental, 2015. **165**: p. 715-722.
191. Mallikarjuna, K., et al., *Synthesis of carbon-doped SnO₂ nanostructures for visible-light-driven photocatalytic hydrogen production from water splitting*. International Journal of Hydrogen Energy, 2020. **45**(57): p. 32789-32796.
192. Kernazhitsky, L., et al., *A comparative study of optical absorption and photocatalytic properties of nanocrystalline single-phase anatase and rutile TiO₂ doped with transition metal cations*. Journal of Solid State Chemistry, 2013. **198**: p. 511-519.
193. Wen, J., et al., *Photocatalysis fundamentals and surface modification of TiO₂ nanomaterials*. Chinese Journal of Catalysis, 2015. **36**(12): p. 2049-2070.
194. Hossen, M.R., et al., *A comparative study of methods for porosity determination of cellulose based porous materials*. Cellulose, 2020. **27**(12): p. 6849-6860.
195. Rose, A., et al., *Photocatalytic Activity and Electron Storage Capability of TiO₂ Aerogels with an Adjustable Surface Area*. ACS Applied Energy Materials, 2022. **5**(12): p. 14966-14978.
196. Thommes, M., et al., *Physisorption of gases, with special reference to the evaluation of surface area and pore size distribution (IUPAC Technical Report)*. Pure and applied chemistry, 2015. **87**(9-10): p. 1051-1069.
197. Fultz, B. and J.M. Howe, *Transmission electron microscopy and diffractometry of materials*. 2012: Springer Science & Business Media.
198. Thomas, J. and T. Gemming, *Analytical transmission electron microscopy: an introduction for operators*. 2014: Springer Science & Business.
199. Niilisk, A., et al., *Structural study of TiO₂ thin films by micro-Raman spectroscopy*. Central European Journal of Physics, 2006. **4**: p. 105-116.
200. Balachandran, U. and N. Eror, *Raman spectra of titanium dioxide*. Journal of Solid State Chemistry, 1982. **42**(3): p. 276-282.
201. Ohsaka, T., S. Yamaoka, and O. Shimomura, *Effect of hydrostatic pressure on the Raman spectrum of anatase (TiO₂)*. Solid State Communications, 1979. **30**(6): p. 345-347.
202. Kelly, S., F.H. Pollak, and M. Tomkiewicz, *Raman spectroscopy as a morphological probe for TiO₂ aerogels*. The Journal of Physical Chemistry B, 1997. **101**(14): p. 2730-2734.
203. Swamy, V., et al., *Finite-size and pressure effects on the Raman spectrum of nanocrystalline anatase TiO₂*. Physical Review B, 2005. **71**(18): p. 184302.
204. Pigeot-Rémy, S., et al., *Size and shape effect on the photocatalytic efficiency of TiO₂ brookite*. Journal of Materials Science, 2019. **54**(2): p. 1213-1225.
205. Tompsett, G., et al., *The Raman spectrum of brookite, TiO₂ (PBCA, Z= 8)*. Journal of Raman Spectroscopy, 1995. **26**(1): p. 57-62.
206. Hu, Y., H.-L. Tsai, and C.-L. Huang, *Effect of brookite phase on the anatase–rutile transition in titania nanoparticles*. Journal of the European Ceramic Society, 2003. **23**(5): p. 691-696.

-
207. Heimo Schnablegger, Y.S., *The SAXS Guide - Getting acquainted with the principles* 4th edition ed. 2017, Austria: Anton Paar GmbH.
208. Scherdel, C., et al., *Advances in the Development of Sol-Gel Materials Combining Small-Angle X-ray Scattering (SAXS) and Machine Learning (ML)*. Processes, 2021. **9**(4): p. 672.
209. Cao, Z., et al., *Doping of chlorine from a neoprene adhesive enhances degradation efficiency of dyes by structured TiO₂-coated photocatalytic fabrics*. Catalysts, 2020. **10**(1): p. 69.
210. Philippe, B., et al., *Valence level character in a mixed perovskite material and determination of the valence band maximum from photoelectron spectroscopy: variation with photon energy*. The Journal of Physical Chemistry C, 2017. **121**(48): p. 26655-26666.
211. Yoldas, B.E., *Hydrolysis of titanium alkoxide and effects of hydrolytic polycondensation parameters*. Journal of Materials Science, 1986. **21**(3): p. 1087-1092.
212. Gau, H.-M., et al., *Chemistry of Ti(OiPr)Cl₃ with Chloride and Oxygen-Containing Ligands: The Roles of Alkoxide and Solvents in the Six-Coordinate Titanium Complexes*. Journal of the American Chemical Society, 1996. **118**(12): p. 2936-2941.
213. Wu, Y.-T., et al., *Stepwise Reactions of TiCl₄ and Ti(OiPr)Cl₃ with 2-Propanol. Variable-Temperature NMR Studies and Crystal Structures of [TiCl₂(OiPr)(HOiPr)(μ-Cl)]₂ and [TiCl₂(OiPr)(HOiPr)(μ-OiPr)]₂*. Inorganic Chemistry, 1996. **35**(20): p. 5948-5952.
214. El Mir, L., et al., *Preparation and optical characterization of transparent, microporous TiO₂ xerogel monoliths*. Materials Science and Engineering: B, 2008. **146**(1-3): p. 69-73.
215. Gizli, N., S.S. Çok, and F. Koç, *Chapter 7 - Aerogel, xerogel, and cryogel: Synthesis, surface chemistry, and properties—Practical environmental applications and the future developments*, in *Advanced Materials for Sustainable Environmental Remediation*, D. Giannakoudakis, L. Meili, and I. Anastopoulos, Editors. 2022, Elsevier. p. 195-229.
216. Yu, J., et al., *Effects of acidic and basic hydrolysis catalysts on the photocatalytic activity and microstructures of bimodal mesoporous titania*. Journal of Catalysis, 2003. **217**(1): p. 69-78.
217. Wu, L., et al., *Preparation of a highly active nanocrystalline TiO₂ photocatalyst from titanium oxo cluster precursor*. Journal of Solid State Chemistry, 2004. **177**(7): p. 2584-2590.
218. Laksmono, J.A., et al., *Adsorption capacity study of ethanol-water mixture for zeolite, activated carbon, and polyvinyl alcohol*. IOP Conference Series: Earth and Environmental Science, 2018. **105**(1): p. 012025.
219. Kubota, S., et al., *Selectivity on Ion Transport across Bilayer Lipid Membranes in the Presence of Gramicidin A*. Analytical Sciences, 2009. **25**(2): p. 189-193.
220. Pazhamalai, P., et al., *Blue TiO₂ nanosheets as a high-performance electrode material for supercapacitors*. Journal of Colloid and Interface Science, 2019. **536**: p. 62-70.
221. Mettry, M.Y., et al., *Transparent Polyimide Aerogels: Controlled Porosity via Minimizing the Phase Separation*. ACS Applied Polymer Materials, 2022. **4**(11): p. 8065-8072.
222. Shi, B., et al., *Preparation and Properties of Highly Transparent SiO₂ Aerogels for Thermal Insulation*. Gels, 2022. **8**(11): p. 744.
223. Degan, G. and M. Tomkiewicz, *TiO₂ Aerogels for Photocatalytic Decontamination of Aquatic Environment*. J. Phy. Chem, 1993. **97**: p. 12651-12655.
224. Woignier, T., et al., *Fractal Structure in Silica and Composites Aerogels*. Gels, 2021. **7**(1): p. 1.
-

225. Simonsen, M.E. and E.G. Sjøgaard, *Identification of Ti Clusters during Nucleation and Growth of Sol–Gel-Derived TiO₂ Nanoparticles*. European Journal of Mass Spectrometry, 2013. **19**(4): p. 265-273.
226. Brenner, A.M., et al., *Porosity by small-angle X-ray scattering (SAXS): comparison with results from mercury penetration and nitrogen adsorption*. Journal of non-crystalline solids, 1995. **185**(1-2): p. 73-77.
227. Schuster, E., et al., *Using SAXS to Reveal the Degree of Bundling in the Polysaccharide Junction Zones of Microrheologically Distinct Pectin Gels*. Biomacromolecules, 2011. **12**(7): p. 2583-2590.
228. Burger, V.M., D.J. Arenas, and C.M. Stultz, *A Structure-free Method for Quantifying Conformational Flexibility in proteins*. Scientific Reports, 2016. **6**(1): p. 29040.
229. Noda, T., et al., *Preparation, characterization, and dilute solution properties of four-branched cage-shaped poly (ethylene oxide)*. Journal of Polymer Science, 2020. **58**(15): p. 2098-2107.
230. Radu, M. and T. Schilling, *Solvent hydrodynamics speed up crystal nucleation in suspensions of hard spheres*. Europhysics Letters, 2014. **105**(2): p. 26001.
231. Walter, D., *Primary particles–agglomerates–aggregates*. Nanomaterials, 2013: p. 9-24.
232. So, W.W., et al., *The crystalline phase stability of titania particles prepared at room temperature by the sol-gel method*. Journal of Materials Science, 2001. **36**(17): p. 4299-4305.
233. Cardew, P.T., *Ostwald Rule of Stages—Myth or Reality?* Crystal Growth & Design, 2023. **23**(6): p. 3958-3969.
234. Briggs, D. and J. Grant, *XPS: Basic principles, spectral features and qualitative analysis*. Surface analysis by Auger and X-ray photoelectron spectroscopy, 2003: p. 31-56.
235. Moitzheim, S., et al., *Chlorine Doping of Amorphous TiO₂ for Increased Capacity and Faster Li⁺-Ion Storage*. Chemistry of Materials, 2017. **29**(23): p. 10007-10018.
236. Wang, X.-K., et al., *Sonochemical synthesis and characterization of Cl-doped TiO₂ and its application in the photodegradation of phthalate ester under visible light irradiation*. Chemical Engineering Journal, 2012. **189-190**: p. 288-294.
237. Filippatos, P.-P., et al., *Preparation of hydrogen, fluorine and chlorine doped and co-doped titanium dioxide photocatalysts: a theoretical and experimental approach*. Scientific Reports, 2021. **11**(1): p. 5700.
238. Henry, M., J.P. Jolivet, and J. Livage, *Aqueous chemistry of metal cations: hydrolysis, condensation and complexation*. Chemistry, Spectroscopy and Applications of Sol-Gel Glasses, 1992: p. 153-206.
239. Nikkanen, J.-P., T. Kanerva, and T. Mäntylä, *The effect of acidity in low-temperature synthesis of titanium dioxide*. Journal of crystal growth, 2007. **304**(1): p. 179-183.
240. Nikkanen, J.-P., et al., *Effect of 2-propanol and water contents on the crystallization and particle size of titanium dioxide synthesized at low-temperature*. Ceramics International, 2014. **40**(3): p. 4429-4435.
241. Guillemot, F., et al., *Ti⁴⁺ to Ti³⁺ conversion of TiO₂ uppermost layer by low-temperature vacuum annealing: interest for titanium biomedical applications*. Journal of colloid and interface Science, 2002. **255**(1): p. 75-78.
242. Barsoum, M., *Fundamentals of ceramics*. 2nd edition ed. Materials Science and Engineering. 2019: CRC press.
243. Cottineau, T., et al., *Intermediate band in the gap of photosensitive hybrid gel based on titanium oxide: role of coordinated ligands during photoreduction*. Journal of Materials Chemistry A, 2014. **2**(29): p. 11499-11508.

-
244. Ganharul, G.K.Q., et al., *Disclosing the hidden presence of Ti³⁺ ions in different TiO₂ crystal structures synthesized at low temperature and photocatalytic evaluation by methylene blue photobleaching*. Journal of Materials Research, 2021. **36**(16): p. 3353-3365.
245. Suriye, K., P. Praserttham, and B. Jongsomjit, *Control of Ti³⁺ surface defect on TiO₂ nanocrystal using various calcination atmospheres as the first step for surface defect creation and its application in photocatalysis*. Applied Surface Science, 2007. **253**(8): p. 3849-3855.
246. Barr, T.L. and S. Seal, *Nature of the use of adventitious carbon as a binding energy standard*. Journal of Vacuum Science & Technology A: Vacuum, Surfaces, and Films, 1995. **13**(3): p. 1239-1246.
247. Ojha, S., *Chapter 7 - Features of chemical properties of metal oxide glass nanocomposites*, in *Metal Oxide Glass Nanocomposites*, S. Bhattacharya, Editor. 2020, Elsevier. p. 147-157.
248. Sato, N., *CHAPTER 2 - THE ENERGY LEVEL OF ELECTRONS*, in *Electrochemistry at Metal and Semiconductor Electrodes*, N. Sato, Editor. 1998, Elsevier Science: Amsterdam. p. 15-59.
249. Bledowski, M., et al., *Visible-light photocurrent response of TiO₂-polyheptazine hybrids: Evidence for interfacial charge-transfer absorption*. Physical Chemistry Chemical Physics, 2011. **13**(48): p. 21511-21519.
250. Howard, C.J., T.M. Sabine, and F. Dickson, *Structural and thermal parameters for rutile and anatase*. Acta Crystallographica Section B, 1991. **47**(4): p. 462-468.
251. Xiong, L.-B., et al., *Ti³⁺ in the surface of titanium dioxide: generation, properties and photocatalytic application*. Journal of Nanomaterials, 2012. **2012**: p. 9-9.
252. Xiao-Quan, C., L. Huan-Bin, and G. Guo-Bang, *Preparation of nanometer crystalline TiO₂ with high photo-catalytic activity by pyrolysis of titanyl organic compounds and photo-catalytic mechanism*. Materials Chemistry and Physics, 2005. **91**(2-3): p. 317-324.
253. Lu, G., A. Linsebigler, and J.T. Yates Jr, *Ti³⁺ defect sites on TiO₂ (110): production and chemical detection of active sites*. The Journal of Physical Chemistry, 1994. **98**(45): p. 11733-11738.
254. Trapalis, C., et al., *Sol-gel processing of titanium-containing thin coatings: Part II XPS Studies*. Journal of materials science, 1993. **28**: p. 1276-1282.
255. González-Elipe, A.R., et al., *Chemical changes in titanate surfaces induced by Ar⁺ ion bombardment*. Surface and Interface Analysis, 1992. **19**(1-12): p. 286-290.
256. Ng, C., et al., *Influence of annealing temperature of WO₃ in photoelectrochemical conversion and energy storage for water splitting*. ACS Applied Materials & Interfaces, 2013. **5**(11): p. 5269-5275.
257. Puskelova, J., et al., *Photocatalytic hydrogen production using TiO₂-Pt aerogels*. Chemical Engineering Journal, 2014. **242**: p. 96-101.
258. Ikeda, S., et al., *Quantitative analysis of defective sites in titanium (IV) oxide photocatalyst powders*. Physical Chemistry Chemical Physics, 2003. **5**(4): p. 778-783.
259. Shahriary, L. and A.A. Athawale, *Graphene oxide synthesized by using modified hummers approach*. Int. J. Renew. Energy Environ. Eng, 2014. **2**(01): p. 58-63.
260. Ahmad, N.A., et al., *The Role of Functional Nanomaterials for Wastewater Remediation*, in *Functional Hybrid Nanomaterials for Environmental Remediation*, A.F. Ismail and P.S. Goh, Editors. 2021, The Royal Society of Chemistry. p. 0.
261. Forster, J., *Funktionalisierung molekularer Vanadium-Oxo-Cluster durch Einbau redoxaktiver Übergangsmetalle*. 2014, Friedrich-Alexander-Universität Erlangen-Nürnberg (FAU).
-

9 Appendix

9.1 Chemicals

Table 9.1-1: Used chemicals for synthesis and characterization. All chemicals were used as received, if not stated otherwise.

Chemical	CAS-Nr.	Manufacturer	Purity
Titanium (IV) tetraisopropoxide	546-68-9	Merck	98%
Hydrochloric acid	7647-01-0	Sigma Aldrich	37%, ACS reagent
<i>i</i> PrOH	67-63-0	Chemsolute	99.8%
EtOH	64-17-5	Roth	>99.9%, ROTISOLV HPLC gradient grade
denatured EtOH	64-17-5	Chemsolute	>99.8%, MEK, IPA und Bitrex®
tin isopropoxide	1184-61-8	Alfa aesar	99% metal basis 10w/v% in <i>i</i> PrOH
vanadium oxytriisopropoxide	5588-84-1	Alfa aesar	96%
MoS ₂	1317-33-5	Sigma-Aldrich	nanopowder $\varnothing=90$ nm, 99% trace metals basis
graphene oxide		Nanografi Nanotechnology AS	2-5 Layer, $\varnothing=7,5$ μm , S _{BET} =420 m ² /g
Cerium (IV) oxide	1306-38-3	Alfa Aesar	REacton®, 99.99% (REO)

9.2 Synthesis Parameters

9.2.1 EtOH Solvent-Based Aerogels

Table 9.2-1: Synthesis parameters of EtOH solvent-based aerogels.

Sample	Equivalents of TTIP:EtOH:HCl:H ₂ O
E1-acid0.05	1:26:0.05:4
E2	1:26:0.11:4
E3	1:26:0.17:4
E4	1:26:0.22:4
E4.1	1:26:0.22:8
E5	1:26:0.27:4
E5.1	1:26:0.27:10
E6	1:26:0.33:4
E6.1	1:26:0.33:12

9.2.2 *i*PrOH Solvent-Based AerogelsTable 9.2-2: Synthesis parameter of *i*PrOH solvent-based aerogels.

Sample	Equivalents of TTIP: <i>i</i> PrOH:HCl:H ₂ O
<i>i</i> P1	1:35:0.05:4
<i>i</i> P2	1:35:0.11:4
<i>i</i> P3	1:35:0.17:4
<i>i</i> P4	1:35:0.22:4
<i>i</i> P4.1	1:35:0.22:8
<i>i</i> P5	1:35:0.27:4
<i>i</i> P5.1	1:35:0.27:10
<i>i</i> P6	1:35:0.33:4
<i>i</i> P6.1	1:35:0.33:12

Table 9.2-3: Synthesis parameter of preliminary experiments of *i*PrOH solvent-based aerogels.

Sample	Equivalents of TTIP: <i>i</i> PrOH:HCl:H ₂ O
<i>i</i> P7.1	1:30:0.05:4
<i>i</i> P7.2	1:30:0.11:4
<i>i</i> P7.3	1:30:0.17:4
<i>i</i> P7.4	1:30:0.22:4
<i>i</i> P7.5	1:30:0.27:4
<i>i</i> P8.1	1:40:0.05:4
<i>i</i> P8.2	1:40:0.11:4
<i>i</i> P8.3	1:40:0.17:4
<i>i</i> P8.4	1:40:0.22:4
<i>i</i> P8.5	1:40:0.27:4
<i>i</i> P9.1	1:45:0.05:4
<i>i</i> P9.2	1:45:0.11:4
<i>i</i> P9.3	1:45:0.17:4
<i>i</i> P9.4	1:45:0.22:4
<i>i</i> P9.5	1:45:0.27:4
<i>i</i> P10.1	1:45:0.05:2
<i>i</i> P10.2	1:45:0.11:2
<i>i</i> P10.3	1:45:0.22:2
<i>i</i> P11.1	1:45:0.05:8
<i>i</i> P11.2	1:45:0.11:8
<i>i</i> P11.3	1:45:0.22:8

9.2.3 Mixed Solvent-Based Aerogels

Table 9.2-4: Synthesis parameters of mixed solvent-based aerogels. In all cases EtOH was added first to the TTIP precursor before *i*PrOH was added. For sample E-*i*P4 to E-*i*P6 water was added diluted in small amounts of solvent, but keeping the total amount of solvent constant.

Sample	Equivalents TTIP:solvent:HCl:H ₂ O	EtOH: <i>i</i> PrOH
E- <i>i</i> P 1	1:26:0.11:4	1:10
E- <i>i</i> P 2	1:26:0.11:4	1:7
E- <i>i</i> P 3	1:26:0.11:4	1:5
E- <i>i</i> P 4	1:26:0.11:4	1:3
E- <i>i</i> P 5	1:26:0.11:4	1:1
E- <i>i</i> P 6	1:26:0.11:4	3:1
E- <i>i</i> P 7	1:26:0.11:4	5:1
E- <i>i</i> P 8	1:26:0.11:4	7:1
E- <i>i</i> P 9	1:26:0.11:4	10:1

9.2.4 Calcined Aerogels

Table 9.2-5: Calcination parameters of EtOH solvent-based aerogels. The aerogels calcined at 300 to 500 °C for 10 hours in air are based on denatured EtOH as solvent in the synthesis. The other calcined samples are based on absol. EtOH as solvent.

Sample	atmosphere	Temperature / °C	Duration / h
E2-A-300-2	air	300	2
E2-A-300-4	air	300	4
E2-A-300-10	air	300	10
E2-A-400-10	air	400	10
E2-A-500-10	air	500	10
E2-V-300-2	vacuum	300	2
E2-V-300-4	vacuum	300	4

9.3 Preliminary Experiments of *i*PrOH Solvent-Based Aerogels

9.3.1 Gelation and Shrinkage Behavior

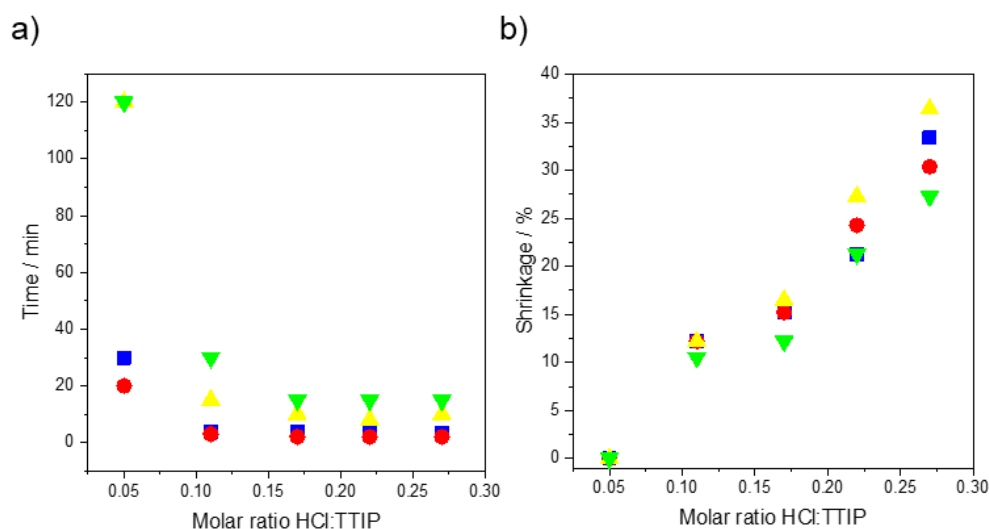


Figure 9.3-1: a) Gelation time and b) shrinkage of *i*P7.1 to *i*P7.5 (blue; *i*PrOH:TTIP 30:1), *i*P8.1 to *i*P8.5 (yellow; *i*PrOH:TTIP 40:1), *i*P9.1 to *i*P9.5 (green; *i*PrOH:TTIP 45:1) and *i*P1 to *i*P5 (red, *i*PrOH:TTIP 35:1) at different HCl molar ratios (HCl:TTIP 0.05:1 to 0.27:1).

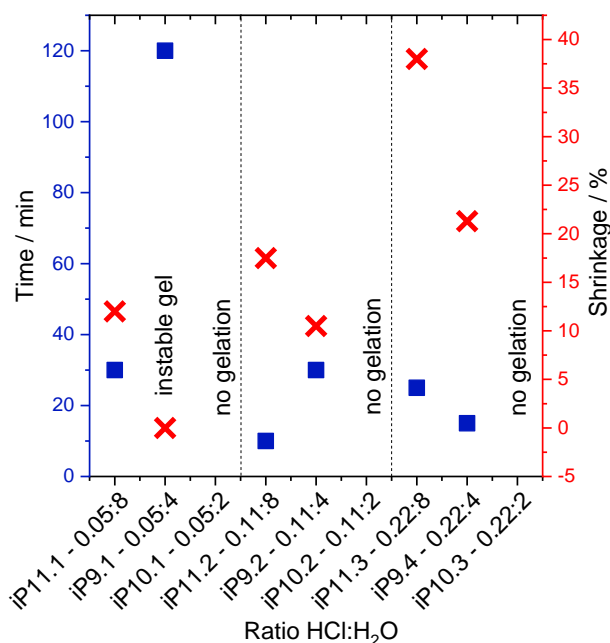


Figure 9.3-2: Gelation time and shrinkage of *i*P9.1 to *i*P9.4, *i*P10.1 to *i*P10.3, and *i*P11.1 to *i*P11.3 (TTIP:*i*PrOH 1:45) at different HCl/H₂O molar ratios.

9.3.2 Density and Porosity

Table 9.3-1: Skeletal density and porosity values of aerogels *iP7.2* (*iPrOH*:*TTIP* 30:1), *iP2* (*iPrOH*:*TTIP* 35:1), *iP8.2* (*iPrOH*:*TTIP* 40:1), *iP9.2* (*iPrOH*:*TTIP* 45:1).

Sample	Skeletal density / g·cm ⁻³	Porosity / %
<i>iP7.2</i>	2.892±0.010	93.6±0.6
<i>iP2</i>	1.895±0.009	90.6±0.9
<i>iP8.2</i>	2.571±0.009	92.4±0.7
<i>iP9.2</i>	2.712±0.004	92.7±0.7

Table 9.3-2: Skeletal density and porosity values of aerogels *iP11.1* to *iP11.3* (*iPrOH*:*TTIP* 45:1) with increasing amount of acid from *iP11.1* to *iP11.3*.

Sample	Skeletal density / g·cm ⁻³	Porosity / %
<i>iP11.1</i>	2.696±0.010	93.1±0.7
<i>iP11.2</i>	2.710±0.004	92.6±0.7
<i>iP11.3</i>	2.711±0.018	79.1±1.8

9.3.3 Surface and Pore Characteristics

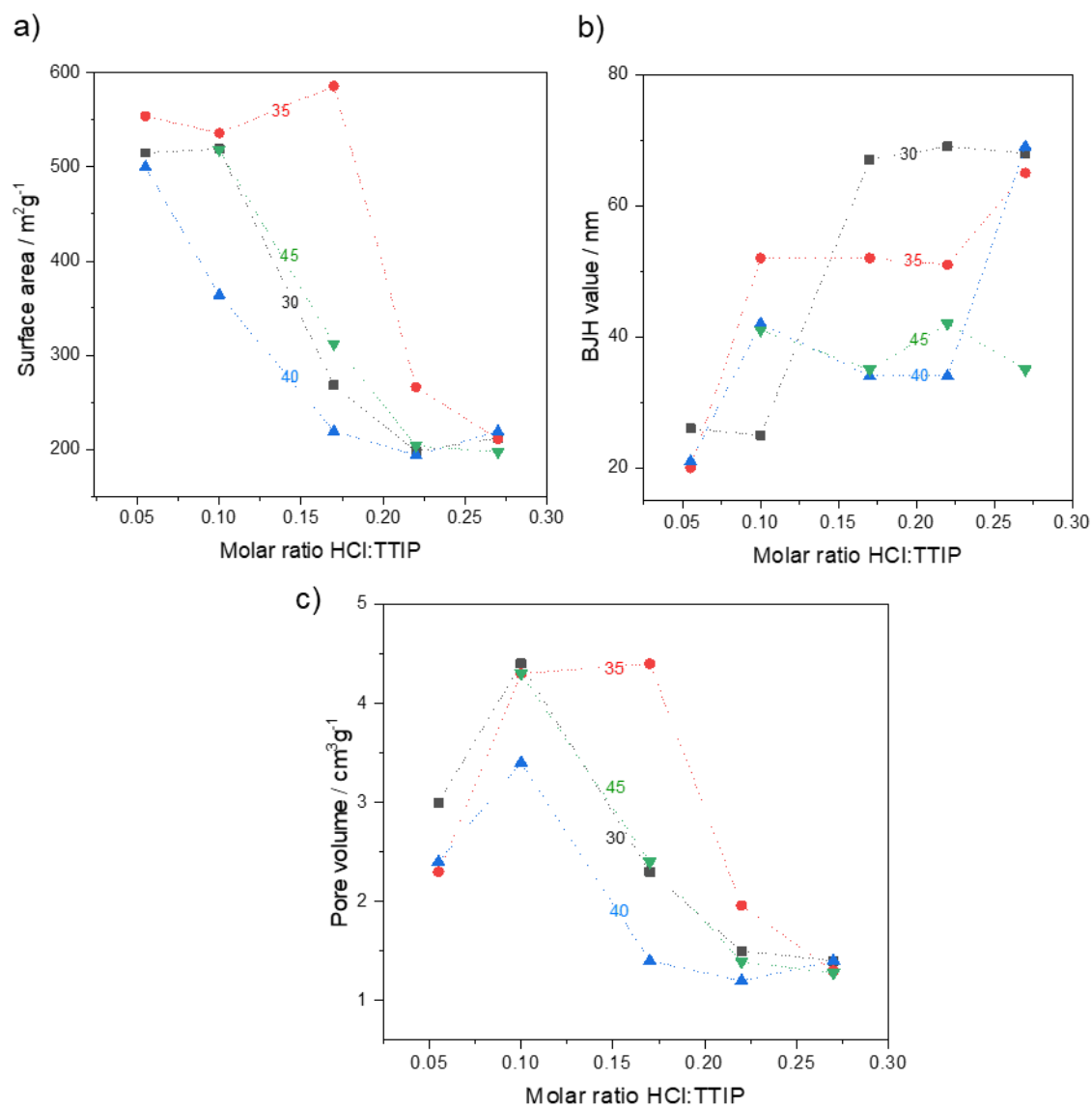


Figure 9.3-3: a) Surface area b) BJH value and c) pore volume of *iP7.1* to *iP7.5* (black; *iPrOH*:*TTIP* 30:1), *iP8.1* to *iP8.5* (blue; *iPrOH*:*TTIP* 40:1), *iP9.1* to *iP9.5* (green; *iPrOH*:*TTIP* 45:1) and *iP1* to *iP5* (red, *iPrOH*:*TTIP* 35:1) at different HCl molar ratios (HCl:*TTIP* 0.05:1 to 0.27:1).

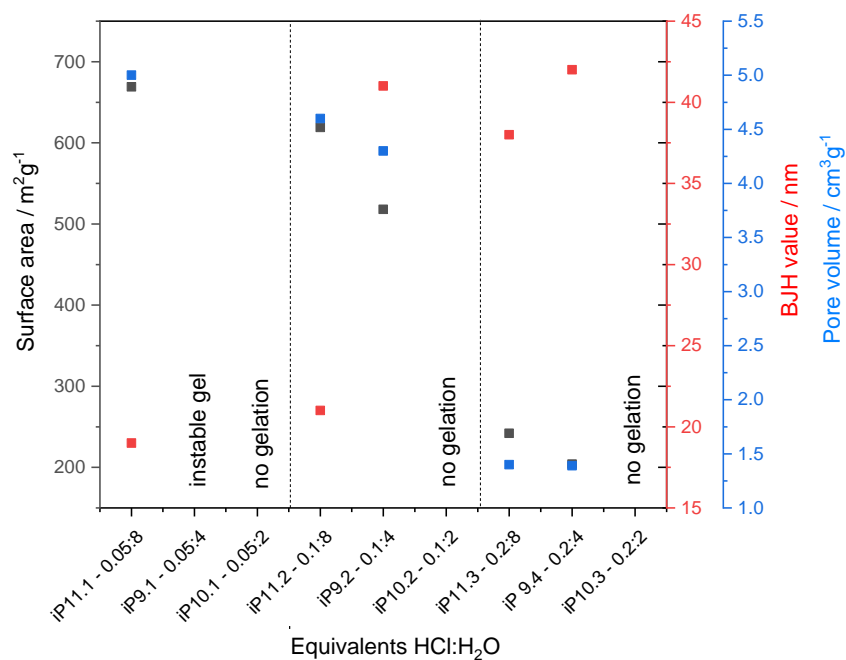


Figure 9.3-4: Surface area (black), BJH value (red) and pore volume (blue) of *iP9.1* to *iP9.4*, *iP10.1* to *iP10.3*, and *iP11.1* to *iP11.3* (TTIP:*iPrOH* 1:45) at different HCl/H₂O molar ratios.

9.3.4 Crystallinity and Phases

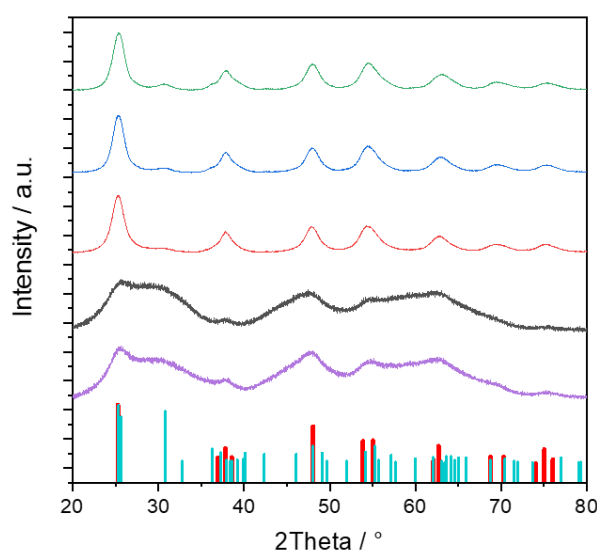


Figure 9.3-5: Diffractograms of aerogel samples *iP7.1*-*iP7.5* with increasing amount of acid from bottom to the top (Equivalents TTIP:*iPrOH*:HCl:H₂O 1:30:0.05-0.27:4) with reference reflection positions of anatase (red), brookite (cyan). Normalized data related to the highest signal.

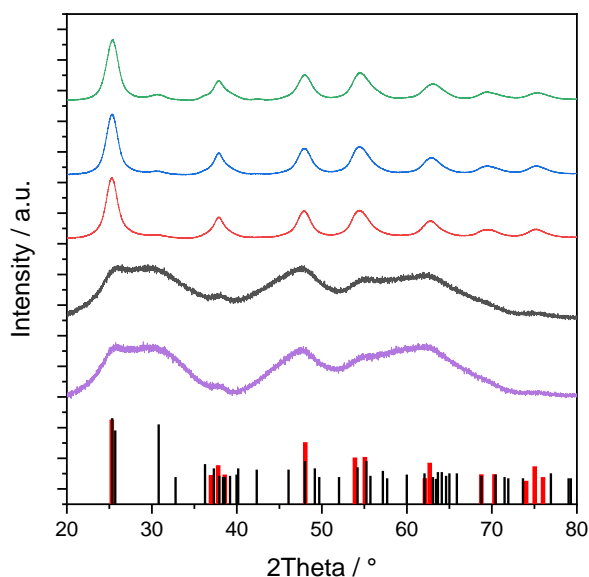


Figure 9.3-6: Diffractograms of aerogel samples *iP8.1-iP8.5* with increasing amount of acid from bottom to the top (Equivalents TTIP:*i*PrOH:HCl:H₂O 1:40:0.05-0.27:4) with reference reflection positions of anatase (red), brookite (black). Normalized data related to the highest signal.

9.4 XRD Reference Reflection Positions

Table 9.4-1: Anatase reflections positions, d-spacing and Miller indices (*hkl*), PDF 12-1272, CuK α = 1,54060 Å.

d spacing / Å	2 θ / °	Intensity	<i>h</i>	<i>k</i>	<i>l</i>
3.52	25.281	1000	1	0	1
2.431	36.947	145	1	0	3
2.378	37.801	296	0	0	4
2.332	38.576	151	1	1	2
1.892	48.05	651	2	0	0
1.6999	53.891	414	1	0	5
1.6665	55.062	423	2	1	1
1.493	62.121	95	2	1	3
1.4808	62.69	333	2	0	4
1.3641	68.762	155	1	1	6
1.3378	70.311	158	2	2	0
1.2795	74.031	55	1	0	7
1.2649	75.032	279	2	1	5
1.2509	76.02	113	3	0	1
1.1894	80.727	60	0	0	8
1.1725	82.139	60	3	0	3
1.1664	82.662	181	2	2	4
1.1608	83.149	122	3	1	2
1.06	93.221	67	2	1	7
1.0517	94.182	134	3	0	5
1.0436	95.143	135	3	2	1

1.0182	98.319	70	1	0	9
1.007	99.804	70	2	0	8
0.9967	101.221	71	3	2	3
0.9555	107.448	148	3	1	6
0.9464	108.963	149	4	0	0
0.9246	112.841	77	3	0	7
0.9192	113.861	77	3	2	5
0.9138	114.909	77	4	1	1
0.8966	118.439	157	2	1	9

Table 9.4-2: Brookite reflection positions, d-spacing and Miller indices (*hkl*), PDF 16-0617, CuK α = 1,54060 Å.

d spacing / Å	2 θ / °	Intensity	<i>h</i>	<i>k</i>	<i>l</i>
3.512	25.34	917	1	2	0
3.465	25.689	744	1	1	1
2.9	30.808	999	1	2	1
2.729	32.791	48	2	0	0
2.476	36.252	326	0	1	2
2.409	37.297	241	2	0	1
2.37	37.934	82	1	3	1
2.344	38.371	55	2	2	0
2.332	38.576	56	2	1	1
2.296	39.205	85	0	4	0
2.254	39.967	115	1	1	2
2.244	40.153	259	0	2	2
2.133	42.34	242	2	2	1
1.969	46.06	262	0	3	2
1.893	48.023	511	2	3	1
1.851	49.184	314	1	3	2
1.833	49.699	71	2	1	2
1.757	52.006	74	2	4	0
1.691	54.198	381	3	2	0
1.662	55.224	582	2	4	1
1.649	55.697	118	1	5	1
1.61	57.168	280	1	1	3
1.597	57.677	41	2	3	2
1.541	59.983	168	1	2	3
1.494	62.075	216	0	5	2
1.473	63.06	88	1	6	0
1.466	63.396	220	3	1	2
1.461	63.639	265	2	5	1
1.452	64.08	267	2	0	3
1.442	64.578	134	1	3	3
1.434	64.982	225	2	1	3
1.417	65.86	228	1	6	1
1.364	68.768	142	4	0	0
1.336	70.42	193	3	3	2
1.319	71.465	98	4	0	1
1.312	71.906	50	2	3	3

1.285	73.662	51	0	0	4
1.238	76.956	261	0	2	4
1.211	79.001	54	4	3	1

Table 9.4-3: Rutile reflection positions, d-spacing and Miller indices (*hkl*), PDF 21-1276, CuK α = 1,54060 Å.

d spacing / Å	2 θ / °	Intensity	<i>h</i>	<i>k</i>	<i>l</i>
3.247	27.447	866	1	1	0
2.487	36.086	565	1	0	1
2.297	39.188	98	2	0	0
2.188	41.226	322	1	1	1
2.054	44.052	137	2	1	0
1.6874	54.323	999	2	1	1
1.6237	56.642	347	2	2	0
1.4797	62.742	190	0	0	2
1.4528	64.04	194	3	1	0
1.4243	65.48	40	2	2	1
1.3598	69.01	414	3	0	1
1.3465	69.79	251	1	1	2
1.3041	72.41	44	3	1	1
1.2739	74.411	23	3	2	0
1.2441	76.51	91	2	0	2
1.2006	79.822	47	2	1	2
1.1702	82.335	145	3	2	1
1.1483	84.26	98	4	0	0
1.1143	87.464	51	4	1	0
1.0936	89.557	206	2	2	2
1.0827	90.708	104	3	3	0
1.0425	95.275	162	4	1	1
1.0364	96.017	163	3	1	2
1.0271	97.177	110	4	2	0
1.0167	98.514	28	3	3	1
0.9703	105.099	58	4	2	1
0.9644	106.019	59	1	0	3
0.9438	109.406	60	1	1	3
0.9072	116.227	124	4	0	2
0.9009	117.527	125	5	1	0

9.5 Ethanol Solvent-Based Aerogels Using Different Solvent Purities

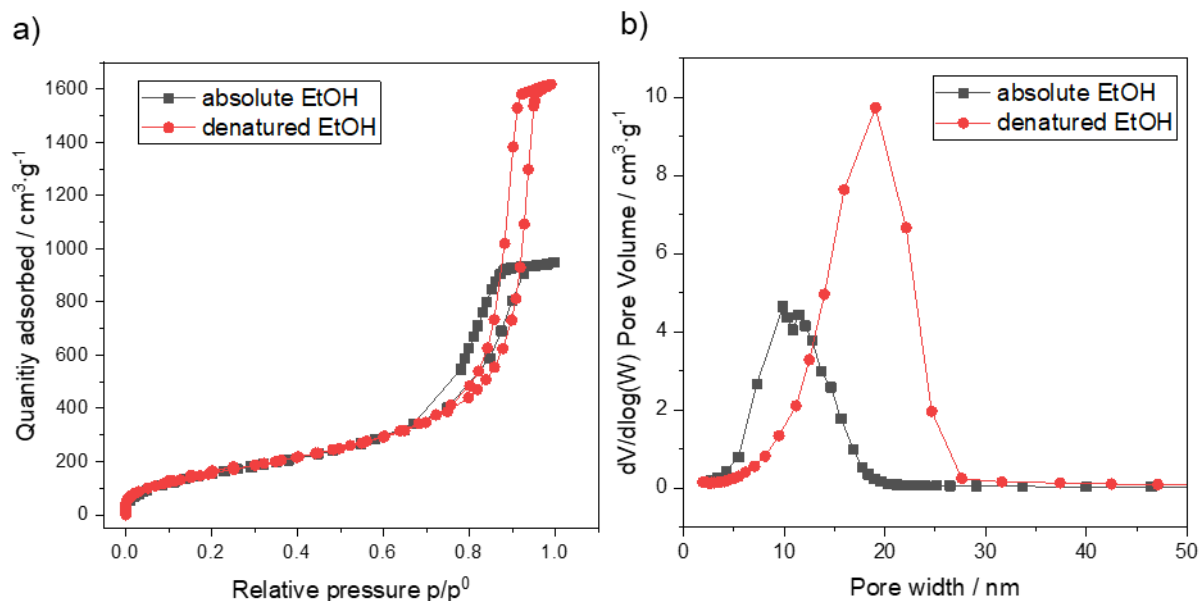


Figure 9.5-1: a) Isotherms and b) pore size distribution of the aerogel sample E2 synthesized using absol. EtOH (black) and denatured EtOH (red).

Table 9.5-1: Physisorption results of the aerogel sample E2 synthesized using absol. EtOH and denatured EtOH and purity of purchased EtOH.

sample	$S_{\text{BET}} / \text{m}^2 \cdot \text{g}^{-1}$	$V_{\text{P}} / \text{cm}^3 \cdot \text{g}^{-1}$	BJH value / nm	Distributor and purity of EtOH
E2/absolute EtOH	600	1.5	11	Roth, >99.9%, ROTISOLV HPLC gradient grade
E2/Denatured EtOH	600	2.5	19	CHEMSOLUTE, denatured with MEK, <i>i</i> PrOH, and Bitrex, 99.8%

9.6 SAXS Curve Fits

9.6.1 Wet Gel E2

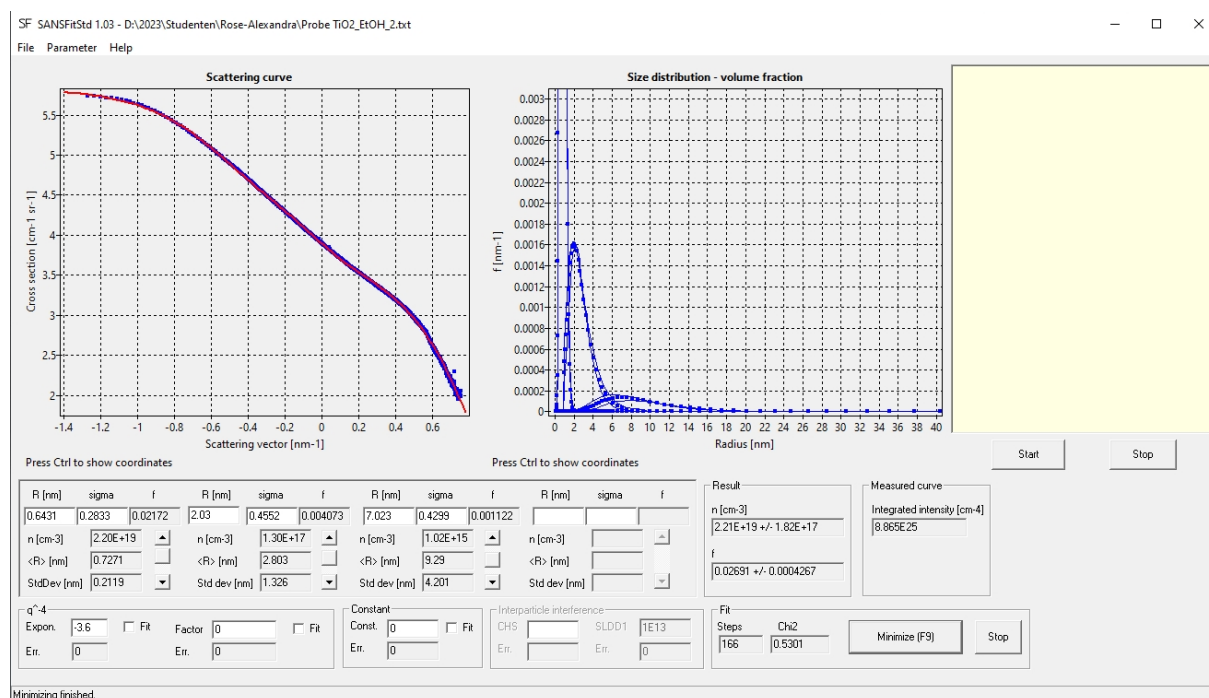


Figure 9.6-1: E2 SAXS analysis in terms of particle size distributions. The following fits are produced with the home-made software SANSFitStd104 on the basis of the two-phase model and multiple particle distributions. The first points of the curves, influenced by the beam stop, were removed from the curves before fitting. Shape of the distributions: lognormal. Shape of the particles: Spheres. No q^{-4} or constant contributions were added.

9.6.2 Wet Gel E5

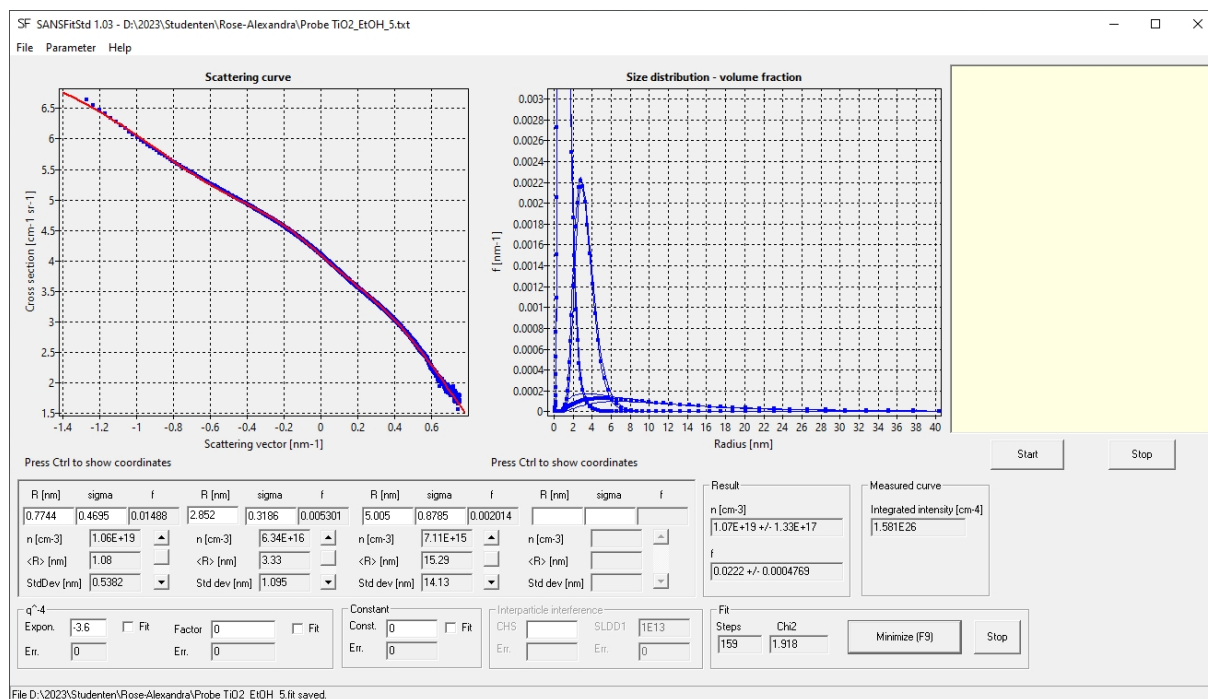


Figure 9.6-2: E5 SAXS analysis in terms of particle size distributions. The following fits are produced with the home-made software SANSFitStd104 on the basis of the two-phase model and multiple particle distributions. The first points of the curves, influenced by the beam stop, were removed from the curves before fitting. Shape of the distributions: lognormal. Shape of the particles: Spheres. No q^{-4} or constant contributions were added.

9.7 XPS

9.7.1 Aerogel Sample E5

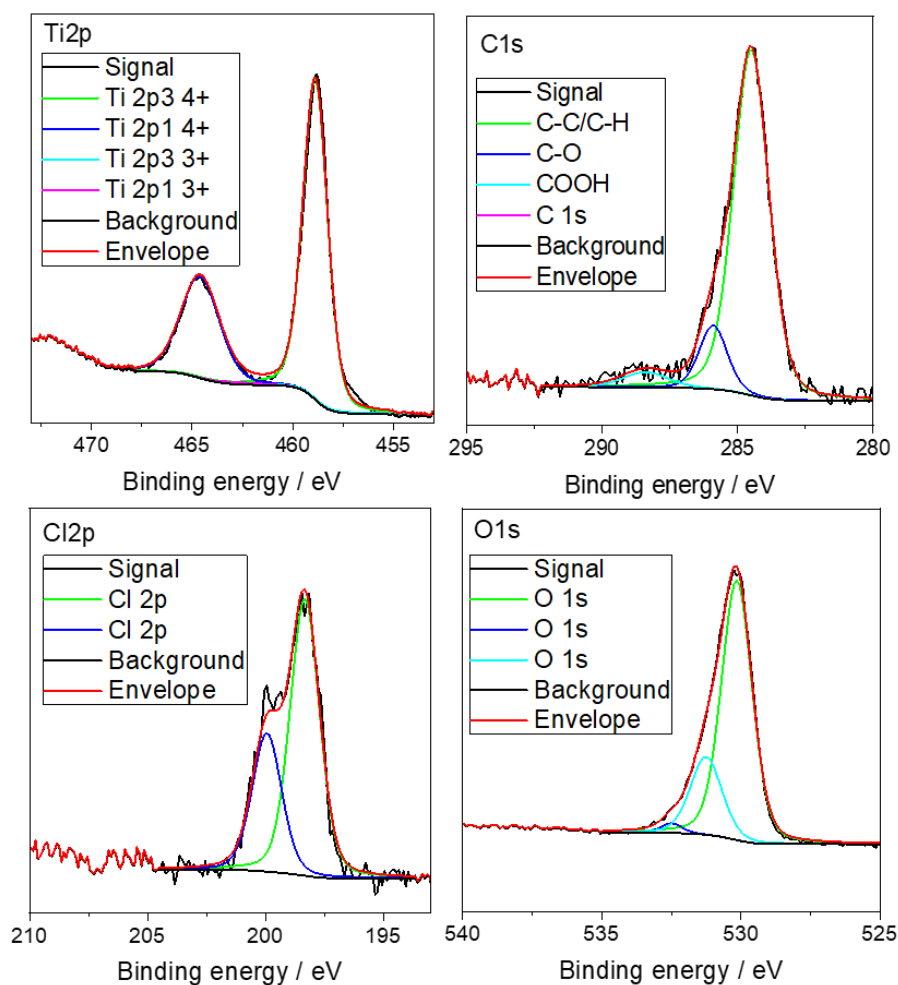


Figure 9.7-1: Ti2p, C1s, Cl2p, and O1s XPS spectra of the aerogel sample E5 (HCl:TTIP 0.27:1; based on absol. EtOH as solvent).

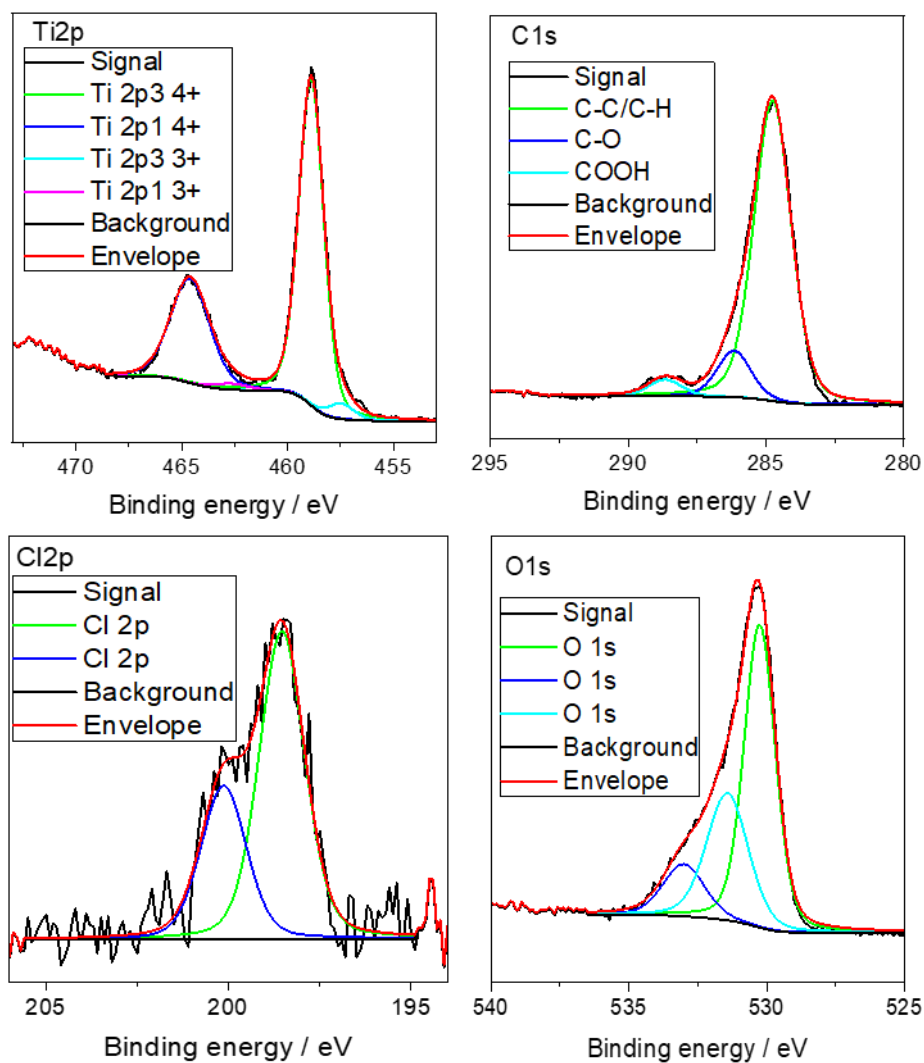
9.7.2 Aerogel Sample *i*P2

Figure 9.7-2: Ti2p, C1s, Cl2p, and O1s XPS spectra of the aerogel sample *i*P2 (HCl:TTIP 0.11:1).

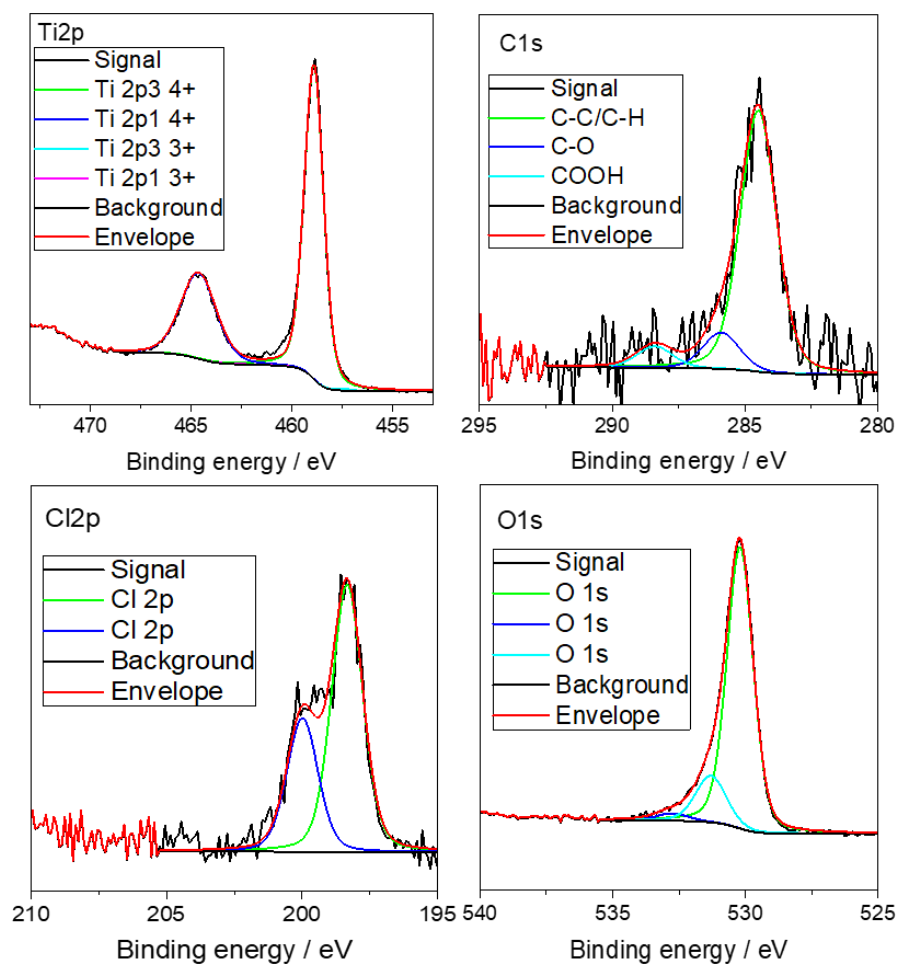
9.7.3 Aerogel Sample *iP5*

Figure 9.7-3: Ti2p, C1s, Cl2p, and O1s XPS spectra of the aerogel sample *iP5* (HCl:TTIP 0.27:1).

9.7.4 Calcined Aerogel Sample E2-A-300

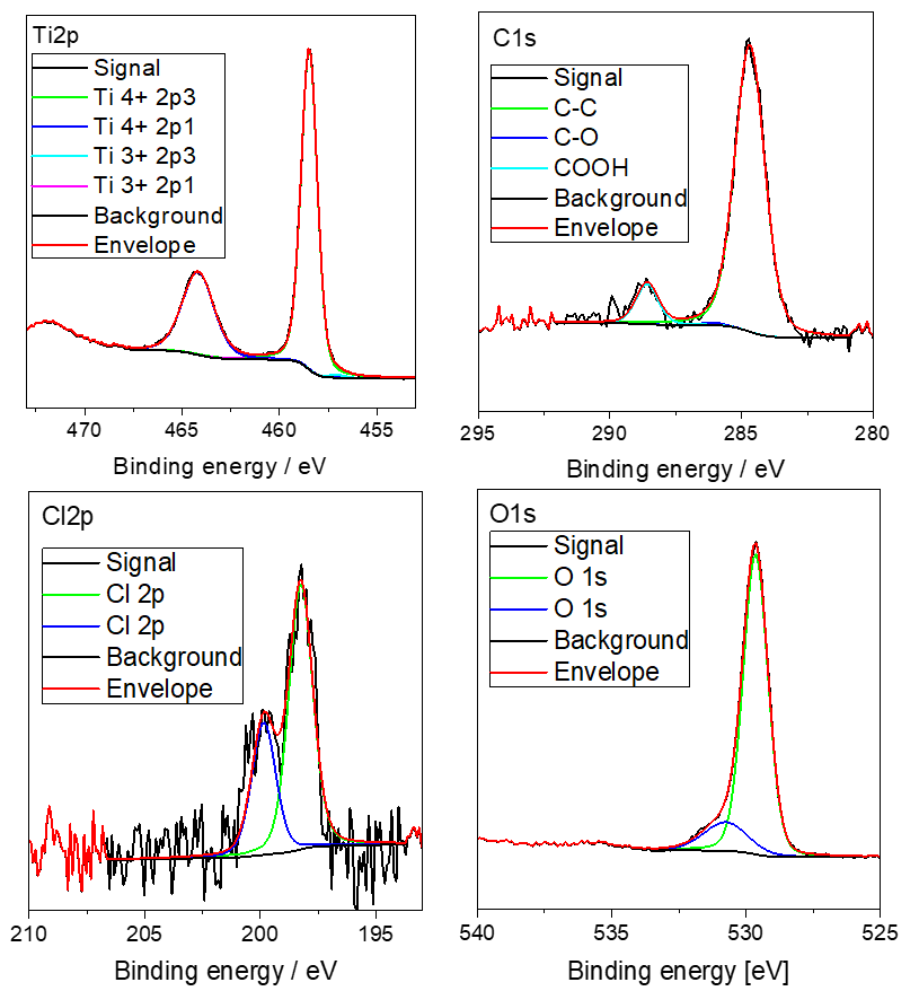


Figure 9.7-4: Ti2p, C1s, Cl2p, and O1s XPS spectra of the calcined aerogel sample E2-A-300.

9.7.5 Calcined Aerogel Sample E2-V-300

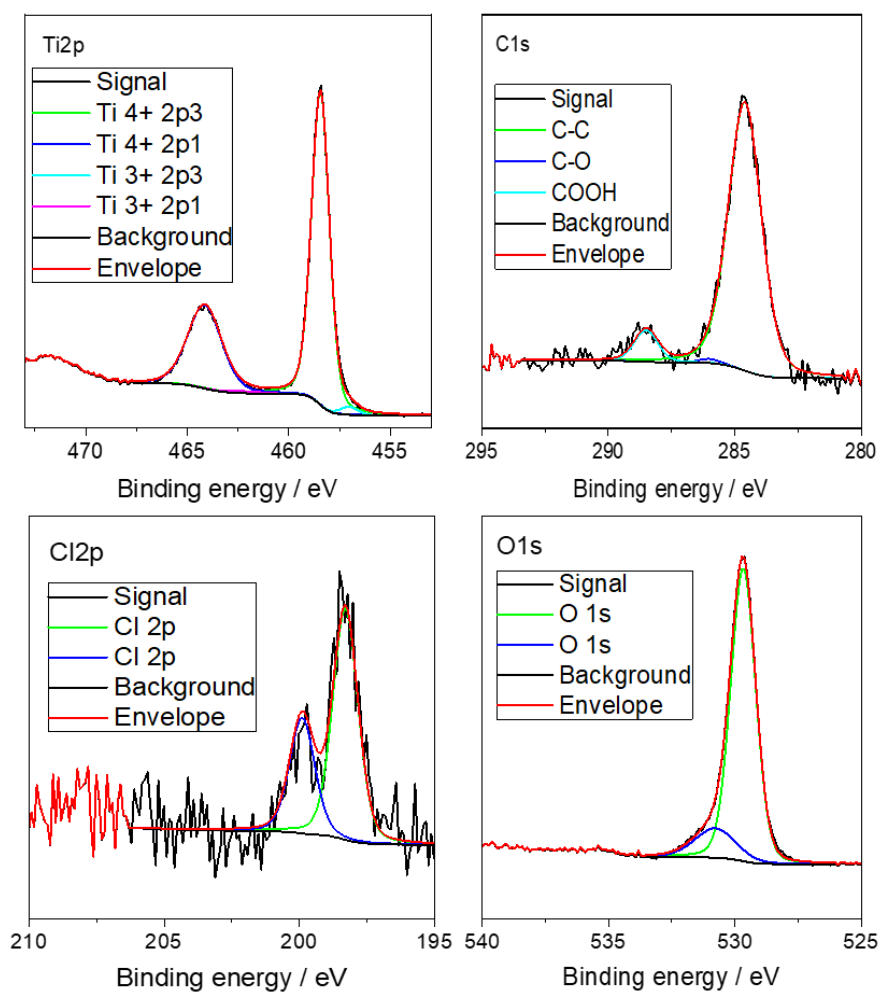


Figure 9.7-5: Ti2p, C1s, Cl2p, and O1s XPS spectra of the calcined aerogel sample E2-V-300.

9.8 UV-Vis/DRS – Tauc Plots and Kubelka-Munk Plots

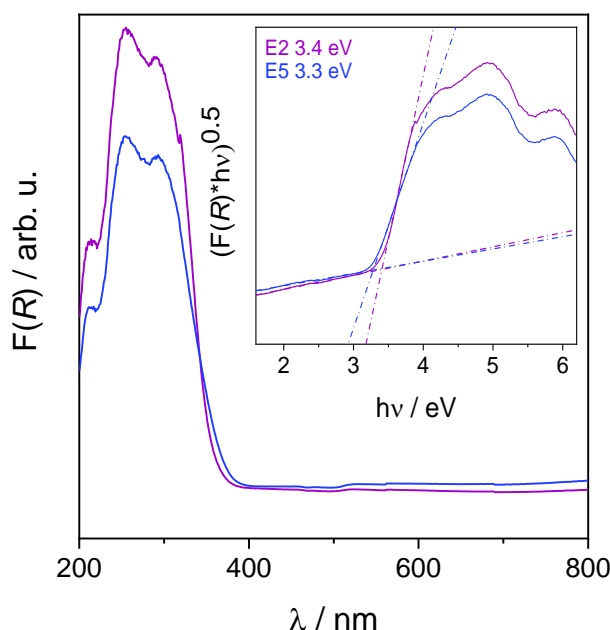


Figure 9.8-1: Kubelka-Munk UV-vis spectra and Tauc plots (inset) of the aerogel E2 (purple), and E5 (blue).

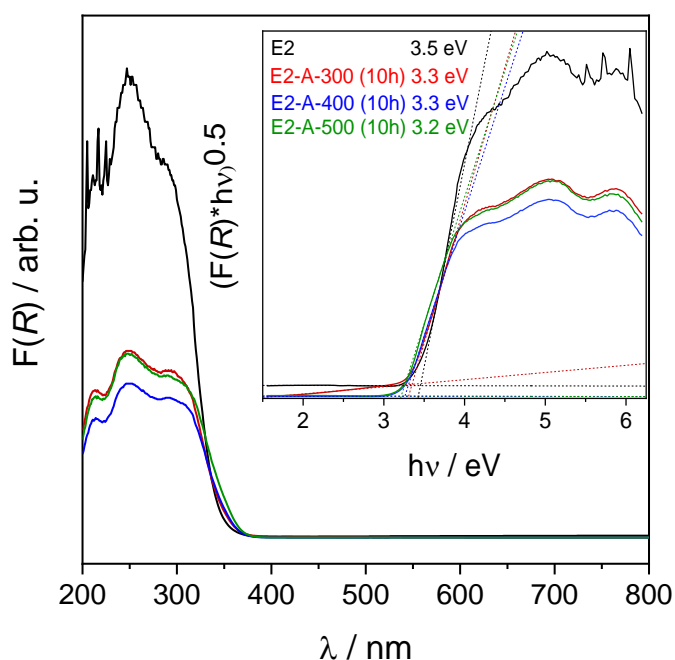


Figure 9.8-2: Kubelka-Munk UV-vis spectra and Tauc plots (inset) of the as-synthesized aerogel E2 (black), the 300 °C (red), the 400 °C (blue), and the 500 °C (green) calcined aerogels. Reprinted (adapted) with permission from A. Rose et al. Photocatalytic Activity and Electron Storage Capability of TiO₂ Aerogels with an Adjustable Surface Area. ACS Applied Energy Materials, 2022. 5(12): p. 14966-14978. Copyright 2022 American Chemical Society.

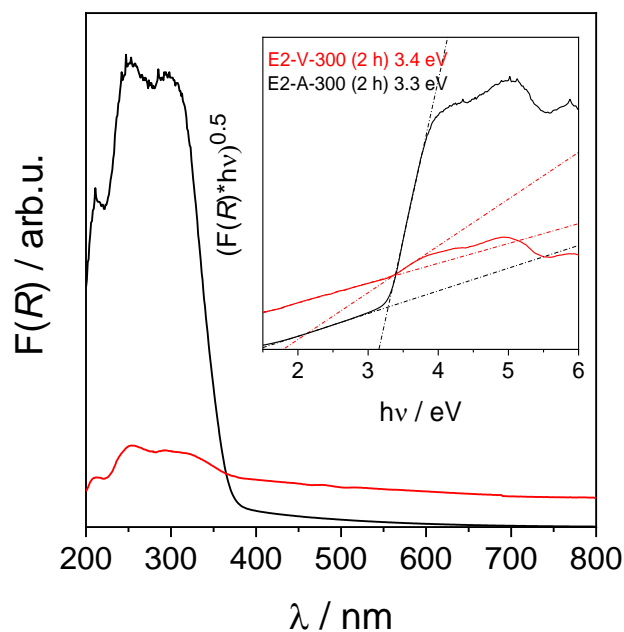


Figure 9.8-3: Kubelka-Munk UV-vis spectra and Tauc plots (inset) of at 300 °C in air calcined (E2-A-300) and in vacuum calcined (E2-V-300) aerogels.

9.9 $^1\text{H-NMR}$

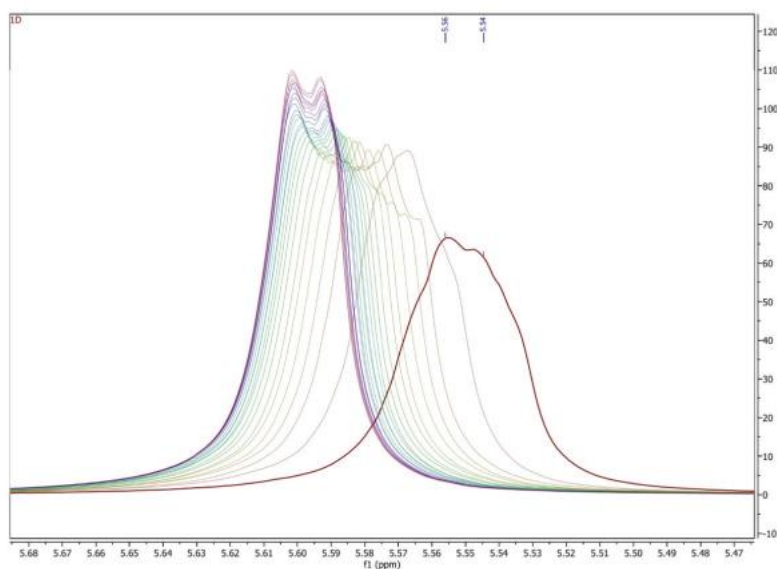


Figure 9.9-1: $^1\text{H-NMR}$ of TTIP in EtOH (80 MHz, no solvent); δ 5.54 (s), 5.56 (s). *In-situ* NMR measurement. O-H signals of EtOH (δ 5.54, 5.56) shift towards δ 5.60 over the course of five minutes indicating an exchange process of EtOH and *i*PrOH on TTIP. s = singlet.

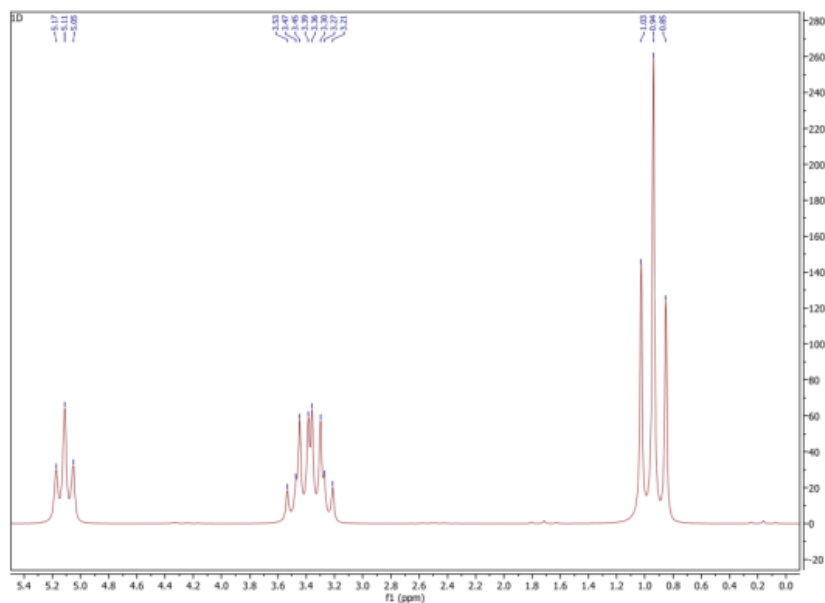


Figure 9.9-2: ^1H -NMR of EtOH (80 MHz, no solvent); δ 0.85- 1.03 (t), 3.21-3.53 (dq), 5.05-5.17 (t), t = triplet, dq = doublet of quartets.

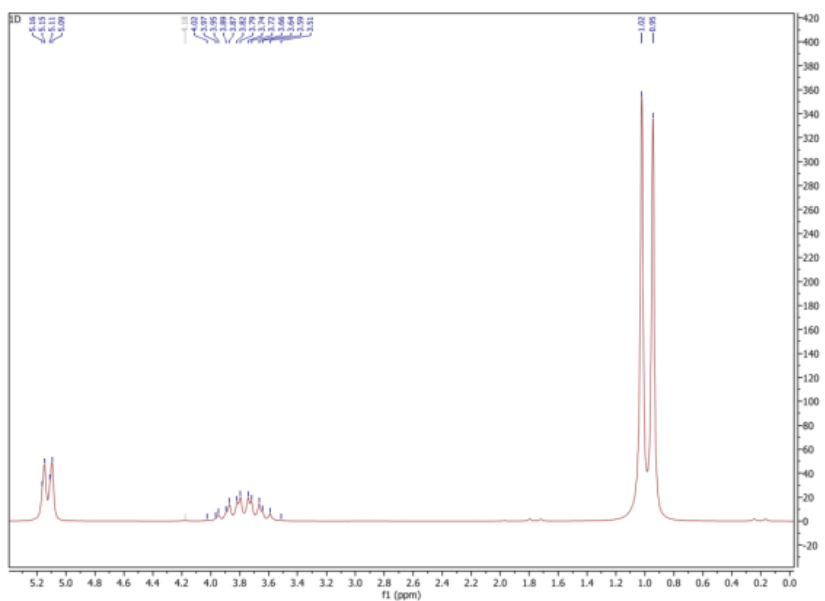


Figure 9.9-3: ^1H -NMR of *i*PrOH (80 MHz, no solvent); δ 0.94-1.02 (d), 3.51-4.18 (m), 5.09-5.16 (dd). d= doublet, m = multiplet, dd = doublet of doublets.

9.10.2 SEM images

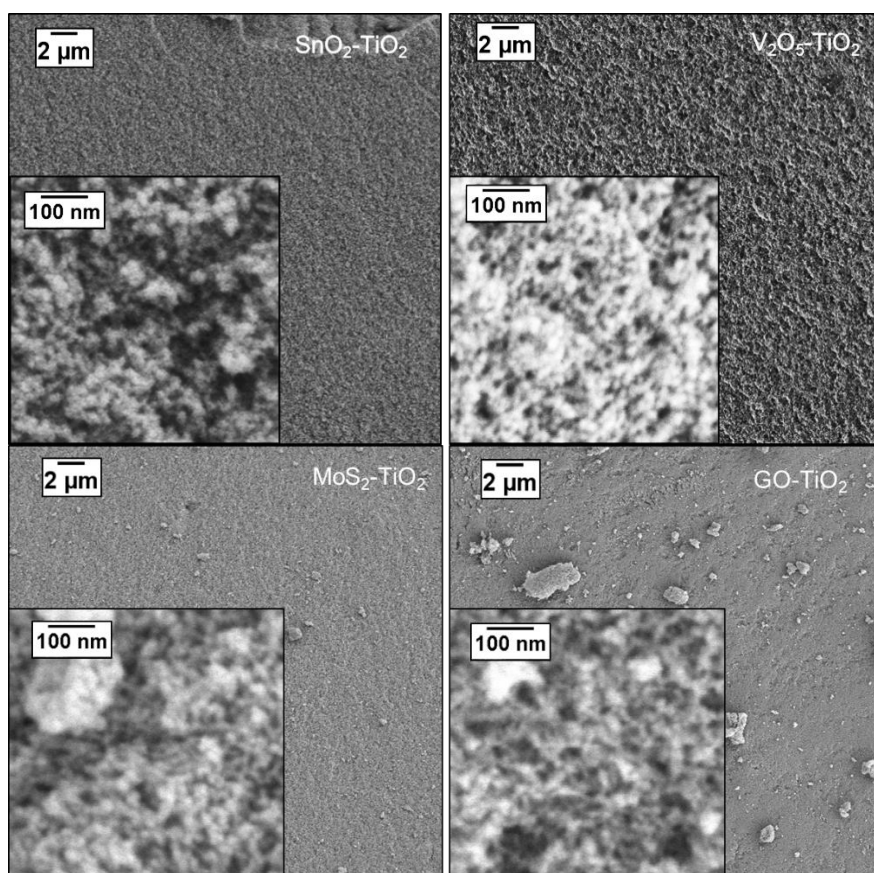


Figure 9.10-2: SEM images of mixed metal oxide and doped aerogel samples. The images were taken at low (2.000x) and high (100.000x) magnification shown as inset.

9.10.3 TEM images

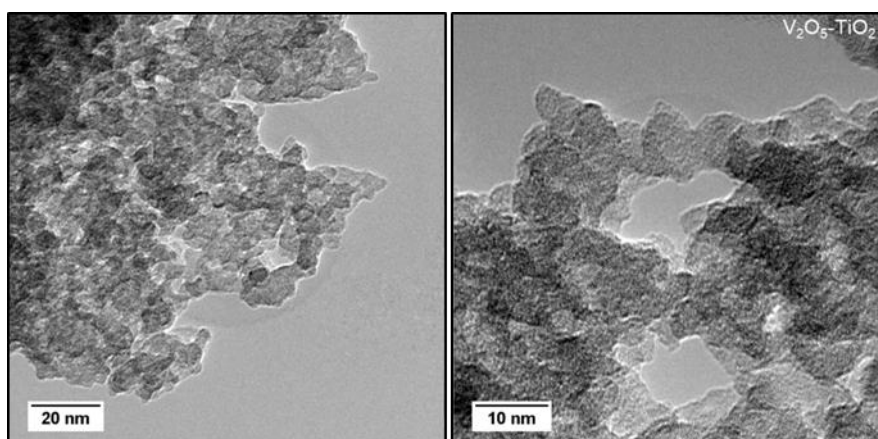
9.10.3.1 $\text{V}_2\text{O}_5\text{-TiO}_2$ 

Figure 9.10-3: TEM images of the $\text{V}_2\text{O}_5\text{-TiO}_2$ aerogel.

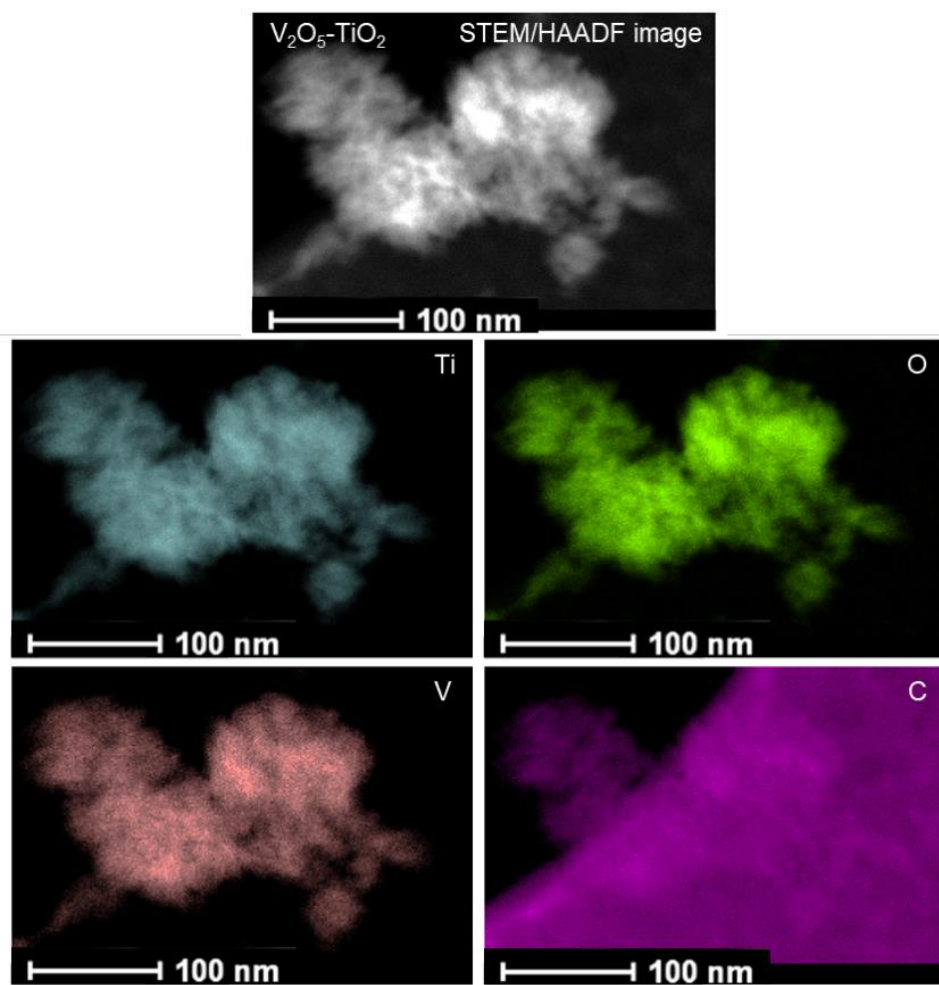


Figure 9.10-4: STEM/HAADF image and STEM-EDS elemental maps (Ti, O, V, C) of the V_2O_5 - TiO_2 aerogel.

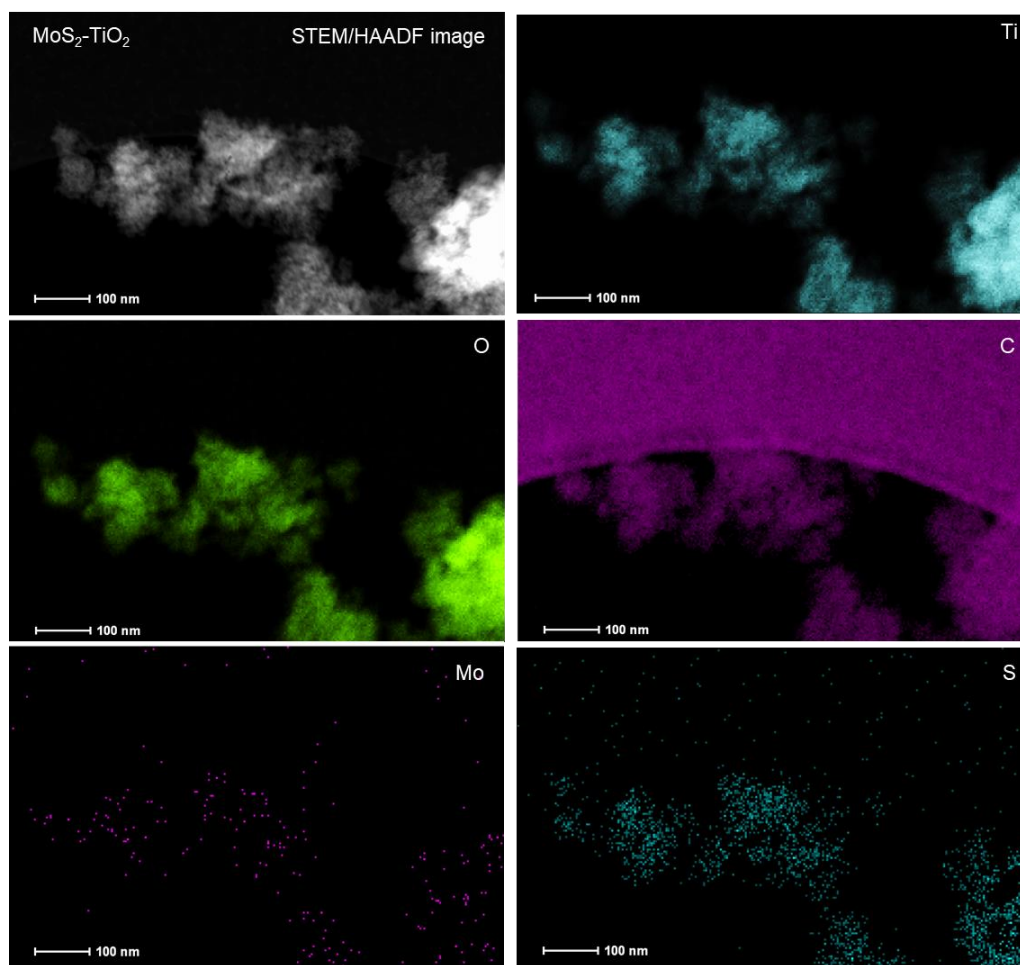
9.10.3.2 MoS₂-TiO₂

Figure 9.10-5: STEM/HAADF image and STEM-EDS elemental maps (Ti, O, C, Mo, S) of the MoS₂-TiO₂ aerogel.

9.10.4 Physisorption results

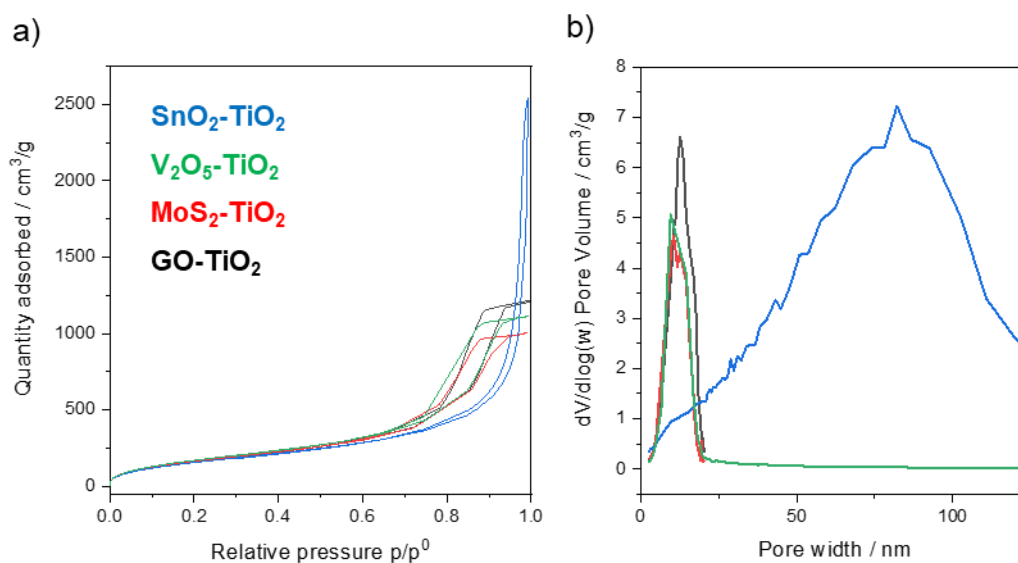


Figure 9.10-6: a) Isotherms and b) pore size distribution of mixed metal oxide and doped aerogels.

Table 9.10-1: Physisorption results of the mixed metal oxide and doped aerogels.

Sample	$S_{\text{BET}} / \text{m}^2 \cdot \text{g}^{-1}$	$V_{\text{P}} / \text{cm}^3 \cdot \text{g}^{-1}$	BJH value / nm
SnO ₂ -TiO ₂	610	3.9	83
V ₂ O ₅ -TiO ₂	669	1.7	10
MoS ₂ -TiO ₂	640	1.6	11
GO-TiO ₂	638	1.9	13

9.10.5 Crystallinity

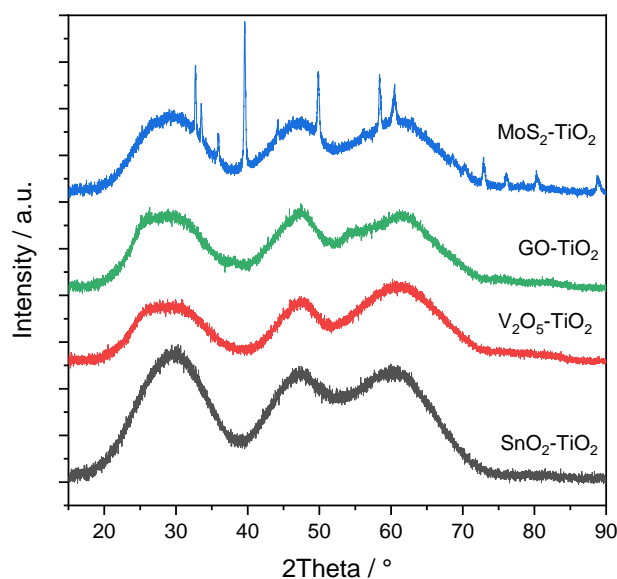


Figure 9.10-7: Diffractograms of the mixed metal oxide and doped aerogels.

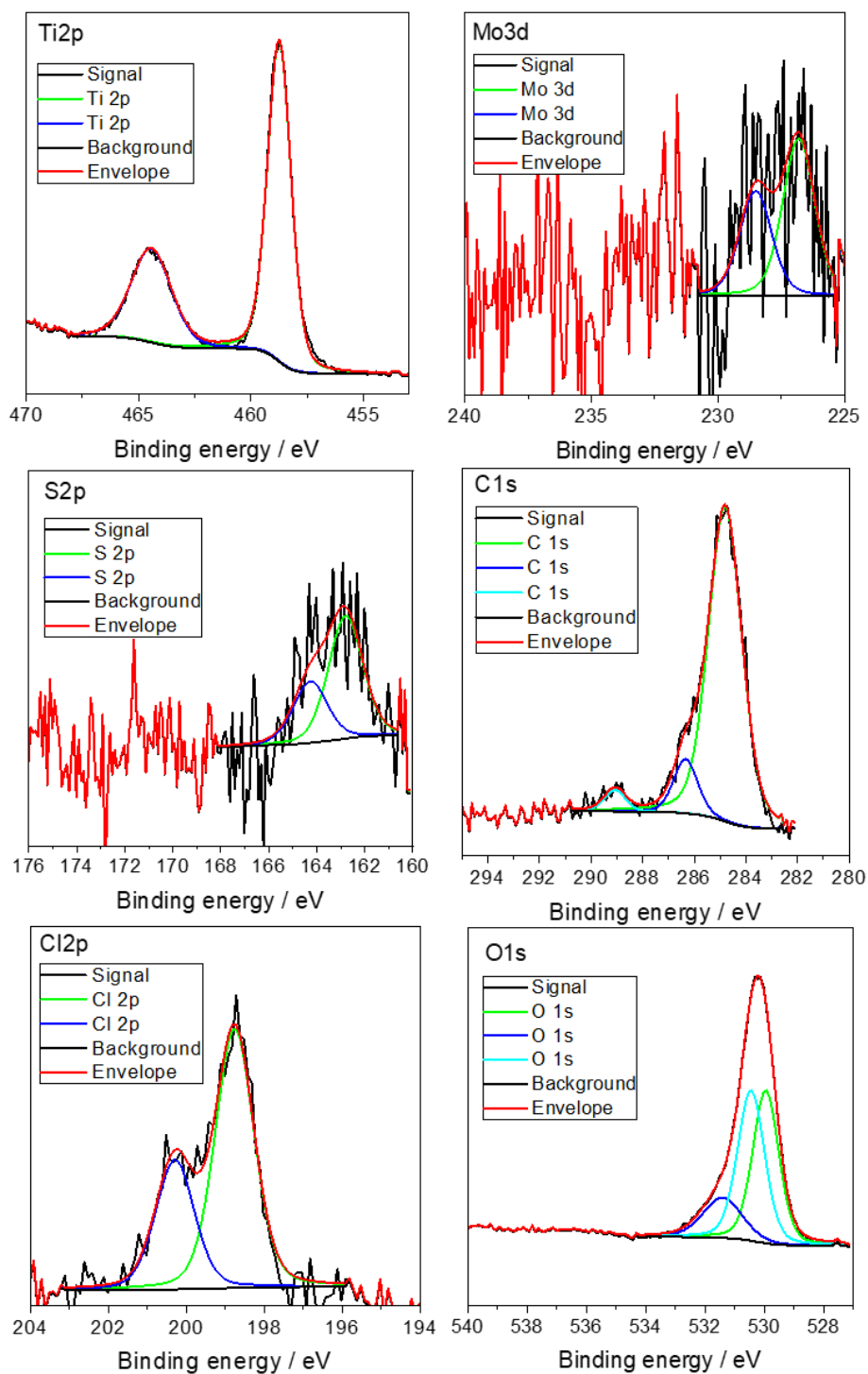
9.10.6 Chemical Composition

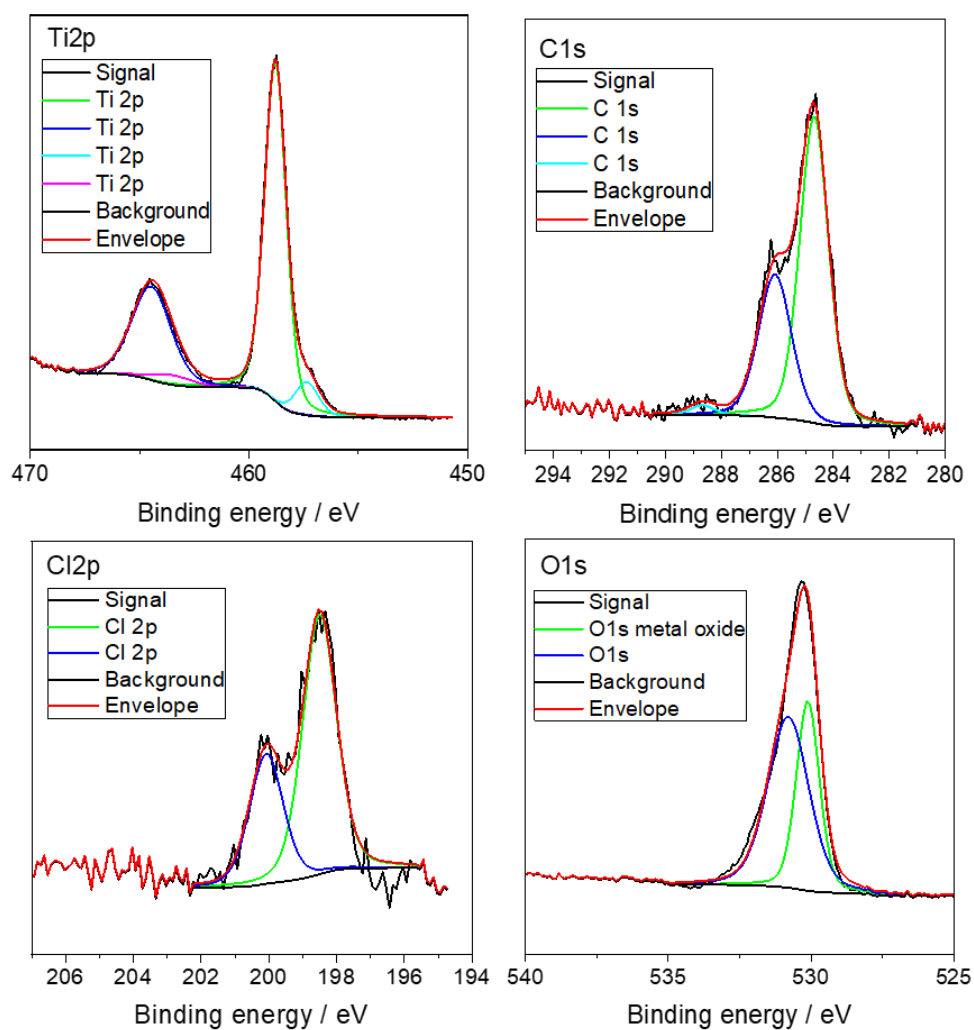
Table 9.10-2: Chemical composition of the mixed metal oxide and doped aerogels.

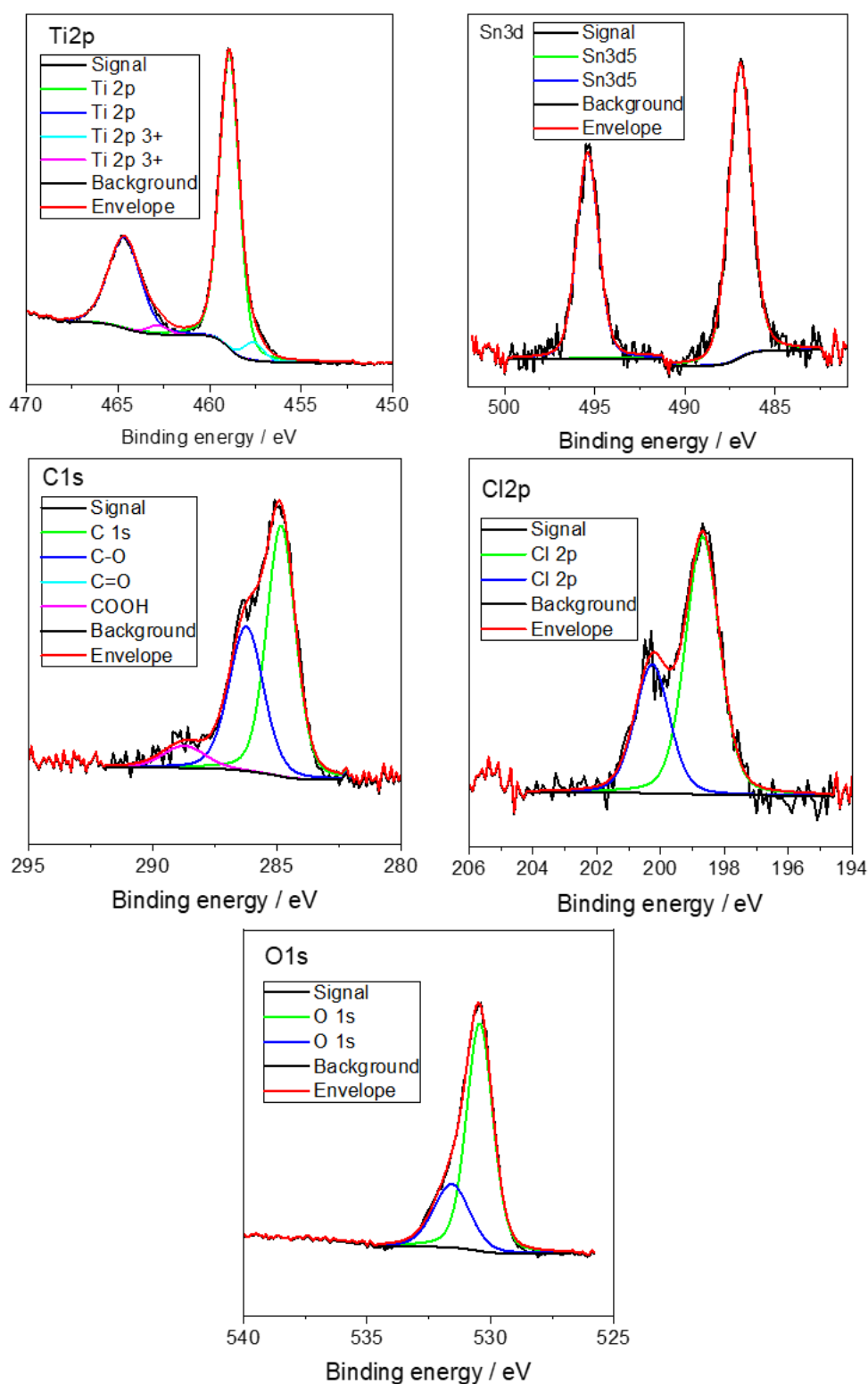
Sample	Ti / at. %	C / at. %	O / at. %	Cl / at. %	Sn / at. %	V / at. %	Mo / at. %	S / at. %
SnO ₂ -TiO ₂	19.29	22.77	52.98	2.31	1.16	-	-	-
V ₂ O ₅ -TiO ₂	23.17	27.45	45.97	2.61	-	0.80	-	-
MoS ₂ -TiO ₂	22.75	20.22	54.00	2.22	-	-	0.10	0.71
GO-TiO ₂	21.25	24.13	52.24	2.34	-	-	-	-

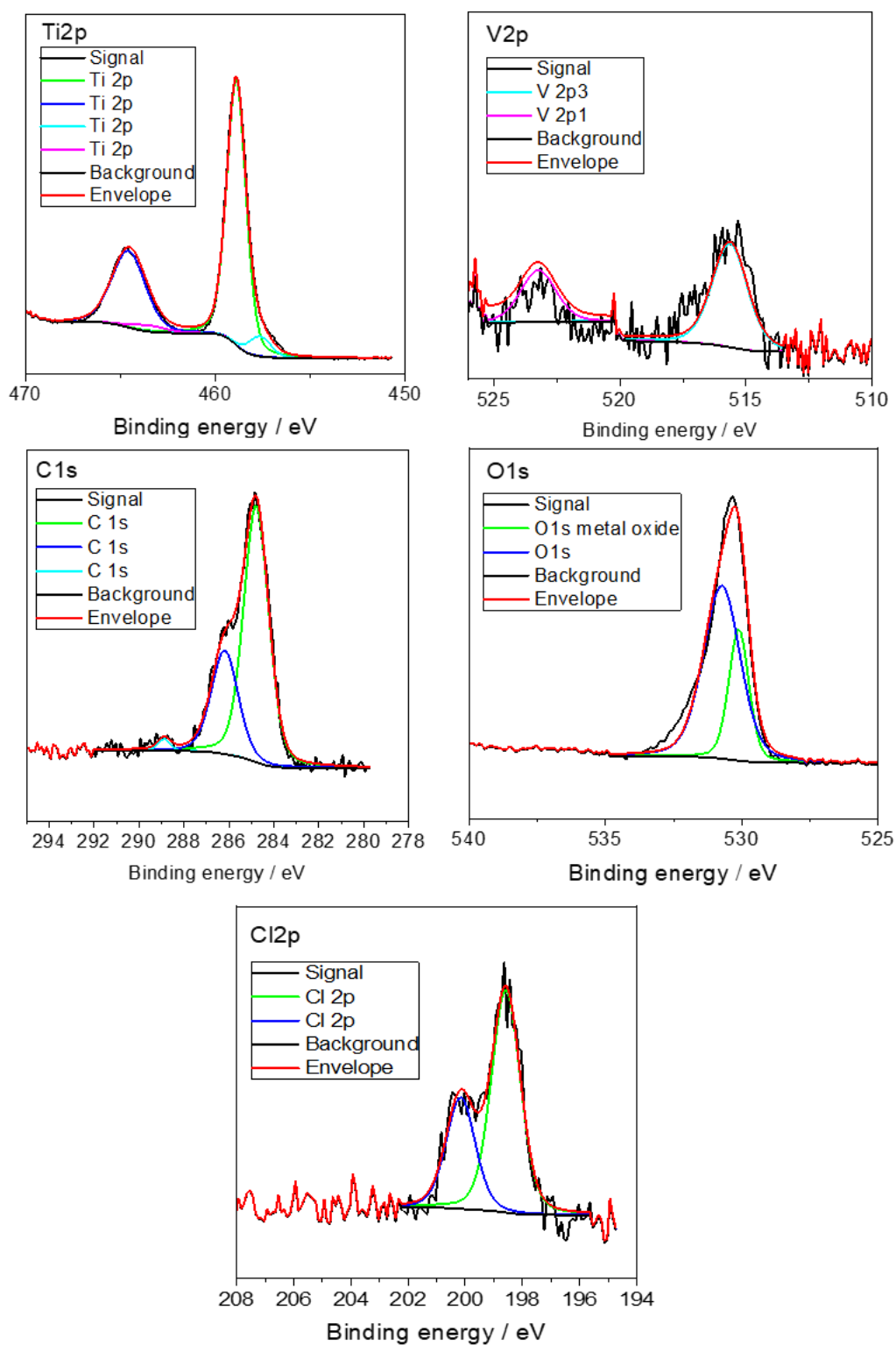
Table 9.10-3: Oxidation states and carbon species of the mixed metal oxide and doped aerogels.

Sample	Ti ³⁺	Ti ⁴⁺
SnO ₂ -TiO ₂	5.86	94.14
V ₂ O ₅ -TiO ₂	7.58	92.42
MoS ₂ -TiO ₂	0	100
GO-TiO ₂	9.76	90.24

9.10.6.1 MoS₂-TiO₂Figure 9.10-8: Ti2p, Mo3d, S2p, C1s, Cl2p, and O1s XPS spectra of the MoS₂-TiO₂ aerogel.

9.10.6.2 GO-TiO₂Figure 9.10-9: Ti2p, C1s, Cl2p, and O1s XPS spectra of the GO-TiO₂ aerogel.

9.10.6.3 SnO₂-TiO₂Figure 9.10-10: Ti2p, Sn3d, C1s, Cl2p, and O1s XPS spectra of the SnO₂-TiO₂ aerogel.

9.10.6.4 V_2O_5 - TiO_2 Figure 9.10-11: Ti2p, V2p, C1s, Cl2p, and O1s XPS spectra of the XPS V_2O_5 - TiO_2 aerogel.

9.10.7 Band Gap and VB Edge

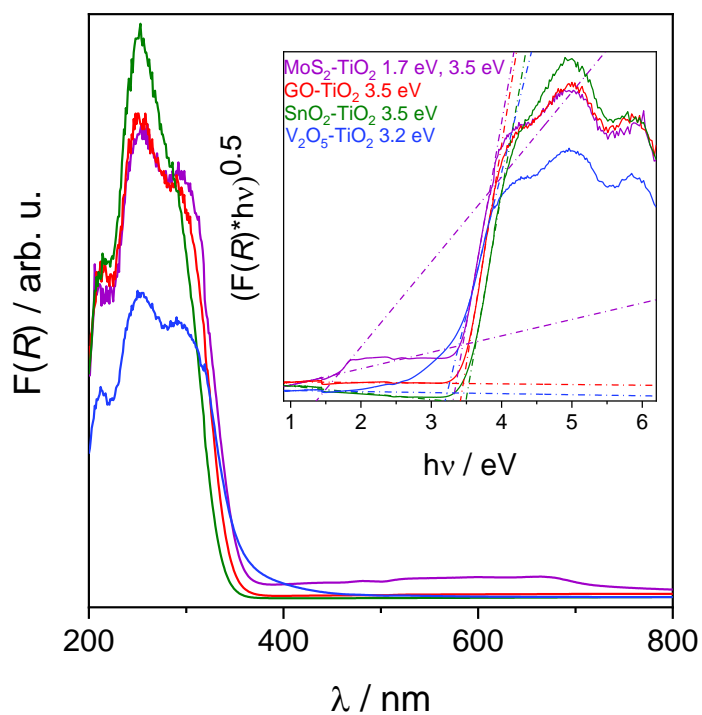


Figure 9.10-12: Kubelka-Munk UV-vis spectra and Tauc plots (inset) of the mixed metal oxide and doped aerogels.

Table 9.10-4: Band gap values, estimated VB and calculated CB of the mixed metal oxide aerogels.

Sample	Indirect band gap / eV	Upper VB edge / eV	Calculated CB edge / eV
SnO ₂ -TiO ₂	3.5	3.4	-0.1
V ₂ O ₅ -TiO ₂	3.2	3.3	-0.1
MoS ₂ -TiO ₂	1.7 (3.5)	1.6	-0.1
GO-TiO ₂	3.5	3.0	-0.5

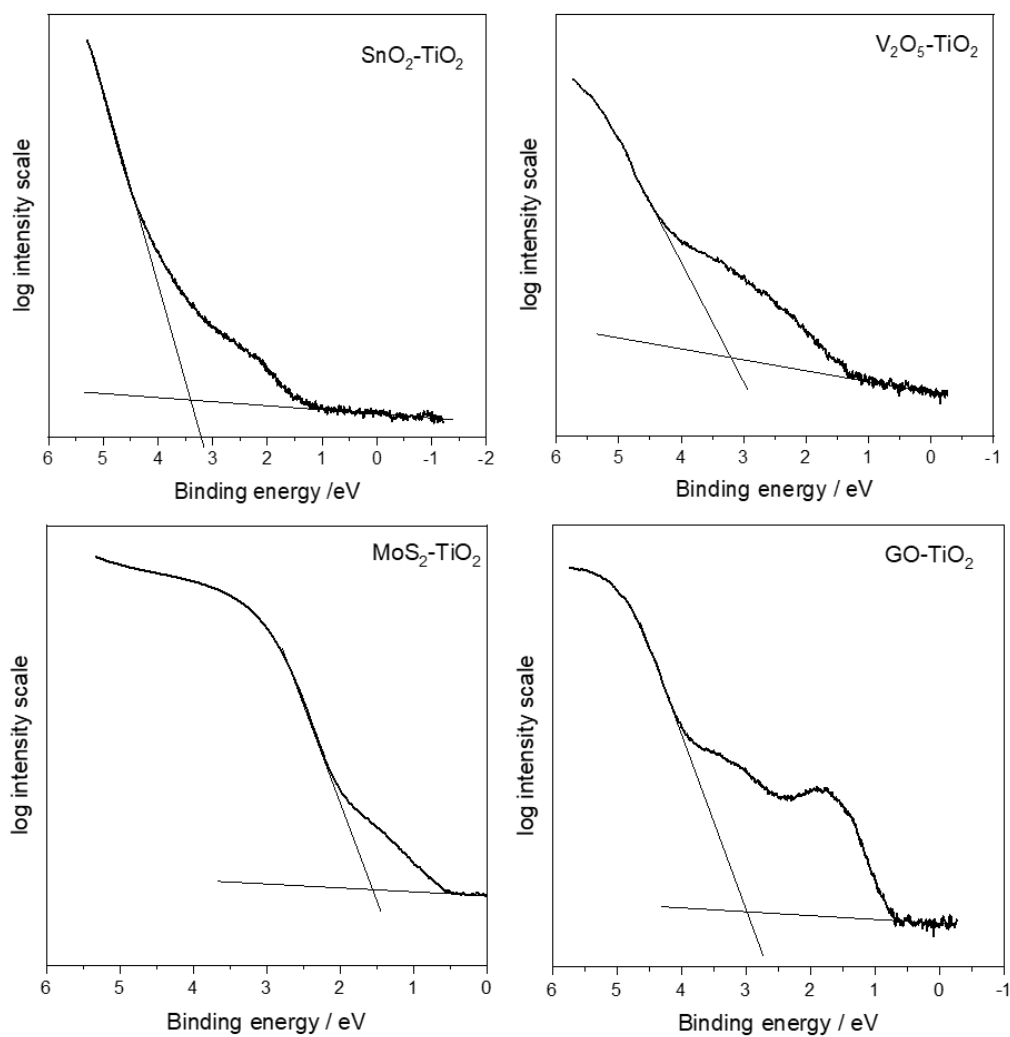


Figure 9.10-13: UPS spectra of the mixed metal oxide aerogels and extrapolation for the determination of the VB edge.

9.11 Eidesstattliche Erklärung

Hiermit versichere ich an Eides statt, dass ich die vorliegende Dissertation selbstständig und ohne die Benutzung anderer als der angegebenen Hilfsmittel und Literatur angefertigt habe. Alle Stellen, die wörtlich oder sinngemäß aus veröffentlichten und nicht veröffentlichten Werken dem Wortlaut oder dem Sinn nach entnommen wurden, sind als solche kenntlich gemacht. Ich versichere an Eides statt, dass diese Dissertation noch keiner anderen Fakultät oder Universität zur Prüfung vorgelegen hat; dass sie - abgesehen von unten angegebenen Teilpublikationen und eingebundenen Artikeln und Manuskripten - noch nicht veröffentlicht worden ist sowie, dass ich eine Veröffentlichung der Dissertation vor Abschluss der Promotion nicht ohne Genehmigung des Promotionsausschusses vornehmen werde. Die Bestimmungen dieser Ordnung sind mir bekannt. Darüber hinaus erkläre ich hiermit, dass ich die Ordnung zur Sicherung guter wissenschaftlicher Praxis und zum Umgang mit wissenschaftlichem Fehlverhalten der Universität zu Köln gelesen und sie bei der Durchführung der Dissertation zugrundeliegenden Arbeiten und der schriftlich verfassten Dissertation beachtet habe und verpflichte mich hiermit, die dort genannten Vorgaben bei allen wissenschaftlichen Tätigkeiten zu beachten und umzusetzen. Ich versichere, dass die eingereichte elektronische Fassung der eingereichten Druckfassung vollständig entspricht.

Teilpublikation:

A. Rose *et al.*, Photocatalytic Activity and Electron Storage Capability of TiO₂ Aerogels with an Adjustable Surface Area. ACS Applied Energy Materials, 2022. 5(12): p. 14966-14978.

Alexandra Rose

Köln, 22.09.2023

9.12 Publications and Conferences

Publications

Alexandra Rose, Anja Hofmann, Pascal Voepel, Barbara Milow and Roland Marschall, Photocatalytic Activity and Electron Storage Capability of TiO₂ Aerogels with an Adjustable Surface Area. ACS Applied Energy Materials, 2022. 5(12): p. 14966-14978.

Conferences

- February 2022 30th ATC Conference: Industrial Inorganic Chemistry – Materials and Processes and 2nd ATC PhD Student Workshop, Frankfurt/online, Deutschland.
Poster/Poster Pitch:
„Synthesis development of mixed metal oxide aerogels using sol-gel process for catalytic applications”
- September 2022 International Seminar on Aerogels, Hamburg, Deutschland.
Poster/Poster Pitch:
“Novel acid-catalyzed sol-gel synthesis route to control the crystallinity and phase formation of highly porous TiO₂ aerogels”
- October 2022 7th International Conference on Multifunctional, Hybrid and nanomaterials, Genua, Italy.
Poster:
“Tunable sol-gel synthesis of TiO₂ aerogels with adjustable surface area and open porosity applied in photocatalytic reactions”

Patents

- August 2022 Herstellung von Kohlenstoff enthaltenden kristallinen Titanoxidaerogelen mit großer Oberfläche und großem Porenvolumen
A. Rose, P. Vöpel, B. Milow,
Application-Nr. 10 2022 121 099.5
eingereicht am 22. August 2022

9.13 Zugänglichkeit von Daten und Materialien

Die Dissertation beinhaltet die Gewinnung von Primärdaten oder die Analyse solcher Daten oder die Reproduzierbarkeit der in der Dissertation dargestellten Ergebnisse setzt die Verfügbarkeit von Datenanalysen, Versuchsprotokollen oder Probenmaterial voraus. Die Daten sind auf dem internen Laufwerk des Instituts für Werkstoff-Forschung (DLR Köln) gesichert (inklusive Backups), sowie die hergestellten Proben archiviert, und den Personen der Abteilung WF-AEG zugänglich (entsprechend den Vorgaben der Erstbetreuerin).

9.14 Lebenslauf

Persönliche Daten:

Name: Alexandra Rose (geb. Ott)

Email: alexandra.rose@dlr.de

Schul- und Hochschulbildung:

- 01/2019-12/2023 Promotion in Anorganischer Chemie (Dr. rer. nat.)
Deutsches Zentrum für Luft- und Raumfahrt e.V. (DLR)
Institut für Werkstoff-Forschung & Universität zu Köln
 Dissertation: "Photocatalytically active aerogels - Development and characterization of (semi-)crystalline titania"
- 01/2020-01/2021 Elternzeit
- 10/2016-10/2018 Masterstudium in Chemie (M.Sc.)
Universität zu Köln
- Masterarbeit: „CMAS/Volcanic ash resistant coatings for TBC and EBC applications based on a novel Y-Si-Fe oxide system.“
 Erasmus-Auslandssemester 09/2017-02/2018
École nationale supérieure de chimie de Montpellier (ENSCM)
- 08/2012-07/2016 Kooperative Ingenieurausbildung zur Chemielaborantin (IHK) und Bachelor of Science in Chemie und Biotechnologie (B.Sc.)
Hochschule Niederrhein & Momentive & Currenta GmbH & Co. OHG
- Bachelorarbeit: „Silicone rubber for hydrosilylation cure - Scale-up for continuous manufacturing”
- 09/2003-07/2012 Allgemeine Hochschulreife
Gymnasium Renningen

Berufserfahrung:

- 11/2018-jetzt Institut für Werkstoff-Forschung (DLR)
 Abteilung Aerogele und Aerogelverbundwerkstoffe
 Wissenschaftliche Mitarbeiterin
- 09/2016-09/2017 Momentive in Leverkusen, Abteilung Technical Service Elastomere,
 Werksstudentin
- 02/2016-07/2016 Momentive in Lostock (UK), Abteilung Elastomere
 Werksstudentin
- 02/2015-03/2015 & 07/2015-08/2015 Momentive in Lostock (UK), Abteilung Elastomere
 Werksstudentin